

# ALTERNATIVE REDOX SYSTEMS FOR THE DYE-SENSITIZED SOLAR CELL

THÈSE N° 2955 (2004)

PRÉSENTÉE À LA FACULTÉ SCIENCES DE BASE

Institut des sciences et ingénierie chimiques

SECTION DE CHIMIE ET GÉNIE CHIMIQUE

ÉCOLE POLYTECHNIQUE FÉDÉRALE DE LAUSANNE

POUR L'OBTENTION DU GRADE DE DOCTEUR ÈS SCIENCES

PAR

**Hervé NUSBAUMER**

ingénieur chimiste diplômé EPF  
de nationalité suisse et originaire de Develier (JU)

acceptée sur proposition du jury:

Prof. M. Grätzel, directeur de thèse

Prof. C. Bignozzi, rapporteur

Prof. C. Comninellis, rapporteur

Dr A. Hagfeldt, rapporteur

Lausanne, EPFL  
2004



*To my wife Catherine*



# Acknowledgments

First of all, I gratefully acknowledge Prof. Michael Grätzel who immediately accepted me in his group and gave me the opportunity to freely work on the subject I had chosen. I also gratefully acknowledge Dr. Oliver Kohle for persuading me to begin this PhD thesis and for the help he gave me all along this work.

I would like to thank all the members of the Laboratory of Photonics and the Interfaces who have contributed to this work. In particular:

- Jacques-Edouard Moser, for all the laser experiments and fruitful discussions on kinetics we had together,
- Shaik M. Zakeeruddin, for the supply of various cobalt complexes and sensitizers as well as profitable discussions,
- Pascal Comte and Raphael Charvet for all the work they carried out on the TiO<sub>2</sub> paste production and different layers preparation,
- Robin Humphry-Baker, for his help with the photoelectrochemical setups, with the Igor software and for correcting part of this report
- Paul Liska, for its initiation to the fabrication and measurement of the dye-sensitized solar cells and its constant help on technical points
- Peng Wang, for his great knowledge in electrochemistry and all the councils he provided me on that subject,
- Pierre Infelta, for his book of thermodynamics, his help with Igor and all computer related problems,
- Peter Péchy, for providing me with some chemical compounds and helping me with the NMR measurements,
- Jessica Krüger, for her council and helps on the silver effect,
- Anthony Burke, for correcting a great part of this report.
- A special thanks to our secretaries, Ms. Gourdou, Ms. Peter, and Ms. Gonthier, for their administrative assistance.

All the mechanical and electronic workshop staffs are acknowledged for the permanent help they gave me.

Dr. David Firmin and Nicolas Eugster are gratefully acknowledged for their help in electrochemical experiments.

I would like to acknowledge Dr. Valery Shklover and Dr. Yuri Slovokhotov for having done all the x-ray, powder x-ray and XPS measurements.

I finally also would like to thank many other friends, for their assistance, for listening to my complaints and particularly for all the fun we had during this period: Robert, Isabelle, Sorina, Florentina, Anne, Christophe, Séverine, Nathalie, Bernard, Alexis, Franck, Udo, Seigo and many other colleagues of the EPFL.

## Abstract

Due to their high efficiencies and their potentially low production costs, dye-sensitized solar cells (DSSC) have attracted much attention during the last few years. The technology is based on a layer made of mesoscopic  $\text{TiO}_2$  film which significantly increases the optical path for light harvesting by the surface-anchored sensitizer molecules, whilst keeping an efficient contact with the electrolytic solution. These sensitizer molecules are often based on ruthenium polypyridyl complexes because of their high absorption coefficients in the visible, but any dye could be used to sensitize the semiconducting  $\text{TiO}_2$ . The standard DSSC usually contain organic electrolytes with dissolved triiodide/iodide as the redox couple. Cells based on alternative electrolytes have been developed and were used in early DSSC designs, but showed somehow deceiving photovoltaic performances. Until now, endeavors to increase the photovoltage of dye-sensitized nanocrystalline cells by replacing iodide by a one-electron, outer-sphere redox couple with a more positive oxidation potential have not succeeded. This has been largely due to limitations imposed by the dark current and the slow diffusion of the alternate mediator.

The work presented here focused on finding efficient alternative redox couples for the DSSC, able to rival the classical triiodide/iodide couple. The tested compounds were triarylaminines, platinum complexes and cobalt complexes.

Triarylaminines and platinum complexes proved considerably less effective than the classical couple in term of photoelectrochemical efficiencies. Cobalt complexes however displayed far more interesting behavior. The experiments carried out demonstrated that the  $[\text{Co}(\text{bip})_2]^{3+/2+}$  complexes were the most suitable candidates to be used as redox mediators as their photoelectrochemical and kinetic behavior rivaled those of the triiodide/iodide redox couple. The system however had to be optimized to reach high efficiencies. Heteroleptic dyes incorporating long alkyl chains were found to be the most appropriate category of dye, boosting further the DSSC efficiency by reducing the dark current within the cells. Co-grafting the sensitizer and co-adsorbent led to an improved photovoltaic efficiency through the increased photocurrent. Silver addition in the dye solution also leads to a global improvement of the photovoltaic parameters. To avoid diffusion problems with the large molecules in the electrolyte, very thin nanocrystalline  $\text{TiO}_2$  layers had to be employed. A  $3 \mu\text{m}$  thick nanoporous layer with a  $3 \mu\text{m}$  scattering layer was found to be optimal. As cobalt complexes may undergo

electrochemical processes on the SnO<sub>2</sub> layer of the photoelectrode, a blocking layer of compact TiO<sub>2</sub> was used to reduce the dark current. The electrochemical regeneration of the cobalt complexes with the SnO<sub>2</sub> is not fast enough to support cell function and the counter electrode must be covered either with platinum or gold layer to ensure a good fill factor.

The optimization of the electrolyte itself mainly concerned the choice of the solvent, the redox mediator concentration, the best degree of oxidation, the additives that can be used to improve the photovoltaic parameters and finally how to increase the redox couple solubility.

The best efficiencies were achieved with an acetonitrile/ethylene carbonate (2:3) solvent mixture, with a total redox mediator concentration between 0.10 to 0.15 M. If 10% of this total concentration is oxidized, the current density reaches its maximum whilst having a negligible effect on the photovoltage.

4-*tert*-butylpyridine (TBP) and lithium perchlorate were tried as additives in the electrolyte, as TBP increases the photovoltage and Li<sup>+</sup> the photocurrent. The optimal concentrations of these two additives was found to be around 0.05 M TBP and 0.1 M LiClO<sub>4</sub> for an electrolyte having a total cobalt complex concentration of 0.1 M.

Mass-transport within the cell is the limiting factor for high currents when using cobalt complexes as redox mediators. Attempts to reduce the solvent viscosity by using alternative solvents to the acetonitrile/ethylene carbonate mixture were not successful. One way to solve the diffusion problem was to irradiate the cell from the counter electrode side. This method works well at high irradiation intensities. Finally, reduction of the distance between the electrodes also enhances diffusion.

The use of [Co(bip)<sub>2</sub>]<sup>3+/2+</sup> complexes, with appropriate dyes and taking into account the optimizations already described above, allowed efficiencies of 8% under an irradiance of 95 W · m<sup>-2</sup>, as well as *IPCEs* over 80% at 540 nm to be obtained. At full sun, efficiencies of over 4% were reached, with short circuit current densities of 9.5 mA · cm<sup>-2</sup> and open circuit voltages of the order of 860 mV.



## Résumé

Les cellules solaires à colorant ont été beaucoup étudiées ces dernières années du fait de leur bonne efficacité et de leur potentiel de production à bas coûts. La technologie à la base de ces cellules repose sur une fine couche d'oxyde de titane ( $\text{TiO}_2$ ) mesoporeux déposée sur une plaque de verre conductrice. De part sa porosité, cette couche, couverte de molécules sensibles à la lumière, permet d'accroître de façon significative le chemin optique et de ce fait d'améliorer la capture de la lumière, ceci tout en conservant une grande surface de contact avec la solution électrolytique. Les molécules sensibilisatrices adsorbées sur le  $\text{TiO}_2$  sont souvent basées sur des complexes de ruthénium polypyridyl, leur coefficient d'absorption étant élevé dans le visible. Habituellement, les cellules solaires à colorant sont remplies avec des électrolytes organiques contenant le couple redox triiodure/iodure. Bien que des cellules solaires basées sur des électrolytes alternatifs fussent développées par le passé, elles n'ont souvent donné que des rendements photovoltaïques décevants. Jusqu'à présent, les tentatives pour accroître la tension des cellules solaires à colorant en remplaçant le iodure par un couple redox doté d'un potentiel d'oxydation plus élevé n'ont donné que peu de résultats, principalement à cause des limitations imposées par le courant au noir et de la lente diffusion du couple redox.

Le travail présenté ici se concentre sur la recherche et l'optimisation de couples redox alternatifs capables de rivaliser avec le couple classique triiodure/iodure. Des triarylamines, des complexes de platine et des complexes de cobalt ont été testés à cet effet.

Contrairement aux complexes de cobalt, les triarylamines et les complexes de platine n'ont pas fournis de rendements photoélectrochimiques compétitifs par rapport au couple classique. Les expériences réalisées durant ce travail ont montré que les complexes  $[\text{Co}(\text{bip})_2]^{3+/2+}$  sont les candidats les mieux à même d'être utilisés comme médiateurs redox. En effet, tant leur comportement photoélectrochimique que cinétique peut rivaliser avec ceux du couple triiodure/iodure. Afin d'atteindre des rendements intéressants, plusieurs optimisations du système ont dû être faites. Il s'est par exemple avéré que la catégorie de sensibilisateurs la plus appropriée était celle des colorants hétéroleptiques. En utilisant des colorants ayant de chaînes alkyl relativement longues, le rendement des cellules solaires a pu encore être amélioré. De plus, l'adsorption simultanée du colorant et d'un co-adsorbeur a permis d'accroître le photocourant. Finalement, l'addition de ions  $\text{Ag}^+$  à la solution de colorant a aussi permis l'amélioration

globale des paramètres photovoltaïques. Des problèmes de diffusion apparaissent lorsque la taille des molécules du médiateur redox est importante. Dès lors, des couches de  $\text{TiO}_2$  nanocristallin très fines ont dûes être employées. L'optimum a été trouvé pour des couches nanoporeuses de  $3 \mu\text{m}$  d'épaisseur et des couches diffusantes de  $3 \mu\text{m}$ . Comme des réactions électrochimiques peuvent avoir lieu entre les complexes de cobalt et le  $\text{SnO}_2$  déposé sur les supports en verre, une couche bloquante de  $\text{TiO}_2$  est nécessaire pour diminuer le courant au noir. Cependant, même si ces réactions sont observées, elles ne sont pas assez rapides pour se passer d'électrocatalyste sur la contre électrode et c'est pourquoi cette dernière doit être couverte d'une couche de platine ou d'or.

L'optimisation de l'électrolyte lui-même s'est faite principalement par le choix du solvant, la concentration du médiateur redox réduit et oxydé, les additifs pouvant être utilisés pour améliorer les paramètres photovoltaïques et finalement la stratégie mise en place pour accroître la solubilité du couple redox.

Les meilleurs rendements ont été obtenus en utilisant le mélange de solvants acétonitrile/éthylène carbonate (2:3). La concentration totale du médiateur redox est optimale lorsqu'elle est comprise entre 0.10 M et 0.15 M. Si 10% de cette concentration totale est oxydée, le photocourant atteint sont maximum et la tension se maintient à des valeurs élevées.

La 4-*tert*-butylpyridine (TBP) et le perchlorate de lithium ont été testés dans l'électrolyte comme additifs. La TBP permet d'accroître la tension et le  $\text{Li}^+$  le courant. Un bon équilibre entre ces deux additifs est atteint lorsque environ 0.05 M de TBP et 0.1 M de  $\text{LiClO}_4$  sont ajoutés à un électrolyte dont la concentration totale en complexes de cobalt est de 0.1 M.

A forte irradiation, alors que le courant augmente, le transport de masse à l'intérieur de la cellule devient limitant. Les tentatives pour diminuer la viscosité de l'électrolyte en utilisant d'autres solvants n'ont pas abouti. Par contre, irradier la cellule depuis la contre électrode et réduire la distance entre les deux électrodes de la cellule diminue notablement les problèmes de diffusion.

L'utilisation de complexes  $[\text{Co}(\text{bip})_2]^{3+/2+}$ , de colorants appropriés et la prise en compte des optimisations décrites ci-dessus ont permis d'obtenir des rendement de l'ordre de 8% sous une irradiation de  $95 \text{ W} \cdot \text{m}^{-2}$ , ainsi que des *IPCE* de plus de 80% à une longueur d'onde de 540 nm. A plein soleil, des rendements de plus de 4% ont été atteints, avec des densités de courant de court-circuit de  $8.5 \text{ mA} \cdot \text{cm}^{-2}$  et des tensions de circuit ouvert de l'ordre de 850 mV.

## Zusammenfassung

Grätzel-Solarzellen sind aufgrund hoher photovoltaischer Wirkungsgrade und ihres Potentials bezüglich niedriger Produktionskosten Gegenstand grossen Interesses in der aktuellen Forschung. Die Grätzel-Technologie basiert auf einer dünnen Schicht aus mesoporösem Titandioxid, welches zum einen aufgrund der grossen inneren Oberfläche die äusserst effiziente Absorption von sichtbarem Licht durch Farbstoffmoleküle mit relativ niedrigem Extinktionskoeffizienten erlaubt, und zum anderen die vollständige Regeneration des Farbstoffs durch direkten Kontakt mit Elektrolyt ermöglicht. Als Farbstoffmoleküle kommen wegen des vorteilhaften Absorptionsspektrums im sichtbaren Spektralbereich bevorzugt Rutheniumpolypyridyl-Komplexe zur Anwendung, wobei allerdings auch andere Farbstoffe zur Sensibilisierung von Titandioxid dienen können. Die klassische Grätzelzelle bedient sich einer organischen Elektrolytflüssigkeit, die das Iod/Iodid-Redoxpaar als Mediator enthält. Dieses Redoxpaar erwies sich in vieler Hinsicht als sehr erfolgreich, ist jedoch auch mit verschiedenen Nachteilen behaftet. Frühere Versuche, dieses Redoxpaar durch ein alternatives Einelektronen-Redoxsystem mit positiverem Redoxpotential zu ersetzen waren nicht von Erfolg gekrönt. Der Grund dafür ist in den erhöhten Dunkelströmen und erheblichen Diffusionsproblemen anderer Mediatoren zu suchen.

Die hier präsentierte Arbeit zielt auf die Entwicklung eines effizienten neuen Mediators für die Grätzelzelle als Ersatz für das Iod/Iodid-Redoxpaar. In die Untersuchungen wurden verschiedene Triarylamine, Platin- und Kobaltkomplexe einbezogen.

Triarylamin- und Platinkomplex-Elektrolyte zeigten sich in Hinsicht auf die photovoltaischen Eigenschaften im Vergleich zum klassischen Iod/Iodid-Elektrolyten unterlegen. Im Gegensatz dazu wiesen Elektrolyte auf Basis von Kobaltkomplexen viel versprechende Eigenschaften auf. In den Experimenten wurde festgestellt, dass insbesondere  $[\text{Co}(\text{bip})_2]^{3+/2+}$ -Komplexe interessante Kandidaten darstellen, weil ihr photoelektrochemisches und kinetisches Verhalten als Redoxmediatoren dem von Iod/Iodid nahe kommt. Verschiedene Optimierungen waren nötig, um hohe photovoltaische Wirkungsgrade erreichen zu können. Rutheniumfarbstoff-Derivate mit Alkylketten wurden als effiziente Sensibilisatoren identifiziert, weil Sie unter anderem den Dunkelstrom reduzierten und somit die Photospannung erhöhten. Die Koadsorption von Farbstoff mit einem Additiv auf der Titandioxidoberfläche ergab höhere

Photoströme, die als Nebeneffekt auch zu einer Photospannungserhöhung führten. Zugabe von Silber-Ionen führte ebenfalls zu einer Zunahme des Solarzellen-Wirkungsgrades. Zur Vermeidung von Diffusionsproblemen mit den im Vergleich zu Iod/Iodid relativ grossen Mediatormolekülen im Elektrolyten wurden sehr dünne Titandioxidschichten verwendet, und eine 3 µm dicke mesoporöse Schicht kombiniert mit einer 3 µm dicken Licht streuenden Schicht wurde als optimal befunden, um den verschiedenen Anforderungen in der Solarzelle zu genügen. Nachdem Kobaltkomplexe unter Umständen elektrochemisch mit der leitfähigen Zinnoxidschicht an der Photoelektrode reagieren, wurden zur weiteren Reduktion des Dunkelstroms blockierende, kompakte Titandioxid-Unterschichten aufgebracht. Die elektrochemische Regeneration der Kobaltkomplexe an der Gegenelektrode der Solarzelle wies eine erhebliche Überspannung auf, so dass sie mit Platin oder Gold überzogen werden musste, um einen günstigen Füllfaktor zu erreichen.

Die Optimierung des Elektrolyten beinhaltete die Auswahl eines geeigneten Lösungsmittels, die Mediator-Konzentration, den Oxidationsgrad und Additive, um in der Summe einen maximalen photovoltaischen Wirkungsgrad zu erhalten. Ein wichtiger Aspekt war die Frage, wie eine genügend hohe Löslichkeit des Redox-Mediators im gewählten Lösungsmittel erreicht werden konnte.

Höchste Wirkungsgrade wurden mit einem Elektrolyten auf Basis einer 2:3-Mischung von Acetonitril/Ethylenkarbonat und einer Mediator-Konzentration von 0,10 – 0,15 M und 10% Oxidationsgrad erreicht. Mit einem Elektrolyten dieser Zusammensetzung erreichte der Photostrom in der Grätzelzelle ein Maximum, ohne die Photospannung signifikant negativ zu beeinflussen.

4-*tert*-Butylpyridine (TBP) und Lithiumperchlorat dienten als zusätzliche Additive im Elektrolyten, wobei TBP einen günstigen Einfluss auf die Photospannung und  $\text{Li}^+$  auf den Photostrom aufwies. Konzentrationen von ca. 0.05 M TBP und 0.1 M  $\text{LiClO}_4$  zeigten optimale Eigenschaften in Elektrolyt-Mischungen in einer 0.1 M Kobaltkomplex-Lösung.

Der limitierende Faktor in der Solarzelle bei sehr hohen Lichtintensitäten bzw. Photoströmen war der Massentransport des Kobalt-Mediators zwischen den beiden Elektroden. Versuche, die Viskosität des Lösungsmittels ausgehend von einer Acetonitril/Ethylencarbonat-Mischung weiter zu reduzieren waren nicht erfolgreich. Ein gangbarer Weg, die Diffusionswiderstände zu reduzieren, war die Beleuchtung via „Rückseite“ bzw. Gegenelektrode der Solarzelle. Bei

hohen Lichtintensitäten wurde so eine klare Verbesserung des Wirkungsgrades erzielt. Als vorteilhaft in Hinsicht verbesserter Diffusion erwies sich ein möglichst geringer Abstand zwischen Photo- und Gegenelektrode.

Die Verwendung von Kobaltkomplexen und den durch Alkylketten modifizierten Rutheniumfarbstoffe, sowie weitere Verbesserungen ermöglichten es, im simulierten Sonnenlicht mit  $95 \text{ W} \cdot \text{m}^{-2}$  Lichtintensität photovoltaische Wirkungsgrade von 8% zu erreichen, bei einem *IPCE* von über 80% bei 540 nm Wellenlänge. Bei Lichtintensitäten, die AM1.5-Sonnenlicht entsprach, wurden Wirkungsgrade von über 4% erreicht mit Kurzschlussströmen um  $8.5 \text{ mA} \cdot \text{cm}^{-2}$  und Photospannungen von bis zu 850 mV.



---

# TABLE OF CONTENT

---

---

INTRODUCTION	1
Photovoltaics - A brief history	2
<i>Classical systems</i> .....	2
<i>Dye-sensitized solar cells</i> .....	5
Photovoltaic technologies - A state-of-the-art	7
<i>Silicon</i> .....	8
<i>III-V cells</i> .....	11
<i>Polycrystalline thin film</i> .....	12
<i>Amorphous silicon</i> .....	14
<i>Photoelectrochemical cells</i> .....	15
<i>Multijunction cells</i> .....	16
Dye-sensitized solar cells	17
<i>Basic principles</i> .....	17
<i>Light harvesting by monomolecular layers</i> .....	19
<i>Mesoscopic oxide semiconductor films</i> .....	20
<i>Photoinduced charge separation at the dye/oxide interface</i> .....	20
<i>Charge-carrier percolation and collection</i> .....	23
<i>Back reaction, recapture of the injected electron by the electrolyte</i> .....	23
<i>Electron transfer dynamics</i> .....	24
Objective of this work	26
References to Chapter 1	27

---

<b>DEVICE PREPARATION AND EXPERIMENTAL METHODS</b>	<b>29</b>
<b>Materials and synthesis</b>	<b>30</b>
<i>TCO coated glass</i> .....	30
<i>Mesoporous oxide paste production</i> .....	30
<i>Diffusive paste production</i> .....	31
<i>Chemicals</i> .....	31
<i>Sensitizers synthesis</i> .....	32
<i>Triarylamine synthesis</i> .....	33
<i>Platinum(II) complexes</i> .....	34
<i>Cobalt complex ligands synthesis</i> .....	34
<i>Cobalt(II) complexes synthesis</i> .....	35
<i>Cobalt(III) complexes synthesis</i> .....	36
<i>Cobalt complexes crystals production</i> .....	36
<b>Device assembly</b>	<b>37</b>
<i>Photoelectrodes</i> .....	37
<i>Counter electrodes</i> .....	40
<i>Electrolytes</i> .....	40
<i>Cell assembly</i> .....	40
<b>Photoelectrochemical characterization</b>	<b>42</b>
<i>Introduction</i> .....	42
<i>Incident photon-to-current conversion efficiency (IPCE)</i> .....	44
<b>Analytical characterization</b>	<b>49</b>
<i>Elemental analysis</i> .....	49
<i>Absorption spectroscopy</i> .....	49
<i>NMR spectroscopy studies</i> .....	49
<i>X-ray photoelectron spectroscopy</i> .....	49
<i>Crystal structure determination</i> .....	49
<i>Powder X-ray diffraction</i> .....	50
<b>Electrochemical methods</b>	<b>51</b>
<b>Laser flash photolysis</b>	<b>52</b>
<b>References to Chapter 2</b>	<b>54</b>
<hr/>	
<b>ALTERNATIVE REDOX COUPLES FOR THE DSSC SYSTEM</b>	<b>55</b>
<b>Introduction</b>	<b>56</b>
<b>Electrolytes based on triarylaminines</b>	<b>58</b>
<i>Introduction</i> .....	58
<i>Electrolytes preparation</i> .....	58
<i>Photoelectrochemical measurements of the triarylaminines</i> .....	60
<i>Electron transfer dynamics</i> .....	63
<i>Conclusion</i> .....	64



Platinum complexes	66
<i>Introduction</i> .....	66
<i>Electrolytes preparation</i> .....	66
<i>Photoelectrochemical measurements of the platinum complexes</i> .....	68
<i>Electron transfer dynamics</i> .....	71
<i>Conclusions</i> .....	73
Cobalt complexes	74
References to Chapter 3	75
<hr/>	
ELECTROLYTES CONTAINING REDOX COUPLES BASED ON COBALT COMPLEXES	77
<hr/>	
Introduction	78
Electrolytes preparation	79
Cobalt complexes screening and characterization	80
<i>Introduction</i> .....	80
<i>Photoelectrochemical screening of cobalt complexes</i> .....	82
<i>NMR spectroscopy studies</i> .....	84
<i>Electrochemical studies</i> .....	93
<i>Elemental analysis of the [Co(dbbip)<sub>2</sub>](ClO<sub>4</sub>)<sub>2</sub> complex</i> .....	101
<i>Reduced and oxidized complexes UV-Vis absorption spectra</i> .....	102
<i>XPS, crystal structure determination and powder X-ray diffraction</i> .....	103
Interfaces optimization	111
<i>Introduction</i> .....	111
<i>Sensitizer - electrolyte interactions</i> .....	111
<i>Alkyl chains length influence</i> .....	120
<i>Co-grafting sensitizer and co-adsorbents</i> .....	126
<i>Silver(I) addition impact</i> .....	130
<i>Photoanode - electrolyte interactions</i> .....	132
<i>Counter electrode - electrolyte interactions</i> .....	134
Optimization of electrolytes	137
<i>Introduction</i> .....	137
<i>Optimization of redox mediator concentration and degree of oxidation</i> .....	137
<i>Additives</i> .....	144
<i>Solvents effect and improvement of the solubility</i> .....	148
Mass-transport optimizations	155
<i>Direction of irradiation</i> .....	155
<i>Distances between electrodes</i> .....	158
<i>Combination of CE illumination and reduced distance between electrodes</i> .....	159
References to Chapter 4	162

---

CONCLUSIONS	165
-------------	-----

---

APPENDIX	169
----------	-----

---

List of symbols	170
Glossary of abbreviations	172
Physical constants	175
Curriculum vitæ	176
<i>Publications</i> .....	176
<i>Conferences</i> .....	176
<i>Posters</i> .....	177

---

# CHAPTER ONE

## Introduction

# 1

---

For many years, the depletion of fossil fuel resources associated with the continually increasing demand is problematic. But also the pollution engendered by the fervent use of these fuel. The most recurrent subject of these preoccupations is the global warming of the planet caused by greenhouse effect gases, and the ensuing climatic changes. In addition to these global ecological problems, the dependence on a few producing countries for this extremely strategic energy source is of great geopolitical concern. All these reasons make that, for the moment, investments is granted in domains of renewable energies on behalf of countries which widely pronounced in favor of the environment during the Kyoto's conference in 1997. On the other hand the industry expects a strong increase of sales in the field of renewables, especially in photovoltaic and thermic solar energy, as well as in the use of biomass and wind energy. Although hydro-electric power is already highly developed in western countries like Switzerland, France, USA or Canada, some developing countries still have big projects in this domain, notably China.

Among all the technologies allowing the production of renewable energy, this work will focus in particularly on photovoltaic energy. Solar energy is not only an abundant renewable energy source, but photovoltaic cells also have another competitive advantage: they can be independent of the grid and therefore are useful in remote areas or for mobile applications.

After a brief history review of photovoltaics, this chapter will focus on existing and newly developed photovoltaic technologies. One attractive new type of photovoltaic system that mimic natural photosynthesis, dye-sensitized solar cells, will be thoroughly discussed. Finally, the objective of this work will be explained in details in the last part of this chapter (page 26).

## 1. Photovoltaics - A brief history

### 1.1. Classical systems<sup>1</sup>

#### *1839 - 1899: Discovery of basic phenomena and properties of photovoltaic materials*

A physical phenomenon allowing light to electricity conversion the photovoltaic effect was discovered in 1839 by the French physicist Alexandre Edmond Becquerel.<sup>[1]</sup> Experimenting with metal electrodes and electrolyte he discovered that the conductance rises with illumination.

Willoughby Smith discovered the photovoltaic effect in selenium in 1873.<sup>[2]</sup> In 1876, with his student R. E. Day, William G. Adams discovered that illuminating a junction between selenium and platinum also has a photovoltaic effect.<sup>[3]</sup> These two discoveries were the foundation for the first selenium solar cell construction, which was built in 1877. Charles Fritts first described them in detail in 1883.

#### *1900 - 1949: Theoretical explanation of the photovoltaic effect and the first solar cells*

The author of the most comprehensive theoretical work about the photovoltaic effect was Albert Einstein, who described the phenomenon in 1904.<sup>[4]</sup> For his theoretical explanation he was awarded a Nobel Prize in 1921. Einstein's theoretical explanation was experimentally proved by Robert Millikan in 1916.

In 1918, a Polish scientist Czochralski discovered a method for monocrystalline silicon production, which enabled monocrystalline solar cells production.<sup>[5]</sup> The first silicon monocrystalline solar cell was constructed in 1941.

In 1932, the photovoltaic effect in cadmium-selenide was observed. Nowadays, CdS belongs among important materials for solar cells production.

#### *1950 - 1969: Intensive space research*

In 1951, the first germanium solar cells have been made. Dr. Dan Trivich of Wayne State University has made some theoretical calculations on solar cell efficiency with different materials

---

1. Adapted from [www.pvresources.com](http://www.pvresources.com) © Denis Lenardic 2001-2003.

in 1953. In 1954, the RCA Laboratories published a report on a CdS photovoltaic effect. The Bell Laboratories published the results of a solar cell operation with 4.5% efficiency. The efficiency was increased to 6% within a few months.

In 1955, the development of a satellite energy supply using solar cells was initiated. Hoffman Electronics-Semiconductor Division introduced a commercial photovoltaic product with 2% efficiency for US\$ 25 per cell with 14 mW peak power. The energy cost was US\$ 1785 per W. In 1957, Hoffman Electronics introduced a solar cell with 8% efficiency. A year later, in 1958, the same company introduced a solar cell with 9% efficiency. The first radiation proof silicon solar cell was produced for the needs of space technology the same year. In 1959, Hoffman Electronics introduced commercially available solar cells with 10% efficiency. A year after, they introduced yet another solar cell with 14% efficiency. The first sun-powered automobile was demonstrated in Chicago, Illinois on August 31<sup>st</sup>, 1955.

During the year 1962, the first commercial telecommunications satellite Telstar, developed by Bell Laboratories, was launched. It was powered by a photovoltaic system having a peak power of 14 W.

In 1963, Sharp Corporation developed the first commercial photovoltaic module from silicon solar cells. The biggest photovoltaic system at the time, the 242 W module field was set up in Japan. A year later, in 1964, Americans applied a 470 W photovoltaic field in the Nimbus space project.

### ***1970 - 1979: Establishment of the biggest photovoltaic companies***

In 1970, Solar Power Corporation was established. Three years later, in 1973, Solarex Corporation was established. At the Delaware University a solar photovoltaic-thermal hybrid system, one of the first photovoltaic systems for domestic application, was developed. A silicon solar cell of US\$ 30 per W was produced. In 1974, the Japanese Sunshine project commenced. A year later, in 1975, Solec International and Solar Technology International were established.

### ***1980 - 1989: Large standalone systems installations***

Many important events in the field of photovoltaics appeared in 1980. ARCO Solar was the first to produce photovoltaic modules with peak power of over 1 MW per year. BP entered solar industry via purchase of Lucas Energy Systems. A seawater desalination system with 10.8 kW

peak power was built in Jeddah, Saudi Arabia the same year. Helios Technology, the oldest European solar cells producer, was established. The world production of photovoltaic modules exceeded 9.3 MW in 1982. Volkswagen began testing photovoltaic systems placed on vehicle roofs with 160 W peak power for vehicle start up.

In 1984, a 1 MW photovoltaic power plant began to operate in Sacramento, California. ARCO Solar introduced the first amorphous modules.

In 1985, researchers of the University of New South Wales in Australia constructed a solar cell with more than 20% efficiency. BP built a power plant in Sydney and shortly after another one in Madrid. In 1986, ARCO Solar introduced the first commercial thin film photovoltaic module. BP got a thin film technology patent for a solar cells production in 1989.

### ***1990 - 1999: Large photovoltaic companies co-operation***

In 1990, Energy Conversion Devices Inc. (ECD) and Canon Inc. established a joint company United Solar Systems Corporation for solar cells production. Siemens bought ARCO Solar and established Siemens Solar Industries, which is nowadays one of the biggest photovoltaic companies in the world. Founded in 1977, Solar Energy Research Institute (SERI) renamed to National Renewable Energy Laboratory (NREL). A year later, in 1991, BP Solar Systems renamed to BP Solar International (BPSI), and became an independent unit within British Petroleum concern. In 1996, BP Solar purchased APS production premises in California, and announced a commercial CIS (copper indium diselenide) solar cells production.

### ***2000 - : Renewable energy and the Stock exchange***

Some photovoltaic and renewable energy resources companies now have shares listed, predominantly in the German stock exchange. Capital mergers in Germany led to large photovoltaic corporation establishments. During 2000 and 2001 production of Japanese producers increased significantly. Sharp and Kyocera each produce modules with peak power equivalent to the annual consumption in Germany. Sanyo is close as well.

## 1.2. Dye-sensitized solar cells<sup>1</sup>

In 1710, Diesbach produced the first synthetic dye, Prussian blue.<sup>[6]</sup> A century later, in 1837, Daguerre made the first photographic images. Fox Talbot followed with the silver halide process in 1839. Although the art of formulating photographic emulsions only became a science with the theoretical analysis of the process by Gurney and Mott in 1938,<sup>[7]</sup> there was constant progress in the overall sensitivity of photographic emulsions, which had been particularly poor for the green to red spectral region. This can now be recognized as due to the semiconductor nature of the silver halides crystals used in photography, whose band gaps range from 2.7 to 3.2 eV. So the photoresponse is negligible for wavelengths longer than 460 nm. It was noted, for example, that the origin of the gelatin used as the support medium for the silver halide grains significantly modified the film sensitivity. In the 20<sup>th</sup> century, it was demonstrated that an organosulphur compound present in calf skin gelatin was responsible,<sup>[8]</sup> and which is now known to have its effect by inducing a nanostructure of silver sulphide on each grain. It can, therefore, be regarded as the first sensitization at a semiconductor heterojunction. It is an interesting convergence of photography and photoelectrochemistry, both of which rely on photo-induced charge separation at a liquid-solid interface. As seen before, the silver halides have band gaps of the order of 2.7–3.2 eV, and are therefore insensitive to much of the visible spectrum. The first panchromatic film, able to render the image of a scene realistically into black and white, followed on the work of Vogel in Berlin after 1873,<sup>[9]</sup> in which he associated dyes with the halide semiconductor grains. The first sensitization of a photoelectrode by Moser followed shortly thereafter, using a similar idea.<sup>[10]</sup> It was confirmed by Rigollot in 1893.<sup>[11]</sup> However, the clear recognition of the parallelism between the two procedures, a realization that the same dyes in principle can function in both<sup>[12]</sup> and a verification that their operating mechanism is by injection of electrons from photo-excited dye molecules into the conduction band of the n-type semiconductor substrates<sup>[13]</sup> date from the 1960s. In subsequent years, the idea developed that the dye could function most efficiently if chemisorbed on the surface of semiconductor.<sup>[14-16]</sup> The concept emerged to use dispersed particles to provide a sufficient interface,<sup>[17]</sup> then photoelectrodes with high surface roughness were employed.<sup>[18,19]</sup> Titanium dioxide became the semiconductor of choice. This material has many advantages for sensitized photochemistry and photoelectrochemistry: it is a low cost, widely available, non-toxic and biocompatible material,

---

1. Adapted from McEvoy, A. J.; Grätzel, M. *Sol. Energy Mater.* **1994**, 32, 221 and Grätzel, M. *Prog. Photovolt. Res. Appl.* **2000**, 8, 171.

and as such is even used in health care products, as well as domestic applications such as paint pigmentation. The standard dye at the time was tris(2,2'-bipyridyl-4,4'-carboxylate) ruthenium(II), the function of the carboxylate being the attachment by chemisorption of the chromophore to the oxide substrate. Progress thereafter, until the announcement in 1991 of the sensitized nanocrystalline photovoltaic device with a conversion efficiency at that time of 7.1% under solar illumination,<sup>[20]</sup> was incremental, a synergy of structure, substrate roughness and morphology, dye photophysics and electrolyte redox chemistry. That evolution has continued progressively since then, with a certified efficiency of now over 10% (see Table 1 on next page).



## 2. Photovoltaic technologies - A state-of-the-art<sup>1</sup>

Table 1 summarized the state-of-the-art for the different photovoltaic technologies. These results are for laboratory small size cells that often have no collect grid.

**Table 1.** Confirmed terrestrial cell efficiencies measured under the global AM 1.5 spectrum ( $1000 \text{ W} \cdot \text{m}^{-2}$ ) at  $25 \text{ }^\circ\text{C}$ . [a] (ap)=aperture area; (t)=total area; (da)=designated irradiance area. [b] FhG-ISE = Fraunhofer-Institut für Solare Energiesysteme; JQA = Japan Quality Assurance. From Green, M. A.; Emery, K. Solar Cell Efficiency Tables 19, *Prog. Photovolt.: Res. Appl.* **2002**; 10:55-61.

Classification	$\eta$ [%]	Area <sup>[a]</sup> [cm <sup>2</sup> ]	$V_{oc}$ [V]	$J_{sc}$ [mA · cm <sup>-2</sup> ]	$FF$ [-]	Test center <sup>[b]</sup> (and date)	Producer
<b>Silicon</b>							
Si (crystalline)	24.7±0.5	4.00 (da)	0.706	42.2	0.83	Sandia (3/99)	UNSW PERL
Si (multicrystalline)	19.8±0.5	1.09 (ap)	0.654	38.1	0.80	Sandia (2/98)	UNSW/Eurosolare
Si (thin-film transfer)	16.6±0.4	4.02 (ap)	0.645	32.8	0.78	FhG-ISE (7/01)	U. Stuttgart
<b>III-V cells</b>							
GaAs (crystalline)	25.1±0.8	3.91 (t)	1.022	28.2	0.87	NREL (3/90)	Kopin
GaAs (thin film)	23.3±0.7	4.00 (ap)	1.011	27.6	0.84	NREL (4/90)	Kopin
GaAs (multicrystalline)	18.2±0.5	4.01 (t)	0.994	23.0	0.80	NREL (11/95)	RTI
InP (crystalline)	21.9±0.7	4.02 (t)	0.878	29.3	0.85	NREL (4/90)	Spire
<b>Polycrystalline thin film</b>							
CuInGaSe <sub>2</sub> (CIGS)	18.4±0.5	1.04 (t)	0.669	35.7	0.77	NREL (2/01)	NREL
CdTe	16.5±0.5	1.13 (ap)	0.845	26.7	0.76	NREL (9/01)	NREL
<b>Amorphous/microcrystalline Si</b>							
Si (nanocrystalline)	10.1±0.2	1.20 (ap)	0.539	24.4	0.77	JQA (12/97)	Kaneka
<b>Photoelectrochemical cells</b>							
Nanocrystalline dye	11.0±0.5	0.25 (ap)	0.795	19.4	0.71	FhG-ISE (12/96)	EPFL, LPI
Nanocrystalline dye (submodule)	4.7±0.2	141.4 (ap)	0.795	11.3	0.59	FhG-ISE (2/98)	INAP
<b>Multijunction cells</b>							
GaInP/GaAs	30.3	4.0 (t)	2.488	14.22	0.86	JQA (4/96)	Japan Energy
GaInP/GaAs/Ge	28.7±1.4	29.93 (t)	2.571	12.95	0.86	NREL (9/99)	Spectrolab
GaAs/CIS (thin film)	25.8±1.3	4.00 (t)	–	–	–	NREL (11/89)	Kopin/Boing
a-Si/CIGS (thin film)	14.6±0.7	2.40 (ap)	–	–	–	NREL (6/88)	ARCO

1. Adapted from <http://www.eere.energy.gov/pv> ©NREL, U.S. Department of Energy.

## 2.1. Silicon

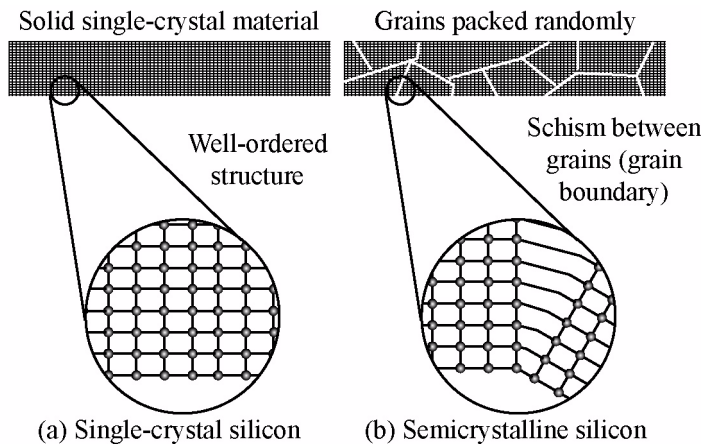


**Figure 1.** Single-crystal material (a) is structurally uniform; there are no disturbances in the orderly arrangement of atoms. Semicrystalline material (b) is made up of several crystals or "grains". At the interfaces of the grains, or "boundaries", the atomic order is disrupted. Here, electrons are more likely to recombine with holes rather than contribute to the electrical circuit.

Therefore the process of purification is expensive. A photovoltaic cell is made of two layers of silicon, which are doped to polarize the junction. To make one of the layers positive, a certain number of atoms of p-type element, like boron, can be incorporated into it. To negatively charge the other layer, a certain number of n-type atoms, like phosphorus, can also be incorporated. When a photon having enough energy is absorbed in this semiconductor, it excites an electron from the valence band into the conduction band, leaving a positively charged hole. This is called the photovoltaic effect. This effect creates a potential difference across a junction of two different materials.

Crystalline silicon (c-Si) is used in several forms: single-crystalline or monocrystalline silicon, multicrystalline or polycrystalline silicon, ribbon and sheet silicon and thin-layer silicon (Figure 1).

### *Si (single-crystal)*

In single-crystal silicon, the molecular structure of the material is uniform because the entire structure is grown from the same or a single crystal. This uniformity is ideal for efficiently transferring electrons through the material. To make an effective photovoltaic cell, silicon is doped to make it n-type and p-type.

Silicon is the most popular solar-cell material for commercial applications because it is so readily abundant (it is actually the second most abundant element in the Earth's crust-second only to oxygen). However, to be useful in solar cells, it must be refined to 99.9999% purity.

To produce the single-crystal, we first melt the high-purity silicon. We then cause it to reform very slowly in contact with a single crystal seed. The silicon adapts to the pattern of the single crystal seed as it cools and solidifies gradually. Not surprisingly, because we start from a seed, this process is called growing a new ingot of single-crystal silicon out of the molten silicon. Several specific processes can be used to accomplish this. The most established and dependable means are the Czochralski method and the floating-zone (FZ) technique.

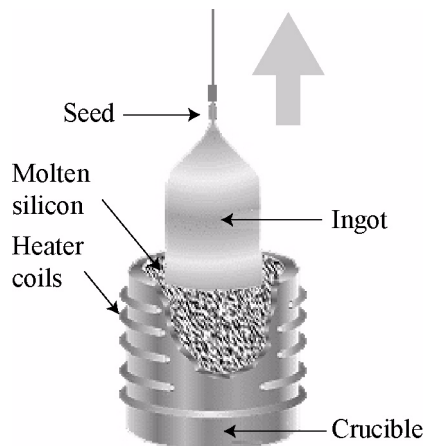


**Figure 2.** The most widely used technique for making single-crystal silicon is the Czochralski process, in which seed of single-crystal silicon contacts the top of molten silicon. As the seed is slowly raised, atoms of the molten silicon solidify in the pattern of the seed and extend the single-crystal structure. © US Department of Energy, USA.

In the Czochralski process, a seed crystal is dipped into a crucible of molten silicon and withdrawn slowly, pulling a cylindrical single crystal as the silicon crystallizes on the seed (Figure 2).

The float zone (FZ) process produces purer crystals, because they are not contaminated by the crucible as Czochralski crystals are. In the FZ process, a silicon rod is set atop a seed crystal and lowered through an electromagnetic coil. The coil's magnetic field induces an electric field in the rod, heating and melting the interface between the rod and the seed. Single-crystal silicon forms at the interface, growing upward as the coils are slowly raised.

Once the single-crystal ingots are produced, they must be sliced to form wafers.

Although single-crystal silicon technology is well developed, the Czochralski, FZ, and ingot-casting processes are complex and expensive. A group of new crystal-producing processes, however, generally called shaped-ribbon growth, could reduce processing costs by forming silicon directly into thin, usable wafers of single-crystal silicon. These methods involve forming thin crystalline sheets directly, thereby avoiding the slicing step required of cylindrical ingots.

These crystals are then cut in ultra-fine layers, doped and connected. The monocrystalline cells allow high efficiencies, in the order of 15% to 25%.

These cells nevertheless suffer from two backdraws: their high price and their long pay off time of the energy investment. This pay off time is the time during which a solar cell must produce

electricity in order to repay the energy that was necessary to produce it. This time can be as long as 7 years for monocrystalline cells. They are nevertheless appropriate for applications requiring high performances, such as electro-solar cars.

### *Si (multicrystalline)*

Multicrystalline silicon consists of several smaller crystals or grains, which introduce boundaries. These boundaries impede the flow of electrons and encourage them to recombine with holes and thereby reduce the power output of the cell. However, multicrystalline silicon is much cheaper to produce than single-crystalline silicon, so researchers are working on other ways of minimizing the effects of grain boundaries.

Multicrystalline silicon can be produced in a variety of ways. The most popular commercial methods involve a casting process in which molten silicon is directly cast into a mold and allowed to solidify into an ingot (Figure 3). Generally, the mold is square, producing an ingot that can be cut and sliced into square cells to fit more compactly into a photovoltaic module.

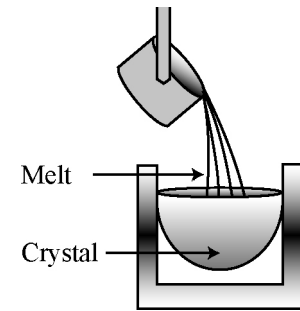


**Figure 3.** The most popular method for making commercial multicrystalline silicon is casting, in which molten silicon is poured directly into a mold and allowed to solidify into an ingot.

### *Si (thin-film transfer)*

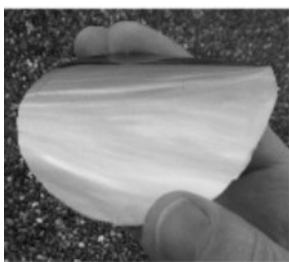


**Figure 4.** Photograph of a 14  $\mu\text{m}$  thick epitaxial silicon film on top of a 1.5  $\mu\text{m}$  thick QMS film, transferred to a plastic foil.

Solar cells based on monocrystalline silicon wafers reached a conversion efficiency close to 25%, and it has been demonstrated that a wafer thinned down to about 50  $\mu\text{m}$  still allows one to obtain a cell efficiency of 21.5%.<sup>[21]</sup> Unfortunately, the thinning of wafers is not suitable for minimizing material expenses and therefore will not lead to decreased production costs. In order to enable economically viable thin film technologies several processes employing the transfer of monocrystalline silicon films onto alternative substrates are currently under investigation by research groups around the world.<sup>[22-26]</sup>

Monocrystalline silicon thin film solar processed by layer transfer using the quasi-monocrystalline silicon (QMS) approach have demonstrate high efficiencies (Figure 4).<sup>[27]</sup>

Chemical vapor deposition serves to epitaxially deposit silicon on QMS films obtained from thermal crystallization of a double layer porous silicon film on a silicon wafer. A separation layer that forms during this crystallization process allows one to separate the epitaxial layer on top of the quasi-monocrystalline film from the starting silicon wafer after solar cell processing. Independently confirmed thin film solar cell efficiencies are 15.4% and 16.6% for thin film solar cells transferred to a glass superstrate with a total silicon film thickness of 24.5  $\mu\text{m}$  and 46.5  $\mu\text{m}$ , respectively, and a cell area of 4  $\text{cm}^2$ . Device simulations indicate an efficiency potential above 20% with material parameters accessible today by introducing an additional back surface reflector.

## 2.2. III-V cells

These photovoltaic technologies, based on Group III and V elements in the Periodic Table, show very high conversion efficiencies under either normal sunlight or sunlight that is concentrated (Figure 5). Single-crystal cells of this type are usually made of gallium arsenide (GaAs). Gallium arsenide can be alloyed with elements such as indium, phosphorus, and aluminum to create semiconductors that respond to different spectral energies.

Gallium is a by-product of the smelting of other metals, notably aluminum and zinc, and it is rarer than gold. Arsenic is not rare, but it is poisonous. Gallium arsenide's use in solar cells has been developing synergistically with its use in light-emitting diodes, lasers, and other optoelectronic devices.

GaAs is especially suitable for use in multijunction (see "Multijunction cells", page 16) and high-efficiency solar cells for several reasons:

1. The GaAs band gap is 1.43 eV, nearly ideal for single-junction solar cells.
2. GaAs has an absorptivity so high it requires a cell only a few microns thick to absorb sunlight (crystalline silicon requires a layer 100 microns or more in thickness).
3. Unlike silicon cells, GaAs cells are relatively insensitive to heat (cell temperatures can often be quite high, especially in concentrator applications).
4. Alloys made from GaAs using aluminum, phosphorus, antimony, or indium have charac-



**Figure 5.** To be cost-effective for terrestrial use, GaAs high-efficiency cells are more appropriate for concentrator systems such as this one at Sandia National Laboratories. © Sandia National Laboratories, USA.

teristics complementary to those of gallium arsenide, allowing great flexibility in cell design.

5. GaAs is very resistant to radiation damage. This, along with its high efficiency, makes GaAs very desirable for space applications.

One of the greatest advantages of gallium arsenide and its alloys as photovoltaic cell materials is the wide range of design options possible. A cell with a GaAs base can have several layers of slightly different compositions that allow a cell designer to precisely control the generation and collection of electrons and holes (again, see “Multijunction cells”, page 16).

The greatest barrier to the success of GaAs cells has been the high cost of a single-crystal GaAs substrate. For this reason, GaAs cells are used primarily in concentrator systems, where the typical concentrator cell is about  $0.25 \text{ cm}^2$  in area and can produce ample power under high concentrations. In this configuration, the cost is low enough to make GaAs cells competitive, assuming that module efficiencies can reach between 20% and 25% and that the cost of the rest of the system can be reduced.

### **2.3. Polycrystalline thin film**

One of the scientific discoveries of the computer semiconductor industry that has shown great potential for the photovoltaic industry is thin-film technology.

Thin film photovoltaic cells use layers of semiconductor materials only a few micrometers thick, attached to an inexpensive backing such as glass, flexible plastic, or stainless steel (Figure 6). Semiconductor materials for use in thin films include amorphous silicon (a-Si) (see “Silicon”, page 8), copper indium diselenide (CIS), and cadmium telluride (CdTe). Because the quantity of semiconductor material required for thin films is far smaller than for traditional photovoltaic cells, the cost of thin film manufacturing is far less than for crystalline silicon solar cells.

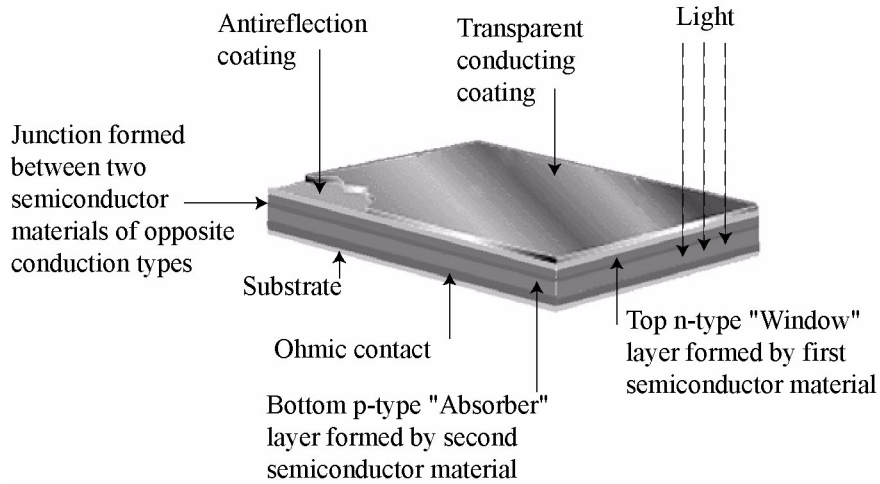


**Figure 6.** Polycrystalline thin-film cells have a heterojunction structure, in which the top layer is made of a different semiconductor material than the bottom semiconductor layer. The top layer, usually n-type, is a window that allows almost all of the light through to the absorbing layer, usually p-type. An ohmic contact is often used to provide a good electrical connection to the substrate.

Rather than growing, slicing, and treating a crystalline ingot (required for single-crystal silicon), a thin layers of the required materials is sequentially deposited. Several different deposition techniques are available, and all of them are potentially cheaper than the ingot-growth techniques required for crystalline silicon. These deposition processes can be scaled up easily so that the same technique used to make a 5 cm × 5 cm laboratory cell can be used to make a 60 cm × 150 cm module.

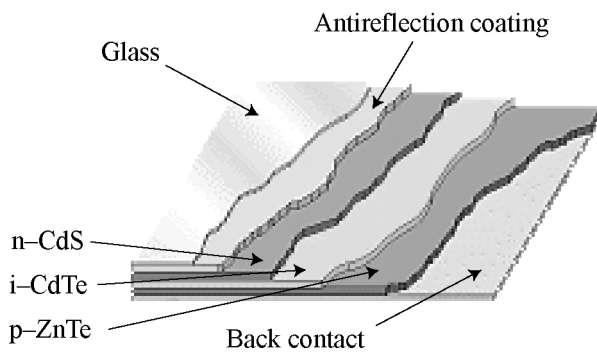


**Figure 7.** One way around contacting problems inherent in typical CdTe cells is to use an n-i-p structure, with an intrinsic layer of CdTe sandwiched between an n-type CdS layer and a p-type ZnTe layer.

Single-crystal cells have to be individually interconnected into a module, but thin-film devices can be made as a single unit. Layer upon layer is deposited sequentially on a glass superstrate, from the antireflection coating and conducting oxide, to the semiconductor material and the back electrical contacts.

Unlike most single-crystal cells, the typical thin-film device does not use a metal grid for the top electrical contact. Instead, it uses a thin layer of a transparent conducting oxide, such as tin oxide. These oxides are highly transparent and conduct electricity very well (see “TCO sub-

strate”, page 37). A separate antireflection coating may be used to top off the device, or the transparent conducting oxide may serve this function as well (Figure 7).

## 2.4. Amorphous silicon

Amorphous solids, like common glass, are materials in which the atoms are not arranged in any particular order. They do not form crystalline structures at all, and they contain large numbers of structural and bonding defects.

They also come from the cuttings from crystal blocks, but these blocks are cast and therefore heterogeneous. Difficulties linked to big crystal growth are then avoided. Efficiency for amorphous silicon cells, in the order of 10%, is slightly lower, but is largely compensated by lower production costs. Producing such cells need less energy (Figure 8).

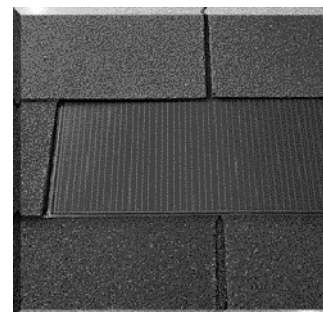


**Figure 8.** The versatility of amorphous silicon is shown in this flexible roof-shingle module. The shingle can be built right into new homes where covenants would prohibit more conventional photovoltaic modules. © NREL.

It wasn't until 1974 that researchers began to realize that amorphous silicon could be used in photovoltaic devices by properly controlling the conditions under which it was deposited and by carefully modifying its composition (Figure 9). Today, amorphous silicon is commonly used for solar-powered consumer devices that have low power requirements (e.g., wrist watches and calculators).

Amorphous silicon absorbs solar radiation 40 times more efficiently than does single-crystal silicon, so a film only about 1 micron thick can absorb 90% of the usable solar energy. This is one of the most important factors affecting its low cost potential. Other principal economic advantages are that amorphous silicon can be produced at a lower temperature and can be deposited on low-cost substrates. These characteristics make amorphous silicon the leading thin-film photovoltaic material.

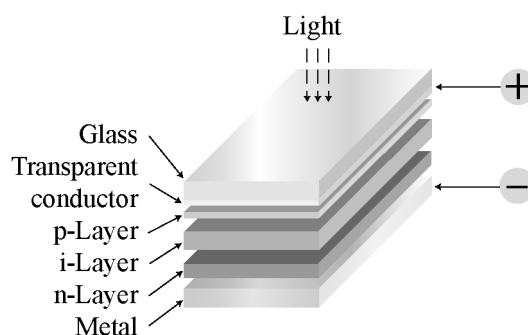


**Figure 9.** The typical amorphous silicon cell employs a p-i-n design, in which an intrinsic layer is sandwiched between a p layer and an n layer.



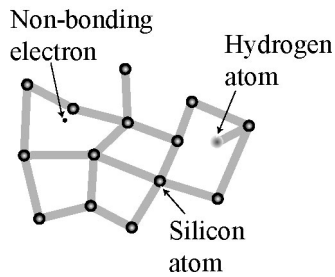


**Figure 10.** Amorphous silicon's random structural characteristics result in deviations like non-bonding electrons. This provides places for electrons to recombine with holes, but this may be neutralized somewhat with atomic hydrogen.

Because amorphous silicon does not have the structural uniformity of crystalline or even multicrystalline silicon, the small deviations result in defects such as non-bonding electrons, where atoms are missing a neighbor to which they can bond. These defects provide places for electrons to recombine with holes rather than contributing to the electrical circuit. Ordinarily, such a material would be unacceptable for electronic devices because the defects limit the flow of current. But if amorphous silicon is deposited in such a way that it contains a small amount of hydrogen (through a process called *hydrogenation*), then the hydrogen atoms combine chemically with many of the non-bonding electrons and thereby permitting electrons to move through the amorphous silicon (Figure 10).

## 2.5. Photoelectrochemical cells

### *Nanocrystalline dye-sensitized solar cells*

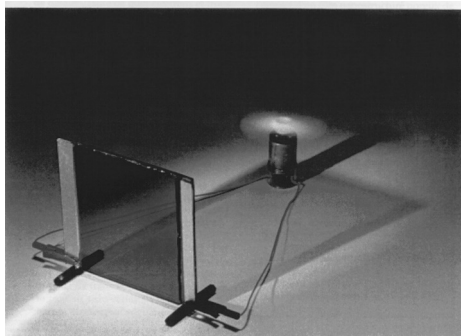


**Figure 11.** A transparent dye-sensitized solar cell running a small motor under a diffuse day-light. ©EPFL-LPI.

In contrast to the conventional systems, where the semiconductor assumes both the task of light absorption and charge carrier transport, the two functions are separated in the dye-sensitized solar cells (DSSC). Light is absorbed by a sensitizer which is anchored to the surface of a wide band gap semiconductor. Charge separation takes place in the dye via photo-induced electron injection from the dye into the conduction band of the solid. Carriers are transported in the con-

duction band of the semiconductor to the charge collector. The use of transition metal complexes having a broad absorption band in conjunction with oxide films of nanocrystalline morphology permits the harvesting of a large fraction of sunlight. Near-quantitative conversion of incident photons into electric current is achieved over a large spectral range extending over the whole visible region. Overall solar (standard AM1.5) to electric conversion efficiencies over 10% have been reached. Further explanations on the dye-sensitized solar cell system are given in paragraph "Dye-sensitized solar cells", page 17.

## 2.6. Multijunction cells

Most common photovoltaic devices use a single junction, or interface, to create an electric field within a semiconductor such as a photovoltaic cell. In a single-junction photovoltaic cell, only photons whose energy is equal to or greater than the band gap of the cell material can free an electron for an electric circuit. In other words, the photovoltaic response of single-junction cells is limited to the portion of the sun's spectrum whose energy is above the band gap of the absorbing material, and lower-energy photons are not used.

One way to get around this limitation is to use two or more different cells, with more than one band gap and more than one junction, to generate a voltage. These are referred to as multijunction cells (also called cascade or tandem cells). Multijunction devices can achieve a higher total conversion efficiency because they can convert more of the energy spectrum of light to electricity (Figure 12).

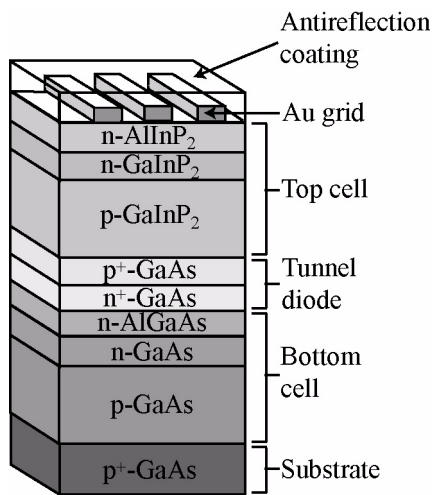


**Figure 13.** This multijunction device uses a top cell of gallium indium phosphide, a tunnel junction, to aid the flow of electrons between the cells, and a bottom cell of gallium arsenide.

Although two-junction cells have been built, most research is focusing on three-junction and four-junction devices, using materials such as germanium (Ge) to capture the lowest-energy light in the lowest layer.

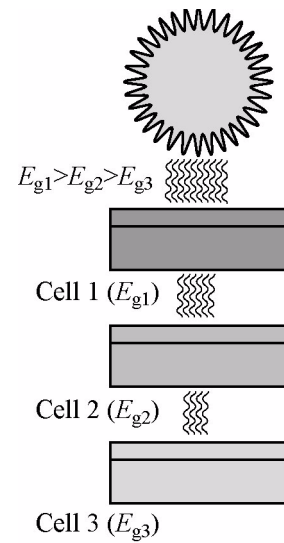


**Figure 12.** A multijunction device is a stack of individual single-junction cells in descending order of band gap ( $E_g$ ). The top cell captures the high-energy photons and passes the rest of the photons on to be absorbed by lower-band-gap cells.

In a typical multijunction photovoltaic cell, individual single-junction cells with different energy band gaps are stacked on top of one another. Sunlight then falls first on the material with the largest band gap, and the highest-energy photons are absorbed. Photons not absorbed in the first cell continue on to the second cell, which absorbs the higher-energy portion of the remaining solar radiation while remaining transparent to the lower-energy photons.

Much of the work in this area uses gallium arsenide and its alloys, as well as using amorphous silicon, copper indium diselenide, and gallium indium phosphide (Figure 13).

## 3. Dye-sensitized solar cells<sup>1</sup>

### 3.1. Basic principles

Conventional solar cells convert light into electricity by exploiting the photovoltaic effect that exists at semiconductor junctions. These photovoltaic devices are based on the concept of charge separation at an interface of two materials of different conduction mechanism, normally between solid-state materials, either n- and p-type regions with electron and hole majority carriers in a single semiconductor material, heterojunctions between different semiconductors or semiconductor-metal junction (Schottky).

In contrast, the photoelectrochemical cells work on a different principle, whereby the processes of light absorption and charge separation are differentiated. Light absorption is performed by a monolayer of dye (S) absorbed chemically at the semiconductor surface (Figure 14). After having been excited (S\*) by a photon of light, the dye is able to transfer an electron to the semiconductor by a process called *injection*. Electrons in the semiconductor are collected through their transport in the electrode. This transport occurs mainly by diffusion.<sup>[28-30]</sup> The original state of the dye is subsequently restored by electron donation from the electrolyte, usually an organic solvent containing redox system, such as the iodide/triiodide couple. This process called *regeneration*. The regeneration of the sensitizer by iodide intercepts the recapture of the conduction band electron by the oxidized dye. The iodide is regenerated in turn by the reduction of triiodide at the counter electrode, the circuit being completed via electron migration through the external load. The theoretical maximum voltage ( $\Delta V$ ) that such a device could deliver corresponds to the difference between the redox (Nernst) potential of the mediator and the quasi-Fermi level of the electron in the semiconductor.

---

1. Adapted from Grätzel, M. *Prog. Photovolt. Res. Appl.* **2000**, 8, 171 and Grätzel, M. *Pure Appl. Chem.* **2001**, 73, 459.

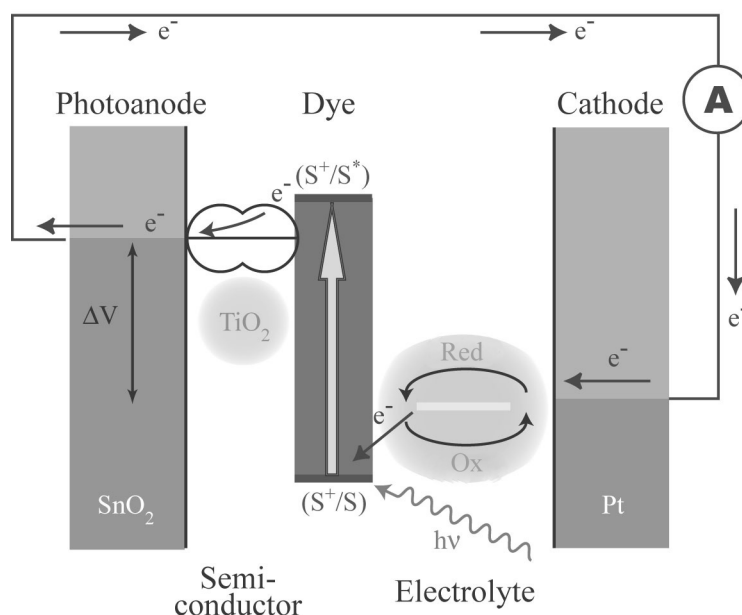


**Figure 14.** Principle of operation of the dye-sensitized nanocrystalline solar cell (DSSC). As in natural photosynthesis, in the artificial analog sunlight sets in action a molecular electron pump. The sensitizer (S) is bound as a monomolecular coating on the surface of a semiconductor oxide, such as  $\text{TiO}_2$ ,  $\text{ZnO}$ ,  $\text{SnO}_2$  or  $\text{Nb}_2\text{O}_5$ . It absorbs the incident solar rays, and is thereby raised to the electronically excited state  $S^*$ . From this state it injects an electron into the conduction band of the mesoporous oxide semiconductor. The conduction band electrons then cross the film and are directed through a charge collector into the external current circuit where electrical work is done. The electrons are then returned to the cell through a counter electrode. Between this counter electrode and the oxide is an electrolyte containing a redox couple, i.e., iodine and iodide. This redox electrolyte allows for the transport of electrical charge between the two electrodes. The electrons reduce triiodide to iodide ions which diffuse from the counter electrode to the nanocrystalline film surface where they regenerate the sensitizer by electron transfer to the sensitizer cations, while simultaneously the iodide is oxidized back to iodine or triiodide. The redox catalytic cycle leading to the conversion of light into electrical current is thereby closed.

The absorption of light by a monolayer of dye is always weak, due to the very small cross section for light absorption of the dye molecules compared to the area they occupied on the surface. A respectable photovoltaic efficiency cannot therefore be obtained by the use of a flat semiconductor surface but rather by use of a porous, nanostructured film of very high surface roughness. When light penetrates the photosensitized, semiconductor sponge, it crosses hundreds of absorbed dye monolayers. The nanocrystalline structure equally allows a certain spreading of the radiation. The final result is a greater absorption of light and its efficient conversion into electricity. The material of choice is  $\text{TiO}_2$  (anatase), although alternative wide band gap oxides such as  $\text{ZnO}$  and  $\text{Nb}_2\text{O}_5$  have also given promising results.<sup>[31,32]</sup> The mesoporous oxide layer is composed of nanometer-sized particles which have been sintered together to allow electronic conduction to take place.

In spite of the heterogeneous structure of the materials, electron diffusion from its bulk to the supporting conductor takes place nearly without losses. Recombination between the injected electron in the conduction band of the semiconductor and the hole on the oxidized dye is indeed very slow compared to the reduction of the latter by the redox mediator in solution. Moreover, the electron-hole recombination in the semiconductor, which is not favorable for the efficiency of the classical photovoltaic cells, does not exist here, because no hole in the valence band corresponds to the electron in the conduction band. The consequence is that even under low irradiance intensities, the efficiency stays the same, on contrary to what is observed with classical systems.

### 3.2. Light harvesting by monomolecular layers

For the absorption of solar rays by a sensitizer attached as a monolayer to the surface of an oxide film there is a fundamental problem of the limited light-capture cross-section of the dye molecule. The cross section  $\sigma$  is related to the molar extinction coefficient  $\varepsilon$  by the formula:

$$\sigma = \frac{\varepsilon \cdot 1000}{N_A} \quad (1.1)$$

Typical  $\varepsilon$  values for dyes lie between  $10^4$  and  $5 \cdot 10^5 \text{ M}^{-1} \text{ cm}^{-1}$  yielding for the light-capture cross-section values between  $0.0016$  and  $0.08 \text{ nm}^2$ .<sup>[33]</sup> The area the sensitizer molecule occupies on the surface of the supporting oxide is much larger, e.g., about  $1\text{--}2 \text{ nm}^2$ .<sup>[33]</sup> Hence, at most a few percent of the incident light can be absorbed. A successful strategy to solve the problem of light absorption through such molecular layers is found in the application of high surface area films consisting of nanocrystalline oxide particles with a diameter of  $10\text{--}20 \text{ nm}$ .<sup>[34]</sup> The mesoporous morphology of the layer plays a crucial role in the harvesting of sunlight. Depending on film thickness, their real surface area can easily be made  $100\text{--}1000$  times larger than the apparent one. This allows for the capture of the incoming photons efficiently despite the fact that the oxide is covered only by a monolayer of dye. When light penetrates the dye-covered oxide “sponge”, it crosses hundreds of adsorbed dye monolayers. Thereby, photons whose energy is close to the absorption maximum of the dye are completely absorbed.<sup>[20]</sup> The mesoporous structure thus mimics the light absorption by green leaves. As the chlorophyll-containing thylakoids are stacked, visible light is absorbed completely by traversing many superimposed vesicles containing the dye.

### 3.3. Mesoscopic oxide semiconductor films

Mesoporous oxide films are commonly produced via a sol-gel type process involving a hydrothermal step (see “Mesoporous oxide paste production”, page 30). The favoured material is titanium dioxide,  $\text{TiO}_2$ . It has many advantages for sensitized photochemistry and photo-electrochemistry as a low cost, widely available, non-toxic materials, and as such is even used in health care products. Moreover, it is insensible to visible light due to its large bandgap of 3.2 eV and begins to absorb only in the near ultraviolet. It can be sensitized by a large variety of dyes, some of them allowing a incident

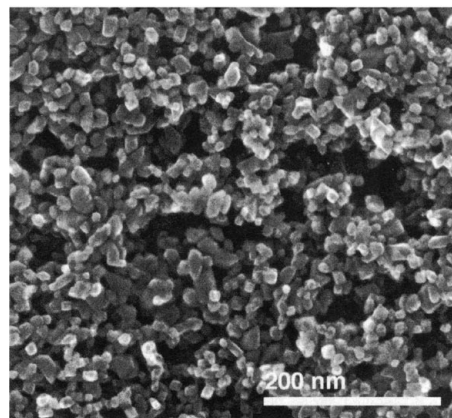


**Figure 15.** SEM image of the surface of a mesoporous film prepared from the hydrothermal  $\text{TiO}_2$  colloid<sup>[34]</sup>.

photon/electron conversion efficiency near unity. The nanoporous structure permits the specific surface concentration of the sensitizing dye to be sufficiently high for total absorption of the incident light, a necessity for efficient solar energy conversion, since the area of the monomolecular distribution of adsorbate is 2–3 orders of magnitude higher than the geometric area of the substrate. Figure 15 illustrates the morphology of such a nanocrystalline  $\text{TiO}_2$  (anatase) layer deposited on a transparent conducting oxide (TCO) glass.

### 3.4. Photoinduced charge separation at the dye/oxide interface

The use of mesoporous oxide films as a substrate to anchor the dye molecules allows sunlight to be harvested over a broad spectral range in the visible region. The dye acts as an electron transfer sensitizer. Upon excitation by light it injects electrons into the conduction band of the oxide resulting in separation of positive and negative charges.

For efficient photoconversion of solar energy, the charge injection must occur with unit quantum yield. Some rate constants for electron transfer from excited dyes into  $\text{TiO}_2$  have been determined by time-resolved laser photolysis experiments. These rates vary over 8 orders of magnitude depending on the type of dye employed. The fastest injection times are observed for dyes with a suitable anchoring group, such as carboxylate or phosphonate substituent or a catechol moiety, through which the sensitizer is firmly grafted onto the surface of titania. The role of these groups is to provide good overlap between the dye molecule's excited-state orbital and the empty acceptor levels, i.e., the  $\text{Ti}^{\text{IV}}$ -3d orbital manifold forming the conduction band of

TiO<sub>2</sub>. The extent of coupling is expressed by the electronic coupling matrix element  $|V|$  which is related to the rate constant for charge injection by the equation:

$$k_i = (2\pi/h)|V|^2\rho \quad (1.2)$$

Here  $h$  is the Planck's constant and  $\rho$  is the density of electronic acceptor states in the conduction band of the semiconductor. The equation assumes that electron transfer from the excited dye molecules into semiconductors is activationless and hence exhibits a temperature-independent rate. This has been confirmed experimentally.<sup>[35]</sup> For example, the charge injection from excited perylene dye was found to be temperature independent from 4 to 300 K.<sup>[12]</sup> The explanation for this is that there is a continuum of electric states in the conduction band accessible to the injected electron, which, combined with the different vibrational levels of the other reaction product, i.e., the oxidized dye, yields a multitude of possible reaction pathways. At least one channel is likely to be barrierless, implying that the driving force of the electron transfer compensates the reorganization energy, i.e., the free energy necessary to rearrange the nuclear coordinates of the dye/solvent system accompanying electron transfer. The activationless channel is the fastest and hence will be the preferred one for the reaction.<sup>[36]</sup>

The most promising results have so far been obtained with ruthenium complexes where at least one of the ligands was 4,4'-dicarboxy-2,2'-bipyridyl. The carboxylate groups serve to attach the Ru-complex to the surface of the oxide and to establish good electronic coupling between the  $\pi^*$  orbital of the ligand, which is the lowest unoccupied orbital (LUMO) of the complex and the 3d wavefunction manifold of the TiO<sub>2</sub> film. The substitution of the bipyridyl with the carboxylate groups lowers the energy of the LUMO. Since the electronic transition is of MLCT (metal-to-ligand-charge transfer) character, optical excitation transfers the electron to a site from which electron injection into the semiconductor can readily occur. With molecules like these, charge injection occurs in the femtosecond time domain.<sup>[36]</sup> By contrast, the recapture of the electrons by the oxidized dye is at least six orders of magnitude slower. The rationale for this behavior is that the back reaction involves a d-orbital localized on the ruthenium metal whose electronic overlap with the TiO<sub>2</sub> conduction band is small. The spatial contraction of the wavefunction upon oxidation of the Ru(II) to the Ru(III) state weakens further the electronic coupling. A second very important contribution to the kinetic retardation of the charge recombination arises from the fact that this process is characterized by a large driving force and small reorganization energy, the respective values for RuL<sub>2</sub>(NCS)<sub>2</sub> being about 1.5 and 0.3 eV, respectively. This

places the electron recapture clearly in the inverted Marcus region, reducing its rate by several orders of magnitude. This provides also a rationale for the observation that this interfacial redox process is almost independent of temperature and is surprisingly insensitive to the environment that is in contact with the film.<sup>[13]</sup>

Of significance for the inhibition of charge recombination is the existence of a local electric field at the surface of the titanium dioxide film. While no depletion layer is formed within the oxide, due to the small size of the particles and their low doping level, a surface field is established spontaneously by proton transfer from the carboxylic acid or phosphonic acid anchoring groups of the ruthenium complex to the oxide surface, producing a surface dipole layer. If the film is placed in contact with a protic solvent the latter can also act as proton donor. In aprotic media,  $\text{Li}^+$  or  $\text{Mg}^{2+}$  are potential determining ions for  $\text{TiO}_2$ ,<sup>[14]</sup> and they may be used to charge the surface positively. The local potential gradient from the negatively charged sensitizer to the positively charged oxide drives the injection in the desired direction. The same field inhibits also the electrons from exiting the solid after injection has taken place.

Investigations have centered so far largely on *cis*-dithiocyanato-bis(2,2'-bipyridyl-4,4'-dicarboxylate)-ruthenium(II),  $\text{RuL}_2(\text{SCN})_2$ , which displays extraordinary properties as a charge-transfer sensitizer.<sup>[15]</sup> The adsorption of this complex onto mesoporous  $\text{TiO}_2$  (anatase) from acetonitrile/*tert*-butanol solvent mixture follows a Langmuir isotherm. The binding constant and the area occupied by the sensitizer at the surface were determined as  $5 \cdot 10^4 \text{ M}^{-1}$  and  $1.6 \text{ nm}^2/\text{molecule}$ , respectively. Model studies, using the dcbpy ligand adsorbed onto single-crystal  $\text{TiO}_2$  (110) rutile, investigated by means of X-ray photoelectron spectroscopy, X-ray absorption spectroscopy, and quantum chemical calculations,<sup>[37]</sup> are in favor of the bridging bidentate configuration illustrated by Figure 16. The dye is attached via two of its four carboxylate groups, which straddle one row of titanium ions.<sup>[38]</sup> The anchoring occurs either through chelation or an ester-type bond to the surface titanium ions.<sup>[18]</sup>



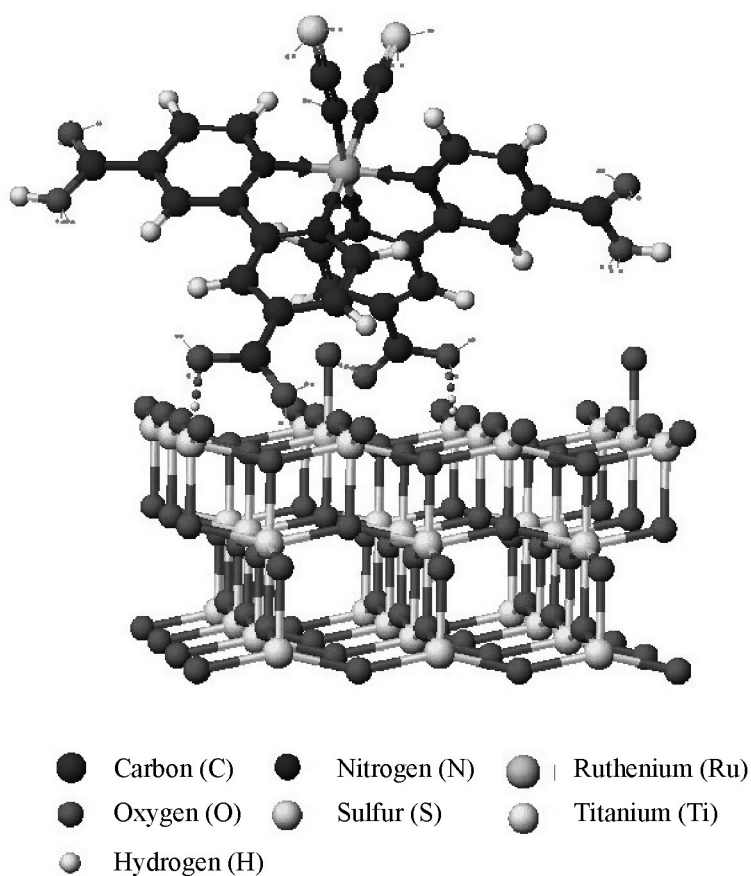


**Figure 16.** Structural representation of a  $\text{Ru}^{\text{II}}(\text{dcbpy})_2(\text{NCS})_2$  molecule adsorbed through two carboxylate groups to the (110) surface of  $\text{TiO}_2$ . From Dr. J.-E. Moser, LPI.

### 3.5. Charge-carrier percolation and collection

The migration of electrons within the  $\text{TiO}_2$  conduction band to the current collector involves charge-carrier percolation over the mesoporous particle network. This important process which leads to nearly quantitative collection of injected electrons is presently attracting a great deal of attention.<sup>[39]</sup> The intriguing findings made with these films can be rationalized in terms of a random walk of the electron via traps. The trapping and detrapping times are broadly distributed.

### 3.6. Back reaction, recapture of the injected electron by the electrolyte

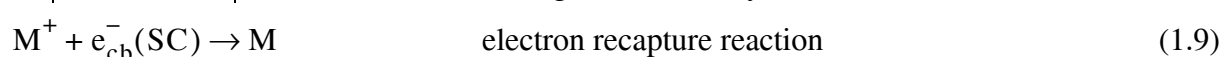
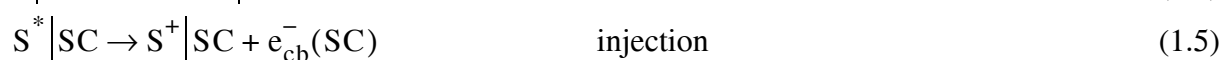
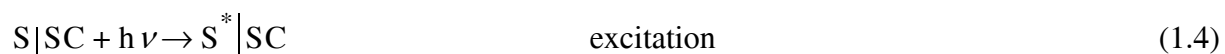
It should be noted that apart from recapture of the electrons by the oxidized dye there is an additional loss channel in the nanocrystalline injection cell which involves reduction of the triiodide ions in the electrolyte present within the mesoporous network.



This reaction can be directly followed by measuring the dark current of the dye loaded film under forward bias. The latter should be kept at a minimal level as it determines the voltage of the photovoltaic cell.

### 3.7. Electron transfer dynamics

As explained above, at the base of the design of the DSSC is a photoanode constituted by a monolayer of a molecular redox dye-sensitizer (S) adsorbed onto a layer of nanocrystalline semiconductor (SC) oxide particles. Upon light absorption by adsorbed molecules (Eq. 1.4), excited states of the photosensitizer readily inject an electron into the conduction band of the solid (Eq. 1.5). Charge injection has been found for numerous efficient systems to occur in the femtosecond time frame,<sup>[36]</sup> thus successfully competing against deactivation of the dye excited state (Eq. 1.6). The electron back transfer from the conduction band to dye cations (Eq. 1.7) takes place much more slowly, typically in the microsecond-millisecond domain.<sup>[18,40]</sup> In the presence of a redox mediator (M), this interfacial charge recombination competes kinetically with the reaction of the mediator with the oxidized sensitizer (Eq. 1.8). Charge transport by the electrolyte in the pores of the semiconductor film to the counter electrode and that of injected electrons within the nanocrystalline film to the back-contact should be fast enough to compete efficiently with the electron recapture reaction (Eq. 1.9).



These electron transfer processes are illustrated in Figure 17.

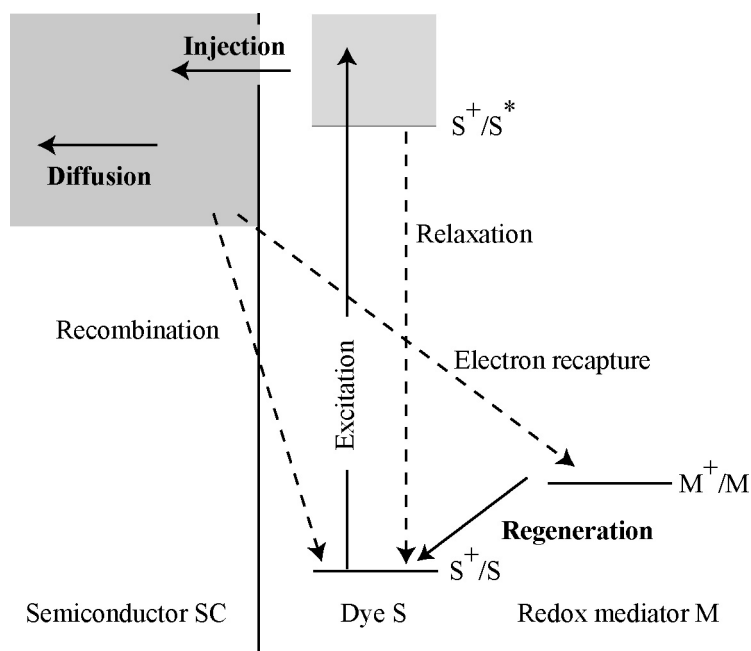


**Figure 17.** Electron transfer processes at the DSSC heterojunction.

Orders of magnitude for the electron transfer rates in the classical DSSC are summarized in Table 2.

**Table 2.** Orders of magnitude for the different electron transfer processes rates taking place in a classical DSSC.

Process	Time frame
Excitation	Femtosecond
Injection	Femtosecond
Relaxation	Picosecond
Recombination	Micro-millisecond
Regeneration of dye	Nanosecond
Electron recapture reaction	Micro-millisecond

## 4. Objective of this work

The essential focus of this thesis is on the electrolytic component of the dye-sensitized solar cells, but by necessity also on the interfaces between the electrodes and the electrolyte. Although the usually used electrolyte in the dye-sensitized solar cells is a solution based on the redox couple triiodide/iodide used with different additives and counter ions, the idea of replacing this couple by others is not a new one. It is interesting to diversify the type of redox couples being able to be used in solar cells. The attraction of this change can be scientific:

- Do comparable non-iodine based electrolytes exist for use in DSSC ?
- How do vary the different electron transfer kinetics involved in the DSSC between these couples ?
- What are their physico-chemical properties in solution ?
- What differences are induced by these couples at the photoelectrochemical properties level ?

The attraction can be technological as well:

- What are their advantages, respectively their practical disadvantages in comparison with the classical couple ?
- Is it possible to optimize one of these electrolyte in order to be effectively usable in a dye-sensitized solar cell ?

This work discuss several different electrolytic systems. In particular, systems based on organic hole conductors, as used in the solid-state dye-sensitized solar cell, and systems based on organo-metallic complexes. Platinum or cobalt complexes are examples. Other systems already studied in the past (halogens, pseudo-halogens, etc.) will also be compared to the ones studied here.

## 5. References to Chapter 1

- [1] Becquerel, A. E. *C. R. Acad. Sci. Paris* **1839**, 9, 561.
- [2] Smith, W. *Nature* **1873**, 303.
- [3] Adams, W. G.; Day, R. E. *Proc. R. Soc. Lond. A* **1877**, 25, 113.
- [4] Einstein, A. *Ann. Phys.* **1905**, 17, 132.
- [5] Czochralski, J. Z. *Phys. Chem.* **1918**, 92, 219.
- [6] *Observ. Misc. Berolinens. ad incrementum scientiarum.* **1710**, 377. Berlin.
- [7] Gurney, R. W.; Mott, N. F. *Proc. R. Soc. Lond. A* **1938**, 164, 151.
- [8] James, T. H. *The Theory of the Photographic Process*, 4th. ed.; Macmillan: New York, 1977.
- [9] West, W. *Proceedings of the Vogel Centennial Symposium. Photogr. Sci. Eng.* **1974**, 18, 35.
- [10] Moser, J. *Monatsch. Chem.* **1887**, 8, 373.
- [11] Rigollot, H. *C. R. Acad. Sci. Paris* **1893**, 116, 561.
- [12] Namba, S.; Hishiki, Y. *J. Phys. Chem.* **1965**, 69, 774.
- [13] Gerischer, H.; Tributsch, H. *Ber. Bunsenges. Phys. Chem.* **1968**, 72, 437.
- [14] Dare-Edwards, M. P.; Goodenough, J. B.; Hammett, A.; Seddon, K. R.; Wright, R. D. *Faraday Disc. Chem. Soc.* **1980**, 70, 285.
- [15] Tsubomura, H.; Matsumura, M.; Noyamaura, Y.; Amamiya, T. *Nature* **1976**, 261, 402.
- [16] Clark, W. D. K.; Sutin, N. *J. Am. Chem. Soc.* **1984**, 99, 676.
- [17] Duonghong, D.; Serpone, N.; Grätzel, M. *Helv. Chim. Acta* **1984**, 67, 1012.
- [18] Desilvestro, J.; Grätzel, M.; Kavan, L.; Moser, J.; Augustynski, J. *J Am Chem Soc* **1985**, 107, 2988.
- [19] Vlachopoulos, N.; Liska, P.; Augustynski, J.; Grätzel, M. *J. Am. Chem. Soc.* **1988**, 101, 1216.
- [20] O'Regan, B.; Grätzel, M. *Nature* **1991**, 353, 737.
- [21] Wang, A.; Zhao, J.; Wenham, S. R.; Green, M. A. *Prog. Photovolt.: Res. & Appl.* **1996**, 4, 55.
- [22] Brendel, R.; Scholten, D. *Appl. Phys. A* **1999**, 69, 201.
- [23] Brendel, R.; Auer, R.; Artmann, H. *Prog. Photovolt.: Res. & Appl.* **2001**, 9, 217.
- [24] Nishida, S.; Nakagawa, K.; Iwane, M.; Iwasaki, Y.; Ukiyo, N.; Mizutani, M.; Shoji, T. *Sol. Energy Mater.* **2001**, 65, 525.

- [25] Tayanaka, H.; Yamauchi, K.; Matsushita, T. Thin-film Crystalline Silicon Solar Cells Obtained by Separation of a Porous Silicon Sacrificial Layer; Proc. 2nd World Conf. on Photovolt. Solar Energy Conversion. **1998**, 1272. Ispra.
- [26] Weber, K. J.; Catchpole, K.; Blakers, A. W. *Crystal Growth* **1998**, 186, 369.
- [27] Rinke, T. J.; Bergmann, R. B.; Werner, J. H. *Appl. Phys. A* **1999**, 68, 705.
- [28] Södergren, S.; Hagfeldt, A.; Olsson, J.; Lindquist, S. E. *J Phys Chem-US* **1994**, 98, 5552.
- [29] Cao, F.; Oskam, G.; Meyer, G. J.; Searson, P. C. *J. Phys. Chem. B* **1996**, 100, 17021.
- [30] Schwarzburg, K.; Willig, F. *J. Phys. Chem. B* **1999**, 103, 5743.
- [31] Tennakone, K.; Kumara, G. R. R. A.; Kottegoda, I. R. M.; Perera, V. P. S. *Chem. Comm.* **1999**, 15, 15.
- [32] Sayama, K.; Suguhara, H.; Arakawa, H. *Chem. Mater.* **1998**, 10, 3825.
- [33] Nazeeruddin, M. K.; Kay, A.; Rodicio, I.; Humphry-Baker, R.; Müller, E.; Liska, P.; Vlachopoulos, N.; Grätzel, M. *J. Am. Chem. Soc.* **1993**, 115, 6382.
- [34] Barbé, C. J.; Arendse, F.; Comte, P.; Jirousek, M.; Lenzmann, F.; Shklover, V.; Grätzel, M. *J. Am. Ceram. Soc* **1997**, 80, 3157.
- [35] Burfeindt, B.; Hannappel, T.; Storck, W.; Willig, F. *J. Phys. Chem.* **1996**, 100, 16463.
- [36] Grätzel, M.; Moser, J. E. Solar Energy Conversion. In *Electron Transfer in Chemistry*; Balzani, V., Ed.; Wiley-VCH: Weinheim, 2001; Vol. 5; pp 589.
- [37] Patthey, L.; Rensmo, H.; Persson, P.; Westermark, K.; Vayssieres, L.; Stathans, A.; Petersson, A.; Brühwiler, P. A.; Siegbahn, H.; Lunell, S.; Martensson, N. *J. Chem. Phys.* **1999**, 110, 5913.
- [38] Finnie, K. S.; Bartlett, J. R.; Woolfrey, L. *Langmuir* **1998**, 14, 2744.
- [39] Hagfeldt, A.; Grätzel, M. *Acc. Chem. Res.* **2000**, 33, 269.
- [40] Haque, S. A.; Tachibana, Y.; Klug, D. R.; Durrant, J. R. *J. Phys. Chem. B* **1998**, 102, 1745.

---

# CHAPTER TWO

## Device preparation and experimental methods

# 2

---

The initial part of this chapter is dedicated to the description of each component used for the preparation of the dye-sensitized solar cells studied in this work. Glass supports, mesoporous oxide pastes, sensitizers, electrolytes and counter electrodes are described, as well as their assembly to form the whole device. The second part of this chapter explains the experimental methods used to analyze the systems under investigation. These experimental methods include photoelectrochemical, analytical and electrochemical characterizations as well as nanosecond laser spectroscopy.

## 1. Materials and synthesis

### 1.1. TCO coated glass

Highly fluorine-doped transparent conducting oxide (TCO) films deposited on glass ( $\text{SnO}_2\text{:F}$ ) were bought from Nippon Sheet Glass<sup>1</sup> (NSG) or Pilkington<sup>2</sup> (TEC15), distributed in Switzerland by Hartford. Table 1 resumes the characteristics of both substrates.

**Table 1.** TCO substrates used for the preparation of DSSC.  $T_{550}$ : transmission at 550 nm. These values are provided by the producers of the respective TCO substrates.

TCO name	Resistivity [ $\Omega$ /sq]	$T_{550}$ [%]	Diffusion [%]	IR reflectance at 10 mm [%]	Glass thickness [mm]
NSG	12	82	–	–	1
TEC15	15	83	<0.7	86	2.3

### 1.2. Mesoporous oxide paste production

Mesoporous oxide pastes were produced by P. Comte, LPI, EPFL. The flow diagram given in Figure 1 summarizes the reaction steps involved in the sol-gel preparation of the films.<sup>[1]</sup>

The precipitation process involves controlled hydrolysis of titanium(IV) isopropoxide, followed by peptization in acid or alkaline water to produce a sol, a mostly colloidal liquid. Autoclaving of these sols (heating at 200–250 °C for 12 h) allows for controlled growth of the primary particles and improves their crystallinity. During this hydrothermal growth smaller particles dissolve and fuse to form larger particles by a process known as *Ostwald ripening*. The resulting  $\text{TiO}_2$  particles consist of anatase or a mixture of anatase and rutile depending on reaction conditions. After removal of solvent and addition of a binder the sol is now ready for deposition on the TCO substrate.

---

1. <http://www.nsg.co.jp/en/>

2. <http://www.pilkington.com/>



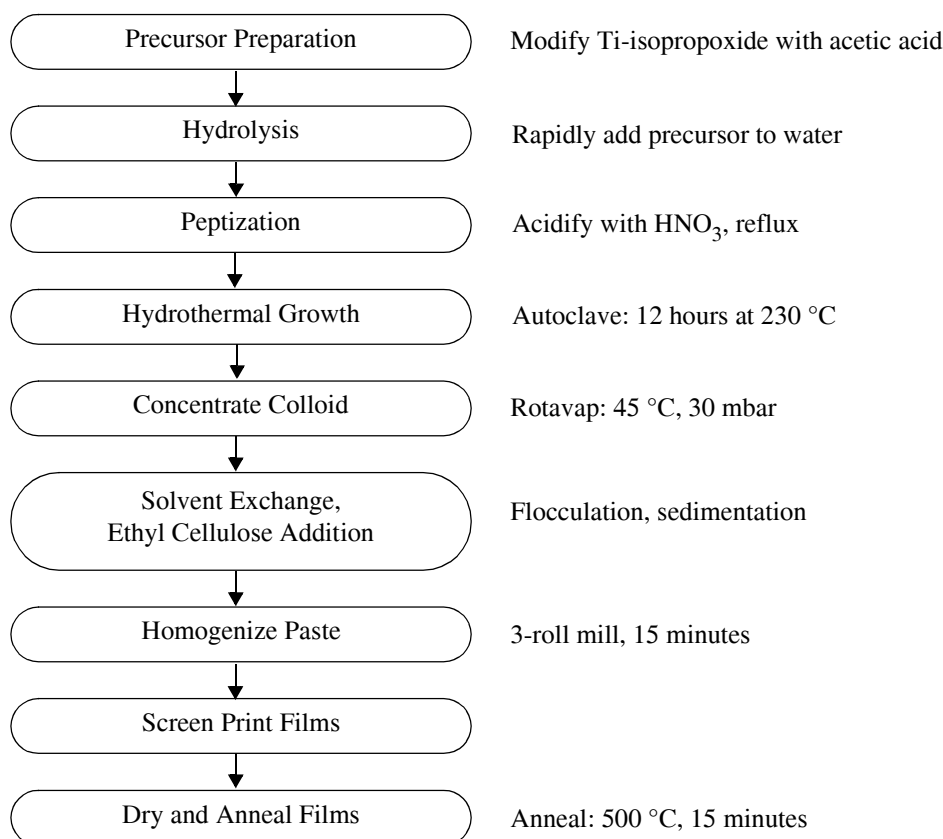


**Figure 1.** Flow diagram for the preparation of the TiO<sub>2</sub> colloids and mesoporous films.

### 1.3. Diffusive paste production

The preparation of the diffusive paste begins with the acidification down to a pH 6 of a colloid paste (TiO<sub>2</sub> anatase particles of about 400 nm diameter in water, pH ~9.5) bought from Catalysts & Chemicals Ind. Co., Ltd., Japan. It then follows the same procedure as described in Figure 1, from the concentration of the acidified colloid with the rotavap step.

### 1.4. Chemicals

All solvents and salts (puriss. grade) were purchased from Fluka or Aldrich and used as such. Common solvents, like acetonitrile, methoxypropionitrile or  $\gamma$ -butyrolactone were distilled to remove water.

Solvents for NMR, with deuterium atoms, were purchased from Dr. Glaser AG Basel.

## 1.5. Sensitizers synthesis

The ruthenium sensitizers listed in Table 2 were synthesized and supplied by Dr. Mhd. Nazeeruddin and Dr. S. Zakeeruddin, LPI, EPFL, accordingly to published procedures.<sup>[2-4]</sup> They were used as received.

**Table 2.** Ruthenium complexes used as sensitizers in this work.

Short names	Full names
N3	<i>cis</i> -di(thiocyanato)-bis(2,2'-bipyridyl-4,4'-dicarboxylic acid)-ruthenium(II)
N719	<i>cis</i> -di(thiocyanato)-bis(2,2'-bipyridyl-4-carboxylate-4'-carboxylic acid)-ruthenium(II)
Z316	<i>cis</i> -di(thiocyanato)-(2,2'-bipyridyl-4,4'-dicarboxylic acid)(4-methyl-4'-hexadecyl-2,2'-bipyridyl)-ruthenium(II)
N820	<i>cis</i> -di(thiocyanato)-(2,2'-bipyridyl-4,4'-dicarboxylic acid)(4,4'-dimethyl-2,2'-bipyridyl)-ruthenium(II)
N823	<i>cis</i> -di(thiocyanato)-(2,2'-bipyridyl-4,4'-dicarboxylic acid)(4,4'-dihexyl-2,2'-bipyridyl)-ruthenium(II)
Z907	<i>cis</i> -di(thiocyanato)-(2,2'-bipyridyl-4,4'-dicarboxylic acid)(4,4'-dinonyl-2,2'-bipyridyl)-ruthenium(II)
N621	<i>cis</i> -di(thiocyanato)-(2,2'-bipyridyl-4,4'-dicarboxylic acid)(4,4'-ditridecyl-2,2'-bipyridyl)-ruthenium(II)

The following example for N719 illustrates the synthesis procedure.<sup>[3]</sup> The ligand L = 2,2'-bipyridyl-4,4'-dicarboxylic acid and  $\text{RuCl}_3 \cdot \text{H}_2\text{O}$  were commercial samples and used without further purification. All other materials were reagent grade and were used as received. 283 mg (0.428 mmol) of  $[\text{RuL}_2\text{Cl}_2] \cdot 2\text{H}_2\text{O}$  was dissolved in 30 mL of DMF under reduced light. To this solution was added 20 mL of 0.1 M aqueous NaOH in order to deprotonate the carboxy groups. Sodium thiocyanate (350 mg, 4.52 mmol) was separately dissolved in 2 mL of  $\text{H}_2\text{O}$  and subsequently added to the above solution. The reaction mixture was stirred and heated to reflux for 6 h under a nitrogen atmosphere. After this time, the reaction mixture was allowed to cool, and the solvent was removed on a rotary evaporator. The resulting solid was dissolved in  $\text{H}_2\text{O}$  and filtered through a sintered glass crucible. The pH of this filtrate was lowered to 2.5 by adding dilute  $\text{HClO}_4$  or  $\text{CF}_3\text{SO}_3\text{H}$ , and the filtrate was placed in a refrigerator overnight. After reaching room temperature, the microcrystalline solid was isolated by suction filtration, washed well with  $\text{H}_2\text{O}$ /acetone-ether solution (1:10) followed by anhydrous diethylether, and air-dried for an hour (yield 80%).

## 1.6. Triarylamine synthesis

This synthesis of tris-(*p*-methoxyethoxy-phenyl)amine shows a typical example of triarylamine synthesis. It has been realized by Dr. S. Zakeeruddin, LPI, EPFL.

In a 250 mL round-bottomed flask equipped with reflux condenser and magnetic stirrer, sodium (1.38 g) freshly cut into small pieces was added to dry 2-methoxyethanol. After complete dissolution, sym-collidine (125 mL) dried over molecular sieve, copper(I) iodide (1.9 g) and the tris-bromophenylamine (4.96 g) were added, and the mixture was heated to reflux for 18 hours with vigorous stirring. It was then filtered whilst hot and the solvents removed on a rotary evaporator. The resulting viscous liquid was extracted with diethylether. The extract was washed by 1 M aqueous HCl and 3–4 times with water. The organic phase was evaporated to get a viscous liquid of tris-(*p*-methoxyethoxyphenyl)amine. The compound was used as such, without any further purification.

Other triarylamines were received by Xerox Research Centre of Canada (DH-TPD, DMPBPA, DM-TPD), Covion Organic Semiconductors, Germany (spiro-OMeTAD), SynTec GmbH, Germany, and used as such.

Table 3 shows the names of these compounds together with their abbreviations.

**Table 3.** Tested triarylamines names and their abbreviations.

Names	Short names
N,N'-diphenyl-N,N'-bis(3-hydroxyphenyl)-(1,1'-biphenyl)-4,4'-diamine	DH-TPD
N,N'-bis-(3,4-dimethylphenyl)biphenyl-4-amine	DMPBPA
N,N'-diphenyl-N,N'-bis(3-methylphenyl)-(1,1'-biphenyl)-4,4'-diamine	DM-TPD
2,2',7,7'-tetrakis-(N,N-di- <i>p</i> -methoxyphenylamine)-9,9'-spirobifluorene	spiro-OMeTAD
4,4',4''-tris-(N-(1-naphthyl)-N-phenylamino)-triphenylamine	1-TNATA
4,4',4''-tris-(N-3-methylphenyl)-N-phenylamino)-triphenylamine	<i>p</i> -MTDATA
tris-( <i>p</i> -methoxyethoxyphenyl)amine	TMEPA

## 1.7. Platinum(II) complexes

The platinum(II) complexes listed in Table 4 were provided by William B. Connick, Department of Chemistry, University of Cincinnati, Ohio, USA.<sup>[5]</sup> They were synthesized using standard methods<sup>[6]</sup> and used as such.

**Table 4.** Abbreviations and full names of platinum complexes used in this work.

Short names	Full names
[Pt(tpy)(pip <sub>2</sub> NCN)]BF <sub>4</sub>	[(1,3-bis(piperdylmethyl)benzene)(2,2':6',2''-terpyridine)]platinum(II) tetrafluoroborate
[Pt(tpy)(phpip <sub>2</sub> NCN)]BF <sub>4</sub>	[(1,3-bis(piperdylmethyl)benzene)(4'-phenyl-2,2':6',2''-terpyridine)]platinum(II) tetrafluoroborate

## 1.8. Cobalt complex ligands synthesis

The ligands listed in Table 5 were synthesized either by Dr. P. Bonhôte or Dr. S. Zakeeruddin, LPI, EPFL, according to published procedures.<sup>[7-9]</sup>

**Table 5.** Ligands used for the cobalt complexes synthesis.

Short name	Full name
bipy	2,2'-bipyridine
dbbip	2,6-bis(1'-n-butylbenzimidazol-2'-yl)pyridine
dmbip	2,6-bis(1'-methylbenzimidazol-2'-yl)pyridine
dmebip	2,6-bis(1'-methoxyethylbenzimidazol-2'-yl)pyridine
dobip	2,6-bis(1'-n-octylbenzimidazol-2'-yl)pyridine
phen	1,10-phenanthroline
terpy	2,2':6',2''-terpyridine
ttpy	4'-(4-tolyl)-2,2':6',2''-terpyridine

## 1.9. Cobalt(II) complexes synthesis

The cobalt complexes listed in Table 6 were also synthesized by Dr. P. Bonhôte or by Dr. S. Zakeeruddin, LPI, EPFL, accordingly to published procedures.<sup>[10,11]</sup> They were used as such.

**Table 6.** Abbreviations and full names of cobalt complexes used in this work.

Short names	Full names
[Co(bipy) <sub>3</sub> ](ClO <sub>4</sub> ) <sub>2</sub>	tris[2,2'-bipyridine]cobalt(II) perchlorate
[Co(bipy) <sub>3</sub> ](OTf) <sub>2</sub>	tris[2,2'-bipyridine]cobalt(II) trifluoromethanesulfonate
[Co(dbbip) <sub>2</sub> ](ClO <sub>4</sub> ) <sub>2</sub>	bis[2,6-bis(1'-butylbenzimidazol-2'-yl)pyridine]cobalt(II) perchlorate
[Co(dmbip) <sub>2</sub> ](ClO <sub>4</sub> ) <sub>2</sub>	bis[2,6-bis(1'-methylbenzimidazol-2'-yl)pyridine]cobalt(II) perchlorate
[Co(dmbip) <sub>2</sub> ](DDS) <sub>2</sub>	bis[2,6-bis(1'-methylbenzimidazol-2'-yl)pyridine]cobalt(II) dodecylsulfonate
[Co(dmbip) <sub>2</sub> ](OTf) <sub>2</sub>	bis[2,6-bis(1'-methylbenzimidazol-2'-yl)pyridine]cobalt(II) trifluoromethanesulfonate
[Co(dmbip) <sub>2</sub> ](PEG <sub>350</sub> BzSO <sub>3</sub> ) <sub>2</sub>	bis[2,6-bis(1'-methylbenzimidazol-2'-yl)pyridine]cobalt(II) polyethylene glycol(350) benzylsulfonate
[Co(dmbip) <sub>2</sub> ](PEG <sub>550</sub> BzSO <sub>3</sub> ) <sub>2</sub>	bis[2,6-bis(1'-methylbenzimidazol-2'-yl)pyridine]cobalt(II) polyethylene glycol(550) benzylsulfonate
[Co(dmbip) <sub>2</sub> ](PF <sub>6</sub> ) <sub>2</sub>	bis[2,6-bis(1'-methylbenzimidazol-2'-yl)pyridine]cobalt(II) hexafluorophosphate
[Co(dmbip) <sub>2</sub> ](PTS) <sub>2</sub>	bis[2,6-bis(1'-methylbenzimidazol-2'-yl)pyridine]cobalt(II) <i>p</i> -toluene sulfonate
[Co(dmebip) <sub>2</sub> ](ClO <sub>4</sub> ) <sub>2</sub>	bis[2,6-bis(1'-methoxyethylbenzimidazol-2'-yl)pyridine]cobalt(II) perchlorate
[Co(dobip) <sub>2</sub> ](ClO <sub>4</sub> ) <sub>2</sub>	bis[2,6-bis(1'-octylbenzimidazol-2'-yl)pyridine]cobalt(II) perchlorate
[Co(phen) <sub>3</sub> ](OTf) <sub>2</sub>	tris[1,10-phenantroline]cobalt(II) trifluoromethanesulfonate
[Co(phen) <sub>3</sub> ](TFSI) <sub>2</sub>	tris[1,10-phenantroline]cobalt(II) bis(trifluoromethanesulfonyl)imide
[Co(terpy) <sub>2</sub> ](ClO <sub>4</sub> ) <sub>2</sub>	bis[2,2':6',2''-terpyridine]cobalt(II) perchlorate
[Co(tppy) <sub>2</sub> ](OTf) <sub>2</sub>	bis[4'-(4-tolyl)-2,2':6',2''-terpyridine]cobalt(II) trifluoromethanesulfonate

Synthesis of cobalt complexes is a simple substitution reaction between  $\text{Co} \cdot n\text{H}_2\text{O}$  and two or three ligands. In a typical synthesis, a solution of  $\text{CoCl}_2$  (0.25 g, 1.05 mmol) in water was added dropwise to an ethanolic solution of ligand (2.11 mmol of terpy, dbbip or dmbip or 3.15 mmol of bipy or phen) at 20 °C, resulting in yellow coloration. Then the  $\text{CoL}_2^{2+}$  or  $\text{CoL}_3^{2+}$  complex was precipitated by addition of an aqueous saturated solution of the required anion. The straw-

yellow crystalline powder was filtered, washed thoroughly with water, ethanol, and diethyl ether, and dried under vacuum.

### 1.10. Cobalt(III) complexes synthesis

Two ways for preparing oxidized cobalt complexes were used:

1. In situ oxidation of Co(II) complexes upon addition of a strong oxidizer,  $\text{NOBF}_4$ .
2. Co(III) synthesis from the precursor reduced species using  $\text{Br}^-$ .

Using the first method, oxidized cobalt complex was obtained by adding nitrosyl tetrafluoroborate,  $\text{NOBF}_4$ , to the reduced form in 1:1 molar ratio at room temperature. The conversion of Co(II) to Co(III) was monitored by  $^1\text{H}$  NMR spectra (Table 10, page 92).

In the second method, some oxidized cobalt complex forms were directly synthesized as described hereafter.

A solution of  $\text{CoCl}_2$  (1.05 mmol) in water is added drop wise to a methanolic solution of (2.11 mmol) ligand and the solution turns yellow immediately. To this solution a methanolic bromine solution is added and the precipitate is formed immediately. The precipitate is then filtered and re-dissolved in acetonitrile solution. To this solution, an excess of sodium perchlorate (in methanol and water) is added and the solution is evaporated to yield the solid. The precipitate is filtered and washed thoroughly with water and ether, and finally dried under vacuum to get the pure oxidized complex.

### 1.11. Cobalt complexes crystals production

The crystals were obtained by taking a saturated acetonitrile solution of Co(II) or Co(III) in a glass tube connected to a chloroform-containing flask. After a week, slow diffusion of chloroform into the acetonitrile solution partially changed the solubility of Co(II) or Co(III). The crystals formed on the walls of glass tube are suitable for X-ray crystallography.

## 2. Device assembly

### 2.1. Photoelectrodes

Photoelectrodes used in this work usually consisted of a  $\text{TiO}_2$  film of a triple-layer structure, deposited onto a TCO substrate. First layer was a compact  $\text{TiO}_2$  blocking underlayer deposited by spray-pyrolysis on the TCO substrate. Second layer was a nanocrystalline mesoporous  $\text{TiO}_2$  layer that will bind the dye molecules. Third layer was a light-scattering layer of large  $\text{TiO}_2$  particles, used to recapture part of the light reflected by the second layer and therefore to enhanced the light harvesting.

#### *TCO substrate*

Coated glass with highly F-doped transparent conducting oxide (TCO) usually serves as a support for the dye-sensitized oxide. It allows light transmission while providing good conductivity for current collection. Other materials can be used instead of TCO, like organic polymers or metal foils, but for this work only TCO was considered. TCO should establish a good mechanical and electrical contact with the dye-sensitized oxide in order to increase electron injection from the latter to the outer circuit. Photoelectrochemical measurements have shown that some electrolytes used in this work can undergo a ohmic contact with the TCO, creating a short circuit of electrons, increasing the dark current losses (see “TCO - electrolyte interaction”, page 133). To prevent this effect, photoelectrodes used with that kind of electrolytes have had a compact  $\text{TiO}_2$  blocking underlayer.

#### *Compact $\text{TiO}_2$ blocking underlayer*

Compact blocking underlayers of spray-pyrolyzed titanium dioxide (80–100 nm thick) were deposited onto a cleaned conducting glass substrate, accordingly to published procedures<sup>[12,13]</sup>. A solution of 0.2 M titanium di-isopropoxide bis(acetylacetonate) in ethanol was sprayed with a chromatographic atomizer 15 times ( $\sim 0.1 \text{ mL} \cdot \text{cm}^{-2}$ ) at a distance of about 20 cm over the conducting glass surface that was maintained at about 400 °C on a temperature-controlled hot-plate. An interval of 10 sec between each spray process was kept. This interval allows the complete evaporation of ethanol and the original temperature to be regained. Pieces of float glass (1 mm thick) were used as mask to protect surfaces from being covered by compact  $\text{TiO}_2$  where

electrical contact will be made for photoelectrochemical characterization. After deposition, treated glass plates were fired at 500 °C for 30 min to remove remaining organic traces.

### *Nanocrystalline TiO<sub>2</sub> layer*

The sol-gel paste, made of colloidal TiO<sub>2</sub> in terpineol solvent, was deposited by screen printing and fired in air for sintering. The film thickness is typically 2–10 micron and the film density about 0.028–0.14 mg · cm<sup>-2</sup> · μm<sup>-1</sup>. The layer was dried at 150 °C for 10 min. A 2–4 micron thick light-scattering layer of a sol containing large particles of about 400 nm was then deposited on top of it, prior to being also dried at 150 °C. The electronic contact between the particles was produced by a brief sintering process at about 500 °C. The temperature program consists of heat ramps and isotherms, that are chosen to regulate the combustion of the additives and the sintering time. This temperature program is shown on Figure 2. A mesoporous structure was thereby formed having a very high effective surface area. Measurements with a Gemini 2327 nitrogen adsorption apparatus of layers samples showed their porosity to be about 65%, the average pore size being 18–20 nm. A large fraction of the particles have a bipyramidal morphology, which is typical for anatase. The exposed surface planes are mostly oriented in the (101) direction. The formation of the latter face is favored by its low surface energy. The mean particle diameter of the oxide is 15–19 nm in this case. Their size and morphology can be adjusted by varying the conditions of the sol gel-type process used for film preparation.

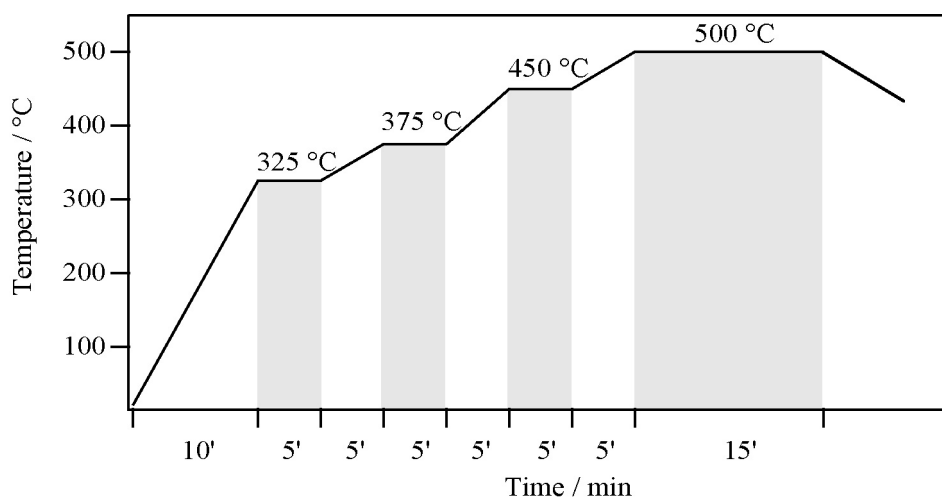


**Figure 2.** Temperature program for TiO<sub>2</sub> films.



A final post-treatment by an aqueous  $\text{TiCl}_4$  solution was then carried out. This treatment has been shown to increase the injection of electrons into the  $\text{TiO}_2$  and thus the delivered current. This effect has been assigned to the increased surface area for dye adsorption and to the formation of a native surface  $\text{TiO}_2$  layer of higher purity.<sup>[12]</sup> Furthermore Ti complexes in  $\text{TiCl}_4$  solution are believed to condense at interparticle necks, thereby increasing the interparticles connection and the electron percolation.  $65 \mu\text{L} \cdot \text{cm}^{-2}$  of a 0.05 M  $\text{TiCl}_4$  solution were applied to the nanocrystalline film for 30 min at 70 °C in a water-saturated desiccator. Contact areas were protected with adhesive tape. Afterwards the samples were washed with a large amount of distilled water and sintered for a second time for 15 minutes at 500 °C. Table 7 gives the physical properties of the different layers used in this work. The roughness factor is calculated with  $\text{Roughness factor} = (1 - \text{Porosity}) \cdot \text{Density} \cdot \text{Specific area}$ , where the density is equal to  $3.84 \text{ g} \cdot \text{cm}^{-3}$  for the  $\text{TiO}_2$  used to prepare the mesoporous layers.

**Table 7.** Physical characteristics of the layers used in this work. [a] These 5  $\mu\text{m}$  layers are deposited on a 1 mm thick non conductive glass used for the laser flash photolysis (see “Laser flash photolysis”, page 52). [b]  $\text{TiCl}_4$  post-treatment decreases the porosity by about 8%.

Name	Type	Porosity before $\text{TiCl}_4$ treatment <sup>[b]</sup> [%]	Particles diameter [nm]	Pores size [nm]	Specific area [ $\text{m}^2 \cdot \text{g}^{-1}$ ]	Roughness factor [ $\mu\text{m}^{-1}$ ]
PC 100	Mesoporous	65	18–19	20	85	114.2
PC 139	Mesoporous	65	15–16	18	100	134.4
HPW 400c	Diffusive	–	400	–	–	–
Layer for laser <sup>[a]</sup>	Mesoporous	66	18–19	20	100	130.6

All photoelectrochemical measurements were carried out using a PC 100 3  $\mu\text{m}$  thick layer and a HPW 400c 3  $\mu\text{m}$  thick layer, except if specified in the relevant experiments.

### *Sensitizer*

Dye derivatization of nanocrystalline oxide films was obtained by immersion of electrodes, heated beforehand under oxygen at 500 °C for 15 min and let cooled to 80 °C, in pure ethanolic or mixed 1:1 acetonitrile/tert-butanol ( $3\text{--}5 \cdot 10^{-4}$  M) sensitizer solutions. The firing at 500 °C

leads to a partially dehydroxylated, highly activated surface for dye adsorption. The  $\text{TiO}_2$  films were dipped in the dye solution for about 24 hours in the dark.

## 2.2. Counter electrodes

Several kinds of counter electrodes were used: nanosized platinum metal clusters on TCO, reflective platinum coated glass and gold layers on TCO.

Nanosized platinum metal clusters were deposited onto clean TCO substrate using a catalyst precursor solution composed of 5 mM solution of hexachloroplatinic(IV) acid hexahydrate in anhydrous isopropanol. 5 to 10  $\mu\text{L} \cdot \text{cm}^{-2}$  of the precursor solution was spread and dried in air for 1 min. Coated electrodes were placed on a temperature controlled hotplate, where temperature was gradually increased and left to stabilize, in order to achieve the electrode surface temperature of 385 °C. The electrode was allowed to cure at the temperature for 10 to 15 min. This technology produces optically transparent electrodes.<sup>[14]</sup>

Reflective platinum coated glasses were prepared by platinum sputtering on TCO glass. TCO was used due to platinum best adhesion quality on this support. The light reflection of this kind of electrodes comes from the thick platinum layer deposited (about 150 nm). The resistivity was 2  $\Omega \text{sq}^{-1}$ . These electrodes were used for open cells (see Paragraph 2.4 hereafter). They were therefore used many times and must be periodically reactivated in the same way as nanosized platinum metal clusters are deposited.

Thin gold layer (about 120 nm) was deposited on glass substrate using chemical vapor deposition on non conductive glass. These electrodes are semi-transparent.

## 2.3. Electrolytes

As electrolytes are the central point of this work, their preparations are described in the relevant chapters.

## 2.4. Cell assembly

Two kinds of DSSC were prepared: open cells and closed cells.

Open cells are cells where the counter electrode was simply pressed against the sensitized semiconductor film using a cell-holder. A drop of the electrolyte had previously been deposited on the counter electrode and was then sandwiched between the two electrodes.

A closed cell is a sealed cell. In this case, small  $\text{TiO}_2$  spots of about  $0.28 \text{ cm}^2$  were used. The photoelectrode was sensitized prior to being sealed with the platinated counter electrode having a pinhole through the glass (Figure 3). The sealing polymer used for this purpose is called Surlyn<sup>®1</sup>, a plastic foil of  $30 \mu\text{m}$  cut as an O-ring. This polymer must be melted by heating in order to bind the glasses together. A special setup allowed the heating of the O-ring only. The electrolyte was then injected through the small hole of the counter electrode with a pump that created a vacuum in the cell. With this technique, the electrolyte filled the gap created by Surlyn<sup>®</sup> between the two electrode and was confined to the surface limited by the O-ring. Finally, the pinhole was sealed with another full round piece of Surlyn<sup>®</sup>, covered by a small piece of glass for mechanical strength.

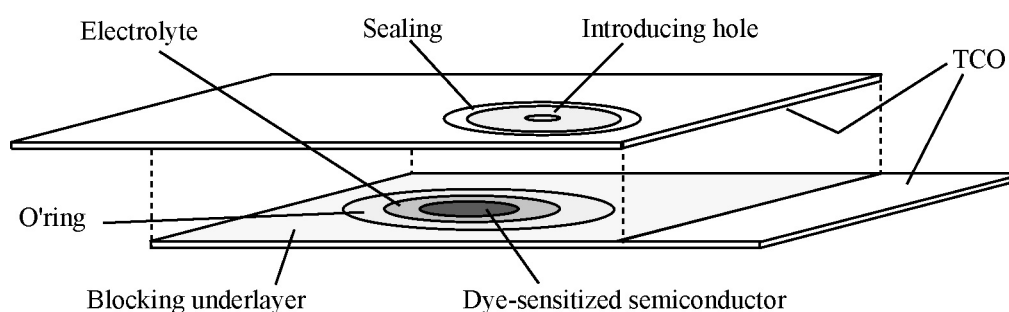


**Figure 3.** Scheme of a closed dye-sensitized solar cell.

---

1. <http://www.dupont.com/industrial-polymers/surlyn>

### 3. Photoelectrochemical characterization

#### 3.1. Introduction

The standard characterization techniques of DSSC include the determination of the current-voltage characteristics under light irradiance of different intensities and the determination of the photocurrent under low intensity monochromatic light.

Current-voltage characteristics of a solar cell may be approximated by the following mathematical expression:

$$I = I_{\text{ph}} - I_s (e^{V_a/V_t} - 1) - \frac{V_a}{R_{\text{sh}}} \quad (2.1)$$

where  $I$  is the current,  $I_s$  the saturation current of the diode, and  $I_{\text{ph}}$  the photocurrent, which is assumed to be independent of the applied voltage  $V_a$ . This applied voltage includes the series resistance  $R_s$ :

$$V_a = V + R_s \cdot I \quad (2.2)$$

$V_t$  is the thermal voltage and is equal to

$$V_t = \frac{n \cdot k \cdot T}{e}, \quad (2.3)$$

with  $n$  as the ideality factor and  $e$  the elementary charge. Eq. 2.1 models the dark current in a one-diode system and therefore is only a simplified representation of the DSSC. Its equivalent circuit is shown in Figure 4. The real structure of the device is more complicated and corresponds to a multi-diode model that take into account the different charge transport processes within the cell.

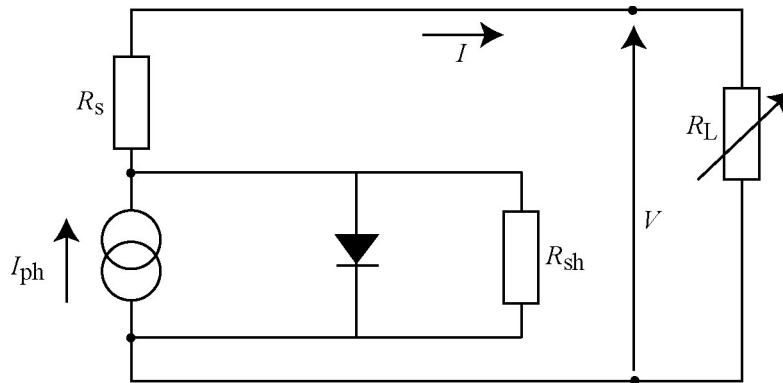


**Figure 4.** The DSSC under light irradiation can be represented as a mix non-perfect current generator (which has a shunt resistance  $R_{sh}$  and a parasite series resistance  $R_s$ ) mounted in parallel to a non-perfect diode.

Figure 5 shows a typical I/V curve in the upper part and a typical power curve in the lower part. The dots represent the maximum power output (“Maximal power output ( $P_m$ )”, page 46).

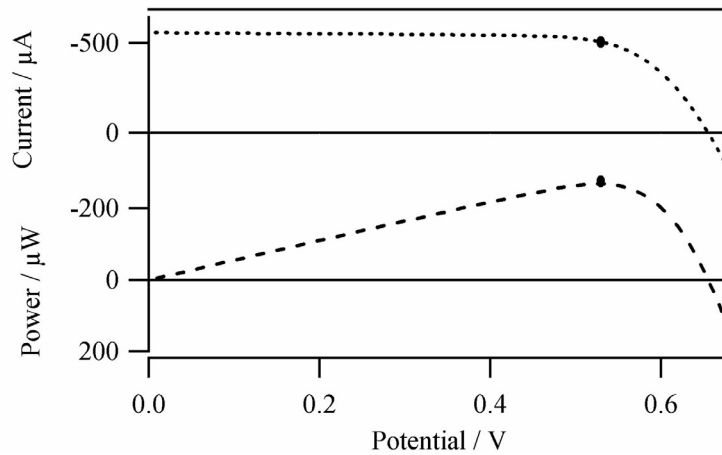


**Figure 5.** Typical curves showing the variations in photocurrent and power as a function of the potential.

Prior to any photoelectrochemical measurements, a mask with an aperture of  $0.44 \text{ cm}^2$  was applied on each cell, delimiting the exposed surface of the cell to a well known surface area, allowing to calculate the short circuit current density ( $\text{mA} \cdot \text{cm}^{-2}$ ).

The incident light power on the DSSC surface, also called irradiance, is expressed in  $\text{W} \cdot \text{m}^{-2}$ .  $1000 \text{ W} \cdot \text{m}^{-2}$  is equivalent to the light power of a full sun (100% Sun) for an air-mass number of 1.5 (AM1.5). Photoelectrochemical data were measured using a 450 W xenon light source that was focused to give  $1000 \text{ W} \cdot \text{m}^{-2}$ , the equivalent of one sun at AM 1.5, at the surface of the test cell. The spectral output of the lamp was matched in the region of 350–750 nm with the aid of a Schott 113 sunlight filter so as to reduce the mismatch between the simulated and the true Solar spectrum to less than 2%. The differing intensities were regulated with neutral wire mesh attenuators. The applied potential and measured cell current were measured using a Keithley model 2400 digital source meter. The current-voltage characteristics of the cell under these conditions were determined by biasing the cell externally and measuring the generated photocurrent. This process was fully automated using IgorPro, a Wavemetrics software.<sup>1</sup> A similar data acquisition system was used to control the incident photon-to-current conversion efficiency (*IPCE*) measurements. Under full computer control, light from a 300 W xenon lamp was focused through a high throughput monochromator onto the photovoltaic cell under test. The monochromator was incremented through the visible spectrum to generate the *IPCE*( $\lambda$ ) curve as defined below,

$$IPCE(\lambda) = 1240 \cdot \frac{J_{sc}}{\lambda \cdot \phi} \quad (2.4)$$

where  $\lambda$  is the wavelength,  $J_{sc}$  is the current at short circuit ( $\text{mA} \cdot \text{cm}^{-2}$ ), and  $\phi$  is the incident radiative flux ( $\text{W} \cdot \text{m}^{-2}$ ). This curve can be derived from the measured absorption spectrum of the adsorbed photosensitizer for comparison.

### 3.2. Incident photon-to-current conversion efficiency (*IPCE*)

The incident photon-to-current conversion efficiency (*IPCE*) is define as the number of electrons generated by light in the external circuit divided by the number of incident photons. The *IPCE* can be expressed in terms of the light harvesting efficiency (*LHE*), the quantum yield of charge injection ( $\Phi_1$ ) and the efficiency of collecting the injected charge at the back contact ( $\eta_c$ )

---

1. <http://www.wavemetrics.com/>

$$IPCE(\lambda) = LHE(\lambda) \cdot \Phi_i \cdot \eta_c \quad (2.5)$$

The light harvesting efficiency is given by

$$LHE(\lambda) = 1 - 10^{-\Gamma \cdot \sigma(\lambda)} \quad (2.6)$$

where  $\Gamma$  is the number of moles of sensitizer per square centimeter of projected surface area of the film and  $\sigma$  the absorption cross section.

The quantum yield of charge injection is given by

$$\Phi_i = k_i / (\Sigma k_d + k_i) \quad (2.7)$$

where  $k_i$  is the rate constant for electron injection and  $\Sigma k_d$  is the sum of all rate constants for the relaxation processes.

### ***Open circuit potential ( $V_{oc}$ )***

The open circuit potential ( $V_{oc}$ ) is the cell potential measured when current within the cell is equal to zero. The equation for the current-voltage characteristics (Eq. 2.1) can then be written and simplified as

$$I_{ph} = I + I_s (e^{V_a/V_t} - 1) \quad (2.8)$$

$V_{oc}$  is obtained from Eq. 2.1 by setting  $I = 0$ . At this condition,  $V_a = V_{oc}$ .

$$I_{ph} = I_s (e^{V_{oc}/V_t} - 1) \quad (2.9)$$

$$V_{oc} = V_t \cdot \ln\left(\frac{I_{ph}}{I_s} + 1\right) \cong V_t \cdot \ln\left(\frac{I_{ph}}{I_s}\right) \quad (2.10)$$

$V_{oc}$  is then a function of the irradiance.

### ***Short circuit current density ( $J_{sc}$ )***

The short circuit current ( $I_{sc}$ ) is the cell photocurrent measured at zero voltage, where the series resistance is minimal. Therefore  $V_a = 0$  and

$$I_{sc} = I_{ph} \quad (2.11)$$

The short circuit current density ( $J_{sc}$ ) is the short circuit current divided by the photoactive surface area of the cell.  $J_{sc}$  is also a function of the irradiance.

### **Maximal power output ( $P_m$ )**

The total power is, accordingly to Ohm's law:

$$P = V_a \cdot I = I_{ph} \cdot V_a - I_s \cdot V_a (e^{V_a/V_t} - 1) \quad (2.12)$$

The maximum power occurs at  $\frac{dP}{dV_a} = 0$ . The voltage and current corresponding to the maximal power point are  $V_m$  and  $I_m$ .

$$\frac{dP}{dV_a} = 0 = I_{ph} - I_s (e^{V_m/V_t} - 1) - \frac{I_s \cdot V_m}{V_t} \cdot e^{V_m/V_t} \quad (2.13)$$

This equation can be rewritten as:

$$V_m = V_t \cdot \ln \left[ \frac{I_{ph} + I_s}{I_s} \cdot \frac{1}{1 + \frac{V_m}{V_t}} \right] \cong V_t \cdot \left[ \frac{V_{oc}}{V_t} - \ln \left( 1 + \frac{V_m}{V_t} \right) \right] \quad (2.14)$$

using Eq. 2.10 for the open circuit voltage  $V_{oc}$ . The most accurate solution is obtained by using numerical methods. The maximum power can be approximated by:

$$P_m = I_m \cdot V_m \cong -I_{ph} \left( 1 - \frac{V_t}{V_m} \right) \left( V_{oc} - V_t \cdot \ln \left( 1 + \frac{V_m}{V_t} \right) \right) \quad (2.15)$$

$$P_m \cong -I_{ph} \left( V_{oc} - V_t \cdot \ln \left( 1 + \frac{V_m}{V_t} \right) - \frac{V_{oc} \cdot V_t}{V_m} \right) \quad (2.16)$$

### **Fill factor (FF)**

The fill factor (FF) measures the cell's quality as a power source and therefore is the ratio of the maximum power to the external short circuit current and open circuit voltage:

$$FF = \frac{I_m \cdot V_m}{I_{sc} \cdot V_{oc}} \quad (2.17)$$

This parameter indicates the deflection of the current-voltage characteristic from a square like curve (Figure 6) and is therefore dependant on:



- the shunt resistance  $R_{sh}$
- the series resistance  $R_s$
- the ideality factor  $n$

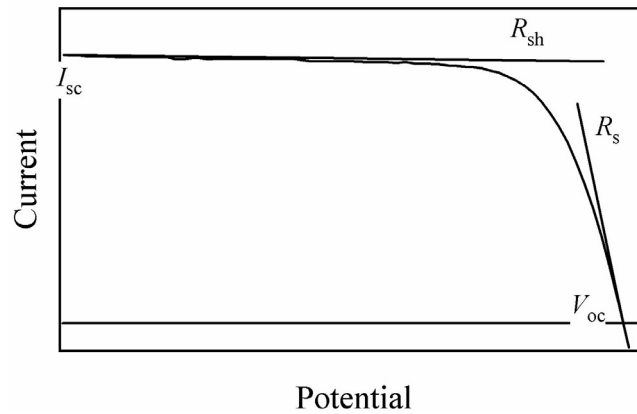


**Figure 6.** Example of I/V curve showing the open circuit potential point ( $V_{oc}$ ) and the short circuit current point ( $I_{sc}$ ). The series resistance  $R_s$  is given by the slope of the tangent line at  $V_{oc}$  and the shunt resistance  $R_{sh}$  is given by the slope of the tangent line at  $I_{sc}$ .

The resistance at  $I_{sc}$  is extremely high. In an equivalent circuit model of a solar cell, it represents a shunt resistance. The resistance at  $V_{oc}$  is on contrary very low. In the equivalent circuit model, it represents a series resistance. Both of these resistance are internal, and represent energy dissipation mechanisms in the cell. Ideally, one would like zero series resistance and infinite shunt resistance, to maximize the fill factor up to unity. The series resistance depends on the material resistivity, on the contact resistance of the electrodes and on the collecting grid resistance if present. The ideality factor is a number which characterizes the slope of a current-voltage plot as measured on a semi-logarithmic scale.

### **Efficiency ( $\eta$ )**

The efficiency describes the performance of the solar cell and is defined as the ratio of the maximum electric power extracted to the incident radiation power on the solar cell surface:

$$\eta = \frac{P_m}{P_{in}} = \frac{I_{sc} \cdot V_{oc} \cdot FF}{P_{in}} \quad (2.18)$$

As the efficiency is a function of  $I_{sc}$ ,  $V_{oc}$  and  $FF$ , improvement of the photovoltaic yield is achieved by optimization of these three parameters.

## 4. Analytical characterization

### 4.1. Elemental analysis

Elemental analysis of C, N and H was performed by Ilse Beetz Mikroanalytisches Laboratorium, Germany.

### 4.2. Absorption spectroscopy

Absorption UV-Visible spectra were recorded in a 1 cm path length quartz cell on a diode array HP 8453 spectrophotometer.

### 4.3. NMR spectroscopy studies

Proton and  $^{13}\text{C}$  NMR spectra were measured with a Bruker ACP-200 spectrometer at 200 MHz and 50.3 MHz, respectively. The reported chemical shifts were against TMS. Deuterated acetonitrile solvent was used for cobalt complexes analysis.

### 4.4. X-ray photoelectron spectroscopy

XPS data were measured with a Kratos XSAM 800 dual-chamber XPS spectrometer equipped with a hemispherical electron energy analyzer using Mg  $K_{\alpha}$  radiation ( $E = 1253.6$  eV) and an energy step of 0.1 eV. The binding energy of 285 eV has been assigned to the dominant C1s contribution (alkyl carbon atoms) for calibration. A surface N:F:Cl element ratio of 4.6:1.8:1 was estimated from the integrated intensities of the corresponding Gaussian XPS lines at 404.5 (1s), 689.9 (1s) and 197.2 eV (2p) respectively, and their photoionization cross sections.<sup>[15]</sup>

### 4.5. Crystal structure determination

X-ray diffraction data were collected at 110 K on a laboratory Bruker SMART diffractometer with a sealed X-ray tube (monochromatized Mo  $K_{\alpha}$  radiation,  $\lambda = 0.71073$  Å). A series of  $\omega$  scans with  $0.3^{\circ}$  frame-width were collected up to  $2\theta = 50^{\circ}$  (three scans with different  $\varphi$  angle). Reflection intensities were integrated using the SAINT program<sup>1</sup>. The SHELXTL program package<sup>2</sup> was used to solve (by direct methods) and to refine the analyzed structures.

---

1. SMART and SAINT, Area detector control and integration software, Ver. 6.01. Bruker Analytical X-ray Systems, Madison, Wisconsin, USA.

#### 4.6. Powder X-ray diffraction

Powder XRD patterns were recorded on the Scintag PADX laboratory diffractometer with Ge detector using Cu  $K_{\alpha}$  radiation ( $\lambda = 1.5418 \text{ \AA}$ ) of a sealed X-ray tube, operating at 45 kV and 45 mA, with Ni filter. Data were collected at room temperature in Bragg-Brentano geometry ( $\theta$ - $\theta$  scanning mode) with the  $2\theta$  step of  $0.02^{\circ}$  in  $3$ – $45^{\circ}$  interval using a stepwise scanning mode and a counting time of about 4 sec per point. Standard procedures applied for processing of the powder diffraction patterns included background removal, smoothing, peak search, and intensity normalization. Lattice parameters have been obtained by indexing 32–35 strongest reflections in the experimental powder patterns using the low-temperature unit cell parameters from the single crystal X-ray study, followed by refinement of the first-order approximation in the PIRUM program.<sup>[16]</sup>

X-ray photoelectron spectroscopy, crystal structure determination and powder X-ray diffraction studies were performed by Y. L. Slovokhotov and I. S. Neretin in the Laboratory of Polymer Structural Studies, Institute of Organoelement Compounds, Russian Academy of Sciences, Moscow.

---

2. SHELXTL, An integrated system for solving, refining and displaying crystal structures from diffraction data, Ver. 5.10. Bruker Analytical X-ray Systems, Madison, Wisconsin, USA.

## 5. Electrochemical methods

Electrochemical data for redox potentials determination were obtained by stationary amperometry using a single-compartment three-electrode cell and a standard potentiostat. The working electrode was a nominal 10  $\mu\text{m}$  diameter platinum ultramicroelectrode (UME) from Bioanalytical Systems (MF-2005), the auxiliary electrode was a platinum wire, the pseudo-reference electrode was a silver wire, and the electrolyte was a 0.01 M tetrabutylammonium hexafluorophosphate ( $\text{TBAPF}_6$ ) solution in acetonitrile. Due to experimental difficulties, no usual reference electrodes was used. The measurements with cobalt complexes were rather compared with measurements made in the same conditions and using 10 mM ferrocene in acetonitrile, which redox potential at 20°C is well known. Finally, all redox potentials were reported against saturated SCE at 20°C.

The diffusion coefficients were measured using a two-electrode cell with an Autolab potentiostat. The working electrode diameter was a measured 10.9  $\mu\text{m}$  platinum UME (Bioanalytical Systems MF-2005) and the counter electrode a platinum wire. The electrolyte was the same as for the redox potential measurements described above.

UME have a characteristic dimension of a few microns. Using an UME leads to a large increase in the material transfer rate, due to the establishment of a cylindrical diffusion flux. The thickness of the diffusion layer is then completely determined by the electrode geometry and is not influenced by the convection in solution.

In case of a microdisk electrode with a radius  $r_d$ , the thickness of the diffusion layer  $\delta$  is

$$\delta = \frac{\pi r_d}{4} \quad (2.19)$$

and the stationary current is then proportional to the concentration in the bulk of the solution  $c = c(\infty)$ , to the diffusion coefficient  $D$  of the reactive species and to the radius  $r_d$

$$I_d = 4nFDcr_d \quad (2.20)$$

As the thickness of the diffusion layer is entirely determined by the electrode geometry and is independent of the diffusion coefficient, then the half-wave potential is given by

$$E_{1/2} = E^{\circ'} + \frac{RT}{nF} \cdot \ln \left[ \frac{D_R}{D_O} \right] \quad (2.21)$$

## 6. Laser flash photolysis

Recombination dynamics at the  $\text{TiO}_2$ /electrolyte interface were studied by means of laser flash photolysis. The dye was excited by pulsed laser photolysis at wavelengths where its absorbance is relatively low to assure a homogeneous absorption profile throughout the dye-sensitized  $\text{TiO}_2$  layer. The excited state decay of the dye or the recovery of its fundamental state was then monitored by the change of the absorbed continuous wave light.

The preparation of samples is quite simple. A drop of pure solvent or of the electrolyte was sandwiched between the dye-sensitized transparent mesoporous  $\text{TiO}_2$  layer (Table 7, page 39) and a thin microscope coverglass. The sample was then subjected to low-intensity flash photolysis immediately after preparation.

Pulsed laser excitation was applied using a broadband optical parametric oscillator pumped by a frequency-tripled Q-switched Nd:YAG laser (30 Hz repetition rate, pulse width at half-height 5 ns). The output of the OPO was tuned at  $\lambda = 480$  nm and attenuated by filters. The beam was expanded by a plano-concave lens to irradiate a large cross-section ( $\sim 1 \text{ cm}^2$ ) of the sample, whose surface was kept at a  $30^\circ$  angle to the excitation beam. The analyzer light, produced by a continuous wave Xe arc lamp, was passed through a first monochromator used to reduce the light intensity, various optical elements, the sample and a second monochromator, prior to being detected by a fast photomultiplier tube. Satisfactory signal-to-noise ratios were typically obtained by averaging over several hundreds laser shots. The acquisition system was a Tektronix DSA 602A digitizing signal analyzer.

The pulsed laser intensity was usually kept at a very low level ( $40 \mu\text{J} \cdot \text{cm}^{-2}$  per pulse) as to ensure that, on the average, less than one electron in the conduction band per oxidized dye molecule pair was produced per nanocrystalline particle upon pulsed irradiation. As well, the intensity of the monochromatic probe light reaching the sample was attenuated to less than  $1 \text{ mW} \cdot \text{cm}^{-2}$  to minimize steady-state carrier concentration. In such conditions, the kinetics of the oxidized dye transient absorption decay could usually be well fitted by a single exponential. Increasing the laser fluence above  $80 \text{ J} \cdot \text{cm}^{-2}$  caused, especially with the cobal complexes, the gradual appearance of a previously observed fast component in the decay, that could not be reduced to first-order kinetics anymore.<sup>[17-19]</sup>

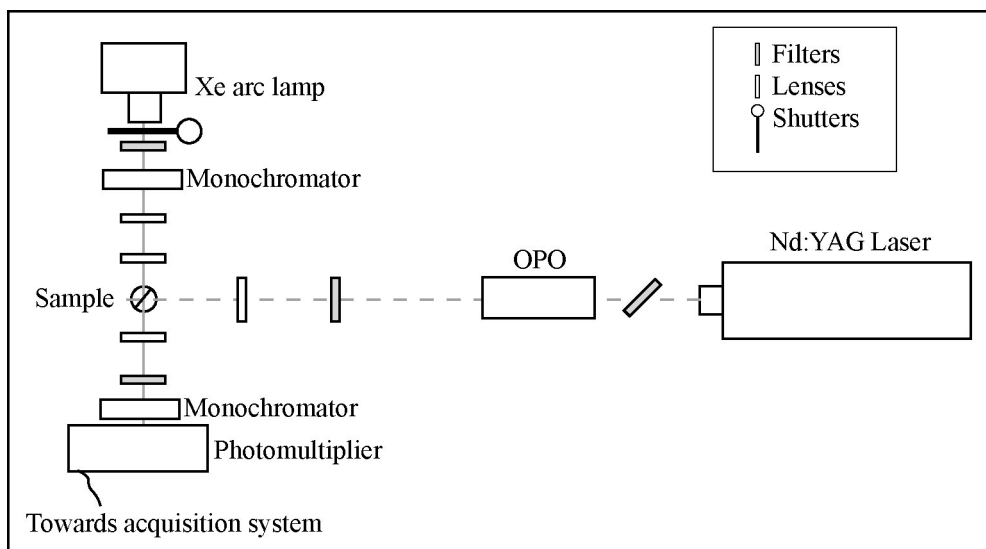


**Figure 7.** Scheme of the setup for the laser flash photolysis experiments.

## 7. References to Chapter 2

- [1] Brooks, K. G.; Burnside, S. D.; Shklover, V.; Comte, P.; Arendse, F.; McEvoy, A. J.; Grätzel, M. *Proc. Am. Ceram. Soc.* **1999**, 115. Indianapolis.
- [2] Nazeeruddin, M. K.; Zakeeruddin, S. M.; Humphry-Baker, R.; Jirousek, M.; Liska, P.; Vlachopoulos, N.; Shklover, V.; Fischer, C.-H.; Grätzel, M. *Inorg. Chem.* **1999**, 38, 6298.
- [3] Nazeeruddin, M. K.; Kay, A.; Rodicio, I.; Humphry-Baker, R.; Müller, E.; Liska, P.; Vlachopoulos, N.; Grätzel, M. *J. Am. Chem. Soc.* **1993**, 115, 6382.
- [4] Zakeeruddin, S. M.; Nazeeruddin, M. K.; Humphry-Baker, R.; Péchy, P.; Quagliotto, P.; Barolo, C.; Viscardi, G.; Grätzel, M. *Langmuir* **2002**, 18, 952.
- [5] Jude, H.; Bauer, J. A. K.; Connick, W. B. *J Am Chem Soc* **2003**, 125, 3446.
- [6] Jude, H.; Bauer, J. A. K.; Connick, W. B. *Inorg Chem* **2002**, 41, 2275.
- [7] Shklover, V.; Eremenko, I. L.; Berke, H.; Nesper, R.; Zakeeruddin, S. M.; Nazeeruddin, M. K.; Grätzel, M. *Inorg Chim Acta* **1994**, 219, 11.
- [8] Dekorte, J. M.; Owens, G. D.; Margerum, D. W. *Inorg Chem* **1979**, 18, 1538.
- [9] Szalda, D. J.; Creutz, C.; Mahajan, D.; Sutin, N. *Inorg. Chem.* **1983**, 22, 2372.
- [10] Piguet, C.; Bocquet, B.; Müller, E.; Williams, A. F. *Helv. Chim. Acta* **1989**, 72, 323.
- [11] Addison, W.; Burke, P. J. *J. Heterocycl. Chem.* **1981**, 18, 803.
- [12] Kay, A. Solar Cells based on Dye-Sensitized Nanocrystalline TiO<sub>2</sub> Electrodes, Ecole Polytechnique Fédérale de Lausanne, 1994.
- [13] Kavan, L.; Grätzel, M. *Electrochim Acta* **1995**, 40, 643.
- [14] Papageorgiou, N.; Maier, W. F.; Grätzel, M. *J. Electrochem. Soc.* **1997**, 144, 876.
- [15] Band, I. M.; Kharitonov, Y. I.; Trzhaskovskaya, M. B. *Atom. Data Nucl. Data Tables* **1979**, 23, 443.
- [16] Werner, P.-E. *Arkiv Kemi* **1969**, 31, 513.
- [17] Haque, S. A.; Tachibana, Y.; Klug, D. R.; Durrant, J. R. *J. Phys. Chem. B* **1998**, 102, 1745.
- [18] Haque, S. A.; Tachibana, Y.; Willis, R. L.; Moser, J. E.; Grätzel, M.; Klug, D. R.; Durrant, J. R. *J. Phys. Chem. B* **2000**, 104, 538.
- [19] Kuciauskas, D.; Freund, M. S.; Gray, H. B.; Winkler, J. R.; Lewis, N. S. *J. Phys. Chem. B* **2001**, 105, 392.



---

# CHAPTER THREE

## Alternative redox couples for the DSSC system

# 3

---

There has been much research to find alternative redox couples to the well-known triiodide/iodide redox couple used in the dye-sensitized solar cell. All couples having a redox potential lower than the potential of the dye anchored on the semiconductor and a large difference in apparent electron transfer rates on photoanode and counter electrode may be a candidate for replacing the triiodide/iodide couple. This alternative couple must also be stable towards light soaking and thermal stress. This chapter gives an overview of the already tested couples and focuses on particular new redox couples tried during this study, such as some triarylamines and metal complexes.

## 1. Introduction

So far, the triiodide/iodide couple has been almost exclusively employed as a redox mediator in DSSCs based on the sensitization of mesoporous titanium dioxide by ruthenium complexes. Very high incident photon-to-current conversion efficiency (*IPCE*) approaching unity has been reached. *IPCE* normally does not exclude light loss due to reflections and glass absorption and a value of 0.85 is therefore the maximum one can expect. In this case, the dye regeneration reaction is, however, complicated by the fact that the conversion of iodide to triiodide involves the transfer of two electrons.<sup>[1]</sup> A large driving force is therefore necessary to carry out the primary oxidation step from iodide to atomic iodine atom or  $I_2^-$ . The resulting potential mismatch between the redox couples of the sensitizer ( $S^+/S$ ) and the mediator ( $I_3^-/I^-$ ) is responsible for large polarization losses ( $\sim 0.6$  V).<sup>[2]</sup>

Therefore, despite its excellent ability to transfer charges within the solar cell, the triiodide/iodide couple has its own disadvantages. As its redox potential is at ca. 0.15 V vs. SCE and the flatband potential of the semiconductor is at  $-0.82$  V vs. SCE at pH 7,<sup>[3]</sup> the maximum theoretical photovoltage available is ca. 0.97 V. With a standard dye, which has a redox potential of about 0.85 V vs. SCE in the fundamental state,<sup>[4]</sup> the redox potential of the redox couple could be optimized to increase the photovoltage, without compromising the dye regeneration. Chemical corrosive reactions between iodide and various metals is also a well known problem of triiodide/iodide couple, especially when trying to make modules, where collecting metallic stripes are mandatory to collect the electrons generated by the cells.

In order to find a competitive couple to the triiodide/iodide one,  $Br_2/Br^-$  and quinone/hydroquinone redox mediators were successfully used in early DSSC designs.<sup>[5]</sup> DSSC made with  $10^{-3}$  M hydroquinone gave a short circuit current of  $0.57$  mA  $cm^{-2}$  and an *IPCE* of 44% when used with tris[2,2'-bipyridyl-4,4'-dicarboxylate]ruthenium(II). Interesting results were also obtained with dye-sensitized  $TiO_2$  in conjunction with hole conductors like phenothiazines.<sup>[6]</sup> Unfortunately, efficient recombination of electrons in  $TiO_2$  films with oxidized phenothiazine compounds results in a low *IPCE*. The high local concentrations present in the colloidal films significantly shorten the lifetimes of oxidized phenothiazines. Attempts to increase charge separated state lifetimes by changing the solvent, ionic strength, and/or the phenothiazine donor have been unsuccessful. One strategy to increase charge separation lifetimes was to covalently bind the donor to the ruthenium(II) sensitizer.

The latter systems provide remarkably long-lived interfacial charge-separated pairs, but show somehow disappointing photovoltaic performances, attributed to an additional short-circuiting pathway constituted by the charge percolation inside the molecular monolayer and to the underlying conducting glass.<sup>[7]</sup>

Recently, pseudo-halogens couples,  $(\text{SCN})_2/\text{SCN}^-$  and  $(\text{SeCN})_2/\text{SeCN}^-$ , were evaluated for their utilization in DSSC.<sup>[8]</sup> Although redox potentials of these mediators are more positive than that of  $\text{I}_3^-/\text{I}^-$ , no improvement on the open circuit potential of the cells was observed. This was explained by the observation that the potentials of both the TCO/dye-sensitized  $\text{TiO}_2$  electrode and the TCO/Pt electrode shift with the equilibrium potential of the redox couple. Upon shifting the redox equilibrium potential more positive, the incident photon-to-current efficiency was found to decrease by a factor of 4 for  $(\text{SeCN})_2/\text{SeCN}^-$  and a factor of 20 for  $(\text{SCN})_2/\text{SCN}^-$  compared with  $\text{I}_3^-/\text{I}^-$ . Transient absorbance studies demonstrated that the lower efficiencies are related to a slower dye regeneration rate when  $\text{SCN}^-$  or  $\text{SeCN}^-$  are used in place of  $\text{I}^-$  (Eq. 1.8, page 24).

Apart from halogens, pseudo-halogens and hole conductor redox couples, metal complexes have been early recognized as potential electron relays and catalysts in photoredox reactions.<sup>[9,10]</sup>

## 2. Electrolytes based on triarylaminines

### 2.1. Introduction

Triarylaminines are widely used as hole conductors in solid-state dye-sensitized solar cells.<sup>[11,12]</sup> and have also been used in liquid DSSC, either coupled with the sensitizer or co-adsorbed on the TiO<sub>2</sub> surface.<sup>[7,13-17]</sup> In this work, triarylaminines have been tried as an electron relay in solution. The screening of different triarylaminines for their suitability to be used as hole conductors in solution was consequently carried out.

### 2.2. Electrolytes preparation

First of all, suitable solvents being able to dissolve the highest possible amount of triarylamine were identified. Once in solution, less than 10% of the triarylaminines were oxidized. A small quantity of ionic liquid was added to this mixture to prevent space charge limitation of the photocurrents. The ionic liquids used were room temperature melts, based on imidazolium cations. These ionic liquids must also be soluble in the solvent of choice.

**Table 1.** Solubilities table for hole conductors in different solvents.

Hole conductor	Solvent	Max. concentration [M]
DM-TPD	Chlorobenzene	0.45
DH-TPD	$\gamma$ -butyrolactone	0.45
DMPBPA	Chlorobenzene	0.80
spiro-MeOTAD	Chlorobenzene	0.20
1-TNATA	1,2-dichloromethane	0.06
<i>p</i> -MTDATA	Toluene	0.30

Seven different triarylaminines were tested as hole conductors in liquid electrolytes. Table 2 represents the chemical structures of these compounds with their abbreviated names (see Table 3, page 33 for their full names). Table 3 gives their molecular weights. All these amines are in a solid state, apart from TMEPA which is liquid under normal conditions.

**Table 2.** Chemical structures of the tested triarylamines and their abbreviations.

DH-TPD	spiro-MeOTAD
DMPBPA	DM-TPD
1-TNATA	<i>p</i> -MTDATA
TMEPA	

**Table 3.** Molecular weights of the triarylaminines screened.

Short name	Molecular weight
DH-TPD	520.62
spiro-MeOTAD	1221.48
DMPBPA	377.52
DM-TPD	516.67
1-TNATA	897.11
<i>p</i> -MTDATA	789.02
TMEPA	467.55

### 2.3. Photoelectrochemical measurements of the triarylaminines

Generally, when using triarylaminines, a blocking TiO<sub>2</sub> underlayer is necessary on the photoelectrode to prevent short-circuiting. In all cases, dye Z316 (see Table 2, page 32) was used to sensitize the mesoporous oxide films and all cells were open cells, build as described in “Cell assembly”, page 40. The counter electrode was a reflective platinum electrode.

Table 4 shows some photoelectrochemical properties of DSSC measured with DH-TPD at high concentration in  $\gamma$ -butyrolactone, and Figure 1 illustrates some *I/V* curves that can be obtained with such measurements.

**Table 4.** Photoelectrochemical properties of DSSC made with DH-TPD in  $\gamma$ -butyrolactone. DMBI stands for 1,2-diethyl-3-butyylimidazolium.

Electrolyte	Irradiance [W · m <sup>-2</sup> ]	V <sub>oc</sub> [mV]	J <sub>sc</sub> [ $\mu$ A · cm <sup>-2</sup> ]	FF [-]	Efficiency [%]
DH-TPD 0.4 M, 10% oxidized	15	405	24	0.49	0.30
	95	440	82	0.53	0.20
DH-TPD 0.46 M, 1% oxidized, with 50 mM of DMBI TFSI	15	435	37	0.46	0.47
	95	295	140	0.32	0.14

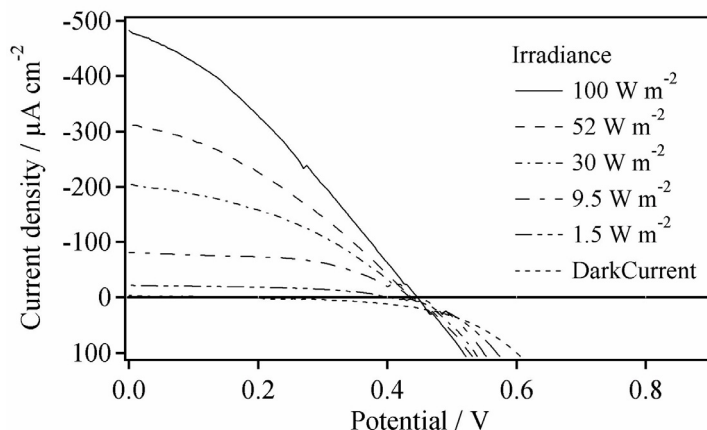


**Figure 1.** I/V curves showing the photoelectrochemical measurements of the DSSC described in Table 4 (DH-TPD 0.4 M, 10% oxidized). At positive currents, inversion of the potential is visible, with lower potentials for higher irradiances.

As can be seen in Figure 1 and in Table 4, the open circuit voltage may be lower at higher irradiances than at lower. This behavior is typical for a photoshunt. As the irradiation intensity increases more charges are created and new pathways are found for charge transport within the cell. These new pathways tend to reduce the shunt resistance and therefore increase the slope of the I/V curve at zero potential.

Figure 2 shows some I/V measurements at  $15 \text{ W} \cdot \text{m}^{-2}$  for the liquid hole conductor called TMEPA, and Table 5 gives the photoelectrochemical properties of this hole conductor when it is oxidized at 10% and used with 0.1 M of ionic liquid. Photoelectrochemical properties of spiro-MeOTAD and *p*-MTDATA when used as hole conductors in liquid DSSC are also reported in Table 5.

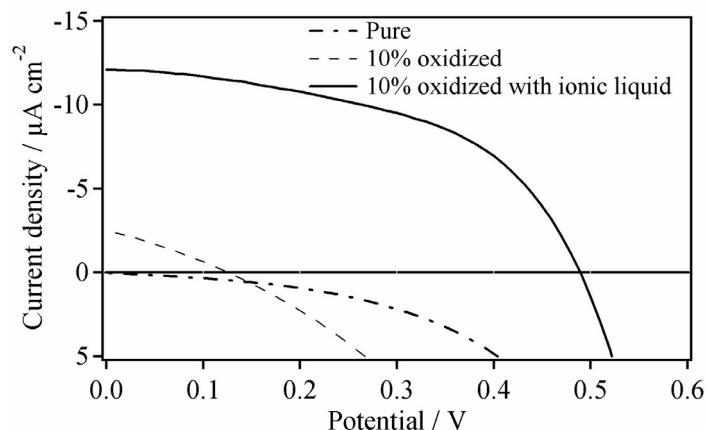


**Figure 2.** I/V curves showing the photoelectrochemical measurements at  $15 \text{ W} \cdot \text{m}^{-2}$  for some DSSCs using TMEPA as hole conductor. This TMEPA was first used pure, then oxidized at 10%, and finally oxidized at 10% with 0.1 M of 1-ethyl-3-methylimidazolium trifluoromethanecarboxylate.

**Table 5.** Photoelectrochemical properties of DSSC made with TMEPA, spiro-MeOTAD, and *p*-MTDATA. EMI stands for 1-ethyl-3-methylimidazolium and TFMC for trifluoromethanecarboxylate.

Electrolyte	Irradiance [ $\text{W} \cdot \text{m}^{-2}$ ]	$V_{oc}$ [mV]	$J_{sc}$ [ $\mu\text{A} \cdot \text{cm}^{-2}$ ]	<i>FF</i> [-]	Efficiency [%]
TMEPA, 10% oxidized, with 0.1 M of EMI	15	540	23	0.73	0.55
TFMC	95	595	145	0.71	0.64
spiro-MeOTAD 0.25 M, 0.2% oxidized, in chlorobenzene, with 13 mM of lithium TFSI	15	530	15	0.54	0.27
	95	565	43	0.31	0.08
<i>p</i> -MTDATA 0.34 M, 10% oxidized, in toluene, with 0.1 M of EMI TFMC	15	575	17	0.28	0.17
	95	580	20	0.31	0.04

No photoelectrochemical measurements were realized with the compounds DM-TPD, DMPBPA and 1-TNATA due to experimental difficulties. For example, 1-TNATA was found to be only slightly soluble in 1,2-dichloromethane (60 mM) among 16 solvents screened. Such a low solubility did not produced any measurable data.



## 2.4. Electron transfer dynamics

DH-TPD used with sensitizer Z316 was kinetically characterized using laser flash photolysis. As explained in “Electron transfer dynamics”, page 24, several electron transfer processes take place at the DSSC heterojunction. These electron transfer processes are summarized here below, where Eq. 3.1 represents the excitation step of the sensitizer, Eq. 3.2 the injection of the electron in the conduction band of  $\text{TiO}_2$ , Eq. 3.3 the relaxation process, Eq. 3.4 the recombination of the electron with the oxidized dye, Eq. 3.5 the regeneration of the oxidized sensitizer by the redox mediator, and Eq. 3.6 the electron recapture reaction from the conduction band to the oxidized redox mediator. These equations are given with their associated kinetic constants.



Figure 3 shows results from nanosecond time resolved laser experiments. The transient optical signal records the concentration of oxidized ruthenium sensitizer following photo-induced electron injection from the dye into the conduction band of the  $\text{TiO}_2$  film.<sup>[18]</sup>

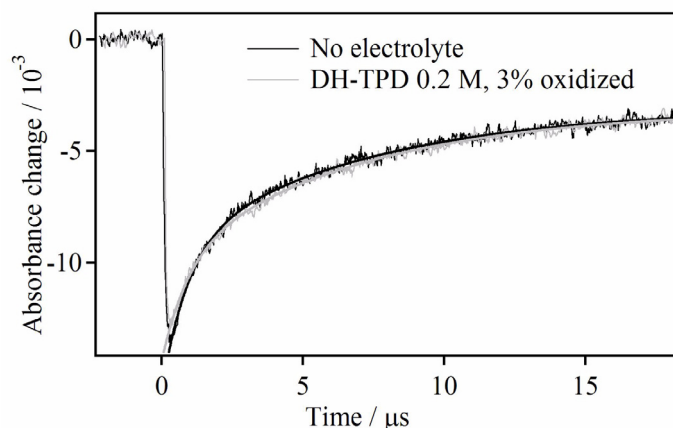


**Figure 3.** Time course of the transient absorbance changes measured upon laser excitation of Z316 dye adsorbed on a nanocrystalline  $\text{TiO}_2$  film in the presence and absence of DH-TPD 0.2 M, 3% oxidized with  $\text{NOBF}_4$ , in EC/PC (1:1). Bleaching signals were measured at 480 nm, employing a 600 nm laser excitation (5 ns fwhm pulse duration,  $1 \text{ mJ} \cdot \text{cm}^{-2}$  pulse fluence).

Both curves in Figure 3 are the same. As addition of DH-TPD as hole conductor instead of pure solvent mixture does not increase the regeneration rate of the dye ground state, one can conclude that the dye regeneration rate using the triarylamine is slower or equivalent to the recombination rate. From the electron transfer dynamics point of view, DH-TPD is not an interesting candidate to be used in DSSC. The relatively fast recovery of the fundamental state of the dye is due to the highly energetic  $1 \text{ mJ} \cdot \text{cm}^{-2}$  pulse fluence, which injects about 25 electrons per  $\text{TiO}_2$  particle, while in a normal working DSSC at stationary state, there is only one electron per particle on an average.

## 2.5. Conclusion

Photoelectrochemical measurements have been carried out with these triarylamines when possible. When used in liquid DSSC, these compounds give only low photovoltaic efficiencies. Although these molecules are widely used as hole conductors in many applications<sup>[15,19,20]</sup> and spiro-OMeTAD has been successfully used in solid-state dye-sensitized solar cells,<sup>[21-23]</sup> it seems that further work is required to make applications in liquid electrolytes suitable, mainly due to solubility problems. In all cases, low photocurrent and *IPCE* were obtained, and transient

current spectra showed a very important diffusion problem. The liquid triaryamine hole conductor, TMEPA, synthesized as described in “Triaryamine synthesis”, page 33, was undoubtedly the most interesting candidate. Due to its intrinsic nature, TMEPA already solved the solubility problem and therefore showed the best performance amongst all the investigated triaryamine hole conductors. Higher efficiencies should be obtainable through the use of purified TMEPA.

### 3. Platinum complexes

#### 3.1. Introduction

Sixth period transition metal compounds typically undergo two-electron changes in oxidation state by inner-sphere mechanisms. This behavior suggests that such a compound could be designed and used as a cooperative two-electron shuttle that can reversibly transfer two electrons at about the same potential in DSSC.<sup>[24]</sup> In the case of platinum, the practical problem is that the interconversion between planar Pt(II) and octahedral Pt(IV) by outer-sphere electron transfer to the dye anchored on the TiO<sub>2</sub> surface is slow and characterized by irreversible electrochemistry because of the accompanying large molecular reorganization.<sup>[25]</sup> This two-electron process can nevertheless undergo a nearly electrochemically reversible two-electron oxidation process if one designs complexes with rigid meridional coordinating ligands and strong donor groups that are capable of stabilizing both four-coordinate Pt(II) and six-coordinate Pt(IV) geometries.<sup>[24]</sup> Examples of such compounds are the [Pt(tpy)(pip<sub>2</sub>NCN)]BF<sub>4</sub> and [Pt(tpy)(phpip<sub>2</sub>NCN)]BF<sub>4</sub> complexes. The [Pt(tpy)(pip<sub>2</sub>NCN)]BF<sub>4</sub> complex undergoes a nearly reversible two-electron oxidation process at  $E^{o'} = 0.40$  V vs. Ag/AgCl in acetonitrile solution.

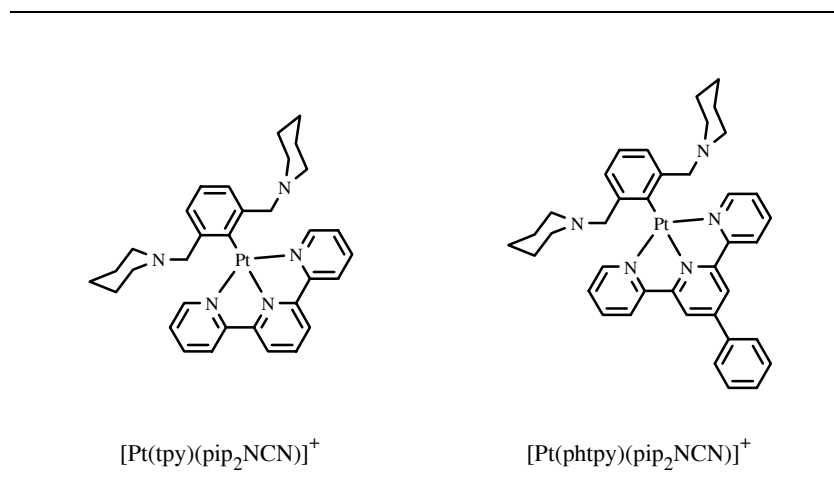
#### 3.2. Electrolytes preparation

Electrolyte solutions were prepared by dissolving a certain amount of platinum complexes in anhydrous solvents, like  $\gamma$ -butyrolactone, methoxyacetonitrile or in solvent mixtures like acetonitrile/ethylene carbonate (2:3) or ethylene carbonate/ $\gamma$ -butyrolactone (1:1). Partial oxidation of Pt(II) complex to Pt(IV) was achieved by adding stoichiometric amounts of NOBF<sub>4</sub> to the solutions at 20 °C under dry air.

Table 6 gives the molecular weights of both platinum complexes studied in this chapter and Table 7 shows the chemical structures of the [Pt(tpy)(pip<sub>2</sub>NCN)]BF<sub>4</sub> and [Pt(phtpy)(pip<sub>2</sub>NCN)]BF<sub>4</sub>.

**Table 6.** Molecular weights of the platinum complexes.

Short name	Molecular weight
[Pt(tpy)(pip <sub>2</sub> NCN)]BF <sub>4</sub>	786.57
[Pt(phtpy)(pip <sub>2</sub> NCN)]BF <sub>4</sub>	862.66

**Table 7.** Chemical structures of the platinum complexes.

Solubilities of [Pt(tpy)(pip<sub>2</sub>NCN)]BF<sub>4</sub> and [Pt(phtpy)(pip<sub>2</sub>NCN)]BF<sub>4</sub> in different solvents were first tested. Table 8 gives these solubilities for both compounds.

**Table 8.** Solubilities table for [Pt(tpy)(pip<sub>2</sub>NCN)]BF<sub>4</sub> and [Pt(phtpy)(pip<sub>2</sub>NCN)]BF<sub>4</sub>.

Compound	Solvent	Concentration max [M]
[Pt(phtpy)(pip <sub>2</sub> NCN)]BF <sub>4</sub>	γBL	0.1
[Pt(phtpy)(pip <sub>2</sub> NCN)]BF <sub>4</sub>	MAN	1.6 · 10 <sup>-4</sup>
[Pt(phtpy)(pip <sub>2</sub> NCN)]BF <sub>4</sub>	γBL/EC (1:1)	0.1
[Pt(tpy)(pip <sub>2</sub> NCN)]BF <sub>4</sub>	AN/EC (2:3)	0.06

The different electrolytes prepared, either with  $[\text{Pt}(\text{tpy})(\text{pip}_2\text{NCN})]\text{BF}_4$  or with  $[\text{Pt}(\text{phtpy})(\text{pip}_2\text{NCN})]\text{BF}_4$ , are listed in Table 9.

**Table 9.** Composition of the different electrolytes used with platinum complexes.

Platinum complex	Solvent	Complex concentration [M]	Reduced/oxidized ratio
$\text{Pt}(\text{phtpy})(\text{pip}_2\text{NCN})\text{BF}_4$	$\gamma\text{BL}$	0.1	100/0
$\text{Pt}(\text{phtpy})(\text{pip}_2\text{NCN})\text{BF}_4$	$\gamma\text{BL}$	0.1	90/10
$\text{Pt}(\text{phtpy})(\text{pip}_2\text{NCN})\text{BF}_4$	$\gamma\text{BL}/\text{EC}$ (1:1)	0.1	90/10
$\text{Pt}(\text{tpy})(\text{pip}_2\text{NCN})\text{BF}_4$	$\text{AN}/\text{EC}$ (2:3)	0.06	90/10
$\text{Pt}(\text{tpy})(\text{pip}_2\text{NCN})\text{BF}_4$	$\text{AN}/\text{EC}$ (2:3)	0.06	70/30

### 3.3. Photoelectrochemical measurements of the platinum complexes

All electrolytes listed in Table 9 were used in open cells with dye Z907 (see Table 2, page 32). The counter electrode was a reflective platinum electrode or another electrocatalyst, when specified in the text.

No remarkable differences in photoelectrochemical results were noted between  $[\text{Pt}(\text{tpy})(\text{pip}_2\text{NCN})]\text{BF}_4$  and  $[\text{Pt}(\text{phtpy})(\text{pip}_2\text{NCN})]\text{BF}_4$  and so either compounds could be used.

First experiments were realized to screen the influence of the oxidation level on the photoelectrochemical properties. Table 10 gives these properties with an electrolyte containing no oxidized species.

**Table 10.** Example of performances obtained with an electrolyte made of  $[\text{Pt}(\text{phtpy})(\text{pip}_2\text{NCN})]\text{BF}_4$  0.1 M, non oxidized, in pure  $\gamma\text{BL}$ .

Irradiance [ $\text{W} \cdot \text{m}^{-2}$ ]	15	95
$V_{\text{oc}}$ [mV]	744	730
$J_{\text{sc}}$ [ $\mu\text{A} \cdot \text{cm}^{-2}$ ]	47	144
$FF$ [-]	0.70	0.28
Efficiency [%]	1.5	0.3

With 10% of the platinum complex oxidized, the current strongly decreased and the efficiency dropped from 1.5% to 0.4% at  $15 \text{ W} \cdot \text{m}^{-2}$ .

On the contrary, non-oxidized  $[\text{Pt}(\text{phtpy})(\text{pip}_2\text{NCN})]\text{BF}_4$  in  $\gamma\text{BL}/\text{EC}$  (1:1) gave poor results, while its 10% oxidized equivalent showed improved values (Table 11).

**Table 11.** Example of performances obtained with an electrolyte made of  $[\text{Pt}(\text{phtpy})(\text{pip}_2\text{NCN})]\text{BF}_4$  0.1 M, 10% oxidized, in  $\gamma\text{BL}/\text{EC}$  (1:1).

Irradiance [ $\text{W} \cdot \text{m}^{-2}$ ]	2	15	95
$V_{\text{oc}}$ [mV]	690	736	768
$J_{\text{sc}}$ [ $\mu\text{A} \cdot \text{cm}^{-2}$ ]	15	80	150
$FF$ [-]	0.85	0.52	0.34
Efficiency [%]	2.2	1.9	0.4

The low photovoltaic properties obtained render a global explanation of these different behaviors difficult. Several factors may however explain the low photovoltaic parameters. First of all, the big size of the molecule associated with viscous solvents have a negative impact on the dye regeneration rate and therefore on the photocurrent. The different electron transfer rates between the platinum complex and the dye or the conduction band of  $\text{TiO}_2$  may also induce unwanted kinetics (see “Electron transfer dynamics” hereafter). Meanwhile, the choice of the counter electrode is important here. For the standard couple,  $\text{I}_3^-/\text{I}^-$ , platinum is the electrocatalyst of choice. The platinum complexes having a different redox potential, the catalytic effect of the compound deposited on the TCO of the counter electrode can play an important role. Figure 4 shows the  $I/V$  curves at  $15 \text{ W} \cdot \text{m}^{-2}$  of an electrolyte based on  $[\text{Pt}(\text{tpy})(\text{pip}_2\text{NCN})]\text{BF}_4$  with three different counter electrode.

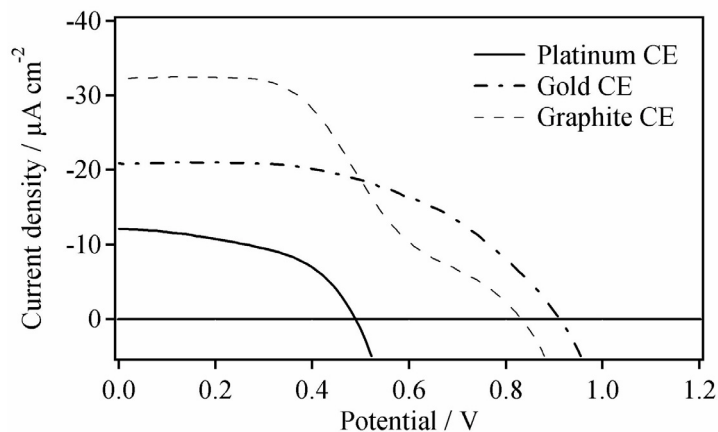


**Figure 4.** Photoelectrochemical measurements made at  $15 \text{ W} \cdot \text{m}^{-2}$  with an electrolyte composed of  $[\text{Pt}(\text{tpy})(\text{pip}_2\text{NCN})]\text{BF}_4$  0.06 M, 10% oxidized, in AN/EC (2:3) and three different counter electrodes (CE).

Contrary to  $\text{I}_3^-/\text{I}^-$ , the platinized counter electrode was not the best choice here and gave a lower current and potential. On the other hand, gold counter electrodes gave a very high  $V_{\text{oc}}$ , reaching 960 mV in the best case at  $15 \text{ W} \cdot \text{m}^{-2}$ . Due to low electron transfer rate with the oxidized complex, graphite counter electrodes are not adapted for platinum complexes as shown in Figure 4.

With a higher oxidation ratio, i.e. 30% of oxidized species, the  $J_{\text{sc}}$  sharply decreased, except for the platinum counter electrode (Figure 5). The  $V_{\text{oc}}$  also slightly decreased, giving less overall efficiency.



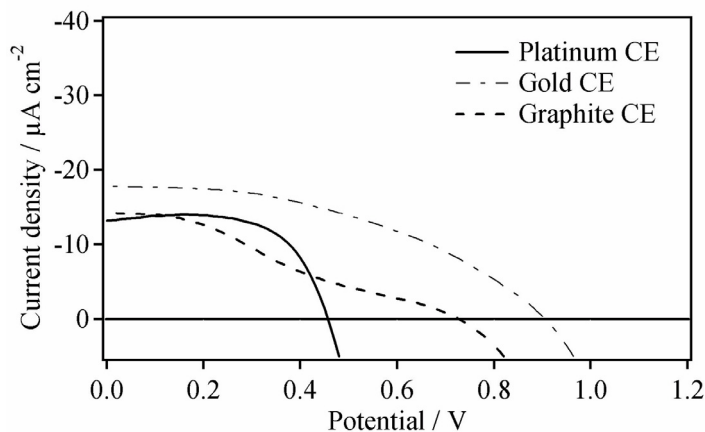


**Figure 5.** Photoelectrochemical measurements made at  $15 \text{ W} \cdot \text{m}^{-2}$  with an electrolyte composed of  $[\text{Pt}(\text{tpy})(\text{pip}_2\text{NCN})]\text{BF}_4$  0.06 M, 30% oxidized, in AN/EC (2:3) and three different counter electrodes (CE).

### 3.4. Electron transfer dynamics

Transient absorbance decay kinetics of the oxidized state of sensitizer Z907 used with an electrolyte containing  $[\text{Pt}(\text{tpy})(\text{pip}_2\text{NCN})]\text{BF}_4$  were measured using laser flash photolysis. Figure 6 shows results from nanosecond time resolved laser experiments. As for the triarylamine measurements, the transient optical signal recorded the concentration of oxidized ruthenium sensitizer following photo-induced electron injection from the dye into the  $\text{TiO}_2$  conduction band. In the absence of platinum (II)/(IV) redox electrolyte, the decrease of the absorption signal gave the dynamics of recombination of the conduction band electrons with the oxidized dye.

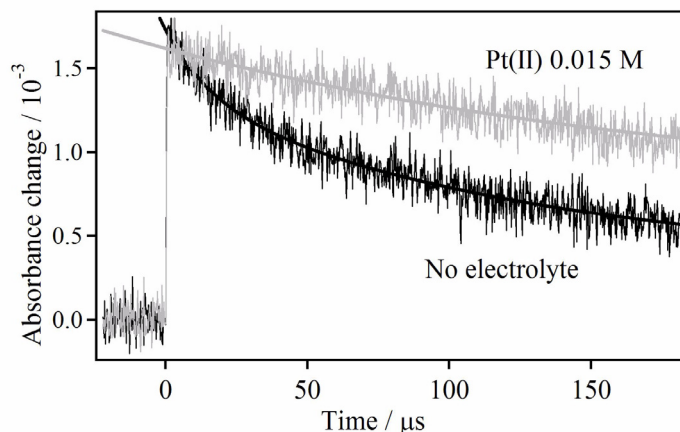


**Figure 6.** Transient absorbance decay kinetics of the oxidized state of Z907 adsorbed on a  $\text{TiO}_2$  nanocrystalline film in the presence and absence of  $[\text{Pt}(\text{tpy})(\text{pip}_2\text{NCN})]\text{BF}_4$  0.015 M in methoxypropionitrile. This solvent was used because of its low viscosity and relative stability for the time that last the laser experiments. Absorbance changes were measured at a probe wavelength of 630 nm, employing 543 nm laser excitation (5 ns fwhm pulse duration,  $50 \mu\text{J} \cdot \text{cm}^{-2}$  pulse fluence).

Curious behavior is observed in Figure 6. The oxidized dye decay was slower in the presence of the electrolyte. It seems that either the electrons in the  $\text{TiO}_2$  conduction band were intercepted by the platinum in solution, or the dye disappeared from the  $\text{TiO}_2$  surface. If the electrons were intercepted by the platinum complex in solution, the dark current recorded by photoelectrochemical measurements should be important. If the dye was removed from the surface, spectrophotometric measurements of the  $\text{TiO}_2$  surface covered with dye molecules should show a different spectrum after having been in contact with the electrolyte. As dark current was not high enough to explain the transient absorbance decay kinetics of the oxidized state of Z907, the removal of the dye from the surface is a preferable hypothesis. Preliminary UV-Vis measurements showed changes of the sensitizer spectrum after having been exposed to the platinum complexes. These changes were enhanced when the cell was irradiated with light. A shift from  $\lambda = 520 \text{ nm}$  to  $\lambda = 476 \text{ nm}$  of the maximum absorbance peak between a fresh dye-covered electrode and an electrode exposed to an electrolyte containing platinum complexes was observed. At  $\lambda = 520 \text{ nm}$ , the absorbance decreased from 1.75 to 1.2 and at  $\lambda = 600 \text{ nm}$  from 0.54 to 0.3. The loss in absorbance was attributed to a removal of the dye from the  $\text{TiO}_2$  surface, while the

blue shift may be due to a chemical bonding between the dye's thiocyanate groups and the platinum center. As the removal of the dye from the nanocrystalline surface is enhanced under irradiation, the oxidized state of the platinum complex may be involved in this process.

The long time needed for the recovery of the dye ground state was due to the low energetic pulse fluence, which injected only one electron per dye molecule, matching the conditions encountered in a working DSSC.

### **3.5. Conclusions**

When using platinum complexes as redox mediator in DSSC a low oxidation of about 10% in a solvent mixture ( $\gamma$ BL/EC) is recommended, as well as the use of a gold covered counter electrode. Even with these optimizations, platinum complexes did not rival the triiodide/iodide couple and did not give any significant results at high irradiance, the fill factor dropping to very low values.

## 4. Cobalt complexes

Contrary to platinum complexes that typically undergo two-electron changes in oxidation state, cobalt complexes redox reaction is a one-electron process. The redox reaction that fits the requirements for a mediator in DSSC is the Co(III)/Co(II) exchange.

Table 12 shows some of the first photoelectrochemical results obtained with a cobalt complexes.

**Table 12.** Example of performances obtained with Z316 and an electrolyte made of  $[\text{Co}(\text{dmbip})_2](\text{ClO}_4)_2$  0.2 M, 3% oxidized, in AN/EC (2:3).

Irradiation intensity [ $\text{W} \cdot \text{m}^{-2}$ ]	15	95	1000
$V_{\text{oc}}$ [mV]	555	635	705
$J_{\text{sc}}$ [ $\mu\text{A} \cdot \text{cm}^{-2}$ ]	40	390	3670
$FF$ [-]	0.70	0.80	0.65
Efficiency [%]	1.00	2.10	1.70

As these first results are far better than those obtained previously using alternative redox couples, the following chapter of this work will be entirely dedicated to cobalt complexes. Next chapter will then deeply analyzed the use and optimization of cobalt complexes as redox mediators in dye-sensitized solar cells.

## 5. References to Chapter 3

- [1] Pelet, S.; Moser, J. E.; Gratzel, M. *J Phys Chem B* **2000**, *104*, 1791.
- [2] Grätzel, M.; Moser, J. E. Solar Energy Conversion. In *Electron Transfer in Chemistry*; Balzani, V., Ed.; Wiley-VCH: Weinheim, 2001; Vol. 5; pp 589.
- [3] Rothenberger, G.; Fitzmaurice, D.; Gratzel, M. *J Phys Chem* **1992**, *96*, 5983.
- [4] Nazeeruddin, M. K.; Kay, A.; Rodicio, I.; Humphry-Baker, R.; Müller, E.; Liska, P.; Vlachopoulos, N.; Grätzel, M. *J. Am. Chem. Soc.* **1993**, *115*, 6382.
- [5] Desilvestro, J.; Gratzel, M.; Kavan, L.; Moser, J.; Augustynski, J. *J Am Chem Soc* **1985**, *107*, 2988.
- [6] Argazzi, R.; Bignozzi, C. A.; Heimer, T. A.; Castellano, F. N.; Meyer, G. J. *J Phys Chem B* **1997**, *101*, 2591.
- [7] Bonhôte, P.; Moser, J. E.; Humphry-Baker, R.; Vlachopoulos, N.; Zakeeruddin, S. M.; Walder, L.; Grätzel, M. *J. Am. Chem. Soc.* **1999**, *121*, 1324.
- [8] Oskam, G.; Bergeron, B. V.; Meyer, G. J.; Searson, P. C. *J. Phys. Chem. B* **2001**, *105*, 6867.
- [9] Sundberg, R. J.; Martin, R. B. *Chem. Rev.* **1974**, *74*, 471.
- [10] Bonhôte, P.; Grätzel, M.; Jirousek, M.; Liska, P.; Pappas, N.; Vlachopoulos, N.; Planta, C. V.; Walder, L. Redox Mediators for Electrochemical Photovoltaic Cells Based on Dye-Sensitized TiO<sub>2</sub> Electrodes; 10th International Conference on Photochemical Conversion and Storage of Solar Energy (IPS-10). **1994**, 191. Interlaken, Switzerland.
- [11] Bach, U. Solid-state dye-sensitized mesoporous TiO<sub>2</sub> solar cells, Ecole Polytechnique Fédérale de Lausanne, 2000.
- [12] Krüger, J. Interface engineering in solid-state dye-sensitized solar cells, Ecole Polytechnique Fédérale de Lausanne, 2003.
- [13] Hagen, J.; Schaffrath, W.; Otschik, P.; Fink, R.; Bacher, A.; Schmidt, H.-W.; Haarer, D. *Synthetic Metals* **1997**, *89*, 215.
- [14] Bonhôte, P.; Gogniat, E.; Tingry, S.; Barbe, C.; Vlachopoulos, N.; Lenzmann, F.; Comte, P.; Gratzel, M. *J Phys Chem B* **1998**, *102*, 1498.
- [15] Thelakkat, M.; Hagen, J.; Haarer, D.; Schmidt, H.-W. *Synthetic Metals* **1999**, *102*, 1125.
- [16] Westermark, K.; Tingry, S.; Persson, P.; Rensmo, H.; Lunell, S.; Hagfeldt, A.; Siegbahn, H. *J Phys Chem B* **2001**, *105*, 7182.
- [17] Peter, K.; Thelakkat, M. *Macromolecules* **2003**, *36*, 1779.

- [18] Moser, J. E.; Noukakis, D.; Bach, U.; Yasuhiro, Y.; Klug, D. R.; Durrant, J. R.; Humphry-Baker, R.; Grätzel, M. *J. Phys. Chem. B* **1998**, *102*, 3649.
- [19] Shirota, Y. *J. Mater. Chem.* **2000**, *10*, 1.
- [20] Gross, M.; Müller, D.; Bräuchle, C.; Meerholz, K. *Synthetic Metals* **1999**, *102*, 1147.
- [21] Krüger, J.; Plass, R.; Cevey, L.; Piccirelli, M.; Gratzel, M.; Bach, U. *Appl Phys Lett* **2001**, *79*, 2085.
- [22] Plass, R.; Pelet, S.; Krueger, J.; Gratzel, M.; Bach, U. *J Phys Chem B* **2002**, *106*, 7578.
- [23] Bach, U.; Lupo, D.; Comte, P.; Moser, J. E.; Weissörtel, F.; Salbeck, J.; Spreitzer, H.; Grätzel, M. *Nature* **1998**, *395*, 583.
- [24] Jude, H.; Bauer, J. A. K.; Connick, W. B. *J Am Chem Soc* **2003**, *125*, 3446.
- [25] Lappin, G. *Redox Mechanisms in Inorganic Chemistry*; Ellis Horwood: New York, 1994.

---

# CHAPTER FOUR

## Electrolytes containing redox couples based on cobalt complexes

# 4

---

The research of alternative redox mediators for the dye-sensitized solar cell has led to interesting results, for example efficiencies can now be reached which were not previously possible other than with couples such as the triiodide/iodide couple. As briefly presented in the last chapter, cobalt complexes demonstrated the greatest performance of all the alternative compounds tried so far. In the present chapter, these promising results have been confirmed and improved, through interfaces, electrolytes and mass-transport optimizations. Screening and characterization of different cobalt complexes, by  $^1\text{H}$  and  $^{13}\text{C}$  NMR spectroscopy, UV/Vis spectrophotometry, elemental analysis and electrochemical methods, as well as optimization of the electrolytes and rationalization of the interaction between these compounds and the sensitizers are described in this chapter.

## 1. Introduction

Co(II) polypyridine, phenanthroline, and imidazole complexes were recognized early as potential electron relays and catalysts in photoredox reactions, since they constitute vitamin B<sub>12</sub> model compounds.<sup>[1]</sup> The possible mechanism of action in the redox system  $[\text{CoL}_2]^{2+}/[\text{CoL}_2]^{3+}$  in solar cells was discussed in 1993<sup>[2]</sup> and crystal and the molecular structure of  $[\text{Co}(\text{dmbip})_2]^{2+/3+}$  was published in 1994.<sup>[3]</sup>  $[\text{Co}(\text{bpy})_3]^{2+/3+}$ ,  $[\text{Co}(\text{phen})_2]^{2+/3+}$  and  $[\text{Co}(\text{5-nitro-phen})_2]^{2+/3+}$  couples, in particular, were then tested in dye-sensitized polycrystalline TiO<sub>2</sub>-based photovoltaic cells, and *IPCEs* of up to 50% were obtained.<sup>[4]</sup> However, in these experiments the reduction of the oxidized Co(III) form of the complex at the conducting glass that serves to support the TiO<sub>2</sub> nanoparticles increased the dark current. Until now, endeavors to increase the photovoltage of dye-sensitized nanocrystalline cells through the replacement of iodide by a one-electron, outer-sphere redox couple, with a more positive oxidation potential, have not succeeded. This is largely due to limitations imposed by the dark current and slow diffusion of the alternative mediator. It has been also inferred from published intensity-modulated photovoltage spectroscopy experiments that the complex mechanism of the oxidation of iodide could in fact be essential to the energy conversion efficiency of DSSCs and that attempts to use simple one-electron redox mediator system instead are unlikely to be successful.<sup>[5,6]</sup>



## 2. Electrolytes preparation

Electrolyte solutions were prepared by dissolving a certain amount of cobalt complex in anhydrous solvents, for example  $\gamma$ -butyrolactone, acetonitrile, methoxypropionitrile or in solvent mixtures such as acetonitrile/ethylene carbonate (2:3). This later solvent mixture, with its high solubility properties and moderate viscosity, was used throughout all the experiments described hereafter, except if specified in the text. When necessary the partial oxidation of Co(II) complex to Co(III) was achieved by adding stoichiometric amounts of solid  $\text{NOBF}_4$ , a one electron acceptor, to the afore mentioned solutions at 20 °C under dry air. The oxidative effect of  $\text{NOBF}_4$  on the reduced cobalt complexes was monitored by NMR and is discussed in “Stoichiometric oxidation of cobalt complexes by  $\text{NOBF}_4$ ”, page 90. For some cobalt complexes, the oxidized form, Co(III), was available and used as such, without the necessity of any external oxidizer (see “Cobalt(III) complexes synthesis”, page 36). The effects of Co(II) and Co(III) concentrations on the photoelectrochemical properties, as well as the influence of additives in the solution will be discussed in the following sections. However, if not specified, the Co(II) and Co(III) complexes concentrations used were  $9 \cdot 10^{-2}$  M and  $1 \cdot 10^{-2}$  M, respectively.

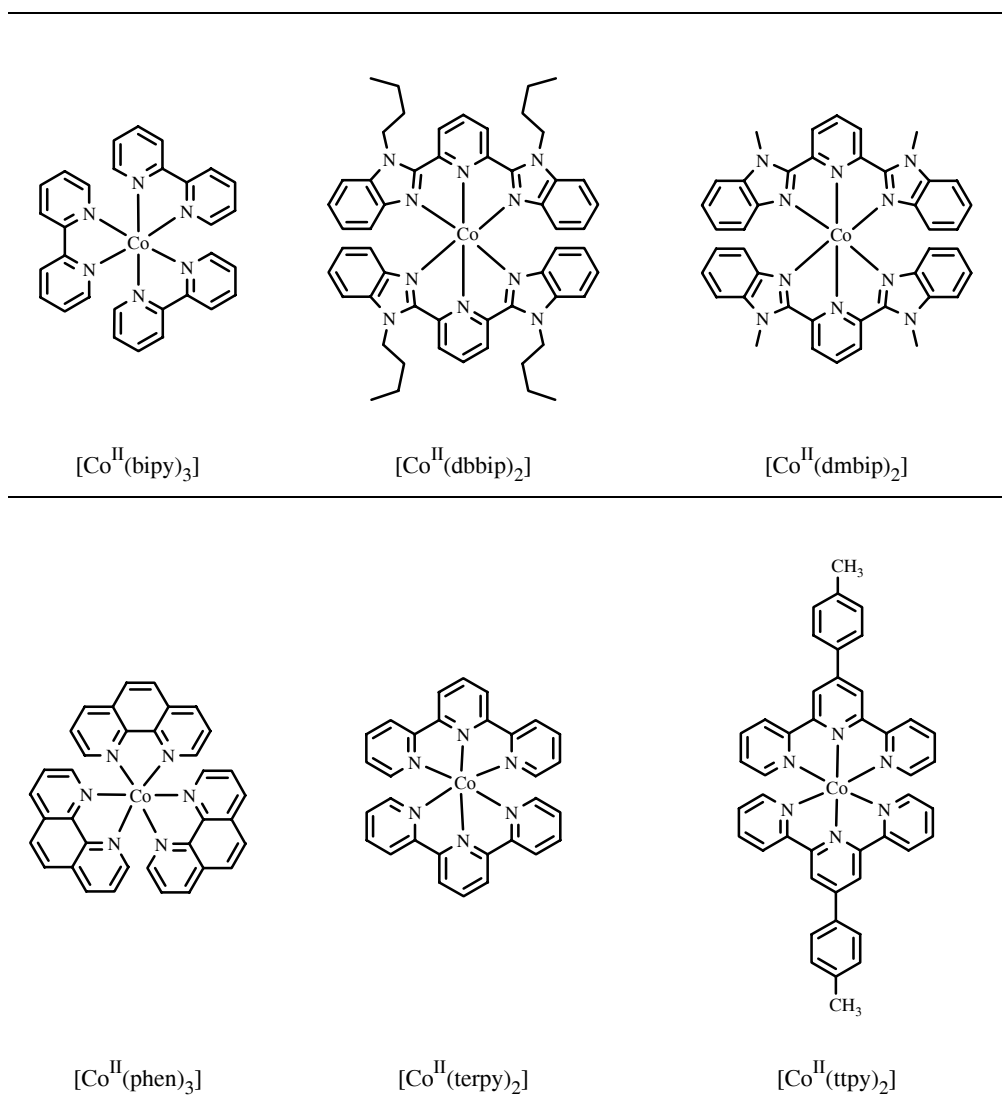
### 3. Cobalt complexes screening and characterization

#### 3.1. Introduction

Table 1 lists the short names and molecular weights of all cobalt complexes studied in this paragraph, while Table 2 gives simplified representations of the cationic part of the complexes.

**Table 1.** Molecular weights of the different cobalt complexes screened in this study.

Short name	Molecular weight
[Co(bipy) <sub>3</sub> ](ClO <sub>4</sub> ) <sub>2</sub>	726.38
[Co(bipy) <sub>3</sub> ](OTf) <sub>2</sub>	825.62
[Co(dbbip) <sub>2</sub> ](ClO <sub>4</sub> ) <sub>2</sub>	1104.94
[Co(dmbip) <sub>2</sub> ](ClO <sub>4</sub> ) <sub>2</sub>	936.62
[Co(dmbip) <sub>2</sub> ](DDS) <sub>2</sub>	1236.50
[Co(dmbip) <sub>2</sub> ](OTf) <sub>2</sub>	1035.86
[Co(dmbip) <sub>2</sub> ](PEG <sub>350</sub> BzSO <sub>3</sub> ) <sub>2</sub>	~ 1810
[Co(dmbip) <sub>2</sub> ](PEG <sub>550</sub> BzSO <sub>3</sub> ) <sub>2</sub>	~ 2210
[Co(dmbip) <sub>2</sub> ](PF <sub>6</sub> ) <sub>2</sub>	1027.64
[Co(dmbip) <sub>2</sub> ](PTS) <sub>2</sub>	1080.10
[Co(phen) <sub>3</sub> ](OTf) <sub>2</sub>	897.69
[Co(phen) <sub>3</sub> ](TFSI) <sub>2</sub>	1159.85
[Co(terpy) <sub>2</sub> ](ClO <sub>4</sub> ) <sub>2</sub>	724.37
[Co(tpy) <sub>2</sub> ](OTf) <sub>2</sub>	1003.85

**Table 2.** Chemical structures of some reduced cobalt complexes without their counter ions.

In general,  $[\text{CoL}_2]^{2+}$  is a coordination entity where the ligands are polydentates, as shown in Table 2. In these compounds, Co(II) has the electronic structure  $d^7$ . The ligands, like phen or bipy, tend to increase the energy of transition between the  $t_{2g}$  and the  $e_g$   $d$ -orbitals of the central metal atom. This induces a strong-field configuration and these complexes have then a low-spin configuration. According to the crystal field theory, the ligand field stabilization energy (*LFSE*), representing the net energy of a  $t_{2g}^x e_g^y$  configuration relative to the average energy of the orbitals is given by

$$LFSE = \left( -\frac{2}{5} \cdot x + \frac{3}{5} \cdot y \right) \cdot \Delta_O \quad (4.1)$$

where  $x = 6$  and  $y = 1$  for Co(II). The stabilization energy is therefore  $1.8\Delta_{\text{O}}$ , where  $\Delta_{\text{O}}$  is the ligand-field splitting parameter, in an octahedral crystal field.

Aromatic ligands have  $\pi^*$  orbitals from low energy and tend to a metal-to-ligand charge transfer (MLCT), increasing  $\Delta_{\text{O}}$  by the  $\pi$ -acceptor interaction and therefore giving this characteristic yellow-orange color to the complexes. Co(III), with an electronic structure  $d^6$ , has a  $t_{2g}^6$  configuration and therefore a *LFSE* which is equal to  $2.4\Delta_{\text{O}}$ .

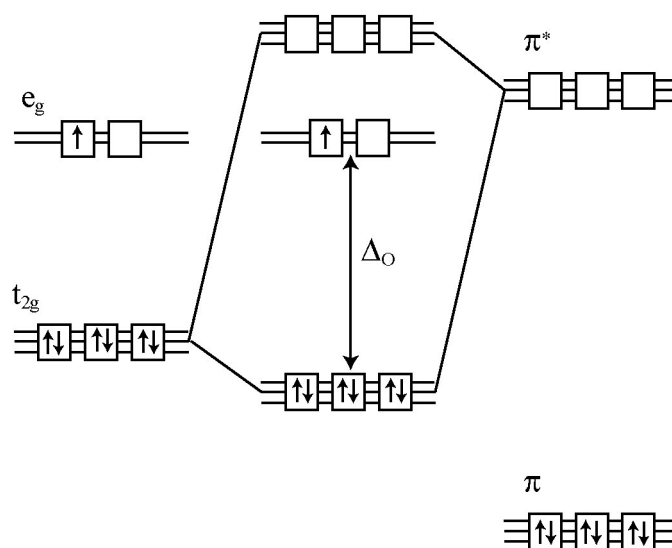


**Figure 1.** Effect of  $\pi$  bonding on the ligand field splitting parameter for a  $d^7$  electronic structure.  $\Delta_{\text{O}}$  increases when the ligands act as  $\pi$  acceptors.

### 3.2. Photoelectrochemical screening of cobalt complexes

The screening of the cobalt complexes listed in Table 1 was carried out to identify the most promising candidates for use as redox mediators in the DSSC. Dye Z907, mesoporous  $2\ \mu\text{m}$  PC 100  $\text{TiO}_2$  layer and diffusive  $4\ \mu\text{m}$  HPW 400c  $\text{TiO}_2$  layer were used. Data on the photoelectrochemical properties such as the incident photon-to-current conversion efficiencies (*IPCE*) values at 540 nm and efficiencies obtained with these redox electrolytes have been compiled in Table 3. Of all the complexes examined, the two complexes  $[\text{Co}(\text{dbbip})_2](\text{ClO}_4)_2$  and  $[\text{Co}(\text{dmbip})_2](\text{ClO}_4)_2$  demonstrated best performance.

**Table 3.** Average photoelectrochemical data obtained from various cobalt complexes used with dye Z907 under an irradiance of  $95 \text{ W} \cdot \text{m}^{-2}$ .  $\text{TiO}_2$  layers:  $2 \mu\text{m}$  PC 100 +  $4 \mu\text{m}$  HPWc. [a] Under  $1000 \text{ W} \cdot \text{m}^{-2}$ . [b] *IPCE* at 540 nm.

Cobalt complex	$V_{\text{oc}}$ [mV]	$J_{\text{sc}}$ [ $\mu\text{A} \cdot \text{cm}^{-2}$ ]	$J_{\text{sc}}^{\text{[a]}}$ [ $\text{mA} \cdot \text{cm}^{-2}$ ]	<i>FF</i> [-]	Efficiency [%]	<i>IPCE</i> <sup>[b]</sup> [%]
[Co(bipy) <sub>3</sub> ](ClO <sub>4</sub> ) <sub>2</sub>	510	280	3.1	0.73	1.1	20
[Co(bipy) <sub>3</sub> ](OTf) <sub>2</sub>	510	230	2.5	0.72	0.9	15
[Co(dbbip) <sub>2</sub> ](ClO <sub>4</sub> ) <sub>2</sub>	660	800	6.5	0.76	4.2	40
[Co(dmbip) <sub>2</sub> ](ClO <sub>4</sub> ) <sub>2</sub>	650	520	4.2	0.76	2.7	25
[Co(dmbip) <sub>2</sub> ](DDS) <sub>2</sub>	650	200	2.4	0.73	1.0	10
[Co(dmbip) <sub>2</sub> ](OTf) <sub>2</sub>	660	410	3.6	0.76	2.1	20
[Co(dmbip) <sub>2</sub> ](PF <sub>6</sub> ) <sub>2</sub>	640	350	3.8	0.75	1.8	15
[Co(dmbip) <sub>2</sub> ](PTS) <sub>2</sub>	650	150	1.8	0.74	0.8	10
[Co(phen) <sub>3</sub> ](OTf) <sub>2</sub>	600	250	3.0	0.75	1.2	15
[Co(phen) <sub>3</sub> ](Tf <sub>2</sub> N) <sub>2</sub>	620	200	2.4	0.73	1.0	15
[Co(terpy) <sub>2</sub> ](ClO <sub>4</sub> ) <sub>2</sub>	470	130	1.4	0.70	0.5	10
[Co(tpy) <sub>2</sub> ](OTf) <sub>2</sub>	500	310	3.2	0.72	1.2	20

Though significant differences were seen in the *IPCE* and short circuit current ( $J_{\text{sc}}$ ) values for all complexes sharing the same cationic part, e.g. bipy, dmbip, or phen,  $V_{\text{oc}}$  remained effectively constant. The  $V_{\text{oc}}$  originates from the redox potential of these complexes, which varies only slightly when changing the counter ion. Redox potentials will be discussed in “Redox potential determination”, page 95. The variation in the  $J_{\text{sc}}$  may be due to some stronger association of the anion with the electroactive cobalt complex, affecting the electron transfer rate from the latter to the oxidized dye. An oversized counter ion, like  $\text{DDS}^-$ , may also hinder the transport of the ions within the electrolyte.

In the photoelectrochemical measurements the linearity between irradiance intensity and photocurrent is often not respected due to mass transfer limitations of the photocurrent. The latter becomes limited by the Co(III) diffusion to the counter electrode at higher light intensity (see “Diffusion coefficient”, page 98). A small superlinearity is sometimes observed between the photocurrent densities at  $95 \text{ W} \cdot \text{m}^{-2}$  and  $1000 \text{ W} \cdot \text{m}^{-2}$ , where  $J_{\text{sc}}$  at 100% Sun is slightly higher

than ten times  $J_{sc}$  at 9.5% Sun. This effect is due to approximate values at lower irradiances, which are extrapolated to take into account the filters used in the experimental setup to decrease the incident light power.

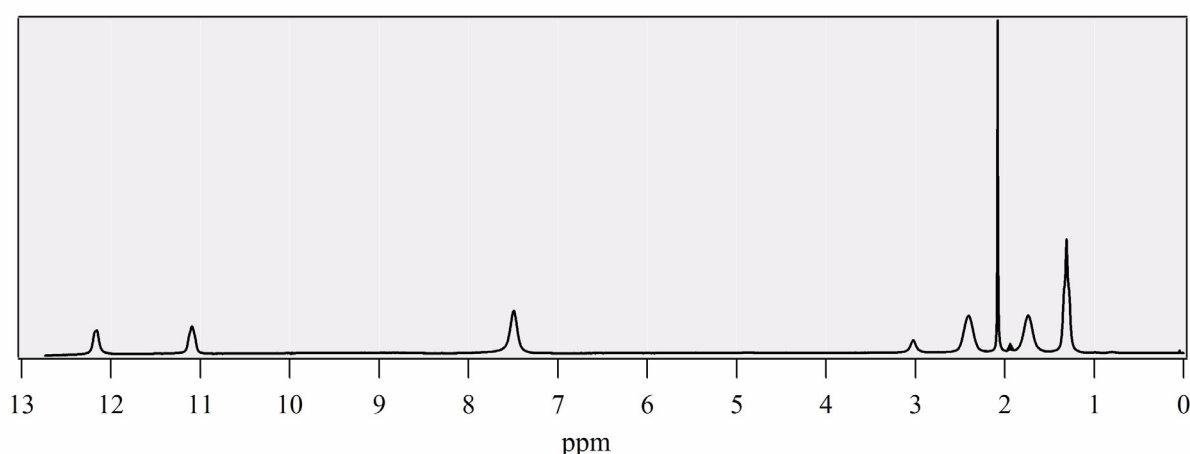
The photovoltaic efficiency of the DSSC with the complex  $[\text{Co}(\text{dbbip})_2](\text{ClO}_4)_2$  was superior to all other redox mediator efficiencies. Hence,  $[\text{Co}(\text{dbbip})_2](\text{ClO}_4)_2$  was used for further investigations.

### 3.3. NMR spectroscopy studies

Proton, coupled  $^{13}\text{C}$  and decoupled  $^{13}\text{C}$  NMR spectra of  $[\text{Co}(\text{dbbip})_2]^{2+}$  and  $[\text{Co}(\text{dbbip})_2]^{3+}$  were measured to facilitate the characterization and determine the purity of these cobalt complexes.

#### *NMR spectra of $[\text{Co}(\text{dbbip})_2]^{2+}$*

Figure 2 shows the  $^1\text{H}$  NMR spectrum of  $[\text{Co}(\text{dbbip})_2]^{2+}$ . The characteristic shape of the peaks is due to the paramagnetic nature of this reduced complex. The structure cannot be determined with such a spectrum but its print can serve as an indicator for the presence of the reduced form in an electrolyte.

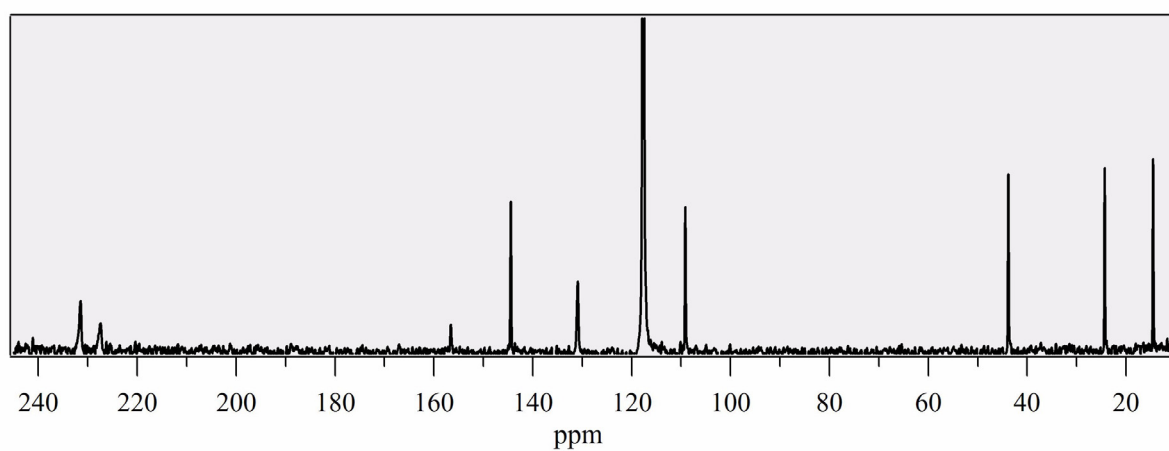


**Figure 2.**  $^1\text{H}$  NMR spectrum of bis[2,6-bis(1'-butylbenzimidazol-2'-yl)pyridine]cobalt(II) in  $\text{CD}_3\text{CN}$ .

**Table 4.**  $^1\text{H}$  NMR data of  $[\text{Co}(\text{dbbip})_2]^{2+}$  in  $\text{CD}_3\text{CN}$ .

Chemical shift [ppm]
12.18
11.10
7.50
3.03
2.41
1.74
1.31

Figure 3 shows the  $^{13}\text{C}$  decoupled NMR spectrum of the same compound. This spectrum gives the carbon print of the molecule.

**Figure 3.**  $^{13}\text{C}$  decoupled NMR spectrum corresponding to the  $^1\text{H}$  NMR spectrum above (Figure 2).

**Table 5.**  $^{13}\text{C}$  decoupled NMR data of  $[\text{Co}(\text{dbbip})_2]^{2+}$  in  $\text{CD}_3\text{CN}$ .

Chemical shift [ppm]
231.40
227.42
156.55
144.41
130.90
109.15
43.82
24.34
14.55

***NMR spectra of  $[\text{Co}(\text{dbbip})_2]^{3+}$***

The oxidized cobalt complex is diamagnetic as a sharp  $^1\text{H}$  NMR spectra can be recorded. Figure 4 shows the proton NMR spectrum of the oxidized form of the cobalt complex, while Table 6 gives basic informations on each peak. With this spectrum, identification of the hydrogen atoms is possible and shown in Figure 5.

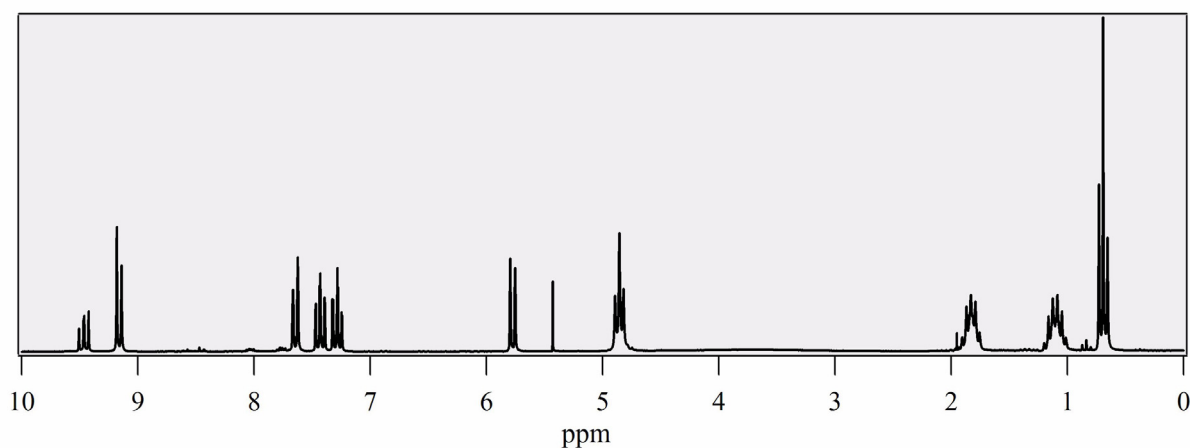


**Figure 4.**  $^1\text{H}$  NMR spectrum of bis[2,6-bis(1'-butylbenzimidazol-2'-yl)pyridine]cobalt(III) in  $\text{CD}_3\text{CN}$ .



**Table 6.**  $^1\text{H}$  NMR data of  $[\text{Co}(\text{dbbip})_2]^{3+}$  in  $\text{CD}_3\text{CN}$ . Letters of *Attribution* refer to Figure 5.

Chemical shift [ppm]	Multiplicity	Coupling constant [Hz]	Integral	Attribution
9.43	t	8.2	2	f
9.12	d	8.2	4	e
7.63	d	8.2	4	g
7.43	ddd	8.2, 7.1, 1.0	4	h
7.27	ddd	8.2, 7.1, 1.0	4	h
5.76	d	8.2	4	i
4.84	t	7.1	8	d
1.82	m	7.8	8	c
1.11	m	7.8	8	b
0.70	t	7.1	12	a

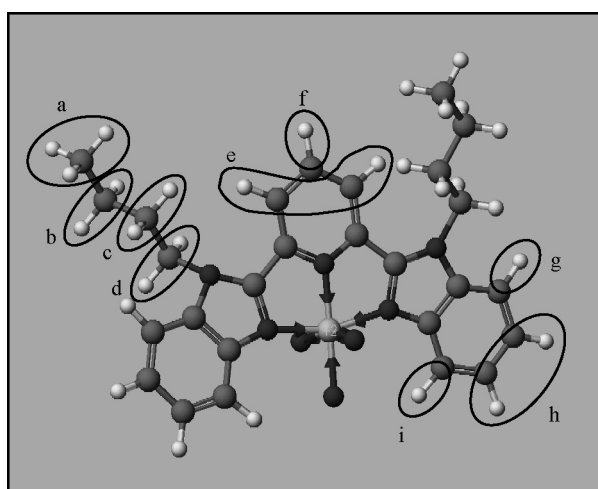
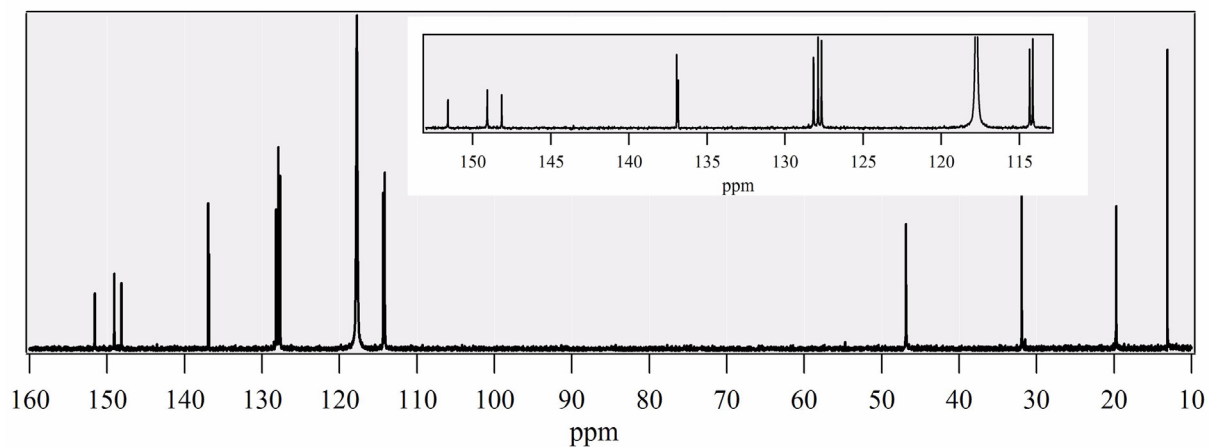
**Figure 5.** Schematic representation of one of the two ligand of the bis[2,6-bis(1'-butylbenzimidazol-2'-yl)pyridine]cobalt(II) molecule outlining the  $^1\text{H}$  NMR active groups. The letters refer to Table 6.

Figure 6 shows the decoupled  $^{13}\text{C}$  NMR spectrum of the oxidized molecule. This decoupled spectrum is useful for the determination of the carbon backbone of the ligand. Table 7 gives the information about each peak present in the spectrum.



**Figure 6.**  $^{13}\text{C}$  decoupled NMR spectrum corresponding to the  $^1\text{H}$  NMR spectrum above (Figure 4). The inset is a zoom of the left part of the main spectrum.

**Table 7.**  $^{13}\text{C}$  decoupled NMR data of  $[\text{Co}(\text{dbbip})_2]^{3+}$  in  $\text{CD}_3\text{CN}$ .

Chemical shift [ppm]
151.58
149.06
148.14
136.95
136.85
128.18
127.88
127.65
114.34
114.15
46.86
31.91
19.71
13.12

Finally, Figure 7 shows the coupled carbon NMR spectrum of this molecule. The coupled spectrum allows the determination of the hydrogen environment of each carbon atom in the ligands of the complex.

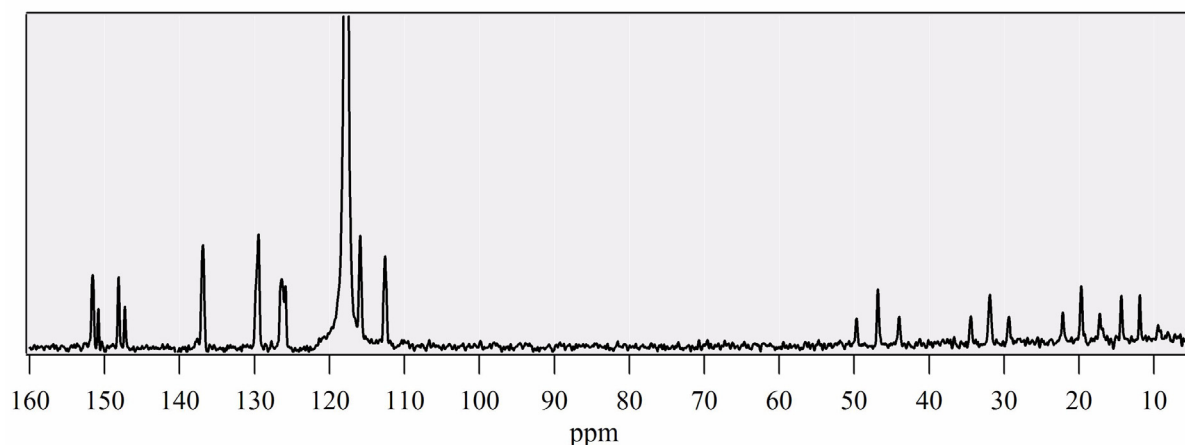


**Figure 7.**  $^{13}\text{C}$  coupled NMR spectrum corresponding to the  $^1\text{H}$  NMR spectrum in Figure 4, page 86.

Table 8 gives information taken from Figure 7 and identifies the position of each carbon atom in the molecule. The positions are shown in Figure 8.

**Table 8.**  $^{13}\text{C}$  coupled NMR data of  $[\text{Co}(\text{dbbip})_2]^{3+}$  in  $\text{CD}_3\text{CN}$ . Numbers in *Attribution* refer to Figure 8.

Chemical shift [ppm]	Multiplicity	Coupling constant [Hz]	Attribution
151.58	s	–	12
149.06	d	700	14
148.14	s	–	11
136.95	s	–	5
136.85	s	–	10
128.18	d	730	7
127.88	d	730	8
127.65	d	730	13
114.34	d	660	6
114.15	d	660	9
46.86	t	570	4

**Table 8.**  $^{13}\text{C}$  coupled NMR data of  $[\text{Co}(\text{dbbip})_2]^{3+}$  in  $\text{CD}_3\text{CN}$ . Numbers in *Attribution* refer to Figure 8.

Chemical shift [ppm]	Multiplicity	Coupling constant [Hz]	Attribution
31.91	t	570	3
19.71	t	570	2
13.12	q	500	1

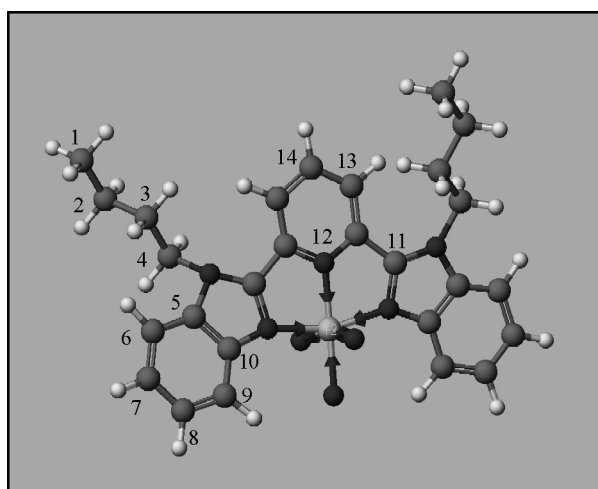


**Figure 8.** Schematic representation of one of the two ligand of the bis[2,6-bis(1'-butylbenzimidazol-2'-yl)pyridine]cobalt(III) molecule outlining the  $^{13}\text{C}$  NMR active atoms. The numbers refer to Table 8.

### *Stoichiometric oxidation of cobalt complexes by $\text{NOBF}_4$*

In order to exactly understand what happened during the oxidation process, the stoichiometric oxidation of  $[\text{Co}(\text{dbbip})_2](\text{ClO}_4)_2$  was studied. This compound was chosen because its oxidized form  $[\text{Co}(\text{dbbip})_2](\text{ClO}_4)_3$  has been previously synthesized, allowing a direct comparison of the NMR spectra of the Co(III) complex obtained by  $\text{NOBF}_4$  oxidation and shown in Figure 4.

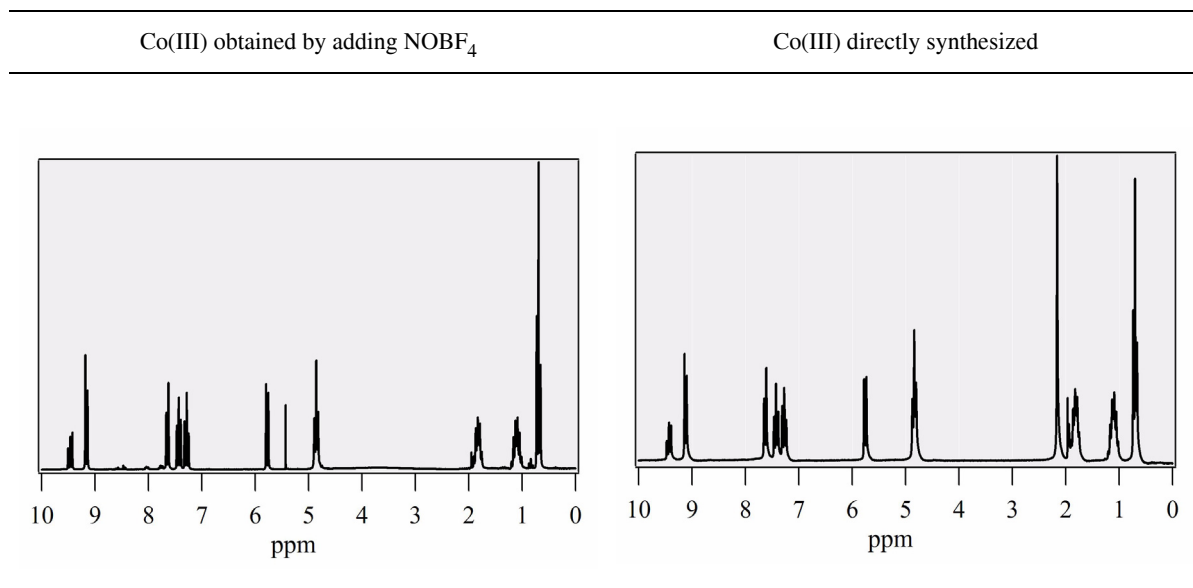
**Table 9.** Comparison of  $^1\text{H}$  NMR spectra of  $[\text{Co}(\text{dbbip})_2]^{3+}$  obtained either by *in situ* chemical oxidation with  $\text{NOBF}_4$  or by direct synthesis.

Table 9 shows two  $^1\text{H}$  NMR spectra. The one to the left was measured using the Co(III) complex obtained upon oxidation of the Co(II) complex with  $\text{NOBF}_4$  and the one to the right using synthesized Co(III) complex. Both spectra are similar and the addition of a stoichiometric amount of  $\text{NOBF}_4$  to the solution of Co(II) complex leads to a pure Co(III) complex. The two supplementary peaks are not associated with hydrogen from the complex, but rather from the solvent.

Table 10 shows the stepwise oxidation of the reduced cobalt complex form. Starting from a pure Co(II) complex solution, a small amount of  $\text{NOBF}_4$  was added and the corresponding NMR spectrum recorded. This operation was repeated several times, up to the complete oxidation of Co(II) into Co(III) and even through the degradation of the complex.  $^1\text{H}$  and  $^{13}\text{C}$  NMR spectroscopy were therefore performed to follow the course of the reaction.

**Table 10.**  $^1\text{H}$  and  $^{13}\text{C}$  NMR spectra of  $[\text{Co}(\text{dbbip})_2]^{2+}$  to  $[\text{Co}(\text{dbbip})_2]^{3+}$  by adding  $\text{NOBF}_4$ .

$\text{Co}^{\text{II}}_{\text{init}}/\text{NO}^+$	$^1\text{H}$	$^{13}\text{C}$
65/0 mM		
65/19 mM		
65/38 mM		
65/61 mM		
65/89 mM		
65/105 mM		

Table 10 therefore represents the NMR spectra of  $[\text{Co}(\text{dbbip})_2]^{2+}$  to  $[\text{Co}(\text{dbbip})_2]^{3+}$  through the intermediate stages, where the two species exist simultaneously in the electrolyte. Addition of  $\text{NOBF}_4$  in stoichiometric amounts leads to the total transformation of Co(II) in Co(III). Peaks at 11.10 ppm and 12.18 ppm indicate the presence of Co(II) in the solution. In the case of  $[\text{Co}(\text{dbbip})_2](\text{ClO}_4)_2$  a degradation process begins to occur after the total oxidation of Co(II). This degradation, probably involving ligand loss from the complex, is however not harmful for solar cells because, as will be discussed later (“Optimization of redox mediator concentration and degree of oxidation”, page 137), a low Co(III) concentration is required for high efficiency. As only ca. 5%–20% of the complex is normally oxidized, no degradation problem will be observed when using this oxidizing agent. Oxidation with  $\text{NOBF}_4$  for a practical application is then specific and controlled for cobalt complexes.

### 3.4. Electrochemical studies

#### *Theory*

An ultramicroelectrode (UME) was chosen to obtain a stationary regime, i.e. fixed  $\delta$  value for the diffusion layer thickness. In the diffusion layer the oxidation is limited by the diffusion of the reduced species and the stationary diffusion current can be described using the following approximation :

$$I_a = nFAD_R \frac{c_R(\infty) - c_R(0)}{\delta_R} \quad (4.2)$$

In an oxidation case, if the applied electrode voltage is high enough, the surface concentration of the reduced species  $c_R(0)$  drops to zero and can be neglected as compared to the concentration in the bulk of the solution [ $c_R(0) \ll c_R(\infty)$ ]. The anodic current therefore reaches a limit value:

$$I_{da} = \frac{nFAD_R c_R(\infty)}{\delta_R} \quad (4.3)$$

The same arguments apply for the cathode:

$$I_{dc} = \frac{-nFAD_O c_O(\infty)}{\delta_O} \quad (4.4)$$

Using Eq. 4.2, interfacial concentrations can be determined as a function of the limiting currents:

$$c_{\text{R}}(0) = c_{\text{R}}(\infty) - \frac{\delta_{\text{R}} I}{nFAD_{\text{R}}} = \frac{\delta_{\text{R}}}{nFAD_{\text{R}}}(I_{\text{da}} - I) \quad (4.5)$$

and

$$c_{\text{O}}(0) = c_{\text{O}}(\infty) - \frac{\delta_{\text{O}} I}{nFAD_{\text{O}}} = \frac{\delta_{\text{O}}}{nFAD_{\text{O}}}(I - I_{\text{dc}}) \quad (4.6)$$

Replacing these values in the following Nernst equation,

$$E = E^{\circ} + \frac{RT}{nF} \ln \left( \frac{c_{\text{O}}(0)}{c_{\text{R}}(0)} \right) \quad (4.7)$$

one get:

$$E = E^{\circ} + \frac{RT}{nF} \cdot \ln \left[ \frac{D_{\text{R}} \delta_{\text{O}}}{D_{\text{O}} \delta_{\text{R}}} \right] + \frac{RT}{nF} \cdot \ln \left[ \frac{I_{\text{dc}} - I}{I - I_{\text{da}}} \right] \quad (4.8)$$

The half-wave potential  $E_{1/2}$  is given when  $I = (I_{\text{da}} + I_{\text{dc}})/2$  :

$$E_{1/2} = E^{\circ} + \frac{RT}{nF} \cdot \ln \left[ \frac{D_{\text{R}} \delta_{\text{O}}}{D_{\text{O}} \delta_{\text{R}}} \right] \quad (4.9)$$

In our case, only the reduced species Co(II) is in the solution. The current-potential curve varies from a zero current to a diffusion limiting current. Therefore, for an oxidation, Eq. 4.8 is reduced to

$$E = E_{1/2} + \frac{RT}{nF} \left[ \frac{I}{I_{\text{da}} - I} \right] \quad (4.10)$$

Drawing a graph  $\ln[I / (I_{\text{da}} - I)]$  as a function of the potential, one get a straight line with a slope of  $(nF/RT)$ . Such a graph is often drawn to control the reversibility of the electrode reaction and to determine the half-wave potential.

Experimentally, limiting diffusion current does not necessarily give a horizontal line, but rather a line with a slope (Figure 9). This may arise from several factors related to the capacitive current or from “parasite” reactions. An empirical equation can be used to take this problem into account.

$$I = I_{\text{da}} \left\{ 1 + B \cdot (E - E_{1/2}) \right\} \left[ \frac{e^{nF(E - E_{1/2})/(RT)}}{1 + e^{nF(E - E_{1/2})/(RT)}} \right] \quad (4.11)$$

The case where  $B = 0$  correspond to Eq. 4.10.



### Redox potential determination

Redox potentials for the cobalt complexes were measured with ferrocene as reference. As example, Figure 9 shows the oxidation reaction of  $[\text{Co}(\text{dbbip})_2](\text{ClO}_4)_2$  on a UME.

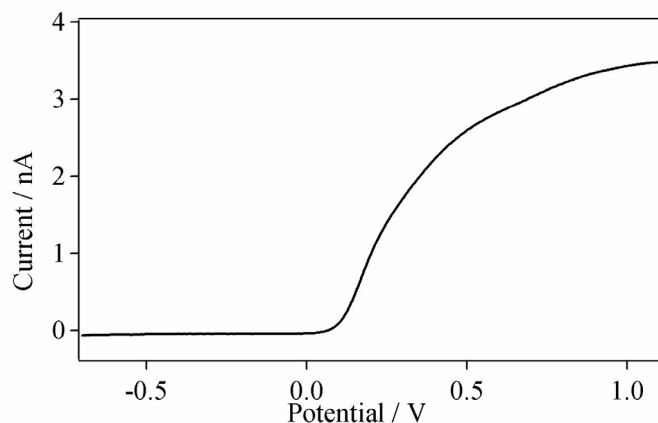


**Figure 9.** Oxidation of  $[\text{Co}(\text{dbbip})_2](\text{ClO}_4)_2$  on an platinum UME with a radius of  $5 \mu\text{m}$ . Sweep rate =  $50 \text{ mV} \cdot \text{s}^{-1}$ .

The results for cobalt complexes versus standard calomel electrode (SCE) are given in Table 11.

**Table 11.** Redox potential versus SCE for a series of cobalt complexes.

Cobalt complexes	$E_{1/2}$ vs. SCE [V]	$E^{\circ}$ [V]
$[\text{Co}(\text{bipy})_3](\text{ClO}_4)_2$	0.310	0.255
$[\text{Co}(\text{bipy})_3](\text{OTf})_2$	0.303	0.248
$[\text{Co}(\text{dbbip})_2](\text{ClO}_4)_2$	0.385	0.330
$[\text{Co}(\text{dmbip})_2](\text{ClO}_4)_2$	0.440	0.385
$[\text{Co}(\text{dmbip})_2](\text{DDS})_2$	0.447	0.392
$[\text{Co}(\text{dmbip})_2](\text{OTf})_2$	0.426	0.371
$[\text{Co}(\text{dmbip})_2](\text{PF}_6)_2$	0.447	0.392
$[\text{Co}(\text{dmbip})_2](\text{PTS})_2$	0.548	0.493
$[\text{Co}(\text{phen})_3](\text{OTf})_2$	0.363	0.308
$[\text{Co}(\text{phen})_3](\text{Tf}_2\text{N})_2$	0.372	0.317
$[\text{Co}(\text{terpy})_2](\text{ClO}_4)_2$	0.250	0.195
$[\text{Co}(\text{ttpy})_2](\text{OTf})_2$	0.197	0.142

For reversible couples in solution, the formal reduction redox potential can be approximated by Eq. 4.12, where in our case  $c_O$  and  $c_R$  are the concentrations of the oxidized and reduced cobalt complexes in the electrolyte, respectively.

$$E^{\circ'} = E_{1/2} + \frac{RT}{nF} \ln \left[ \frac{c_O}{c_R} \right] \quad (4.12)$$

As the standard concentration is 0.01 M for the oxidized species and 0.09 M for the reduced one, the  $E^{\circ'}$  for each cobalt complex can be calculated from  $E_{1/2}$ . The values have been reported in Table 11.

The open circuit voltage  $V_{oc}$  is determined by the difference between the Fermi energies of the illuminated photoelectrode and the platinum-coated TCO electrode. If we assumed that the Fermi energy of the photoelectrode is independent of the redox couple and that the Fermi energy of the counter electrode is close to the redox energy of the electrolyte when the concentration ratio of the oxidized species to the reduced one is kept constant, a considerable increase in the open circuit voltage could be achieved by using a couple of higher redox potential than that of  $I_3^-/I^-$  ( $E^{\circ'} = 0.15$  V vs. SCE in acetonitrile). However, selecting a redox couple with a more positive equilibrium potential does not necessarily translate into an increase of the open circuit potential. The potentials of both the photoelectrode and the counter electrode shift with the equilibrium potential of the redox couple.<sup>[7]</sup> Moreover, there should be adequate potential difference between the dye and the redox couple to provide a sufficient driving force for Co(II) to regenerate the oxidized state of the dye. The influence of redox mediator potential on the  $V_{oc}$  of the dye-sensitized solar cell can be nevertheless seen for several cobalt complexes in Table 12. For example, increasing the redox couple potential  $E^{\circ'}$  by 0.19 V, from  $[Co(terpy)_2](ClO_4)_2$  to  $[Co(dmbip)_2](ClO_4)_2$ , results in an increase of 0.18 V in  $V_{oc}$ . Some complexes do not exhibit such a trend, like  $[Co(dmbip)_2](PTS)_2$ , where the redox potential is highly positive ( $E^{\circ'} = 0.493$  V) though the open circuit voltage is similar to  $[Co(dbip)_2](ClO_4)_2$ , which has a redox potential of  $E^{\circ'} = 0.330$  V. Moreover, differences up to 122 mV were also found in the redox potentials of  $[Co(dmbip)_2]^{2+}$  complexes upon varying the counter ion.

**Table 12.** Redox potential and open circuit potential under 95  $W \cdot m^{-2}$  comparison for a whole series of cobalt complexes.

Cobalt complexes	$E^{\circ'}$ [V]	$V_{oc}$ [mV]
[Co(tpy) <sub>2</sub> ](OTf) <sub>2</sub>	0.142	500
[Co(terpy) <sub>2</sub> ](ClO <sub>4</sub> ) <sub>2</sub>	0.195	470
[Co(bipy) <sub>3</sub> ](OTf) <sub>2</sub>	0.248	510
[Co(bipy) <sub>3</sub> ](ClO <sub>4</sub> ) <sub>2</sub>	0.255	510
[Co(phen) <sub>3</sub> ](OTf) <sub>2</sub>	0.308	600
[Co(phen) <sub>3</sub> ](Tf <sub>2</sub> N) <sub>2</sub>	0.317	620
[Co(dbbip) <sub>2</sub> ](ClO <sub>4</sub> ) <sub>2</sub>	0.330	660
[Co(dmbip) <sub>2</sub> ](OTf) <sub>2</sub>	0.371	660
[Co(dmbip) <sub>2</sub> ](ClO <sub>4</sub> ) <sub>2</sub>	0.385	650
[Co(dmbip) <sub>2</sub> ](DDS) <sub>2</sub>	0.392	650
[Co(dmbip) <sub>2</sub> ](PF <sub>6</sub> ) <sub>2</sub>	0.392	640
[Co(dmbip) <sub>2</sub> ](PTS) <sub>2</sub>	0.493	650

These differences in redox potential between the [Co(dmbip)<sub>2</sub>](X)<sub>2</sub> may be due to the different ion pairing energies between the cation and various anions. The ion pairing energy affects the activity coefficients and, through the Nernst equation (Eq. 4.13), the redox potential.

$$E = E^{\circ'} + \frac{RT}{nF} \ln \left( \frac{a_O}{a_R} \right) \quad (4.13)$$

During electrochemical measurements, the generated currents tended to drop slightly with time. This problem may arise from a successive deposition of the complexes on the platinum surface of the UME, decreasing the active area of the electrode. It is then very important to clean the UME between each measurement.

### Diffusion coefficient

It is also possible to use an UME to determine the diffusion coefficient of a species in solution. Firstly the UME diameter must be determined with a standard electroactive species and as such an electrolyte composed of 7.29 mM  $\text{K}_3\text{Fe}(\text{CN})_6$  and 0.5 M KCl in acetonitrile was prepared. As the diffusion coefficient of  $\text{K}_3\text{Fe}(\text{CN})_6$  in acetonitrile is known,  $D = 7.17 \cdot 10^{-6} \text{ cm}^2 \cdot \text{s}^{-1}$  at 20 °C and (see Eq. 2.20, page 51)

$$I_d = 4nFDcr \quad (4.14)$$

one can calculate  $r$  if the limiting diffusion current  $I_d$  is known. Figure 10 shows the limiting diffusion current for this electrolyte.

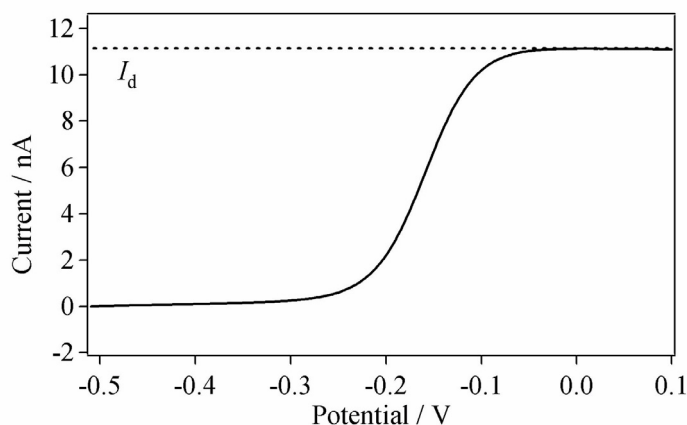


**Figure 10.** Limiting diffusion current measured with an UME for 7.29 mM  $\text{K}_3\text{Fe}(\text{CN})_6$  and 0.5 M KCl in acetonitrile. At 0.1 V, this limiting diffusion current  $I_d = 10.95 \text{ nA}$ .

In this case, as  $I_d = 10.95 \text{ nA}$ , then  $r = 5.43 \text{ }\mu\text{m}$ .

Once  $r$  is known, the diffusion coefficient is determined using electrolytes containing 50.1 mM tetrabutylammonium  $\text{PF}_6$  in acetonitrile with varying concentrations of  $[\text{Co}(\text{dbbip})_2](\text{ClO}_4)_2$ . In this case, concentrations of cobalt complex used were 2.90, 4.65, 5.95, and 7.76  $\text{mol} \cdot \text{m}^{-3}$ , respectively.

If one reports several limiting diffusion currents as a function of the concentration of the species in solution (Figure 11) Eq. 4.15, derived from Eq. 4.14, can be used to determine the diffusion coefficient.

$$D = \frac{\text{slope}}{4nFr} \quad (4.15)$$

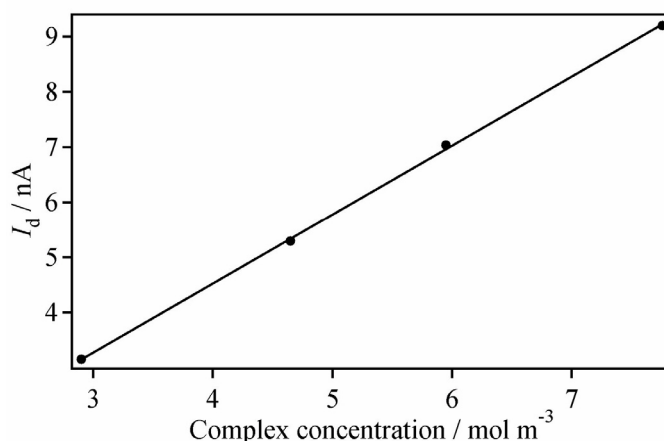


**Figure 11.** Limiting current  $I_d$  as a function of the cobalt complex  $[\text{Co}(\text{dbbip})_2](\text{ClO}_4)_2$  concentration in acetonitrile. The value of the slope is  $1.618 \cdot 10^{-9}$ .

With a slope of  $1.618 \cdot 10^{-9}$ , one finds that  $D = 7.72 \cdot 10^{-6} \text{ cm}^2 \cdot \text{s}^{-1}$  for  $\text{Co}(\text{dbbip})_2(\text{ClO}_4)_2$  in acetonitrile at 20 °C.

Based on cyclic voltammograms recorded at a sweep rate of  $200 \text{ mV} \cdot \text{s}^{-1}$  in a three electrode configuration using a platinum disc working electrode ( $a = 500 \text{ }\mu\text{m}$ ), a gold disc electrode ( $a = 125 \text{ }\mu\text{m}$ ), and a platinum wire pseudo reference electrode,  $D$  has been measured for the same cobalt complex by Cameron et al. in acetonitrile/ethylene carbonate (2:3) solvent mixture.<sup>[8]</sup> They found  $D = 1.9 \cdot 10^{-6} \text{ cm}^2 \cdot \text{s}^{-1}$  for Co(II) and  $D = 1.1 \cdot 10^{-6} \text{ cm}^2 \cdot \text{s}^{-1}$  for Co(III) using parallel plate thin layer cells. The electrode materials for these cells were sputtered platinum, TCO coated glass, and TCO coated with a  $\text{TiO}_2$  blocking layer. A platinum-coated TCO counter electrode completed the sandwich type cells. These substantially lower values of  $D$  they obtained are due to the use of a more viscous solvent mixture than the pure acetonitrile used here.

The diffusion coefficient found using Eq. 4.15 can be compared with a diffusion coefficient calculated from the diameter of the  $[\text{Co}(\text{dbbip})_2]^{2+}$  molecule whose geometry is assimilated to a sphere of radius  $r$  and the Stokes-Einstein relation. An optimized molecular geometry for the  $[\text{Co}(\text{dbbip})_2]^{2+}$  molecule was calculated with the CAChe software<sup>1</sup> from Fujitsu Limited using MOPAC with PM3 parameters. The radius of the molecule was taken as  $r = 15 \text{ \AA}$  and a circle with  $30 \text{ \AA}$  of diameter is represented on Figure 12.

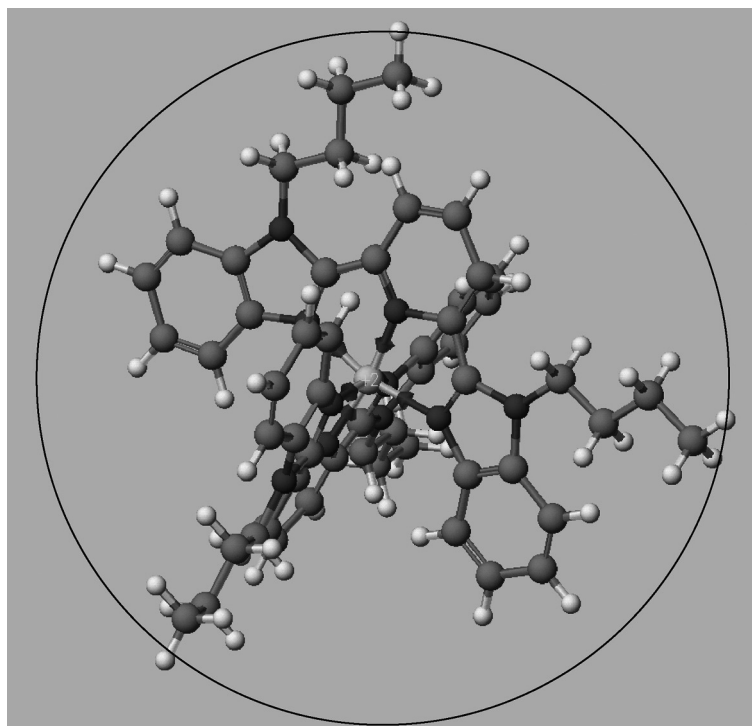


**Figure 12.** Optimized geometry of the  $[\text{Co}(\text{dbbip})_2]^{2+}$  molecule, with an estimated diameter of  $30 \text{ \AA}$ .

The Stokes' relation gives the frictional constant  $f$  for a sphere of radius  $r$  in a medium of a certain viscosity  $\eta$  (Eq. 4.16).

$$f = 6\pi a\eta \quad (4.16)$$

---

1. <http://www.cachesoftware.com>

The Stokes-Einstein relation (Eq. 4.17) between  $f$  and the diffusion coefficient  $D$  gives the diffusion coefficient as a function of the radius of the molecule, the temperature and the viscosity of the solvent (Eq. 4.18).

$$f = \frac{k_B T}{D} \quad (4.17)$$

$$D = \frac{k_B T}{6\pi a \eta} \quad (4.18)$$

The viscosity of acetonitrile is well known and its value at 15 °C is  $\eta = 0.38$  cP or  $\eta = 0.00038$  Pa · s. The radius was determined as  $r = 15$  Å, giving a theoretical diffusion coefficient of  $D = 7.40 \cdot 10^{-6}$  cm<sup>2</sup> · s<sup>-1</sup>, compared to the experimental  $D = 7.72 \cdot 10^{-6}$  cm<sup>2</sup> · s<sup>-1</sup>.

### 3.5. Elemental analysis of the [Co(dbpip)<sub>2</sub>](ClO<sub>4</sub>)<sub>2</sub> complex

Elemental analysis of C, H, N and Co was performed by the Ilse Beetz Mikroanalytisches Laboratorium, Kronach, Germany, on 7.665 mg of [Co(dbpip)<sub>2</sub>](ClO<sub>4</sub>)<sub>2</sub>. The sample was separated in two portions, 4.868 mg and 2.797 mg, and each was dried at room temperature under vacuum on P<sub>2</sub>O<sub>5</sub>. No reduction of mass was observed after the drying process, which confirmed that the samples were already water-free. The first part was used for the C, H and Co analysis while the second was used to determine the N and once again the Co content.

With the first 4.868 mg sample, 10.460 mg of CO<sub>2</sub> was obtained along with 2.290 mg of H<sub>2</sub>O, giving C 58.64% and H 5.26% respectively. The missing mass was attributed to cobalt, with 0.350 mg of Co<sub>3</sub>O<sub>4</sub> giving 5.28% of Co.

The second 2.797 mg sample gave 0.323 cm<sup>3</sup> of nitrogen at 24 °C (721 mmHg), suggesting N 12.59%. Again the missing mass was attributed to cobalt and 0.193 mg of Co<sub>3</sub>O<sub>4</sub> give 5.07% of Co.

The theoretical analysis of [Co(dbpip)<sub>2</sub>](ClO<sub>4</sub>)<sub>2</sub> gave a molar mass of 1104.966 g · mol<sup>-1</sup> (C<sub>54</sub>H<sub>58</sub>N<sub>10</sub>CoC<sub>12</sub>O<sub>8</sub>).

The results of the elemental analysis for [Co(dbpip)<sub>2</sub>](ClO<sub>4</sub>)<sub>2</sub> are given in Table 13.

**Table 13.** Composition of  $[\text{Co}(\text{dbbip})_2](\text{ClO}_4)_2$  as determined by elemental analysis. For comparison the calculated percentages are given with the % of error. The percentage given for Co is the mean value obtained from the two sets of results.

Element	Analysis	Calculation	Difference
C	58.64%	58.70%	0.10%
H	5.26%	5.29%	0.59%
N	12.59%	12.68%	0.68%
Co	5.18%	5.33%	2.96%

The error is low ( $< 1\%$ ) for the analyzed and calculated results of the C, H and N. With the Co however, the percentage of Co could only be calculated indirectly from the C, H and N analysis. The value is not quantitative and hence there is a greater margin of error in the results. The purity of the complex was already confirmed through NMR measurements (see “NMR spectra of  $[\text{Co}(\text{dbbip})_2]^{2+}$ ”, page 84), with a resolution  $< 1\%$ .

### 3.6. Reduced and oxidized complexes UV-Vis absorption spectra

One condition for the employment of a redox couple in the DSSCs is that the light absorption of the oxidized and reduced form in the visible region should be as low as possible. This is especially true for the illumination of the counter electrode, as the visible light must be able to reach the photoelectrode. The dye has a maximum absorption in the visible domain at about 540 nm in acetonitrile and hence the extinction coefficient of the electrolytic solution should be of a minimum around that wavelength. It is also useful to know the UV-Vis spectra of both the oxidized and reduced cobalt complexes to help determine the best wavelengths for laser flash photolysis measurements. Here the wavelength of the probe pulse should not interfere with the wavelength used for excitation if the rate of dye regeneration is to be observed (see “Laser flash photolysis”, page 52).

The  $[\text{Co}(\text{dbbip})_2]^{2+}$  and  $[\text{Co}(\text{dbbip})_2]^{3+}$  species were characterized by UV-Vis spectrophotometry. As the extinction coefficient of the reduced and oxidized species are very high, diluted solutions were used to avoid saturation of the spectrophotometer. The concentrations used for Co(II) and Co(III) were  $7.69 \cdot 10^{-6}$  M and  $6.56 \cdot 10^{-6}$  M, respectively.



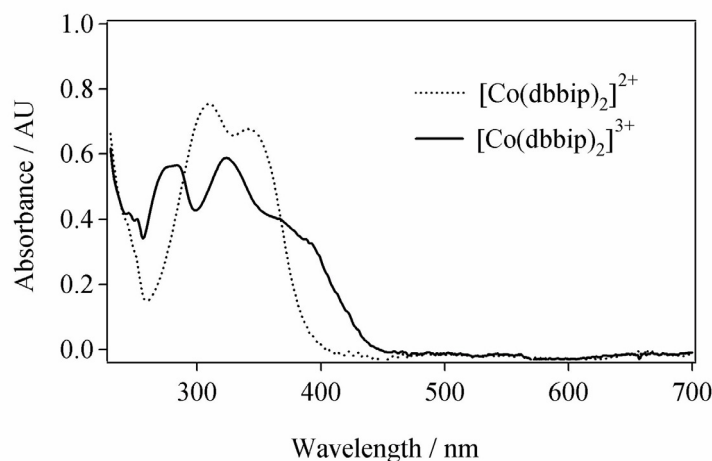


**Figure 13.** UV-VIS spectra of  $[\text{Co}(\text{dbbip})_2]^{2+}$  and  $[\text{Co}(\text{dbbip})_2]^{3+}$  in  $\text{CH}_3\text{CN}$ .

The UV-Vis spectra shown in Figure 13 indicate that the complexes have an absorption maxima in the near UV region. The complex  $[\text{Co}(\text{dbbip})_2]^{2+}$  has  $\lambda_{\text{max}}(\epsilon) = 310 \text{ nm} (52'000)$ ,  $345 \text{ nm} (50'000)$  and  $[\text{Co}(\text{dbbip})_2]^{3+}$   $\lambda_{\text{max}}(\epsilon) = 276 \text{ nm} (44'000)$ ,  $323 \text{ nm} (45'000)$ . Only the absorption tails can be seen in the visible region, with  $\epsilon_{480}(\text{Co}^{\text{II}}) = 1.3 \cdot 10^2 \text{ mol}^{-1} \cdot \text{dm}^3 \cdot \text{cm}^{-1}$  and  $\epsilon_{480}(\text{Co}^{\text{III}}) = 2.6 \cdot 10^2 \text{ mol}^{-1} \cdot \text{dm}^3 \cdot \text{cm}^{-1}$ . This low absorption in the visible region allows the use of highly concentrated electrolytic solutions in counter electrode illuminated solar cells, without significant reduction in the visible light available for absorption by the sensitizer.

### 3.7. XPS, crystal structure determination and powder X-ray diffraction

The results of the single crystal X-ray diffraction studies of  $[\text{Co}(\text{dbbip})_2]^{n+}$  perchlorates, both in the reduced Co(II) and oxidized Co(III) forms, are presented below. The crystal structures and packing patterns were analyzed. The  $[\text{Co}(\text{dbbip})_2]^{3+}$  crystals were obtained by stoichiometric oxidation of  $[\text{Co}(\text{dbbip})_2]^{2+}$  with  $\text{NOBF}_4$ , leading to a mixture of  $\text{ClO}_4^-$  and  $\text{BF}_4^-$  counter ions within the crystal.

Light yellow triclinic single crystals of  $[\text{Co}(\text{dbbip})_2]^{2+}$  ( $a = 14.859(7)$ ,  $b = 16.608(8)$ ,  $c = 22.282(16) \text{ \AA}$ ,  $\alpha = 73.01(1)$ ,  $\beta = 81.64(1)$ ,  $\gamma = 85.98(1)^\circ$ ,  $V = 5201 \text{ \AA}^3$ , space group  $P-1$ ,  $Z = 4$ ) had a rather irregular shape and a relatively poor scattering power, hence 25'893 reflections were collected, with 18'220 independent and only 3'674 observed ones ( $F > 4\sigma$ ).

The crystal structure of  $[\text{Co}(\text{dbbip})_2]^{2+}$  was solved initially in a non-centrosymmetric P 1 group. The P  $\bar{1}$  group was chosen based on the results of the refinement. Due to a small number of observed reflections, the final refinement was performed in a full-matrix least squares on  $F^2$  with only Co, Cl and O atoms (of two ordered perchlorate anions) in anisotropic approximations, giving  $R = 14.7\%$ . All other non-hydrogen atoms were refined isotropically. Hydrogen atoms were included in the refinement based on calculated positions using the riding motion model.

A reflection data set from a small yellow plate-like monoclinic single crystal of  $[\text{Co}(\text{dbbip})_2]^{3+}$  ( $a = 21.99(1)$ ,  $b = 23.49(1)$ ,  $c = 22.05(1)$  Å,  $\beta = 96.15(2)^\circ$ ,  $V = 11325$  Å<sup>3</sup>, space group P 2<sub>1</sub>/c,  $Z = 8$ ) was collected. 92'300 reflections were measured, with 18'884 independent and 7'493 observed, under the same experimental conditions as for  $[\text{Co}(\text{dbbip})_2]^{2+}$ . The structure was initially solved in the triclinic P  $\bar{1}$  space group, where four independent  $[\text{Co}(\text{dbbip})_2]^{3+}$  cations, related into geometrically equivalent pairs, and twelve counter ions were revealed. Since geometric parameters of all the symmetry-related ions are within the experimental error both for P  $\bar{1}$  and P 1 groups, the P 2<sub>1</sub>/c space group with two independent  $[\text{Co}(\text{dbbip})_2]^{3+}$  cations, differing by conformations of their Bu<sup>n</sup> fragments, and six counter ions was finally chosen in accordance with the systematic absence of I(hkl) data. A block-diagonal least squares refinement on  $F^2$  converged to  $R = 8.0\%$  using all the data in anisotropic approximation for all atoms except disordered counter ions and Bu<sup>n</sup> fragments. Hydrogen atoms were mostly observable in the Difference Fourier Map, but refinement of the geometric positions was made using the riding motion model. A rotational disorder of two of six anions and three Bu<sup>n</sup> fragments was revealed in the final stages of the refinement. The ratio of disordered ClO<sub>4</sub><sup>-</sup>/BF<sub>4</sub><sup>-</sup> counter ions that have close geometric parameters, was determined by variation of B/Cl occupancies of the central atomic position, with terminal atoms refined as oxygens due to a closeness of O and F scattering factors.

X-ray photoelectron spectroscopy (XPS) and powder X-ray diffraction (XRD) were used to characterize these complexes as bulk samples.

In powder XRD experiments, lattice parameters for  $[\text{Co}(\text{dbbip})_2]^{2+}$  and  $[\text{Co}(\text{dbbip})_2]^{3+}$  were obtained by indexing the 32 (for  $[\text{Co}(\text{dbbip})_2]^{2+}$ ) and 35 (for  $[\text{Co}(\text{dbbip})_2]^{3+}$ ) strongest reflections in the experimental powder patterns.

### Structure of $[\text{Co}(\text{dbbip})_2]^{2+}$ and $[\text{Co}(\text{dbbip})_2]^{3+}$ in comparison with $[\text{Co}(\text{dmbip})_2]^{2+}$

The crystal structures and packing arrangements in  $[\text{Co}(\text{dbbip})_2]^{2+}$  and  $[\text{Co}(\text{dbbip})_2]^{3+}$  display strong similarities with  $[\text{Co}(\text{dmbip})_2]^{2+}$ , whose single crystal X-ray study was reported earlier.<sup>[3]</sup> Each of these three crystal structures contain two symmetrically independent cationic cobalt complexes. Unlike  $[\text{Co}(\text{dmbip})_2]^{2+}$ , which contains solvent (4-methyl-1,3-dioxolan-2-one) molecules besides  $[\text{Co}(\text{dmbip})_2]^{2+}$  cations and hexafluorophosphate anions, both  $[\text{Co}(\text{dbbip})_2]^{2+}$  and  $[\text{Co}(\text{dbbip})_2]^{3+}$  are solvent-free.

The geometry of their  $[\text{Co}(\text{dbbip})_2]^{n+}$  cations (Figure 14 and Table 14) is characterized by a distorted octahedral environment of six nitrogen atoms similar to that found in  $[\text{Co}(\text{dmbip})_2]^{2+}$ . Main bond distances and bond angles for all three complexes, averaged within the idealized  $D_2$  symmetry and shown in Table 14, are in a good agreement with each other. They also correspond well with the geometric parameters in  $M(\text{bip})$  moiety (where bip stands for any substituted 2,6-bis(benzimidazol-2'-yl)pyridine ligand) averaged over the other structures taken from Cambridge Structure Database (CSD), as well as in the non-coordinated dmbip ligand.<sup>[9]</sup>

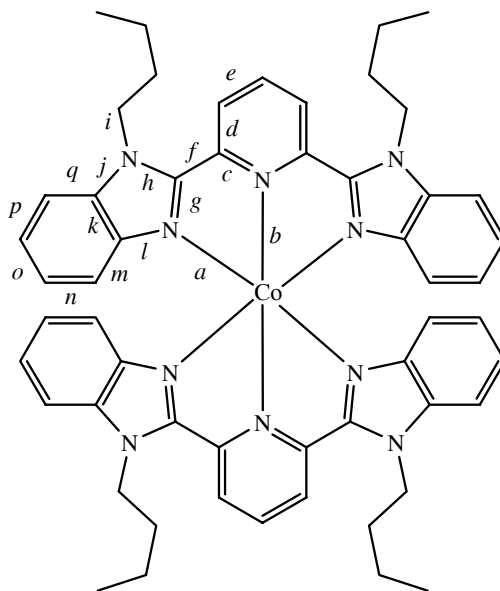


**Figure 14.** Structure of  $[\text{Co}(\text{dbbip})_2]^{n+}$  moiety. Main bond lengths within the idealized  $D_2$  symmetry (denoted with letters) are shown in Table 14 in comparison with published data on related compounds. Average dihedral angles between dbbip ligands are  $76^\circ$  in  $[\text{Co}(\text{dbbip})_2]^{2+}$  and  $82^\circ$  in  $[\text{Co}(\text{dbbip})_2]^{3+}$ , transoid N-Co-N bond angles of b-b type  $169^\circ$  and  $179^\circ$ , respectively.

**Table 14.** Geometry of metal cations (see Figure 14 for notations) in  $[\text{Co}(\text{dbbip})_2]^{3+}$  and  $[\text{Co}(\text{dbbip})_2]^{2+}$ , and published data. [a] From [5] [b] From [9].

	$[\text{Co}(\text{dmbip})_2]^{2+}$ [a]	$[\text{Co}(\text{dbbip})_2]^{2+}$	$[\text{Co}(\text{dbbip})_2]^{3+}$	M(bip) fragment (CSD)	dmbip [b]
	bond distances [Å]				
<i>a</i>	2.121	2.11	1.921	–	–
<i>b</i>	2.077	2.08	1.880	–	–
<i>c</i>	1.341	1.37	1.358	1.352	1.344
<i>d</i>	1.402	1.37	1.386	1.382	1.393
<i>e</i>	1.374	1.36	1.383	1.383	1.379
<i>f</i>	1.483	1.48	1.457	1.455	1.474
<i>g</i>	1.321	1.32	1.345	1.326	1.325
<i>h</i>	1.359	1.38	1.355	1.353	1.378
<i>i</i>	1.468	1.45	1.475	–	1.461
<i>j</i>	1.401	1.36	1.392	1.384	1.379
<i>k</i>	1.378	1.41	1.345	1.395	1.401
<i>l</i>	1.398	1.38	1.398	1.393	1.390
<i>m</i>	1.383	1.39	1.399	1.387	1.398
<i>n</i>	1.378	1.42	1.381	1.369	1.382
<i>o</i>	1.381	1.39	1.400	1.399	1.400
<i>p</i>	1.368	1.36	1.374	1.380	1.377
<i>q</i>	1.378	1.41	1.402	1.392	1.398

The crystal structure of  $[\text{Co}(\text{dbbip})_2]^{2+}$  was difficult to determine due to the inherent poor reflection of its single crystals (ten individual crystals were studied). Nevertheless, two independent  $[\text{Co}(\text{dbbip})_2]^{2+}$  cations were identified. These differed in the conformations of their partially disordered n-butyl fragments, and four  $\text{ClO}_4^-$  counter ions, including two ordered and two disordered ones. The closest  $\text{C}\cdots\text{N}$  and  $\text{C}\cdots\text{C}$  intermolecular contacts lie within the range 3.36–3.53 Å (Figure 15). Estimated standard deviations in the C-N and C-C distances in ordered fragments are generally 0.02–0.03 Å, and the average geometric parameters are in accordance with other M(bip)-containing derivatives (Table 14). The main Co-N bond distances in  $[\text{Co}(\text{dbbip})_2]^{2+}$  (2.06(1)–2.17(2), av. 2.10 Å) are almost identical to  $[\text{Co}(\text{dmbip})_2]^{2+}$  (2.11 Å). This is in agreement with 2+ oxidation state of the Co atom in both complexes.

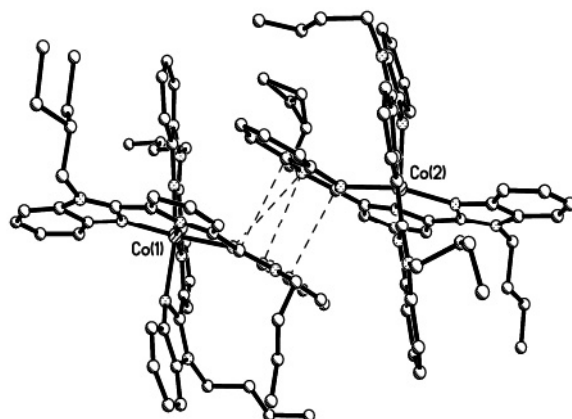


**Figure 15.** A quasi-centrosymmetric pair of crystallographically independent  $[\text{Co}(\text{dbpip})_2]^{2+}$  cations. The closest  $\text{C}\cdots\text{N}$  and  $\text{C}\cdots\text{C}$  intermolecular contacts (dashed lines) lie in the range 3.36–3.53 Å.

The crystal structure of  $[\text{Co}(\text{dbbip})_2]^{3+}$  contains two independent cations (Figure 16) in general positions and six independent counter ions of tetrahedral geometry, two of which are rotationally disordered.

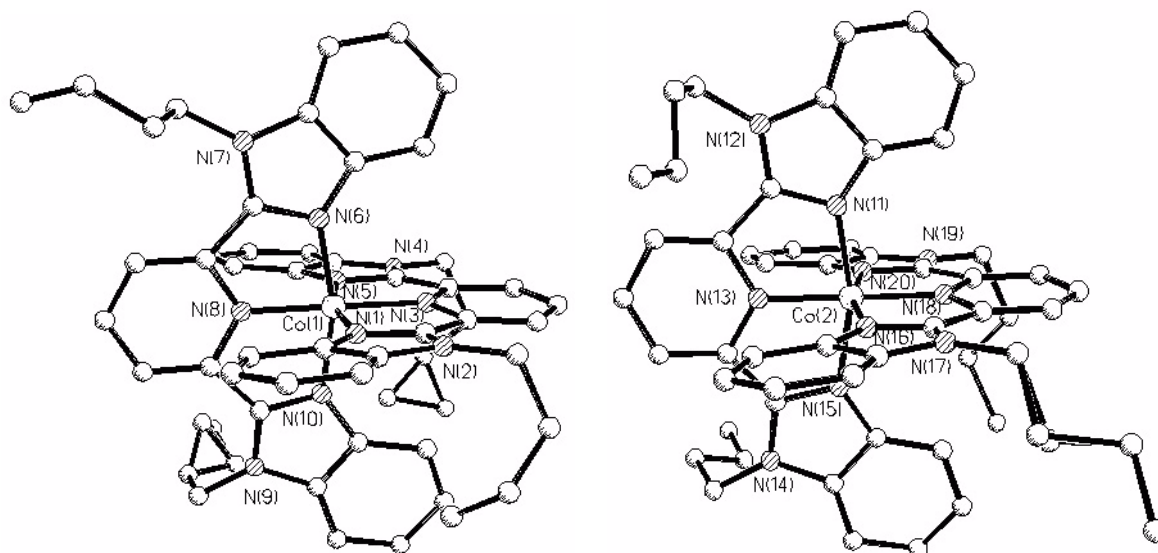


**Figure 16.** Two symmetrically independent  $[\text{Co}(\text{dbbip})_2]^{3+}$  cations, differing by conformations of their (partially disordered) n-butyl fragments. Hydrogen atoms have been omitted for clarity.

Partial occupancies of the central atomic positions in tetrahedral anions by B and Cl atoms, refined by the least squares, give the stoichiometry  $[\text{Co}(\text{dbbip})_2](\text{ClO}_4)_{2.3}(\text{BF}_4)_{0.7}$ . Bond distances and bond angles in ordered moieties of two independent cations are within the experimental error. The average Co-N distance of 1.91 Å points unequivocally to the Co(III) oxidation state, being almost 0.2 Å shorter than in  $[\text{Co}(\text{dbbip})_2]^{2+}$  and  $[\text{Co}(\text{dmbip})_2]^{2+}$ .<sup>[3]</sup> This was also confirmed as related Co(II) complexes such as bis[4'-terpyridone]cobalt(II) perchlorate monohydrate have bond length Co-N of 1.99–2.15, av. 2.09 Å.<sup>[10]</sup> The average Co-N bond length of 1.91 Å in Co(III) complexes is also common, e.g. bis[2-(2-(phenylamido)phenylazo)pyridine]cobalt(III) perchlorate.<sup>[11]</sup> Enlargement of the metal center moving from e.g.  $[\text{Co}(\text{dbbip})_2]^{2+}$  to  $[\text{Co}(\text{dbbip})_2]^{3+}$ , is also accompanied with more distorted environment, which corresponds to a stronger “squeeze” of the cations.

### *Crystal packing in $[\text{Co}(\text{dbbip})_2]^{2+}$ and $[\text{Co}(\text{dbbip})_2]^{3+}$*

Molecular packing in both the crystals of  $[\text{Co}(\text{dbbip})_2]^{2+}$  and  $[\text{Co}(\text{dbbip})_2]^{3+}$  is rather similar to  $[\text{Co}(\text{dmbip})_2]^{2+}$ ,<sup>[3]</sup> consisting of the layers of  $[\text{Co}(\text{dbbip})_2]^{n+}$  cations parallel to  $(a,b)$  plane. In  $[\text{Co}(\text{dbbip})_2]^{2+}$ , such layers are composed of zigzag cationic chains along (100) direction (Figure 17, left), whereas in  $[\text{Co}(\text{dbbip})_2]^{3+}$  the layers are composed of the columns of cations, running along (210) direction (Figure 17, right), with anions between the layers in both cases. The closest Co...Co distances between neighboring cations in the layer in  $[\text{Co}(\text{dbbip})_2]^{2+}$  and  $[\text{Co}(\text{dbbip})_2]^{3+}$  are 8.42 Å and 10.64 Å, respectively (9.76 Å in  $[\text{Co}(\text{dmbip})_2]^{2+}$ ).<sup>[3]</sup> Noteworthy, side hydrocarbon chains attached to  $[\text{Co}(\text{bip})_2]^{n+}$  moiety (methyl in  $[\text{Co}(\text{dmbip})_2]^{2+}$ , n-butyl in  $[\text{Co}(\text{dbbip})_2]^{2+}$  and  $[\text{Co}(\text{dbbip})_2]^{3+}$ ) point towards the neighboring cationic layer in all three structures, creating conditions to larger interlayer separation in the structures with the same counter ions due to steric effects of bulkier carbohydrate fragments.

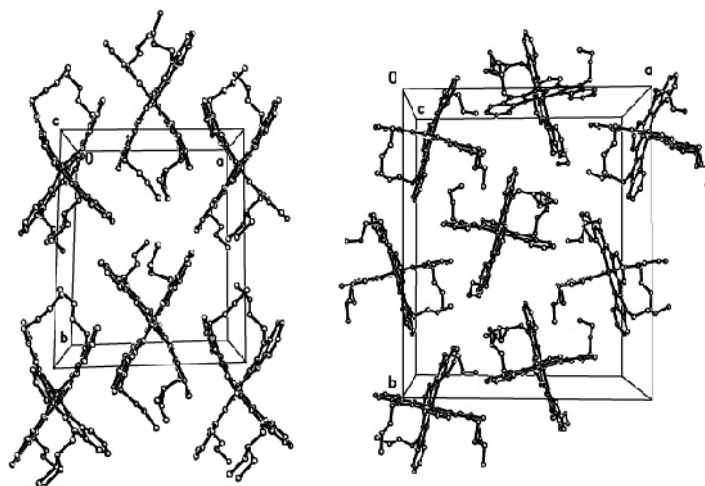


**Figure 17.** Cationic layer in  $[\text{Co}(\text{dbpip})_2]^{2+}$  (left) and  $[\text{Co}(\text{dbpip})_2]^{3+}$  (right) viewed along (001) direction.

Two of six symmetrically independent mixed anionic positions in  $[\text{Co}(\text{dbpip})_2]^{3+}$  are substantially closer to  $[\text{Co}(\text{dbpip})_2]^{3+}$  ( $\text{Cl}(1)\cdots\text{Co}(1)$  5.29 Å,  $\text{Cl}(2)\cdots\text{Co}(2)$  4.96 Å) than four others (6.42–6.99 Å). Such an “ion pairing” was not observed in other related metal complexes, including  $[\text{Co}(\text{dmbip})_2]^{2+}$  and  $[\text{Co}(\text{dbpip})_2]^{2+}$ , where closest  $\text{Co}\cdots\text{P}$  and  $\text{Co}\cdots\text{Cl}$  distances lie in the ranges 6.74–6.95 Å<sup>[3]</sup> and 6.05–6.50 Å, respectively.

### *Content of counter ions in $[\text{Co}(\text{dbpip})_2]^{3+}$*

Due to a generally low diffraction capability of the oxidized  $[\text{Co}(\text{dbpip})_2]^{n+}$  salts, more suitable single crystals of  $[\text{Co}(\text{dbpip})_2]^{3+}$  were prepared by oxidation of  $[\text{Co}(\text{dbpip})_2]^{2+}$  with  $\text{NOBF}_4$  and therefore contain some amount of tetrafluoroborate counter ions. The  $\text{BF}_4^-$  content was estimated by three methods: (i) an elemental analysis, corresponding to ca. 0.6  $\text{BF}_4^-$  anions per  $[\text{Co}(\text{dbpip})_2]^{3+}$  ion, (ii) XPS data that gave a semiquantitative N:F:Cl ratio of 4.6:1.8:1, corresponding to ca. 0.9  $\text{BF}_4^-$ , and (iii) the results of a least-squares refinement of their single crystal structure. The latter, which may not be representative of the tetrafluoroborate content in the bulk sample, agrees with the direct estimation in method (i). The composition of  $[\text{Co}(\text{dbpip})_2]^{3+}$  was finally chosen as  $[\text{Co}(\text{dbpip})_2](\text{ClO}_4)_{2.3}(\text{BF}_4)_{0.7}$  from the refinement of its crystal structure,

with the almost isometric  $\text{ClO}_4^-$  and  $\text{BF}_4^-$  anions replacing each other in all independent anionic positions.

Room-temperature powder patterns of bulk  $[\text{Co}(\text{dbbip})_2]^{2+}$  and  $[\text{Co}(\text{dbbip})_2]^{3+}$  were indexed using unit cell parameters obtained from their low-temperature single crystals' study. The presence of two relatively strong non-indexed lines observed in XRD data of  $[\text{Co}(\text{dbbip})_2]^{3+}$  points to the admixture of another, as yet unidentified crystalline component in the bulk sample of the oxidized  $[\text{Co}(\text{dbbip})_2]^{3+}$  complex. This observation agrees with the fractional element of the proposed structure of  $[\text{Co}(\text{dbbip})_2]^{3+}$  determined by elemental analysis and XPS. Nevertheless, a reasonable agreement of unit cell parameters in  $[\text{Co}(\text{dbbip})_2]^{2+}$  and  $[\text{Co}(\text{dbbip})_2]^{3+}$  obtained by single crystal (110 K) and powder XRD diffraction (296 K) showed that the bulk samples of both  $[\text{Co}(\text{dbbip})_2]^{n+}$  complexes generally corresponded to their formulas as determined by single crystal X-ray studies.



## 4. Interfaces optimization

### 4.1. Introduction

In the dye-sensitized solar cells most reactions take place at the interfaces. Optimization of the interfaces of the photoelectrode is required to reduce the electron recombination between the  $\text{TiO}_2$  and the oxidized dye, and help prevent the back electron transfer between the  $\text{TiO}_2$  and the electrolyte. This goal may be achieved through optimization of the sensitizer - electrolyte interactions or the semiconductor layers properties, respectively. It can also be useful to optimize the interfaces to enhance the photovoltaic parameters, e.g. photocurrent or photovoltage. This may be achieved by changing the electrolyte composition, adding co-adsorbers on the  $\text{TiO}_2$  surface, or improving the dye surface density on semiconductor. The interface between the counter electrode and the electrolyte must also be optimized, to increase the electron transfer rate and improve the fill factor.

### 4.2. Sensitizer - electrolyte interactions

#### *Introduction*

Solar cells with electrolytes containing cobalt complex redox systems with different sensitizers were investigated, either using photoelectrochemical methods or laser flash photolysis. The interaction between the sensitizer and the redox mediator is of prime importance for the regeneration rate of the oxidized dye and therefore its ability to sustain the photocurrent in the output circuit. The interaction between these two chemical compounds involves energetic, steric, and electrostatic considerations. Table 15 lists the sensitizers and the cobalt complexes used in this part of the chapter.

**Table 15.** Short names of the sensitizers and the cobalt complexes used to study the interaction between dye and electrolyte. Full names are given in Table 2, page 32 for the dyes and in Table 6, page 35 for the cobalt complexes.

Sensitizers	Cobalt complexes
N3	[Co(bipy) <sub>3</sub> ](ClO <sub>4</sub> ) <sub>2</sub>
N621	[Co(dbbp) <sub>2</sub> ](ClO <sub>4</sub> ) <sub>2</sub>
N719	[Co(dmbip) <sub>2</sub> ](ClO <sub>4</sub> ) <sub>2</sub>
N820	[Co(dmbip) <sub>2</sub> ](DDS) <sub>2</sub>
N823	[Co(dmbip) <sub>2</sub> ](OTf) <sub>2</sub>
Z316	[Co(phen) <sub>3</sub> ](TFSI) <sub>2</sub>
Z907	[Co(terpy) <sub>2</sub> ](ClO <sub>4</sub> ) <sub>2</sub>
	[Co(dobip) <sub>2</sub> ](ClO <sub>4</sub> ) <sub>2</sub>

### *Photoelectrochemical measurements*

Preliminary screening of the dyes N719, Z316 and Z907 with the electrolyte containing [Co(dbbp)<sub>2</sub>](ClO<sub>4</sub>)<sub>2</sub> showed that N719 gives inferior injection efficiencies and short circuit photocurrents  $J_{sc}$  in comparison with Z316 and Z907. The  $J_{sc}$  at  $95 \text{ W} \cdot \text{m}^{-2}$  of N719 was less than half of that of the heteroleptic (different ligands) dyes (Table 16). The superior performance of the heteroleptic dyes, i.e. Z316 and Z907, also manifests itself in the overall solar AM1.5 light-to-electric power conversion efficiencies. The I/V curves for N719, Z316 and Z907 have been compared in Figure 18. The power outputs of dyes Z316 and Z907 at the optimal power point exceed that of N719 by a factor of 2 (Table 16).

**Table 16.** Average photoelectrochemical data obtained at  $95 \text{ W} \cdot \text{m}^{-2}$  for DSSCs using  $[\text{Co}(\text{dbbip})_2](\text{ClO}_4)_2$   $0.09 \text{ M}$ ,  $[\text{Co}(\text{dbbip})_2](\text{ClO}_4)_3$   $0.01 \text{ M}$  in AN/EC (2:3) with three different sensitizers.

Sensitizer	$V_{\text{oc}}$ [mV]	$J_{\text{sc}}$ [ $\mu\text{A} \cdot \text{cm}^{-2}$ ]	$FF$ [-]	Efficiency [%]	Power output [ $\mu\text{W} \cdot \text{cm}^{-2}$ ]
N719	620	390	0.75	1.90	175
Z316	625	830	0.75	4.11	385
Z907	700	880	0.77	4.96	460

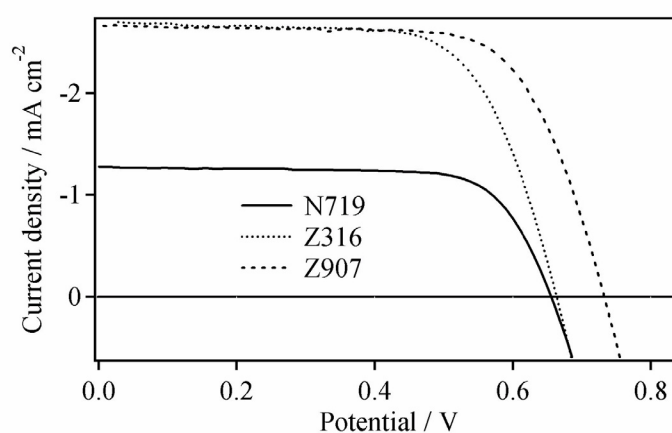


**Figure 18.** Example of I/V curves obtained with photovoltaic cells using different sensitizers, with an irradiance of  $300 \text{ W} \cdot \text{m}^{-2}$ . Electrolyte contained  $[\text{Co}(\text{dbbip})_2](\text{ClO}_4)_2$   $0.09 \text{ M}$  and its oxidized forms  $0.01 \text{ M}$ , in AN/EC (2:3).

Once the heteroleptic dyes Z316 and Z907 were identified as the best sensitizers, different cobalt complexes were screened to find the optimal electrolyte. It was found that  $[\text{Co}(\text{dbbip})_2](\text{ClO}_4)_2$  gave the best results. Table 17 illustrates some photoelectrochemical results obtained with six cobalt complexes used as redox mediators in open DSSCs.

**Table 17.** Photoelectrochemical data obtained at  $95 \text{ W} \cdot \text{m}^{-2}$  with different cobalt complexes and two heteroleptic dyes. Co(II) complexes 0.09 M, Co(III) complexes 0.01 M, in AN/EC (2:3).

Cobalt complex	$V_{oc}$ [mV]		$J_{sc}$ [ $\mu\text{A} \cdot \text{cm}^{-2}$ ]		$FF$ [-]		Efficiency [%]		Power output [ $\mu\text{W} \cdot \text{cm}^{-2}$ ]	
	Z316	Z907	Z316	Z907	Z316	Z907	Z316	Z907	Z316	Z907
[Co(bipy) <sub>3</sub> ](ClO <sub>4</sub> ) <sub>2</sub>	420	445	760	620	0.59	0.63	1.95	1.80	185	170
[Co(dmbip) <sub>2</sub> ](ClO <sub>4</sub> ) <sub>2</sub>	570	595	945	1020	0.64	0.71	3.64	4.56	345	425
[Co(dmbip) <sub>2</sub> ](DDS) <sub>2</sub>	560	605	425	460	0.74	0.71	1.83	2.07	175	195
[Co(dmbip) <sub>2</sub> ](OTf) <sub>2</sub>	690	610	375	730	0.71	0.69	2.39	3.25	215	305
[Co(phen) <sub>3</sub> ](TFSI) <sub>2</sub>	530	540	635	605	0.70	0.68	2.42	2.33	225	220
[Co(terpy) <sub>2</sub> ](ClO <sub>4</sub> ) <sub>2</sub>	405	400	395	405	0.61	0.47	1.02	0.80	95	75

For dmbip cobalt complexes, the same trend was observed as in Table 16 for [Co(dmbip)<sub>2</sub>](ClO<sub>4</sub>)<sub>2</sub> with Z316 and Z907, i.e. a higher open circuit voltage with Z907 and a more or less equal short circuit current, which lead to a higher overall efficiency. For the bipy, phen and terpy cobalt complexes, the efficiency was however better with Z316. The highest efficiency is observed with Z907 used in combination with [Co(dmbip)<sub>2</sub>](ClO<sub>4</sub>)<sub>2</sub>.

Differences between Table 17 and Table 3, page 83, come from the use of different mesoporous TiO<sub>2</sub> layers. The photocurrent is proportional to the dye surface density on semiconductor. A PC 139 mesoporous TiO<sub>2</sub> layer has a roughness factor of 134 per  $\mu\text{m}$  (see Table 7, page 39) and layers used for the cells reported in Table 17 were 3  $\mu\text{m}$  thick, giving a total roughness of 400. The PC 100 mesoporous TiO<sub>2</sub> layer, used in Table 3, has a roughness factor of 114  $\mu\text{m}$  and layers used for the cells reported in Table 3 were 2  $\mu\text{m}$  thick, giving a total roughness of 228. The ratio between 400 and 228 is roughly of the same order of magnitude as the ratio of the photocurrents reported in Table 17 and Table 3 for the same electrolyte. Finally, as the surface increases, the recombination between the electrons in the conduction band of TiO<sub>2</sub> and the oxidized dye molecules also increases, reducing the output voltage. With its higher specific surface, cells using PC 139 generate less voltage than those using PC 100. This explains why  $J_{sc}$  values are generally two times higher in Table 17 and  $V_{oc}$  50–80 mV lower.

As Z907 was identified as the most promising dye for cobalt complexes with bip ligands, new derivatives of Z907 with varying chain lengths were synthesized. These dyes, N820, N823, and N621, having two methyl, hexyl, and tridecanyl chains respectively, are described in Table 2, page 32. Figure 19 shows some I/V curves of  $[\text{Co}(\text{dbbip})_2](\text{ClO}_4)_2$  used with these dyes and Z907, and Table 18 shows comparison of some photovoltaic data for these cells.

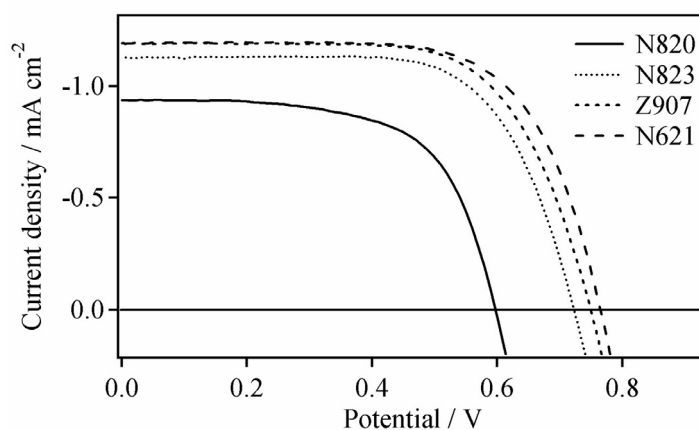


**Figure 19.** Example of I/V curves of DSSCs measured at  $300 \text{ W} \cdot \text{m}^{-2}$  with four different sensitizers and  $[\text{Co}(\text{dbbip})_2](\text{ClO}_4)_2$  0.09 M,  $[\text{Co}(\text{dbbip})_2](\text{ClO}_4)_3$  0.01 M,  $\text{LiClO}_4$  0.2 M, TBP 0.1 M, in AN/EC (2:3).

**Table 18.** Average photoelectrochemical data obtained at  $95 \text{ W} \cdot \text{m}^{-2}$  with four different sensitizers and electrolyte as described in Figure 19.

Sensitizer	$V_{\text{oc}}$ [mV]	$J_{\text{sc}}$ [ $\text{mA} \cdot \text{cm}^{-2}$ ]	$FF$ [-]	Efficiency [%]	Power output [ $\mu\text{W} \cdot \text{cm}^{-2}$ ]
N820	560	0.90	0.75	3.99	370
N823	675	1.30	0.74	6.70	620
Z907	710	1.30	0.69	6.74	630
N621	725	1.35	0.72	7.31	680

Amongst these four dyes, all heteroleptic and differing only in their chain length, N621, with two tridecanyl chains, performed best. For further discussion on these sensitizers, see “Alkyl chains length influence”, page 120.

### *Electron transfer dynamics*

[Co(dbip)<sub>2</sub>](ClO<sub>4</sub>)<sub>2</sub> used with sensitizer N719 was characterized kinetically using laser flash photolysis and compared with the classical triiodide/iodide couple, N719 being the dye of choice with this latter couple. Electron transfer processes in DSSC have already been mentioned in “Electron transfer dynamics”, page 24. These electron transfer processes are summarized here above for a better understanding.



Figure 20 shows the results from the nanosecond time resolved laser experiments. In the absence of cobalt (II)/(III) redox electrolyte, the decrease of the absorption signal reflects the dynamics of recombination of the conduction band electrons with the oxidized dye (Eq. 4.22). The kinetics of the oxidized dye transient absorption decay could be well fitted by a single exponential, with a rate constant  $k_b = 4.2 \cdot 10^3 \text{ s}^{-1}$ .

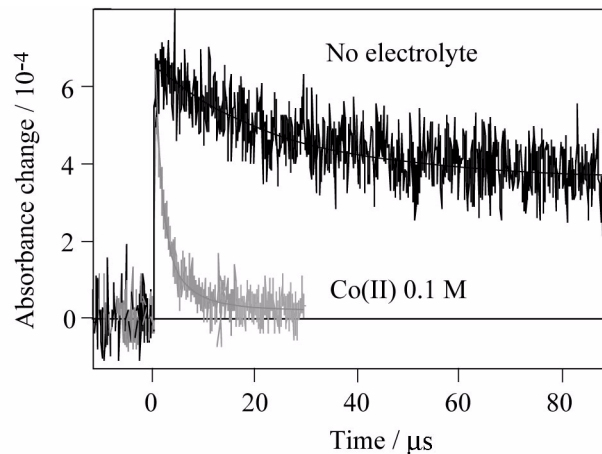


**Figure 20.** Transient absorbance decay kinetics of the oxidized state of N719 ( $S^+$ ) adsorbed on a  $TiO_2$  nanocrystalline film in the presence and absence of  $[Co(dbip)_2](ClO_4)_2$  0.1 M in AN/EC (2:3) solvent mixture. Absorbance changes were measured at a probe wavelength of 620 nm, employing 510 nm laser excitation (5 ns fwhm pulse duration,  $40 \mu J \cdot cm^{-2}$  pulse fluence).

In the presence of  $[Co(dbip)_2]^{2+}$ , the decay of the oxidized dye signal was strongly accelerated, indicating that the recombination is efficiently intercepted by the mediator. The temporal behavior of the  $S^+$  transient absorption was found again to correspond to a simple exponential. In this case, however, an increase of the laser intensity by nearly two orders of magnitude did not cause any significant change in the decay rate. From this observation it is inferred that the kinetics of the interception reaction (Eq. 4.23) is clearly independent from the recombination process (Eq. 4.22) and is indeed first-order in  $S^+$  concentration. In the presence of 0.1 M  $[Co(dbip)_2]^{2+}$ , the rate constant for oxidation of the mediator by the oxidized states  $S^+$  of the sensitizer was determined to be  $k_m = 5.0 \cdot 10^5 s^{-1}$ . This value is about three times lower than the reciprocal half reaction time  $1/\tau_{1/2} = 1.7 \cdot 10^6 s^{-1}$  of the dye ground state recovery measured with 0.1 M *tert*-butylammonium iodide.<sup>[12]</sup>

Figure 21 compares N719 with Z907, a heteroleptic dye. The transient absorbance signal measured at  $\lambda = 630$  nm monitors the concentration of the oxidized sensitizer species produced on photoinduced electron injection into  $TiO_2$  conduction band.

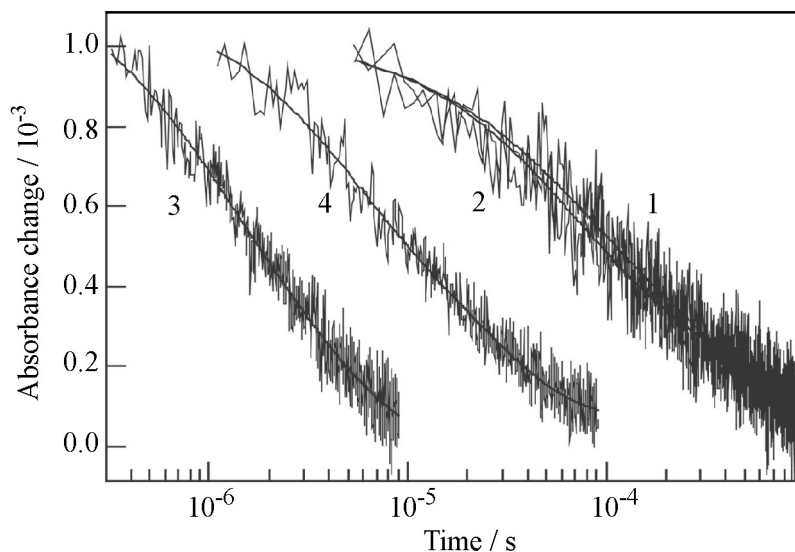


**Figure 21.** Time course of the transient absorbance changes obtained on nanosecond pulsed laser excitation ( $\lambda = 510$  nm, 5 ns fwhm pulse duration,  $30 \mu\text{J} \cdot \text{cm}^{-2}$  pulse fluence) of dye sensitizer N719 (traces 1 and 3) and Z907 (traces 2 and 4) adsorbed on mesoporous  $\text{TiO}_2$  films. Transient absorbance signals were measured at  $\lambda = 630$  nm in the presence of pure AN/EC (2:3), traces 1 and 2, or with  $[\text{Co}(\text{dbbip})_2](\text{ClO}_4)_2$  0.1 M, traces 3 and 4.

In the absence of the mediator, the decay of the signal recorded under open circuit conditions was solely due to recombination. The kinetics of this process were quite similar for dyes N719 and Z907, with a  $\text{S}^+$  half reaction time of the order of  $\tau_{1/2} = 100 \mu\text{s}$ , as seen in Figure 20. As expected, the addition of the mediator  $[\text{Co}(\text{dbbip})_2](\text{ClO}_4)_2$  0.1 M reduced the lifetime  $\tau$  of the oxidized species intercepting the above charge-recombination process. Surprisingly, the kinetics of the dye regeneration were found to be much faster for sensitizer N719 ( $\tau_{1/2} \approx 2 \mu\text{s}$ ) than for the dye Z907 ( $\tau_{1/2} \approx 10 \mu\text{s}$ ). Although decay kinetics could not be described accurately by simple exponentials, the quantum yield  $\Phi_r$  for dye cation interception by the mediator can be approximated by Eq. 4.25, where  $k_r$  is the first-order rate constant for the reduction of the sensitizer's oxidized species by the mediator, and  $k_b$  the rate constant for recombination from the conduction band to the same dye cations.

$$\Phi_r = \frac{k_r}{k_r + k_b} \quad (4.25)$$



Assuming in a crude approximation that  $k_b = 1/\tau_{1/2} \approx 4 \cdot 10^3 \text{ s}^{-1}$ ,  $k_r(\text{N719}) = 1/\tau_{1/2}(\text{N719}) \approx 5 \cdot 10^5 \text{ s}^{-1}$  and  $k_r(\text{Z907}) = 1/\tau_{1/2}(\text{Z907}) \approx 10^5 \text{ s}^{-1}$ , dye regeneration quantum yields of  $\Phi_r(\text{N719}) \approx 0.99$  and  $\Phi_r(\text{Z907}) \approx 0.91$  can be estimated for the two sensitizers. These results show that N719 suffers neither from fast recombination nor from reduced interception efficiency. Kinetic parameters deduced from laser experiments therefore cannot be invoked to explain the lower photovoltaic performance of this sensitizer compared to the amphiphilic dye Z907.

### *Discussion*

Heteroleptic complexes like Z907 or N621 carry two long alkyl chains attached at 4,4'-positions of the 2,2'-bipyridine ligand. These groups may sterically hinder the approach of the cobalt complex, which has four butyl chains of its own. Complex N719 does not bear any alkyl chains and its regeneration by Co(II) is indeed kinetically favored. The increase in photocurrent however obtained using Z907 instead of N719 can be explained as follows. Adsorption of N719 onto the  $\text{TiO}_2$  surface imparts a negative  $\zeta$  potential to the nanocrystals.<sup>[12]</sup> This increases the coulombic attraction between the adsorbed sensitizer and the positively charged cobalt complexes, hindering the redox species mobility within the cell.<sup>[13]</sup> Moreover, the electrostatic attraction between N719 and the redox species is expected to increase with the positive charge density on the cobalt complex, sterically hindering the oxidized dye regeneration. The effect of Co(III) concentration on the sensitizer regeneration rate is discussed in more details in "Influence of the mediator concentration and the oxidation degree on the electron transfer dynamics", page 141. By contrast, the heteroleptic complexes Z316 and Z907 carry two negative charges less than N719. In the case of these heteroleptic dyes, the ion-pairing effect is then reduced and the current and voltage can be higher.

### *Conclusions*

Of all cobalt complexes tested,  $[\text{Co}(\text{dbbip})_2](\text{ClO}_4)_2$  was identified as the most promising, (see "Photoelectrochemical screening of cobalt complexes", page 82). The best results are obtained with heteroleptic sensitizers in place of the classical N719 dye.

### 4.3. Alkyl chains length influence

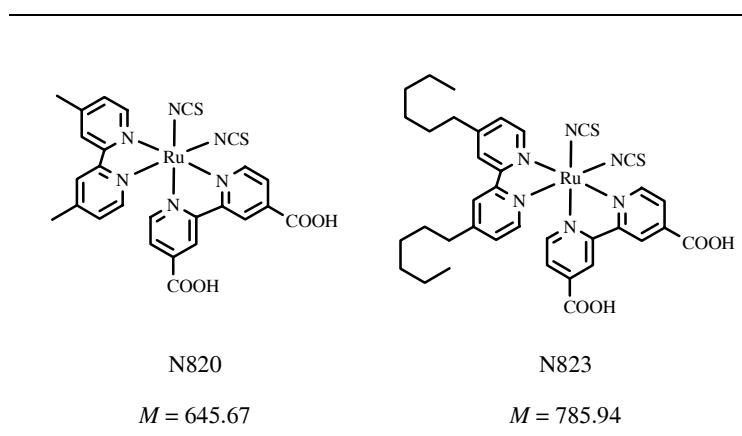
#### *Introduction*

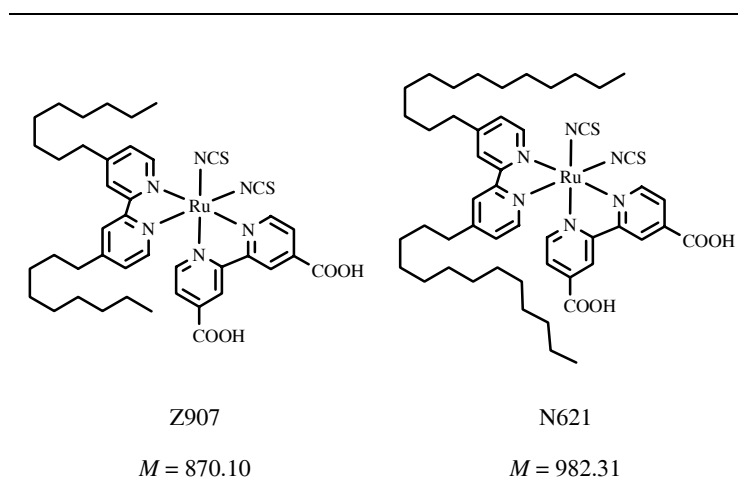
As was seen in “Sensitizer - electrolyte interactions”, page 111, the molecular structure of the dye has an important impact on the photovoltaic efficiency of a DSSC. Replacing a homoleptic dyes like N719 by heteroleptic ones like Z316 in cells with cobalt complexes as a redox mediator can double the photocurrent. In Figure 18, one also saw that the open circuit potential differed greatly with varying substituents of the sensitizer ligands. Figure 19 clearly demonstrated this phenomenon, with four dyes differing only in their alkyl chain length. In this chapter, the influence of the dye chain length will be studied in more detail along with the influence of the cobalt complex chain length.

#### *Photoelectrochemical measurements*

An electrolyte composed of  $[\text{Co}(\text{dbbip})_2](\text{ClO}_4)_2$  0.09 M,  $[\text{Co}(\text{dbbip})_2](\text{ClO}_4)_3$  0.01 M,  $\text{LiClO}_4$  0.2 M, TBP 0.1 M in AN/EC (2:3) was chosen for N820, N823, Z907 and N621. The chemical structures and molecular weights of these dyes have been given in Table 19.

**Table 19.** Structures of the four sensitizers used to study the alkyl chain length influence.



**Table 19.** Structures of the four sensitizers used to study the alkyl chain length influence.

The results of the photoelectrochemical measurements are given in Table 20.

**Table 20.** Average photoelectrochemical data obtained at  $95 \text{ W} \cdot \text{m}^{-2}$  with the four different sensitizers and  $[\text{Co}(\text{dbbip})_2](\text{ClO}_4)_2$  0.09 M,  $[\text{Co}(\text{dbbip})_2](\text{ClO}_4)_3$  0.01 M,  $\text{LiClO}_4$  0.2 M, TBP 0.1 M, in AN/EC (2:3).

Sensitizer	$V_{oc}$ [mV]	$J_{sc}$ [ $\text{mA} \cdot \text{cm}^{-2}$ ]	$FF$ [-]	Efficiency [%]	Power output [ $\mu\text{W} \cdot \text{cm}^{-2}$ ]	$IPCE$ at 540 nm [%]
N820	560	0.90	0.75	3.99	370	47
N823	675	1.30	0.74	6.70	620	72
Z907	710	1.30	0.69	6.74	630	75
N621	725	1.35	0.72	7.31	680	76

From Table 20, one clearly sees that increasing the chain length from e.g. C1 to C13, has a beneficial impact on the photovoltaic parameters, i.e. current and voltage, which leads to an increased overall efficiency and power output level.

The increasing performances are partially due to a reduction of the dark current associated with chain length, as shown in Figure 22, where the dark currents for the four dyes have been reported as a function of the applied potential.

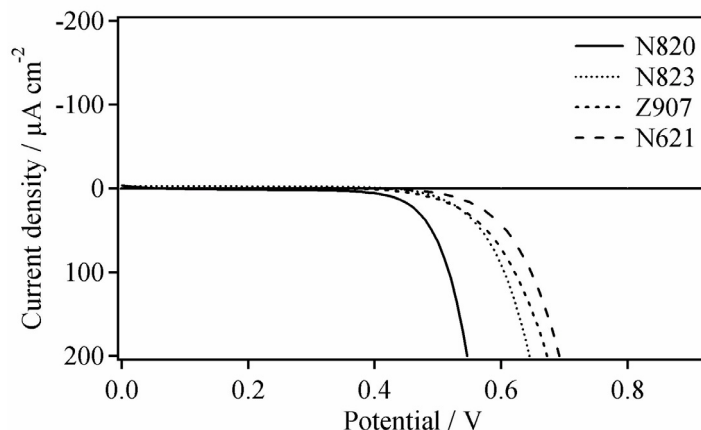


**Figure 22.** Example of dark currents of DSSCs measured with four different dyes and  $[\text{Co}(\text{dbbip})_2](\text{ClO}_4)_2$  0.09 M,  $[\text{Co}(\text{dbbip})_2](\text{ClO}_4)_3$  0.01 M,  $\text{LiClO}_4$  0.2 M, TBP 0.1 M, in AN/EC (2:3).

As discussed in page 119, long alky chains may sterically hinder the approach of the cobalt complex, reducing the probability of electron recapture by the oxidized cobalt complex. The longer the alkyl chain, the lower the probability of electron recapture. The dark currents reported in Figure 22 illustrate this behavior.

Apart from the sensitizers varying chain length, the chain length of the cobalt complex itself may have an impact on the photovoltaic parameters. Hence the influence of the chain length for the cobalt complexes was monitored with photoelectrochemical measurements. Other cobalt complexes with octyl chains,  $[\text{Co}(\text{dobip})_2](\text{ClO}_4)_2$  and  $[\text{Co}(\text{dobip})_2](\text{ClO}_4)_3$ , were synthesized according to the procedure described page 34 - 36. The photoelectrochemical measurements of electrolytes containing either  $[\text{Co}(\text{dmbip})_2](\text{ClO}_4)_2$ ,  $[\text{Co}(\text{dbbip})_2](\text{ClO}_4)_2$  or  $[\text{Co}(\text{dobip})_2](\text{ClO}_4)_2$  gave the results shown in Figure 23 and Table 21.

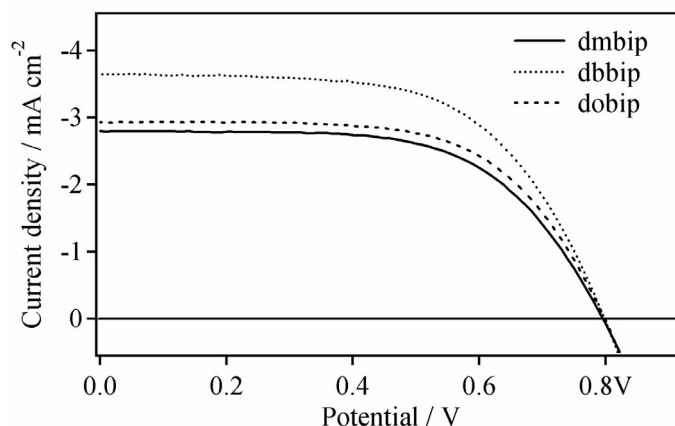


**Figure 23.** Example of I/V curves of DSSCs measured at  $300 \text{ W} \cdot \text{m}^{-2}$  with Z907 and three different electrolytes based on cobalt bip complexes. All electrolytes were made of  $[\text{Co}(\text{dx}(\text{bip})_2)(\text{ClO}_4)_2]$  0.09 M,  $[\text{Co}(\text{dx}(\text{bip})_2)(\text{ClO}_4)_3]$  0.01 M,  $\text{LiClO}_4$  0.2 M, TBP 0.1 M, in AN/EC (2:3). x in  $[\text{Co}(\text{dx}(\text{bip})_2)]$  being either m (methyl), b (butyl), or o (octyl).

**Table 21.** Average photoelectrochemical data obtained at  $95 \text{ W} \cdot \text{m}^{-2}$  with Z907 and three different electrolytes based on cobalt bip complexes. Electrolytes are the same as described in Figure 23.

bip group	$V_{\text{oc}}$ [mV]	$J_{\text{sc}}$ [ $\text{mA} \cdot \text{cm}^{-2}$ ]	$FF$ [-]	Efficiency [%]	Power output [ $\mu\text{W} \cdot \text{cm}^{-2}$ ]	$IPCE$ at 540 nm [%]
dmbip	740	1.29	0.67	6.68	635	68
dbbip	755	1.32	0.67	7.06	670	69
dobip	760	1.31	0.65	6.75	640	66

The chain length reaches a maximum photovoltaic performance with C4 and then tails off. As has already been seen with the dyes, increasing the chain length lead to better photovoltaic results. The same applies to the cobalt complexes, with the difference that the redox molecules must diffuse within the cell between the counter electrode and the photoelectrode. There is no beneficial effect for chain length greater than C4 due to the loss of mobility in the electrolyte.

### Electron transfer dynamics

The influence of the four dyes N820, N823, Z907, and N621, on the recombination and regeneration rates was studied by laser flash photolysis. To study the recombination, measurements were carried out using pure MPN as a solvent instead of an electrolyte. Figure 24 displays the time course of the transient absorbance changes for each dye. The kinetics of the recombination changed as the chain length increased, the fastest being observed with dye N820 and the slowest with N621, having the shortest and longest alkyl chains, respectively. Comparison between the recombination and regeneration kinetics of each dye gives an idea of how the sensitizer should behave in a DSSC.

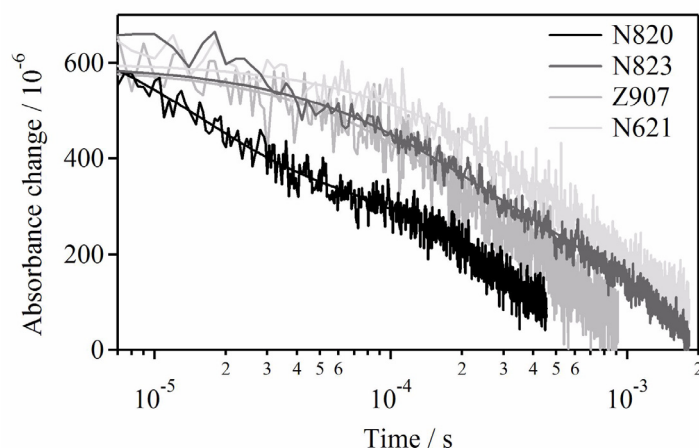


**Figure 24.** Time course of the transient absorbance changes obtained on nanosecond pulsed laser excitation ( $\lambda = 532$  nm, 15 ns fwhm pulse duration,  $30 \mu\text{J} \cdot \text{cm}^{-2}$  pulse fluence) of dye sensitizers N820, N823, Z907, and N621 adsorbed on mesoporous  $\text{TiO}_2$  films. Transient absorbance signals were measured at  $\lambda = 630$  nm in the presence of pure MPN. The behavior of N820 up to  $10^{-4}$  is due to dye instability. Nevertheless the general trend with N820 is acceptable.

To study the dyes regeneration rates, an electrolyte composed of  $[\text{Co}(\text{dbbip})_2](\text{ClO}_4)_2$  0.1 M, in MPN was chosen. Figure 25 shows the time course of the transient absorbance changes for the four dyes. Using this electrolyte, Z907 showed the fastest regeneration rate of the dye ground state.

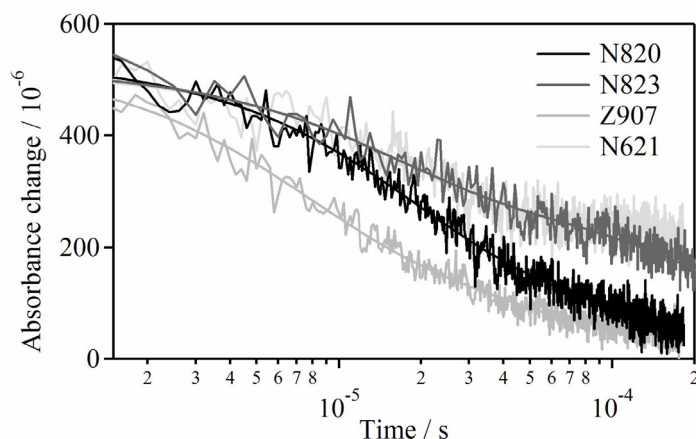


**Figure 25.** Time course of the transient absorbance changes obtained on nanosecond pulsed laser excitation ( $\lambda = 532$  nm, 15 ns fwhm pulse duration,  $30 \mu\text{J} \cdot \text{cm}^{-2}$  pulse fluence) of dye sensitizers N820, N823, Z907, and N621 adsorbed on mesoporous  $\text{TiO}_2$  films. Transient absorbance signals were measured at  $\lambda = 630$  nm in the presence of  $[\text{Co}(\text{dbbip})_2](\text{ClO}_4)_2$  0.1 M in MPN.

Table 22 compiles the half reaction times of the recombination and regeneration of each dye. N820 had the fastest recombination process, the value of which is close to that measured for regeneration, making this dye the least effective for DSSC applications. The dye N823 demonstrated slower recombination times with respect to a larger regeneration time. In DSSC's, N823 gave better results than N820. The Z907, having approximately the same recombination time as N823 but a greater difference with its regeneration time, gave slightly better efficiencies when used in DSSC's. Finally, N621 had the greatest recombination time and difference between recombination and regeneration times. This dye effectively gave the best efficiencies with the  $[\text{Co}^{\text{III/II}}(\text{dbbip})_2]$  redox couple.

**Table 22.** Half reaction time  $\tau_{1/2}$  for sensitizers N820, N823, Z907, and N621, with pure MPN solvent and with an electrolyte containing  $[\text{Co}(\text{dbbip})_2](\text{ClO}_4)_2$  0.1 M in MPN. Efficiencies are reported from Table 20.

Sensitizer	$\tau_{1/2}$ [ $\mu\text{s}$ ] (without electrolyte)	$\tau_{1/2}$ [ $\mu\text{s}$ ] (with $[\text{Co}(\text{dbbip})_2]^{2+}$ 0.1 M)	Efficiency [%]
N820	50	20	3.99
N823	250	70	6.70
Z907	280	22	6.74
N621	600	70	7.31

#### 4.4. Co-grafting sensitizer and co-adsorbents

##### *Introduction*

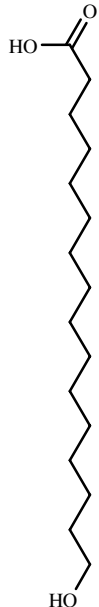
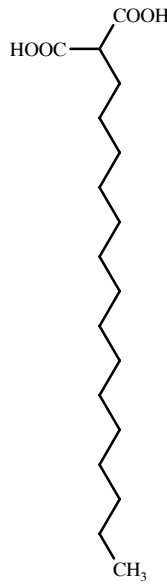
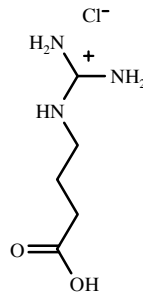
It has been shown that a remarkable increase in the photovoltaic performance can be achieved by co-grafting hexadecylmalonic acid with Z907 sensitizer onto nanocrystalline  $\text{TiO}_2$  films.<sup>[14]</sup> Co-grafting of the two amphiphilicities resulted in the formation of a mixed monolayer more tightly packed than when the sensitizer is absorbed alone.

Usually, increasing the open circuit potential reduces the injection rate by diminishing the driving force between the energy level of the excited state of the dye and the semiconductor conduction band. Nevertheless, the main limiting factor when using cobalt redox couple is the diffusion of the species within the electrolyte (see “Photoelectrochemical screening of cobalt complexes”, page 82). As the limiting factor is the cobalt ions diffusion, using co-grafting of sensitizer and co-adsorbents to tune the flatband potential of the photoanode should not negatively affect the DSSC efficiency. Consequently, co-adsorption of molecules increasing the flatband potential should benefit a cell based on cobalt complexes.

Co-absorbers used here are presented in Table 23, with their abbreviated names and molecular weights.



**Table 23.** Chemical structures of the co-adsorber used to modify the TiO<sub>2</sub> flatband potential, with their names, abbreviated names, and molecular weights.

Chemical structure			
Compound's name	16-Hydroxyhexadecanoic acid	Hexadecylmalonic acid	4-Guanidinobutyrate chloride
Abbreviation	HHDA	HDMA	GB
Molecular weight	272.42	314.46	182.63

### ***Co-grafting Z907 with HDMA, HHDA or GB***

The dye Z907 and a standard electrolyte composed of [Co(dbbip)<sub>2</sub>](ClO<sub>4</sub>)<sub>2</sub> 0.09 M, Co(dbbip)<sub>2</sub>](ClO<sub>4</sub>)<sub>3</sub> 0.01 M, LiClO<sub>4</sub> 0.2 M, and TBP 0.1 M in AN/EC (2:3) were used for all experiments. HDMA, HHDA and GB were added to different Z907 solutions with a molar ratio of 1:1. Table 24 gives some results obtained with the different dye solutions.

**Table 24.** Average photoelectrochemical data obtained at  $95 \text{ W} \cdot \text{m}^{-2}$  with Z907 and Z907 + HDMA (1:1), Z907 + HHDA (1:1) and Z907 + GB (1:1). The electrolyte was made of  $[\text{Co}(\text{dbbip})_2](\text{ClO}_4)_2$  0.09 M,  $[\text{Co}(\text{dbbip})_2](\text{ClO}_4)_3$  0.01 M,  $\text{LiClO}_4$  0.2 M, TBP 0.1 M, in AN/EC (2:3).

Dye solution	$V_{\text{oc}}$ [mV]	$J_{\text{sc}}$ [mA · cm <sup>-2</sup> ]	$FF$ [-]	Efficiency [%]	Power output [μW · cm <sup>-2</sup> ]
Z907	765	1.35	0.70	7.55	710
Z907 + HDMA	780	1.15	0.71	6.78	630
Z907 + HHDA	775	1.40	0.71	7.91	740
Z907 + GB	800	1.25	0.71	7.58	710

A comparison of the photovoltaic results using the different dye solutions clearly shows the positive effect of co-adsorbers. As expected, there is a shift of the flatband potential, increasing the  $V_{\text{oc}}$  by +10 mV in the case of HHDA and up to +35 mV with GB. The effect of co-adsorber on the current is not so clear, with only HHDA showing a positive effect. For HDMA, the increased photovoltage combined with a significant decrease in the current leads to a lower efficiency and output power. On the contrary, both the  $V_{\text{oc}}$  and  $J_{\text{sc}}$  are increased with HHDA, improving the efficiency by 4.5%. For GB, the increase of  $V_{\text{oc}}$  is compensated by a small decrease of  $J_{\text{sc}}$ .

The higher current observed with HHDA may be explained by an increase of the electron diffusion in the  $\text{TiO}_2$ . This enhanced diffusion comes from a reduction of the density of traps in the semiconductor. In the diffusion model, electrons travel through the events of trapping and de-trapping with thermal excitation. It has been observed that the diffusion coefficient  $D$  was increased by dye adsorption, as well as by benzoic acid adsorption.<sup>[15]</sup> Adsorption of dye reduces the density of electrons in traps by hindering the trap access. Adsorption of co-adsorber further decrease the trap access, allowing more electrons to travel faster in the  $\text{TiO}_2$ .

Co-adsorber on the surface acts as a barrier towards electron recapture reactions. Long chains present in the HHDA co-adsorber increase the distance  $d$  between the redox electrolyte and the electrons in the  $\text{TiO}_2$ . If  $d$  increases then, accordingly to the Gamov equation (Eq. 4.26), the electron transfer rate  $k_{\text{el}}$  will decrease.

$$k_{\text{el}} \propto e^{-\beta \cdot (d - d_0)} \tag{4.26}$$

Co-adsorbers also act like spacers between dye molecules, hindering electron hopping. All these effects tend to reduce the dark current in a DSSC, as shown in Figure 26.

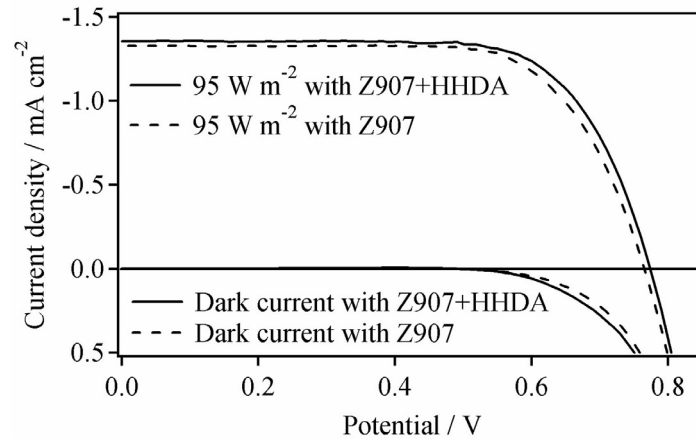


**Figure 26.** Influence of co-grafting Z907 with HHDA on the dark current and the photocurrent at  $95 \text{ W} \cdot \text{m}^{-2}$ . Electrolyte consisted in  $[\text{Co}(\text{dbbip})_2](\text{ClO}_4)_2$  0.09 M,  $[\text{Co}(\text{dbbip})_2](\text{ClO}_4)_3$  0.01 M,  $\text{LiClO}_4$  0.2 M, TBP 0.1 M, in AN/EC (2:3).

As a decrease of the dark current also decreases the reversed saturation current  $I_s$  one sees from Eq. 4.27 that this has the effect of increasing the  $V_{oc}$ , as observed in Table 24 and in Figure 26.

$$V_{oc} \cong V_t \cdot \ln\left(\frac{I_{ph}}{I_s}\right), \quad (4.27)$$

with  $V_t$  being the thermal voltage (see Eq. 2.3, page 42).

The lower current densities seen for HDMA and GB may result from the intrinsic nature of these compounds. HDMA has two carboxylic acid groups, both able to bind with the  $\text{TiO}_2$  surface. The competition between this molecule and the dye molecule to bind to the surface is stronger than in the case of HHDA or GB, which have only one carboxylic acid group each. Hence the dye density on the surface is lower with HDMA and the gain of co-adsorbence is lost. In the case of HHDA, the lower dye density is balanced by the increase of current and voltage resulting from its presence on the  $\text{TiO}_2$ . Despite the lower adsorption energy for the GB this relatively small molecule may still compete with the dye as a result of its small size.

## 4.5. Silver(I) addition impact

### *Introduction*

It has been shown that Ag(I) ions, incorporated into the dye surface layer of a solid-state DSSC, significantly improve the current-voltage characteristics.<sup>[16]</sup> Silver ions introduced into a dye solution are incorporated into the dye surface layer during the dye uptake. By means of ATR-FTIR spectroscopy and UV/Vis, it has been shown that the silver ions coordinate to the ambidentate thiocyanate ligand. The silver modification of the dye was found to increase the dye uptake by 38% and offers therefore a simple method to increase light harvesting whilst still using a thin TiO<sub>2</sub> layer. The increased short circuit currents upon silver modification were attributed to the increased dye uptake. Silver ions were found to function as a bridging element between two thiocyanate ligands. The dye interaction via the silver ions is thought to assist the dye assembly on the TiO<sub>2</sub> surface. Accordingly the smaller size of the dimer allows more dye molecules to be adsorbed. The significant increase of  $V_{oc}$  in the presence of silver ions was assigned to a decreased interfacial charge recombination and a greater light harvesting. The high density of the dye molecule layer bearing the silver cations is expected to block the electron recapture from the TiO<sub>2</sub> by the redox couple.<sup>[16]</sup>

### *Cell preparation*

The DSSC incorporating silver were prepared exactly in the same manner as “standard” cells. The only difference being the dye solution. Instead of immersing the photoelectrode in pure sensitizer solution made of dye  $3-5 \cdot 10^{-4}$  M in ethanol or acetonitrile/tert-butanol (1:1) solvents, 0.5 M dye equivalent of silver nitrate is added to the solution. A solution of AgNO<sub>3</sub> 0.02 M in acetonitrile was prepared and 15  $\mu$ L of it was added to 2 mL of dye solution  $3 \cdot 10^{-4}$  M.

### *Photoelectrochemical measurements*

The first cells were prepared with silver modified Z907 and [Co(dbbip)<sub>2</sub>](ClO<sub>4</sub>)<sub>2</sub> 0.09 M, [Co(dbbip)<sub>2</sub>](ClO<sub>4</sub>)<sub>3</sub> 0.01 M in AN/EC (2:3) and compared with control standard cells. Subsequent cells used the same electrolyte, but with addition of LiClO<sub>4</sub> 0.2 M and TBP 0.1 M. The addition of these additives has proven beneficial (see “Additives”, page 144) and so they were also tested here. Photoelectrochemical data is reported in Table 25 for an incident light intensity of  $15 \text{ W} \cdot \text{m}^{-2}$  and in Table 26 for  $95 \text{ W} \cdot \text{m}^{-2}$ .

**Table 25.** Average photoelectrochemical data obtained at  $15 \text{ W} \cdot \text{m}^{-2}$  for DSSCs with Z907 with and without  $\text{AgNO}_3$  and  $[\text{Co}(\text{dbbip})_2](\text{ClO}_4)_2$  0.09 M,  $[\text{Co}(\text{dbbip})_2](\text{ClO}_4)_3$  0.01 M with and without  $\text{LiClO}_4$  0.2 M and TBP 0.1 M. *IPCE* are given at 540 nm.

Sensitizer solution	Electrolyte	$V_{oc}$ [mV]	$J_{sc}$ [ $\mu\text{A} \cdot \text{cm}^{-2}$ ]	<i>FF</i> [-]	Efficiency [%]	Power output [ $\mu\text{W} \cdot \text{cm}^{-2}$ ]	<i>IPCE</i> [%]
Pure Z907	Co(II)/Co(III)	610	115	0.77	3.33	50	45
Z907 + $\text{Ag}^+$	Co(II)/Co(III)	630	125	0.72	3.46	55	40
Pure Z907	Co(II)/Co(III) + $\text{Li}^+$ + TBP	675	215	0.73	6.61	100	70
Z907 + $\text{Ag}^+$	Co(II)/Co(III) + $\text{Li}^+$ + TBP	685	225	0.73	7.04	110	70

**Table 26.** Average photoelectrochemical data obtained at  $95 \text{ W} \cdot \text{m}^{-2}$  for DSSCs with Z907 with and without  $\text{AgNO}_3$  and  $[\text{Co}(\text{dbbip})_2](\text{ClO}_4)_2$  0.09 M,  $[\text{Co}(\text{dbbip})_2](\text{ClO}_4)_3$  0.01 M with and without  $\text{LiClO}_4$  0.2 M and TBP 0.1 M. *IPCE* are given at 540 nm.

Sensitizer solution	Electrolyte	$V_{oc}$ [mV]	$J_{sc}$ [ $\text{mA} \cdot \text{cm}^{-2}$ ]	<i>FF</i> [-]	Efficiency [%]	Power output [ $\mu\text{W} \cdot \text{cm}^{-2}$ ]	<i>IPCE</i> [%]
Pure Z907	Co(II)/Co(III)	700	0.75	0.74	4.12	390	45
Z907 + $\text{Ag}^+$	Co(II)/Co(III)	715	0.80	0.72	4.39	415	40
Pure Z907	Co(II)/Co(III) + $\text{Li}^+$ + TBP	770	1.25	0.67	6.84	650	70
Z907 + $\text{Ag}^+$	Co(II)/Co(III) + $\text{Li}^+$ + TBP	760	1.30	0.68	7.12	675	70

For the two different electrolytes, the changes upon silver addition are the same. The addition of silver ions to the dye solution allows an increase in the short circuit current of  $10 \mu\text{A} \cdot \text{cm}^{-2}$  at  $15 \text{ W} \cdot \text{m}^{-2}$  and  $50 \mu\text{A} \cdot \text{cm}^{-2}$  at  $95 \text{ W} \cdot \text{m}^{-2}$ . It also has a small impact on the photovoltage, increasing it by ca. 15 mV. The net result is an overall gain in efficiency of 5%. This trend is the same as has been reported for solid-state DSSC.<sup>[16]</sup>

The use of silver(I) in DSSC with cobalt redox couple increases the photovoltaic parameters, including maximal output power, voltage, current and thus efficiency.

## 4.6. Photoanode - electrolyte interactions

### *Introduction*

The photovoltaic performances of cobalt based solar cells were found to be strongly influenced by the structure of the mesoporous TiO<sub>2</sub> films. The photoanode has a triple-layered structure, in which the first layer is a compact blocking TiO<sub>2</sub> film, the second a transparent TiO<sub>2</sub> layer with particles of about 20 nm, and the third a scattering film with large TiO<sub>2</sub> particles of 400 nm of diameter (see “Photoelectrodes”, page 37).

### *Semiconductor - electrolyte interaction*

For the experiments described hereafter, PC 100 mesoporous layers and HPW 400c diffusive layers were used. As shown in Table 27 and in Figure 27, the *IPCE* values and consequently the photocurrent decrease with increasing thickness of the nanocrystalline TiO<sub>2</sub> layer. Apparently, for thicker films a significant fraction of the injected electrons recombine before reaching the current collector. Enhanced recombination is also responsible for the decreased open circuit photovoltage  $V_{oc}$ , though surprisingly, the fill factor (*FF*) values appear to change only slightly for the different film thicknesses. However, the interpretation should be made with caution, as the fill factor reflects the relative losses due to internal cell resistance and hence is affected by both  $J_{sc}$  and  $V_{oc}$ . On the other hand, increasing the TiO<sub>2</sub> scattering layer thickness has a beneficial effect on the current, which translates into an increase of the efficiency.

**Table 27.** Average photoelectrochemical data at  $95 \text{ W} \cdot \text{m}^{-2}$  for varying thicknesses of TiO<sub>2</sub> layers with Z907 and [Co(dbpip)<sub>2</sub>](ClO<sub>4</sub>)<sub>2</sub> 0.185 M, 5% oxidized in AN/EC(2:3) [a] Transparent mesoporous PC 100 layer (particles Ø 18 nm). [b] Scattering HPW 400c layer (particles Ø 400 nm). *IPCE* are given at 540 nm.

Layer 1 <sup>[a]</sup> [µm]	Layer 2 <sup>[b]</sup> [µm]	$V_{oc}$ [mV]	$J_{sc}$ [mA · cm <sup>-2</sup> ]	<i>FF</i> [-]	Efficiency [%]	<i>IPCE</i> [%]
2	2	625	1.10	0.65	4.6	70
2	4	590	1.35	0.65	5.5	68
4	2	565	1.15	0.65	4.4	59
4	4	560	1.25	0.70	5.0	59
6	2	590	1.00	0.75	4.6	48
10	2.5	570	0.75	0.65	3.0	38

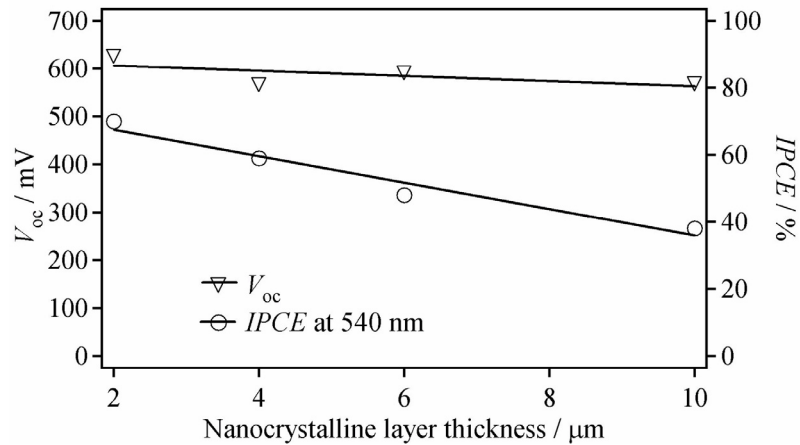


**Figure 27.** Influence of the nanocrystalline layer thickness on the open circuit voltage measured under  $95 \text{ W} \cdot \text{m}^{-2}$  and on the *IPCE*. Electrolyte and dye are the same as in Table 27.

### *TCO - electrolyte interaction*

Apart from this  $\text{TiO}_2$  - electrolyte interaction, another interaction between the electrolyte and the TCO of the photoelectrode has to be analyzed.

At the photoanode, the unwanted reduction of  $\text{Co(III)}$  to  $\text{Co(II)}$  at the transparent conductive glass (TCO, fluorine doped  $\text{SnO}_2$ ) may compete with the reaction at the counter electrode and therefore short circuit the current in the external circuit. In conventional DSSCs employing the triiodide/iodide redox couple, good performances can be achieved without the necessity of a blocking layer to coat the TCO prior to deposition of the porous nanocrystalline layer. These cells perform well because the rate of electron transfer from the  $\text{SnO}_2$  substrate to  $\text{I}_3^-$  is a very slow two electron process.<sup>[8]</sup> Evidence for  $\text{Co(III)}$  complex reduction on the  $\text{SnO}_2$  surface not covered by the compact  $\text{TiO}_2$  layer but exposed to the electrolyte is shown in Figure 28. The deposition of a compact  $\text{TiO}_2$  film on the conducting glass therefore had a beneficial effect on the I/V curves. Hence a compact underlayer is highly recommended when using cobalt complexes as redox mediators in liquid-electrolyte DSSC.

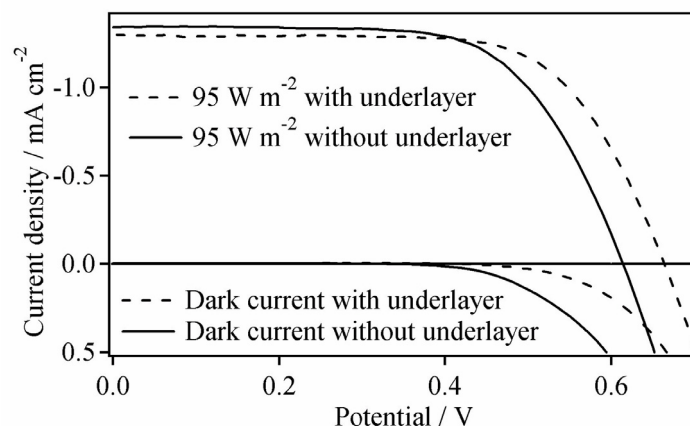


**Figure 28.** Influence of a blocking titanium oxide underlayer on the dark current and the photocurrent at  $95 \text{ W} \cdot \text{m}^{-2}$ . Sensitizer Z907 was used with  $[\text{Co}(\text{dbbip})_2](\text{ClO}_4)_2$  0.09 M and its oxidized form 0.01 M, in AN/EC (2:3).

The same conclusion was drawn by Cameron et al. using thin layer cells with a platinum coated counter electrode paired with an uncoated TCO electrode.<sup>[8]</sup> They explained that the reduction of Co(III), which represents a loss mechanism in DSSC, is more facile than oxidation of Co(II) at the TCO, due to electron tunnelling through the depletion layer formed at the TCO-electrolyte interface. They found a standard heterogeneous rate constant  $k^\circ$  of  $1.4 \cdot 10^{-6} \text{ cm} \cdot \text{s}^{-1}$  for the Co(III)/Co(II) couple. This value is more than two orders of magnitude higher than that of  $\text{I}_3^-/\text{I}^-$  couple, explaining why a blocking layer is necessary to prevent losses when using cobalt complexes.

#### 4.7. Counter electrode - electrolyte interactions

As seen above, the  $[\text{Co}^{\text{III/II}}(\text{dbbip})_2]$  redox couple exhibits reversible electrochemical behavior on  $\text{SnO}_2$ . The reduction of Co(III) to Co(II) should be fast enough to render the use of additional electrocatalysts, such as platinum, superfluous. To test this hypothesis, TCO glass with and without catalytic coatings of platinum were examined as counter electrodes. The I/V curves observed with untreated TCO glass showed a sigmoid shape indicating that the current is limited at low overvoltage by the interfacial charge-transfer resistance (Figure 29). As a result, poor fill factors were obtained with the plain  $\text{SnO}_2$  counter electrode and as can be seen depositing elec-



trocatalytic platinum on the  $\text{SnO}_2$  film led to a marked improvement in the I/V characteristics. Figure 29 also shows an I/V curve for electrocatalytic gold under the same conditions. The small drop in photocurrent ( $\sim 60 \mu\text{A} \cdot \text{cm}^{-2}$  at  $95 \text{ W} \cdot \text{m}^{-2}$ ) is compensated by an increase of the photovoltage ( $\sim 40 \text{ mV}$ ), giving the same efficiency. Gold is therefore a suitable catalyst. In the absence of an appropriate electrocatalyst, fluorine-doped tin dioxide cannot function adequately as counter electrode, despite the higher exchange current density for the  $[\text{Co}^{\text{III/II}}(\text{dbbip})_2]$  couple compared to the triiodide/iodide couple.

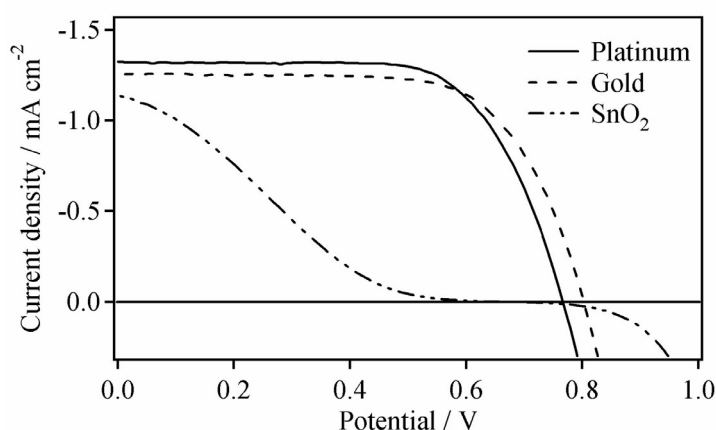


**Figure 29.** Influence of the electrocatalyst deposited on the counter electrode, measured under  $95 \text{ W} \cdot \text{m}^{-2}$ . Sensitizer Z907 was used with  $[\text{Co}(\text{dbbip})_2](\text{ClO}_4)_2$  0.09 M,  $[\text{Co}(\text{dbbip})_2](\text{ClO}_4)_3$  0.01 M,  $\text{LiClO}_4$  0.2 M, TBP 0.1 M, in AN/EC (2:3).

Cameron et al. also controlled the inefficiency of plain  $\text{SnO}_2$  as electrocatalyst, with standard heterogeneous rate constants  $k^\circ = 1.4 \cdot 10^{-6} \text{ cm} \cdot \text{s}^{-1}$  for F-doped  $\text{SnO}_2$  and  $k^\circ = 2.5 \cdot 10^{-4} \text{ cm} \cdot \text{s}^{-1}$  for platinum coated electrodes.<sup>[8]</sup> They also predicted higher voltages using gold over platinum as an electrocatalyst due to its higher rate constant.

Figure 30 shows the voltamograms for a gold and a platinum electrode recorded at a sweep rate of  $100 \text{ mV} \cdot \text{s}^{-1}$ . Cyclic voltammetry was carried out in a conventional three electrode setup, using either a gold or a platinum disc ( $A = 0.7 \text{ cm}^2$ ) working electrode in a de-oxygenated solution consisting of  $[\text{Co}(\text{dbbip})_2](\text{ClO}_4)_2$  2 mM and  $\text{LiClO}_4$  0.2 M in acetonitrile. An Ag/AgCl reference electrode was used. The voltamogram for gold is typical for a quasi-reversible behavior associated with rather slow electron transfer kinetics, with a peak separation of 72 mV, rather

than the 59 mV required for the reversibility. The peak separation measured using the platinum electrode was 219 mV.

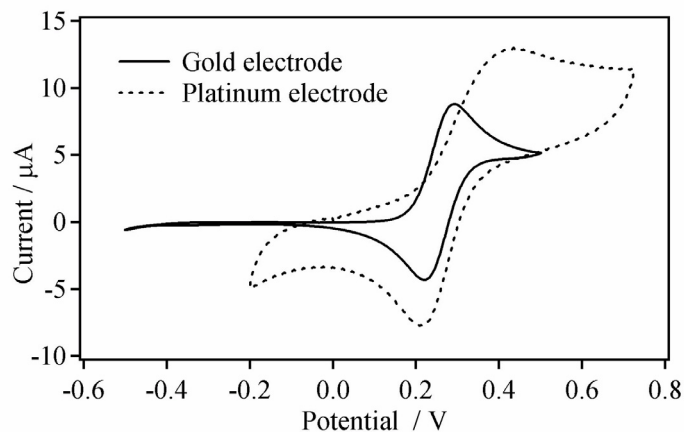


**Figure 30.** Cyclic voltammogram showing quasi-reversible behavior of the  $[\text{Co}(\text{dbbip})_2](\text{ClO}_4)_2$  system at either a gold or a platinum electrode ( $A = 0.7 \text{ cm}^2$ ). Electrolyte was composed of  $[\text{Co}(\text{dbbip})_2](\text{ClO}_4)_2$  2 mM and  $\text{LiClO}_4$  0.2 M in acetonitrile. Sweep rate:  $100 \text{ mV} \cdot \text{s}^{-1}$ .

Cameron et al., using the same system as described in “Diffusion coefficient”, page 98, measured a peak separation of 76 mV and 110 mV for the gold and platinum electrodes respectively.<sup>[8]</sup>

## 5. Optimization of electrolytes

### 5.1. Introduction

The first cells containing cobalt electrolytes gave promising results. DSSCs with  $[\text{Co}(\text{dmbip})_2](\text{ClO}_4)_2$  0.2 M, 3% oxidized with  $\text{NOBF}_4$ , in AN/EC (2:3) gave 1.0%, 2.1%, and 1.7% efficiencies at  $15 \text{ W m}^{-2}$ ,  $95 \text{ W} \cdot \text{m}^{-2}$ , and  $1000 \text{ W} \cdot \text{m}^{-2}$  respectively (“Cobalt complexes”, page 74). This chapter will be dedicated to the optimization of the electrolyte itself, in order to reach the maximal efficiency. The optimization of the electrolyte was achieved by screening the following parameters:

- The optimal redox mediator concentration.
- The optimal percentage of oxidized species in electrolyte.
- Which additives can be used to improve the photovoltaic parameters.
- How to increase the solubility of the complexes or their concentrations in a given solvent.

### 5.2. Optimization of redox mediator concentration and degree of oxidation

#### *Photoelectrochemical monitoring of the mediator concentration influence*

To test the effect of redox mediator concentration, on both the photovoltaic performance and the dynamics of dye regeneration, four solutions with different concentrations of  $[\text{Co}(\text{dbbip})_2](\text{ClO}_4)_2$  (0.05, 0.10, 0.15 and 0.20 M) were prepared. They were all partially oxidized to the same extent and contained 90% of  $[\text{Co}(\text{dbbip})_2]^{2+}$ . As shown in Table 28 and in Figure 31, the photovoltage is independent of the cobalt complex concentration above 0.05 M. The voltage is equal to the difference between the anodic and the cathodic overpotentials, and not dependant on the redox couple concentration. In contrast, the efficiency increases from 3.7 to  $5.5 \text{ mA} \cdot \text{cm}^{-2}$  when the redox mediator concentration is increased from 0.05 to 0.10 M and then remains constant, the increase in conductivity being compensated for by the increase in viscosity, which slows down the diffusion of the oxidized species.

**Table 28.** Average photoelectrochemical data obtained at  $1000 \text{ W} \cdot \text{m}^{-2}$  for DSSCs showing the influence of the redox mediator concentration on the photovoltaic parameters. The Co(III)/Co(II) concentration ratio was maintained at 0.1. The sensitizer was Z907.

Cobalt concentration [M]	$V_{oc}$ [mV]	$J_{sc}$ [mA · cm <sup>-2</sup> ]	$FF$ [-]	Efficiency [%]	$IPCE$ at 540 nm [%]
0.05	780	3.75	0.57	1.66	30
0.10	775	5.50	0.53	2.28	30
0.15	775	5.30	0.52	2.15	28
0.20	760	5.45	0.48	1.99	30

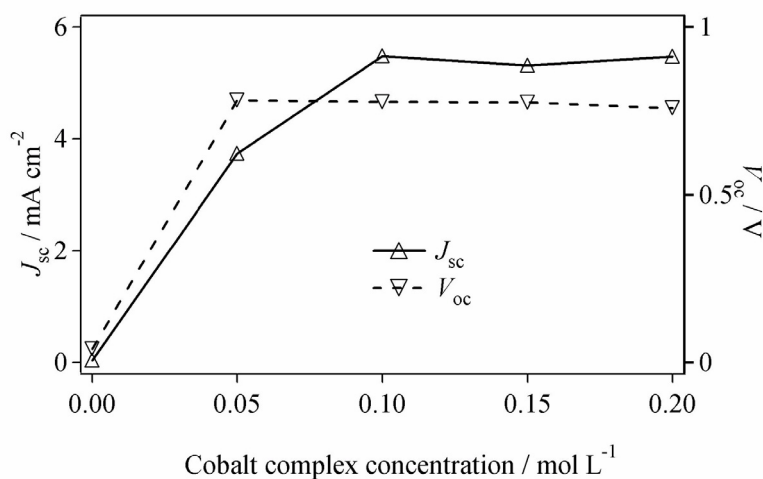


**Figure 31.** Influence of the redox mediator concentration on the short circuit current density and open circuit voltage measured under full AM1.5 sunlight. Efficiency and  $IPCE$  at 540 nm (not shown) exhibit the same behavior as current density and photovoltage, respectively. The Co(III)/Co(II) concentration ratio was maintained at 0.1. The sensitizer was Z907.

The increase in conductivity compensated for by an increase of viscosity can be monitored by studying the current dynamics, measuring the photocurrent at a given irradiation intensity for given time periods, typically several seconds. Figure 32 shows the current dynamics at full sun for the four cobalt complex concentrations represented in Figure 31.

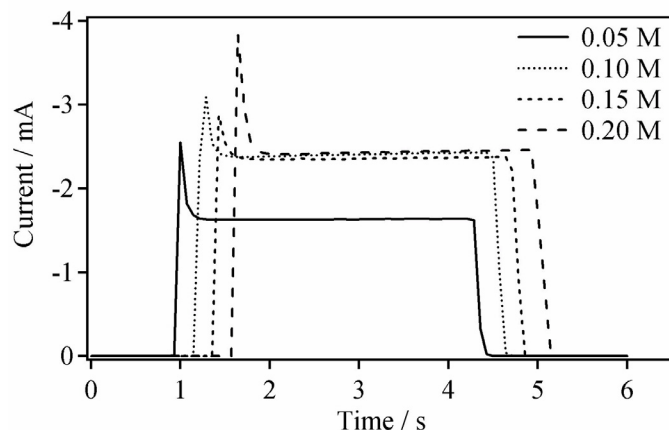


**Figure 32.** Example of current dynamics measured at  $1000 \text{ W} \cdot \text{m}^{-2}$  with DSSCs described in Figure 31.

The above current dynamics enable the initial current drops that occur during the first tenths of second to be calculated. 0.9 mA, 0.7 mA, 0.5 mA, and 1.4 mA were found for a concentration of 0.05 M, 0.10 M, 0.15 M, and 0.20 M, respectively. When the concentration increases, the current drop is reduced and maximum photocurrent is observed, because the conductivity of the electrolyte increases with the concentration. The viscosity of highly concentrated electrolytes, like 0.20 M, becomes a limiting factor and induces a large current drop, e.g. in this case a drop of 1.4 mA was seen. Finally, it can clearly be seen that the current after 1 second is dramatically increased between 0.05 M and 0.10 M, and then stays more or less constant when the concentration is increased, as seen in Figure 31.

To summarize, raising the cobalt complex concentration increases the photocurrent, but this effect is compensated by the increase of the viscosity for concentrations higher than 0.15 M in AN/EC (2:3) and a decrease of the  $FF$ . A concentration between 0.10 M to 0.15 M is therefore optimal with this solvent mixture and cobalt complex.

### ***Degree of oxidation***

The Co(III)/Co(II) concentration ratio is also expected to have an impact on the photovoltaic performance. To quantify this effect and find the optimal degree of oxidation, four different electrolytes were prepared, each one containing initially 0.1 M of  $[\text{Co}(\text{dbbip})_2](\text{ClO}_4)_2$ , which

was converted in varying proportions to Co(III) by adding  $\text{NOBF}_4$ . A Co(III)/Co(II) ratio of 1:9 was found to be optimal. The current density is adversely affected by higher Co(III) concentrations, as shown in Table 29 and in Figure 33 and this is attributed to the lack of Co(II) for the reduction of the oxidized dye. The regeneration of the dye by the Co(II) complex may also be impaired by the association of Co(III) with the sensitizer.

**Table 29.** Average photoelectrochemical data obtained at  $1000 \text{ W} \cdot \text{m}^{-2}$  for DSSCs with Z907, showing the influence of Co(III)/Co(II) concentrations ratios in AN/EC (2:3) on the photovoltaic parameters.

Co(III)/Co(II) concentration ratio	$V_{oc}$	$J_{sc}$	$FF$	Efficiency	$IPCE$ at 540 nm
[-]	[mV]	[ $\text{mA} \cdot \text{cm}^{-2}$ ]	[-]	[%]	[%]
0.00	800	1.85	0.45	0.66	70
0.11	785	6.35	0.54	2.71	40
0.25	770	5.65	0.59	2.48	25
1.00	560	0.85	0.57	0.27	5

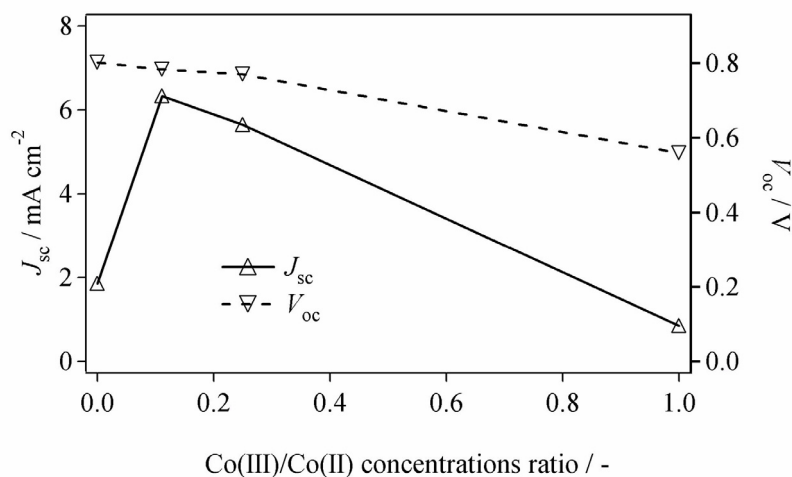


**Figure 33.** Influence of Co(III)/Co(II) concentrations ratios in AN/EC (2:3) on short circuit current density and open circuit voltage at  $1000 \text{ W} \cdot \text{m}^{-2}$ , with Z907. Efficiency and  $IPCE$  at 540 nm (not shown) exhibit the same behavior as current density and photovoltage, respectively.

The voltage drop observed upon increasing the Co(III)/Co(II) ratio is related, through the Nernst equation (Eq. 4.7, page 94), to the change in the redox potential of the electrolyte and therefore the difference between the anodic and the cathodic overpotentials.

### *Influence of the mediator concentration and the oxidation degree on the electron transfer dynamics*

The influence of the cobalt complex concentration and its oxidation ratio upon the regeneration rate of the homoleptic dye N719 was measured using laser flash photolysis.

Dependence of the pseudo first-order rate constant  $k_m$  for  $[\text{Co}(\text{dbbip})_2]^{2+}$  on the mediator's concentration is displayed in Figure 34. Two different regimes can be clearly identified. Above a threshold of  $10^{-2}$  M, higher concentrations of the mediator resulted in a linear increase of the apparent rate, thus yielding a second-order rate constant for the interception reaction of  $k_m'' = 2.9 \cdot 10^6 \text{ mol}^{-1} \cdot \text{L} \cdot \text{s}^{-1}$ . This value is approximately one order of magnitude smaller than that reported for dye ground state recovery in the presence of sodium iodide ( $k_m'' = 2 \cdot 10^7 \text{ mol}^{-1} \cdot \text{L} \cdot \text{s}^{-1}$ ).<sup>[17]</sup> At mediator concentrations below  $10^{-2}$  M, static interception appears to take place mainly from species adsorbed on the surface or associated with dye molecules. As the  $\text{TiO}_2$  surface covered by N719 dye is negatively charged,<sup>[12]</sup> electrostatic adsorption of the mediator's di-cations is quite efficient. Contrary to the case of iodide, where a cooperative effect of adsorbed cations was observed,<sup>[12]</sup> addition of 0.1 M of  $\text{Li}^+$  perchlorate did not yield any noticeable change in the interception kinetics measured with the cobalt complex. Static interception compensates for the intrinsically slower reduction of  $\text{S}^+$  by  $[\text{Co}(\text{dbbip})_2]^{2+}$ , resulting in observed pseudo first-order rate similar to those obtained with the triiodide/iodide system.

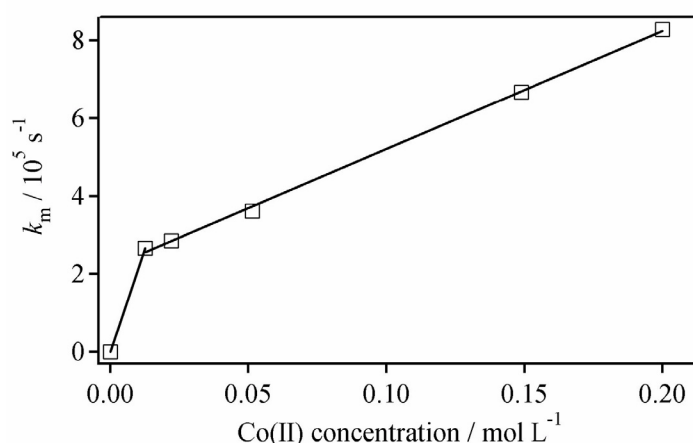


**Figure 34.** Plot of the first order rate constant  $k_m$  [ $\text{s}^{-1}$ ] fitted from the decay kinetics of the oxidized state of N719 ( $\text{S}^+$ ) adsorbed on  $\text{TiO}_2$  nanocrystalline films in the presence of an increasing concentration of the Co(II) complex mediator in AN/EC (2:3).

Simultaneously with the decay of the oxidized dye transient absorption, the recovery of the bleached dye ground state was monitored at  $\lambda_{\text{obs}} = 480$  nm. After the 10  $\mu\text{s}$  delay, due to the interception reaction, a weak positive absorption was observed at the same wavelength. The latter signal was assigned to the Co(III) ions in the electrolyte, whose absorption tail in the visible is characterized by a larger extinction coefficient than that of the reduced species (see “Reduced and oxidized complexes UV-Vis absorption spectra”, page 102). This long lifetime transient absorption eventually decayed over ca. 1 ms, due to the electron recapture process (Eq. 4.24, page 116), whose first-order rate constant was determined directly as being  $k_r = 3 \cdot 10^3 \text{ s}^{-1}$ . The two-electron recapture reaction for the triiodide/iodide system was reported to take place with a pseudo second-order rate constant of  $1.1 \cdot 10^4 \text{ mol}^{-1} \cdot \text{L} \cdot \text{s}^{-1}$  at  $[\text{I}_3^-] = 5 \cdot 10^{-2} \text{ M}$ .<sup>[18]</sup> In a functioning DSSC, where sufficient charge transport at the counter electrode is ensured by a concentration of the oxidized form of the mediator of typically 0.1 M, the recapture of injected electrons by the Co(III) complex mediator is therefore expected to be only slightly faster than in the case of triiodide.

As seen previously (“Sensitizer - electrolyte interactions”, page 111), the negative charge density on the semiconductor particle surface can be reduced through the use of heteroleptic dyes, which contain only two carboxylic groups and are therefore characterized by a neutral charge.

The influence of the cobalt complex concentration and the ratio of the oxidized species upon the regeneration rate of the heteroleptic dyes Z316 and Z907 was also therefore measured.

Figure 35 is the same as Figure 34, but with sensitizers Z316 and Z907. With these dyes, no dependence of  $k_m$  on the mediator’s concentration was observed. Although with N719 the increase of  $k_m$  with the cobalt complex concentration suggested a competition kinetics. In the case of Z316 or Z907 it seemed that a saturation already occurred at low concentrations. This effect is difficult to explain, but may come from hydrophobic attraction between the alkyl chains of the dyes and the butyl parts of the cobalt complex. The steric cage created by the long alkyl chains of the sensitizers may also explain the low  $k_m$  value as compared to that obtained with N719, which is about four times higher at 0.18 M than for Z316 and eight times higher than for Z907, which has two long alkyl chains per dye molecule.



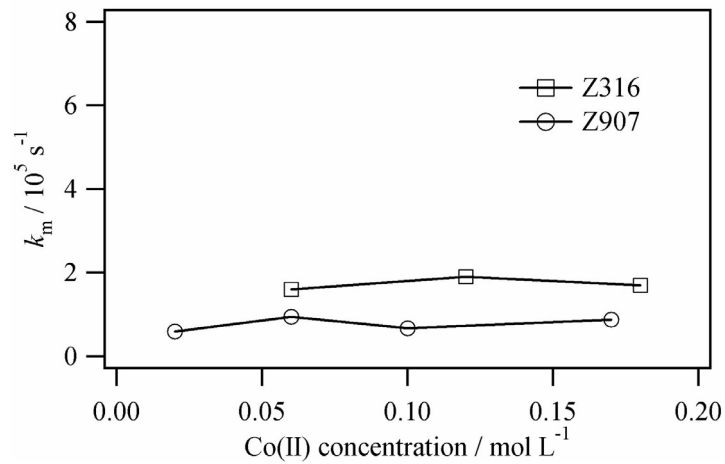


**Figure 35.** Plot of the first order rate constant  $k_m$  [ $\text{s}^{-1}$ ] fitted from the decay kinetics of the oxidized state of Z316 or Z907 adsorbed on  $\text{TiO}_2$  nanocrystalline films in the presence of an increasing concentration of the Co(II) complex mediator in AN/EC (2:3).

Figure 36 for N719 and Figure 37 for Z907 show that partially oxidizing the cobalt complex significantly slows the regeneration of the sensitizer. This is attributed to the replacement of the adsorbed  $[\text{Co}(\text{dbbip})_2]^{2+}$  by  $[\text{Co}(\text{dbbip})_2]^{3+}$  species at the interface next to the sensitizer. The electrostatic binding on the negatively charged  $\text{TiO}_2$  surface is indeed expected to increase with the positive charge density on the cobalt complex. The same behavior as in Figure 37 was also observed with dye Z316.

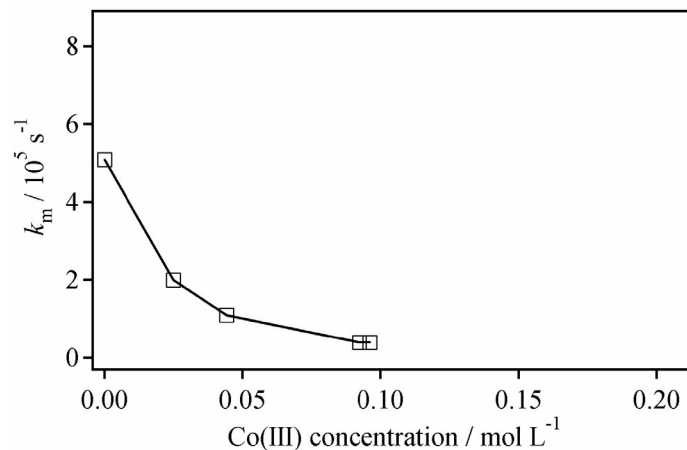


**Figure 36.** Plot of the first order rate constant  $k_m$  [ $\text{s}^{-1}$ ] fitted from the decay kinetics of the oxidized state of N719 ( $\text{S}^+$ ) adsorbed on  $\text{TiO}_2$  nanocrystalline films in the presence of an increasing concentration of oxidized species in AN/EC (2:3). The total complex concentration in solution is 0.10 M. Partial oxidation of the Co(II) complex to Co(III) with  $\text{NOBF}_4$  caused the kinetics of the interception reaction to decrease markedly.

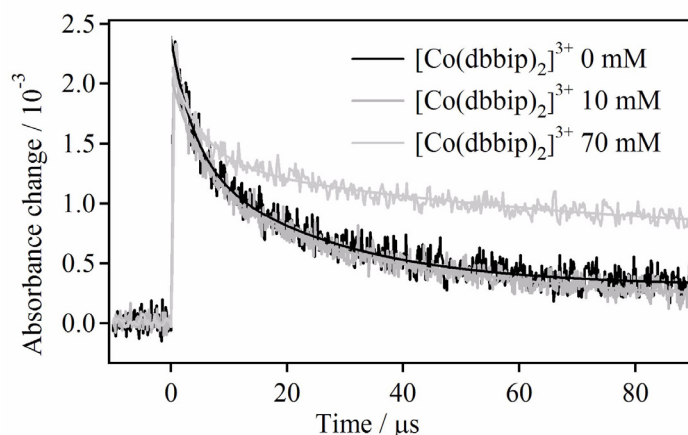


**Figure 37.** Transient absorbance decay kinetics of the oxidized state of Z907 ( $S^+$ ) adsorbed on a  $TiO_2$  nanocrystalline film in the presence of an increasing concentration of oxidized species in AN/EC (2:3). The total complex concentration in solution is 0.10 M. Absorbance changes were measured at a probe wavelength of 620 nm, employing 510 nm laser excitation (5 ns fwhm pulse duration,  $40 \mu J \cdot cm^{-2}$  pulse fluence).

### 5.3. Additives

As was shown previously for the triiodide/iodide based electrolytes,<sup>[19,20]</sup> additives can be used to optimize the electrolyte composition and improve the solar-cell performance. Our studies focused on 4-*tert*-butylpyridine (TBP) and lithium perchlorate additives. TBP is known to passivate recombination centers and therefore reduce back electron transfer from  $TiO_2$ , resulting in higher open circuit photovoltages. The  $LiClO_4$  in the electrolyte system increases the photocurrent due to the adsorption of  $Li^+$  on the  $TiO_2$  at high concentrations,<sup>[20,21]</sup> and shifts the flatband potential of  $TiO_2$  to more positive values<sup>[22]</sup> and this enhances the charge-collection efficiency of the oxide film. Hence, it is important to use both  $LiClO_4$  and TBP to increase the  $J_{sc}$  and  $V_{oc}$  values.

A series of DSSCs with varying quantities of TBP were compared in terms of their influence on photovoltaic parameters (Table 30 and Figure 38).

**Table 30.** Average photoelectrochemical data obtained at  $95 \text{ W} \cdot \text{m}^{-2}$  for DSSCs with Z907,  $[\text{Co}(\text{dbbip})_2](\text{ClO}_4)_2$  0.09 M and its oxidized form 0.01 M, in AN/EC (2:3), showing the effect of 4-*tert*-butylpyridine (TBP) concentration on photovoltaic parameters.

TBP concentration [M]	$V_{\text{oc}}$ [mV]	$J_{\text{sc}}$ [ $\text{mA} \cdot \text{cm}^{-2}$ ]	$FF$ [-]	Efficiency [%]	$IPCE$ at 540 nm [%]
0.00	685	0.95	0.73	4.89	50
0.03	740	1.00	0.73	5.71	50
0.08	750	0.90	0.74	5.38	50
0.19	780	0.90	0.74	5.26	45

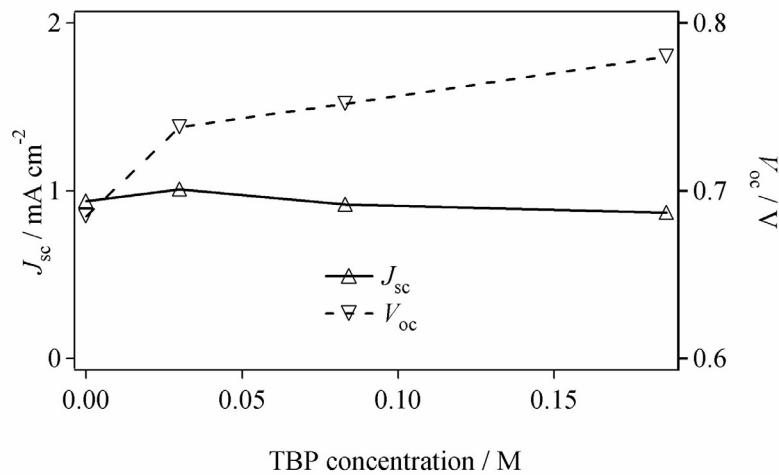


**Figure 38.** Effect of 4-*tert*-butylpyridine (TBP) concentration on short circuit current density and open circuit voltage at  $95 \text{ W} \cdot \text{m}^{-2}$ . Only the photovoltage continues to increase with increasing concentration of TBP. Conditions are the same as in Table 30.

As expected, addition of TBP increased the photovoltage by about 100 mV at  $95 \text{ W} \cdot \text{m}^{-2}$ . Its action on the reduction of the electron back transfer is clearly shown in Figure 39, where the dark currents decrease with the respective increase of TBP concentration in the electrolyte.

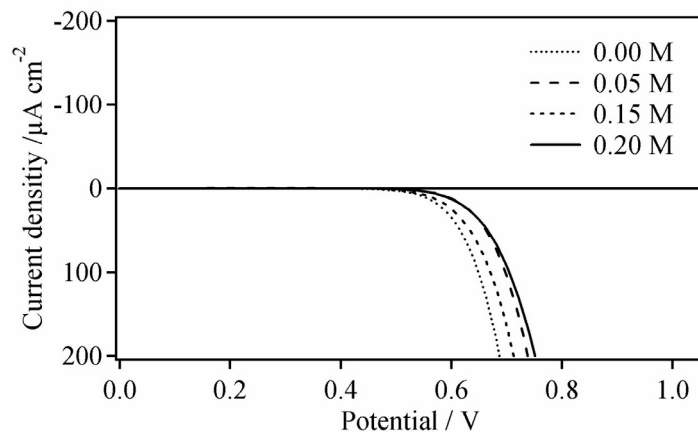


**Figure 39.** Example of dark current of DSSCs measured with an increasing concentration of TBP in  $[\text{Co}(\text{dbbip})_2(\text{ClO}_4)_2]$  0.09 M,  $[\text{Co}(\text{dbbip})_2(\text{ClO}_4)_3]$  0.01 M, in AN/EC (2:3).

Impact of  $\text{LiClO}_4$  addition is shown in Table 31 and Figure 40.

**Table 31.** Average photoelectrochemical data obtained at  $95 \text{ W} \cdot \text{m}^{-2}$  for DSSCs showing the effect of  $\text{LiClO}_4$  concentration on photovoltaic parameters. Conditions are the same as in Table 30.

$\text{LiClO}_4$ concentration [M]	$V_{\text{oc}}$ [mV]	$J_{\text{sc}}$ [ $\text{mA} \cdot \text{cm}^{-2}$ ]	$FF$ [-]	Efficiency [%]	$IPCE$ at 540 nm [%]
0.0	725	0.75	0.73	4.11	50
0.1	670	1.30	0.70	6.42	75
0.2	665	1.35	0.68	6.35	75
0.3	655	1.35	0.68	6.37	80

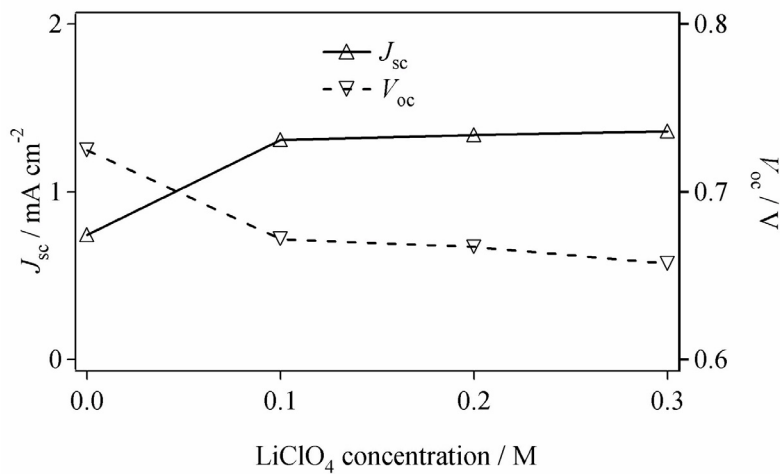


**Figure 40.** Effect of LiClO<sub>4</sub> concentration on short circuit current density and open circuit voltage measured at 95 W · m<sup>-2</sup>. Conditions are the same as in Table 30.

The addition of LiClO<sub>4</sub> nearly doubles the photocurrent at 95 W · m<sup>-2</sup>, whilst decreasing the photovoltage by less than 100 mV for any concentration. In general, this decrease of photovoltage by Li<sup>+</sup> addition is similar to that of classic triiodide/iodide-based liquid electrolytes, but less pronounced; a typical electrolyte based on triiodide/iodide in a nitrile solvent will show a decrease of at least 150 mV on addition of 0.1 M of Li<sup>+</sup>. This decrease of the photovoltage is the direct consequence of the shift to more positive values of the TiO<sub>2</sub> flatband potential.

In contrast to our results, an increase in the photovoltage was observed by Sapp et al. on the addition of Li<sup>+</sup> ions, which is attributed to an increase in the effective overpotential for the reduction of the sensitizer at the photoelectrode on addition of Li<sup>+</sup> to the solution.<sup>[23]</sup>

Efficiencies obtained upon addition of variable concentrations of TBP and LiClO<sub>4</sub> to the electrolytic solution are shown in Figure 41.

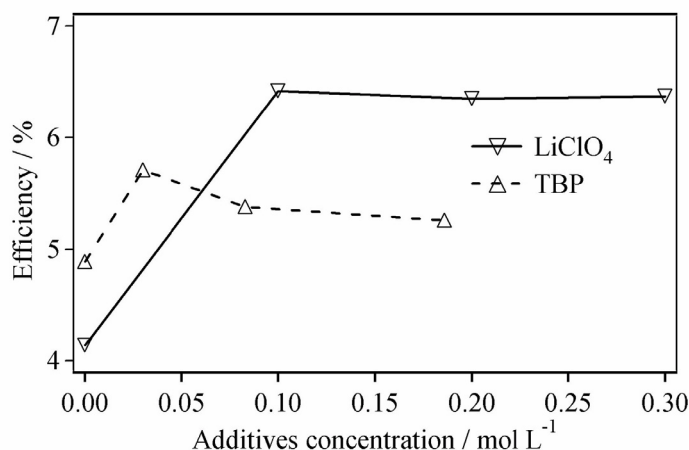


**Figure 41.** Effect of TBP and LiClO<sub>4</sub> concentrations on efficiency measured at 95 W · m<sup>-2</sup>. Conditions are the same as in Table 30.

Combining these two additives at their best concentration gives the results shown in Table 32.

**Table 32.** Average photoelectrochemical data obtained with Z907 and [Co(dbbip)<sub>2</sub>](ClO<sub>4</sub>)<sub>2</sub> 0.09 M, [Co(dbbip)<sub>2</sub>](ClO<sub>4</sub>)<sub>3</sub> 0.01 M, LiClO<sub>4</sub> 0.2 M, TBP 0.1 M in AN/EC (2:3).

Irradiance [W · m <sup>-2</sup> ]	V <sub>oc</sub> [mV]	J <sub>sc</sub> [mA · cm <sup>-2</sup> ]	FF [-]	Efficiency [%]	IPCE at 540 nm [%]
15	665	0.22	0.72	6.45	70
95	755	1.32	0.70	7.06	70
1000	830	6.50	0.57	2.90	70

## 5.4. Solvents effect and improvement of the solubility

### Introduction

The nature of the solvent has an important effect on the global stability of the DSSC as well as on the photovoltaic performances, the diffusion of the species in solution being directly related to the solvent viscosity.

Some solvents may lead to higher photovoltaic efficiency but may be inadequate for industrial applications. Others may be of preference for large scale use, but redox couples may have a very low solubility.

Two ways were chosen here. The first one was to screen the characteristics of different solvents used with cobalt complexes through their solubilization potential and photoelectrochemical properties. The second one was the synthesis of a new cobalt complex, presenting higher solubility characteristics.

### *Solvent effect*

**Table 33.** Maximum solubility for  $[\text{Co}(\text{dbbip})_2](\text{ClO}_4)_2$  in different solvents and solvent mixtures.

Solvent	Max. concentration [M]
Ethylene carbonate/propylene carbonate (1:1)	> 0.2
Acetonitrile/ethylene carbonate (2:3)	0.19
$\gamma$ -butyrolactone	0.18
3-methoxypropionitrile	0.11
Methoxyacetonitrile	0.10
Acetonitrile	0.05
Valeronitrile	0.05
3-(2-(2-methoxy-ethoxy)ethoxy)propionitrile	0.03
Propionitrile	0.01
Ethanol	~ 0
Toluene	~ 0
Butanol	~ 0

As the solubility of cobalt complexes is low for many solvents, only AN/EC (2:3),  $\gamma$ -butyrolactone, and 3-methoxypropionitrile were used as solvents for the preparation of the electrolytes used in DSSCs.

Results for  $\gamma$ -butyrolactone are given in Table 34, Table 35 and Figure 42.

**Table 34.** Average photoelectrochemical data obtained at  $95 \text{ W} \cdot \text{m}^{-2}$  for DSSCs using Z907 and  $[\text{Co}(\text{dbbip})_2](\text{ClO}_4)_2$  at two different concentrations, 5% oxidized, in  $\gamma$ -butyrolactone.

Cobalt concentration [M]	$V_{\text{oc}}$ [mV]	$J_{\text{sc}}$ [ $\mu\text{A} \cdot \text{cm}^{-2}$ ]	$FF$ [-]	Efficiency [%]	$IPCE$ at 540 nm [%]
0.1	685	745	0.73	3.91	30
0.18	680	940	0.70	4.72	45

The results obtained for  $[\text{Co}(\text{dbbip})_2](\text{ClO}_4)_2$  0.18 M, 5% oxidized, in pure  $\gamma$ -butyrolactone are as good as those obtained with  $[\text{Co}(\text{dbbip})_2](\text{ClO}_4)_2$  0.1 M, 10% oxidized, in AN/EC (2:3), that gives an efficiency of ca. 4.7%. Therefore  $\gamma$ -butyrolactone is an efficient alternative to the solvent mixture AN/EC when used with  $[\text{Co}(\text{dbbip})_2](\text{ClO}_4)_2$ .

A more efficient electrolyte,  $[\text{Co}(\text{dbbip})_2](\text{ClO}_4)_2$  0.09 M,  $[\text{Co}(\text{dbbip})_2](\text{ClO}_4)_3$  0.01 M,  $\text{LiClO}_4$  0.2 M and TBP 0.1 M, solubilized in the AN/EC (2:3) solvent mixture was compared to another electrolyte with the same compounds dissolved in pure  $\gamma$ -butyrolactone. Results are given in Table 35 while Figure 42 shows examples of I/V curves under an irradiance of  $95 \text{ W} \cdot \text{m}^{-2}$  for both electrolytes.

**Table 35.** Average photoelectrochemical data obtained at  $95 \text{ W} \cdot \text{m}^{-2}$  for DSSCs using Z907 and  $[\text{Co}(\text{dbbip})_2](\text{ClO}_4)_2$  0.09 M,  $[\text{Co}(\text{dbbip})_2](\text{ClO}_4)_3$  0.01 M,  $\text{LiClO}_4$  0.2 M and TBP 0.1 M either in AN/EC (2:3), or in  $\gamma$ -butyrolactone.

Solvent	$V_{\text{oc}}$ [mV]	$J_{\text{sc}}$ [ $\text{mA} \cdot \text{cm}^{-2}$ ]	$FF$ [-]	Efficiency [%]	$IPCE$ at 540 nm [%]
AN/EC (2:3)	765	1.35	0.73	7.88	75
$\gamma$ -butyrolactone	775	1.00	0.68	5.54	55



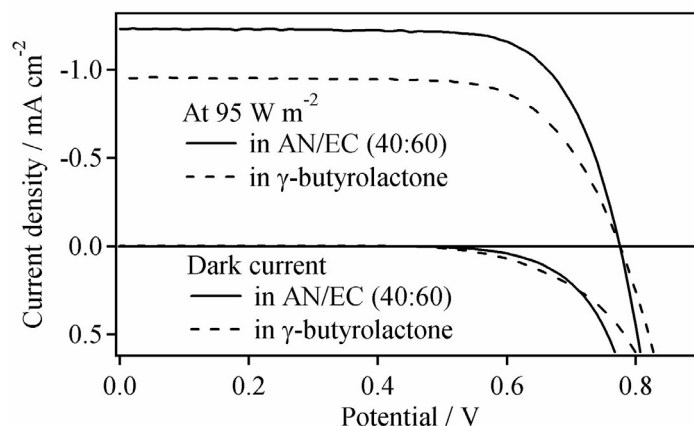


**Figure 42.** Example of the solvent influence on the dark current and the photocurrent at  $95 \text{ W} \cdot \text{m}^{-2}$ . Sensitizer Z907 was used with the same electrolytes as described in Table 35.

The addition of  $\text{LiClO}_4$  and TBP to the electrolyte leads to a significant improvement of the photovoltaic properties. A comparison between Table 34 and Table 35 shows an increase of the efficiency by 40%. Still, at that concentration of 0.1 M of cobalt complex, the use of the solvent mixture gives higher photocurrents and therefore better efficiencies than the use of  $\gamma$ -butyrolactone.

Results for methoxypropionitrile are given in Table 36

**Table 36.** Average photoelectrochemical data obtained at  $95 \text{ W} \cdot \text{m}^{-2}$  for DSSCs using Z907 and  $[\text{Co}(\text{dbbip})_2](\text{ClO}_4)_2$  or  $[\text{Co}(\text{dobip})_2](\text{ClO}_4)_2$  at 0.1 M, 10% oxidized, in methoxypropionitrile, with  $\text{LiClO}_4$  0.2 M and TBP 0.1 M.

Cobalt bip	$V_{\text{oc}}$ [mV]	$J_{\text{sc}}$ [mA · cm <sup>-2</sup> ]	$FF$ [-]	Efficiency [%]	$IPCE$ at 540 nm [%]
dbbip	700	0.90	0.75	4.89	40
dobip	710	1.10	0.74	6.15	45

Using  $[\text{Co}(\text{dbbip})_2](\text{ClO}_4)_2$  in methoxypropionitrile is less efficient than in the solvent mixture, but when using  $[\text{Co}(\text{dobip})_2](\text{ClO}_4)_2$ , the photovoltaic properties are considerably better and nearly reach those obtained with AN/EC (2:3), where the efficiency is ca. 6.7%.

The solvent mixture AN/EC (2:3) remains the solvent of choice for cobalt complexes regarding the photovoltaic efficiencies. Nevertheless,  $\gamma$ -butyrolactone used with higher redox mediator concentrations (0.18 M) can give some interesting results, as well as methoxypropionitrile used with the  $[\text{Co}^{\text{III/II}}(\text{dobip})_2]$  couple.

### *Use of $[\text{Co}(\text{dmebip})_2](\text{ClO}_4)_2$ as redox mediator in DSSC*

One way to improve the solubility of cobalt complexes in a solvent is to change their hydrophilicity. To increase the hydrophilicity, a cobalt complex based on bip ligand, but with alcoxy groups, was synthesized according to the method described in “Cobalt(II) complexes synthesis”, page 35. The structure of this complex is given in Figure 43.

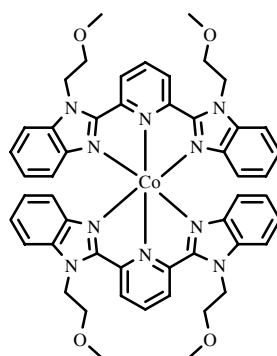


**Figure 43.** Chemical structure of  $[\text{Co}(\text{dmebip})_2]^{2+}$ .

DSSCs with an electrolyte containing  $[\text{Co}(\text{dmebip})_2](\text{ClO}_4)_2$  0.09 M and  $[\text{Co}(\text{dmebip})_2](\text{ClO}_4)_2$  0.01 M in AN/EC (2:3) were first measured to compare its efficiency with that of  $[\text{Co}(\text{dbbip})_2](\text{ClO}_4)_2$ . The measured data is presented in Table 37. Compared to  $[\text{Co}(\text{dbbip})_2](\text{ClO}_4)_2$ ,  $[\text{Co}(\text{dmebip})_2](\text{ClO}_4)_2$  gives similar efficiencies (see Table 32 for comparison).

**Table 37.** Average photoelectrochemical data obtained at  $95 \text{ W} \cdot \text{m}^{-2}$  for DSSCs using Z907 and  $[\text{Co}(\text{dmebip})_2](\text{ClO}_4)_2$  0.09 M,  $[\text{Co}(\text{dmebip})_2](\text{ClO}_4)_3$  0.01 M, in AN/EC (2:3), and the same electrolyte, but with  $\text{LiClO}_4$  0.2 M and TBP 0.1 M added to it.

Electrolyte	$V_{oc}$ [mV]	$J_{sc}$ [mA · cm <sup>-2</sup> ]	$FF$ [-]	Efficiency [%]	$IPCE$ at 540 nm [%]
Cobalt complexes	665	0.55	0.76	3.01	30
Cobalt complexes + additives	740	1.30	0.71	7.30	75

Adding alcoxy groups to the complex sometimes increases its solubility. However only 0.15 M in AN/EC (2:3) was achievable, instead of 0.18 M with  $[\text{Co}(\text{dbbip})_2](\text{ClO}_4)_2$ . Nevertheless,  $[\text{Co}(\text{dmebip})_2](\text{ClO}_4)_2$  was also tested in solvent mixtures composed of methoxypropionitrile (MPN) and acetonitrile (AN), with different ratios. Table 38 gives the main photovoltaic results for each solvent ratio.

**Table 38.** Average photoelectrochemical data obtained at  $95 \text{ W} \cdot \text{m}^{-2}$  for DSSCs using Z907 and  $[\text{Co}(\text{dmebip})_2](\text{ClO}_4)_2$  0.09 M,  $[\text{Co}(\text{dmebip})_2](\text{ClO}_4)_3$  0.01 M, in different ratios of MPN/AN, without additives.

MPN/AN	$V_{oc}$ [mV]	$J_{sc}$ [μA · cm <sup>-2</sup> ]	$FF$ [-]	Efficiency [%]
100/0	805	190	0.71	1.13
70/30	845	385	0.64	2.18
60/40	805	605	0.56	2.88

In MPN/AN solvents, this electrolyte gives a very high open circuit voltage, e.g. 950 mV at full sun for the 70:30 mixture. As AN is less viscous than MPN, the more AN in the solution, the higher the current. As the fill factor decreases due to solvent properties, the efficiency does not improve as it could have.

Finally,  $[\text{Co}(\text{dmebip})_2](\text{ClO}_4)_2$  was tested in  $\gamma$ -butyrolactone, with a total concentration of 0.17 M, 10% being oxidized into Co(III). The results are presented in Table 39.

**Table 39.** Average photoelectrochemical data for DSSCs using Z907 and  $[\text{Co}(\text{dmebip})_2](\text{ClO}_4)_2$  0.15 M,  $[\text{Co}(\text{dmebip})_2](\text{ClO}_4)_3$  0.02 M, in  $\gamma$ -butyrolactone, without additives.

Irradiance [W · m <sup>-2</sup> ]	V <sub>oc</sub> [mV]	J <sub>sc</sub> [μA · cm <sup>-2</sup> ]	FF [-]	Efficiency [%]
15	560	30	0.66	0.63
95	650	255	0.66	1.13
1000	730	2090	0.53	0.81

Although the redox mediator concentration in  $\gamma$ -butyrolactone is higher, the photovoltaic efficiency of this electrolytic solution is lower than that reached with the solvent mixture AN/EC. This is due to a drop in the photocurrent resulting from the higher viscosity of  $\gamma$ -butyrolactone.

Comparing the photoelectrochemical values between Table 38 for the pure MPN and Table 39 at 95 W · m<sup>-2</sup>, one sees that the photovoltage is much higher and the photocurrent lower with MPN. The overall efficiency remains about the same between the two solvents.

Attempts to increase the efficiency of DSSCs by using an alkoxy cobalt complex did not succeed. Adding methoxyethoxy groups to the complex did not increase its solubility as expected. For a higher solubility, longer chains with several units of methoxyethoxy should be added, with the negative effect of increasing the molecular weight of the molecule and its viscosity once in solution. The MPN/AN solvent mixture creates an ideal environment for a very high voltage, but with its low *FF*, the efficiency remains under expectations.

## 6. Mass-transport optimizations

### 6.1. Direction of irradiation

The variation of photocurrent upon illuminating a cell from the photoanode (PA) or counter electrode (CE) side was studied. Mass-transport effects are clearly an issue for electrolytes based on cobalt mediators, in particular under full-sunlight irradiance, for which the current densities exceed  $5 \text{ mA} \cdot \text{cm}^{-2}$ . In this case, both the oxidized and reduced complexes are subject to mass-transport limitation, while for triiodide/iodide-based electrolytes, diffusion restrictions on the current arised only from triiodide ions.<sup>[24]</sup>

Limiting current within a cell with no bulk liquid layer can be modelled for a monochromatic incident light, assuming that the light attenuation inside the cell is only due to absorption by the dye according to Beer-Lambert's law and ignoring the light scattering and the photon losses at the various interface.<sup>[24]</sup> For a cell irradiated from the photoanode side (PA), Eq. 4.28 gives the limiting current when the diffusion of Co(III) towards the counter electrode becomes limiting.

$$I_d = \frac{\varepsilon_p \cdot F \cdot D_O \cdot c_O(\text{init})}{l} \cdot f_{\text{PA}}(A) \quad (4.28)$$

where

$$f_{\text{PA}}(A) = 2 \cdot \frac{A^2 \cdot (\ln 10)^2 \cdot (10^A - 1)}{A^2 \cdot (\ln 10)^2 \cdot 10^A + 2 \cdot A \cdot \ln 10 - 2 \cdot (10^A - 1)} \quad (4.29)$$

For a cell irradiated from the counter electrode side (CE), Eq. 4.30 gives the limiting current when the diffusion of Co(III) towards the counter electrode becomes limiting.

$$I_d = \frac{\varepsilon_p \cdot F \cdot D_O \cdot c_O(\text{init})}{l} \cdot f_{\text{CE}}(A) \quad (4.30)$$

where

$$f_{\text{CE}}(A) = 2 \cdot \frac{A^2 \cdot (\ln 10)^2 \cdot (1 - 10^A)}{A^2 \cdot (\ln 10)^2 - 2 \cdot 10^A \cdot A \cdot \ln 10 + 2 \cdot (10^A - 1)} \quad (4.31)$$

$\varepsilon_p$  is the nanocrystalline  $\text{TiO}_2$  porosity,  $l$  the  $\text{TiO}_2$  film thickness and  $A$  the monochromatic absorption of the  $\text{TiO}_2$ /sensitizer “solution” in the cell. Figure 44 represents the evolution of the factors  $f_{\text{PA}}(A)$  and  $f_{\text{CE}}(A)$  for an increase of light absorbance. For Eq. 4.28, an increase in absorbance, at constant  $l$ , of the porous material implies a decrease in the limiting current. This is understandable since as the absorbance increases, the  $\text{Co(III)}$  is generated further away from the counter electrode. On contrary, with Eq. 4.30, an increase in the absorbance implies an increase in the limiting current. The  $\text{Co(III)}$  ions are formed closer to the counter electrode, thus diffusion of  $\text{Co(III)}$  towards the cathode will become limiting at higher current density values.

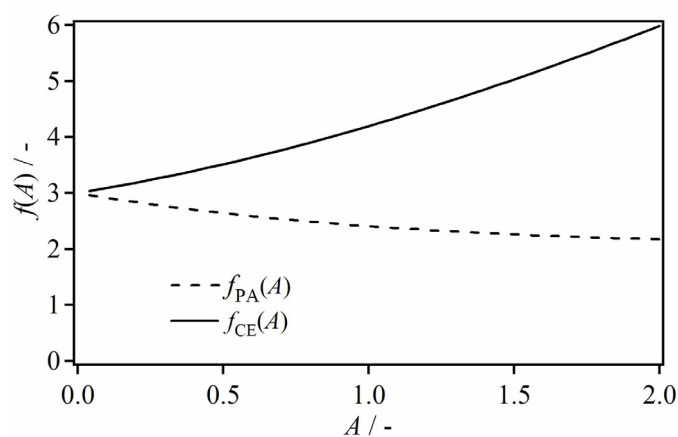


**Figure 44.** Factors affecting the limiting current as absorbance is increased in PA side or CE side irradiation.

The effect of irradiation from the PA or the CE side was studied using closed cells with either a normal  $\text{TiO}_2$  layer structure (nanocrystalline layer then diffusive layer on top) for PA side illumination, or reversed  $\text{TiO}_2$  layer structure (diffusive layer first, then nanocrystalline layer on top) for counter electrode side illumination.

As shown in Figure 45, in the low-current region, where mass transport is not too limiting, PA illumination gave superior currents. In spite of the low absorption coefficient of the electrolyte, photons are however still absorbed.

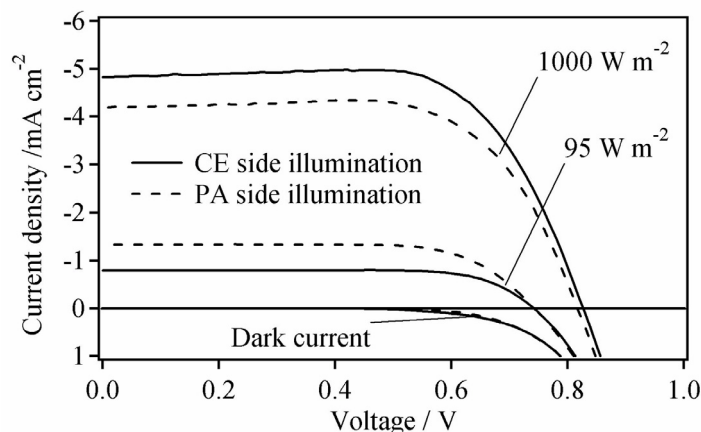


**Figure 45.** Examples of I/V curves showing the differences between photoanode-side (PA) and counter electrode-side (CE) illumination for an irradiance of  $1000 \text{ W} \cdot \text{m}^{-2}$ ,  $95 \text{ W} \cdot \text{m}^{-2}$  and dark current, with Z907,  $[\text{Co}(\text{dbbip})_2](\text{ClO}_4)_2$   $0.09 \text{ M}$ ,  $[\text{Co}(\text{dbbip})_2](\text{ClO}_4)_3$   $0.01 \text{ M}$ , TBP  $0.2 \text{ M}$ , and  $\text{LiClO}_4$   $0.2 \text{ M}$ , in AN/EC (2:3).

The loss due to the electrolyte absorption is overcompensated at high irradiance intensity by the improvement in mass transport. Mass-transport limitation manifests itself as a deviation from a linear dependence of the current density on light intensity. The current density at which this takes place is much higher with CE irradiation than with PA irradiation. This implies that when the mass transport is limiting, it is preferable to provide irradiation from the CE side to improve the linearity of the performance with light intensity by alleviating the diffusion problems in the cell.

This improvement in mass transport at high irradiance is clearly shown in Figure 46, where the current dynamics measured from  $1 \text{ W} \cdot \text{m}^{-2}$  to  $1000 \text{ W} \cdot \text{m}^{-2}$  are notably more stable under CE side illumination. This figure also shows that the irradiation intensity at which the light absorption by the electrolyte and the gain obtained by mass transport improvement is around  $530 \text{ W} \cdot \text{m}^{-2}$ , where the currents are nearly equal.

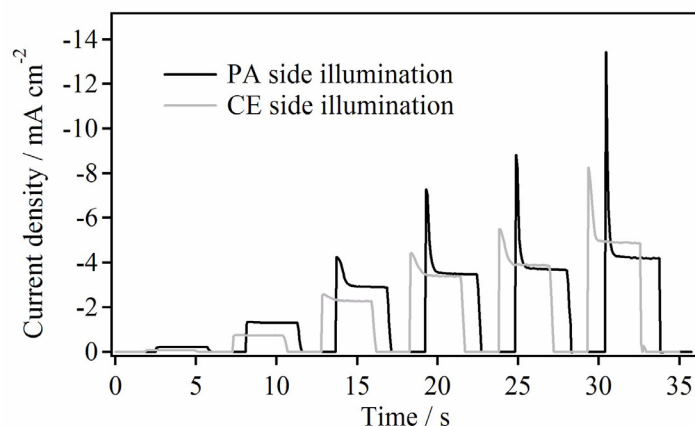


**Figure 46.** Example of current dynamics measured, from left to right, at  $10 \text{ W} \cdot \text{m}^{-2}$ ,  $100 \text{ W} \cdot \text{m}^{-2}$ ,  $300 \text{ W} \cdot \text{m}^{-2}$ ,  $530 \text{ W} \cdot \text{m}^{-2}$ ,  $640 \text{ W} \cdot \text{m}^{-2}$ , and  $1000 \text{ W} \cdot \text{m}^{-2}$ , with Z907 and  $[\text{Co}(\text{dbbip})_2](\text{ClO}_4)_2$   $0.09 \text{ M}$ ,  $[\text{Co}(\text{dbbip})_2](\text{ClO}_4)_3$   $0.01 \text{ M}$ , TBP  $0.2 \text{ M}$ ,  $\text{LiClO}_4$   $0.2 \text{ M}$ , in AN/EC (2:3).

## 6.2. Distances between electrodes

The diffusion layer thickness is also an important parameter when diffusion is the limiting factor. Increasing the distance between the two electrodes renders the diffusion path longer, decreasing the available current. This effect should be especially marked at high irradiation intensities.

Limiting current within a cell with bulk liquid layer can be modelled, assuming a constant intensity photon flux in time and an absorption of the cell sufficiently small that the photon flux going through the cell can be considered as constant over the entire thickness.<sup>[24]</sup> For that kind of cell, Eq. 4.32 gives the limiting current due to Co(III) diffusion.

$$I_{d(\text{bulk})} = \frac{\varepsilon_p \cdot F \cdot D_O \cdot c_O(\text{init})}{l} \cdot \frac{3 \cdot \left(1 + \frac{b}{1 \cdot \varepsilon_p}\right)}{\frac{1}{f_{\text{PA}}(A)} + 3 \cdot \varepsilon_p \cdot \frac{b}{l} + \frac{3}{2} \cdot \left(\frac{b}{l}\right)^2} \quad (4.32)$$



$b$  is the bulk layer thickness and  $l$  the  $\text{TiO}_2$  nanocrystalline film thickness. If the ratio  $b/l$  increases then the limiting current in the bulk layer decreases, as long as the  $\text{TiO}_2$  film porosity is higher than 50%.

Cells with two different gaps between the electrodes were photoelectrochemically measured and current dynamics recorded. Figure 47 shows the resulting transient curves, for a  $b/l$  ratio changing from about 1.7 to 10.

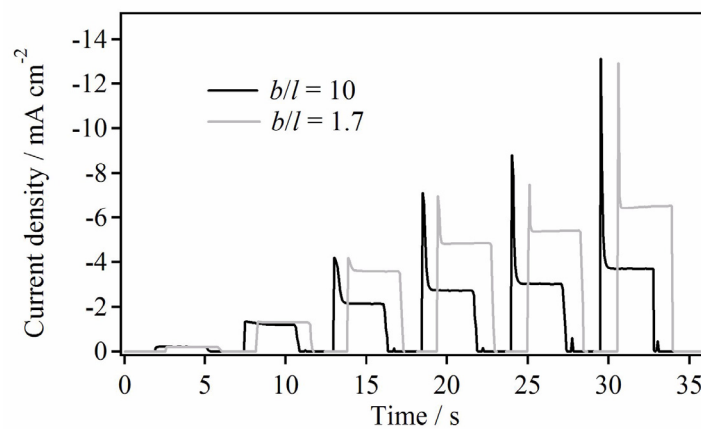


**Figure 47.** Example of current dynamics measured, from left to right, at  $10 \text{ W} \cdot \text{m}^{-2}$ ,  $100 \text{ W} \cdot \text{m}^{-2}$ ,  $300 \text{ W} \cdot \text{m}^{-2}$ ,  $530 \text{ W} \cdot \text{m}^{-2}$ ,  $640 \text{ W} \cdot \text{m}^{-2}$ , and  $1000 \text{ W} \cdot \text{m}^{-2}$ , with Z907 and  $[\text{Co}(\text{dbbip})_2](\text{ClO}_4)_2$  0.09 M,  $[\text{Co}(\text{dbbip})_2](\text{ClO}_4)_3$  0.01 M, TBP 0.2 M,  $\text{LiClO}_4$  0.2 M, in AN/EC (2:3).  $b/l$  ratio varies from 1.7 (open cells) to 10 (closed cells).

Even though the current density is the same during the first tenth of second, it rapidly decreases proportionally with  $b$ . As expected, this behavior is more marked at high irradiation intensities, where the diffusion limiting factor becomes dominant.

### 6.3. Combination of CE illumination and reduced distance between electrodes

Combining a small distance between the electrodes with a counter electrode side illumination may help to reduce the diffusion problems within the DSSC. Again this effect should be the highest at high irradiation intensities.

In order to test this, open cells with reversed TiO<sub>2</sub> layers were prepared. 4 μm of diffusive TiO<sub>2</sub> were screen-printed on the blocking layer and 3 μm of nanocrystalline TiO<sub>2</sub> were deposited on top of it. These cells were open cells, reducing the *b/l* ratio to about 1.7. An example of current dynamics spectrum is shown in Figure 48.

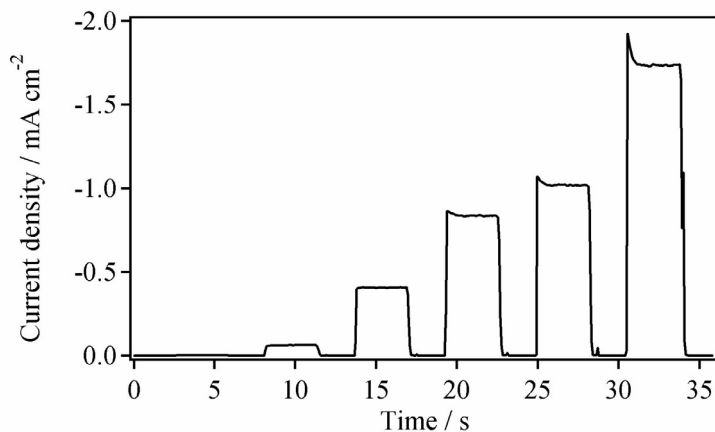


**Figure 48.** Example of current dynamics measured, from left to right, at 100 W · m<sup>-2</sup>, 300 W · m<sup>-2</sup>, 530 W · m<sup>-2</sup>, 640 W · m<sup>-2</sup>, and 1000 W · m<sup>-2</sup>, with Z907 and [Co(dbbip)<sub>2</sub>](ClO<sub>4</sub>)<sub>2</sub> 0.09 M, [Co(dbbip)<sub>2</sub>](ClO<sub>4</sub>)<sub>3</sub> 0.01 M, without additives, in AN/EC (2:3). *b/l* = 1.7.

Combining CE side illumination with a reduced distance between electrodes drastically reduces the diffusion problems within the solar cell and the linearity of the  $J_{sc}$  as a function of the irradiance intensity was maintained (Figure 49). As the incoming light has to cross part of the electrolyte before reaching the dye anchored on the TiO<sub>2</sub>, the incident radiative flux  $\phi_0$  will decrease to  $\phi$  accordingly to Eq. 4.33.

$$\phi = \phi_0 \cdot 10^{-(\varepsilon \cdot c \cdot l)} \quad (4.33)$$

As  $\phi$  is related to  $J_{sc}$  through Eq. 4.34, a diminution of  $\phi$  will therefore reduce the value of  $J_{sc}$ .

$$IPCE(\lambda) = 1240 \cdot \frac{J_{sc}}{\lambda \cdot \phi} \quad (4.34)$$

Figure 49 also displays the values of  $J_{sc}$  as a function of irradiance intensity for a normal TiO<sub>2</sub> layer (diffusive layer on top of the nanoporous one).

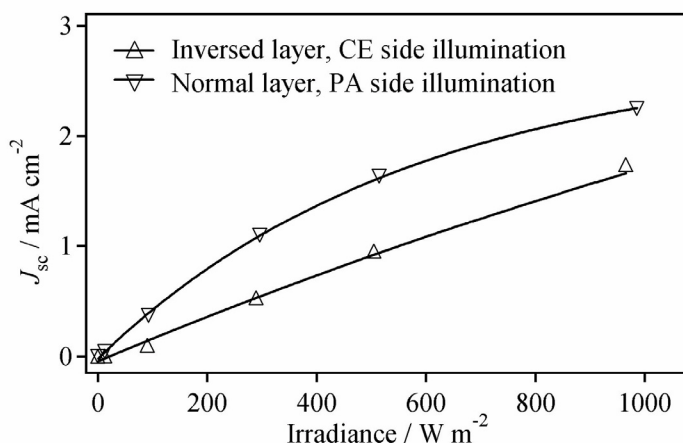


**Figure 49.** Short circuit current density as a function of irradiance for a normal layer with nanocrystalline  $\text{TiO}_2$  deposited on a TCO glass and covered by a diffusive  $\text{TiO}_2$  layer and for an inverted layer, where the nanocrystalline layer is on top of the diffusive one. With the normal layer, the cells were irradiated from the photoanode side whereas for the inverted layer they were illuminated from the counter electrode side.

In spite of the linearity of the  $J_{sc}$  with the increasing irradiance is no longer respected in a normal layer configuration, the difference of short circuit current density between the two types of cells is clearly in favor of the normal layer, the incident radiative flux arriving directly on the dye molecules, without first crossing the electrolyte.

## 7. References to Chapter 4

- [1] Sundberg, R. J.; Martin, R. B. *Chem. Rev.* **1974**, *74*, 471.
- [2] Shklover, V.; Liska, P.; Zakeeruddin, S. M.; Nazeeruddin, M. K.; Grätzel, M.; Nesper, R.; Hermann, R. SPIE 38th Int. Symp. Optical Applied Science and Engineering. **1993**, San Diego, CA.
- [3] Shklover, V.; Eremenko, I. L.; Berke, H.; Nesper, R.; Zakeeruddin, S. M.; Nazeeruddin, M. K.; Gratzel, M. *Inorg Chim Acta* **1994**, *219*, 11.
- [4] Bonhôte, P.; Grätzel, M.; Jirousek, M.; Liska, P.; Pappas, N.; Vlachopoulos, N.; Planta, C. V.; Walder, L. Redox Mediators for Electrochemical Photovoltaic Cells Based on Dye-Sensitized TiO<sub>2</sub> Electrodes; 10th International Conference on Photochemical Conversion and Storage of Solar Energy (IPS-10). **1994**, 191. Interlaken, Switzerland.
- [5] Fisher, A. C.; Peter, L. M.; Ponomarev, E. A.; Walker, A. B.; Wijayantha, K. G. U. *J. Phys. Chem. B* **2000**, *104*, 949.
- [6] Duffy, N. W.; Peter, L. M.; Rajapakse, R. M. G.; Wijayantha, K. G. U. *Electrochem. Commun.* **2000**, *2*, 658.
- [7] Oskam, G.; Bergeron, B. V.; Meyer, G. J.; Searson, P. C. *J. Phys. Chem. B* **2001**, *105*, 6867.
- [8] Cameron, P. J.; Peter, L. M. *Coordination Chemistry Reviews* **2003**.
- [9] Benech, J.-M.; Piguet, C.; Bernardinelli, G.; Bunzli, J.-C. G.; Hopfgartner, G. *J. Chem. Soc., Dalton Trans.* **2001**, 684.
- [10] Gaspar, A. B.; Munoz, M. C.; Niel, V.; Real, J. A. *Inorg. Chem.* **2001**, *40*, 9.
- [11] Saha, A.; Ghosh, A. K.; Majumdar, P.; Mitra, K. N.; Mondal, S.; Rajak, K. K.; Falvello, L. R.; Goswami, S. *Organometallics* **1999**, *18*, 3772.
- [12] Pelet, S.; Moser, J. E.; Gratzel, M. *J Phys Chem B* **2000**, *104*, 1791.
- [13] Nusbaumer, H.; Moser, J. E.; Zakeeruddin, S. M.; Nazeeruddin, M. K.; Grätzel, M. *J. Phys. Chem. B* **2001**, *105*, 10461.
- [14] Wang, P.; Zakeeruddin, S. M.; Comte, P.; Charvet, R.; Humphry-Baker, R.; Grätzel, M. *J. Phys. Chem. B* **2004**.
- [15] Nakade, S.; Saito, Y.; Kubo, W.; Kanzaki, T.; Kitamura, T.; Wada, Y.; Yanagida, S. *Electrochemistry Communications* **2003**, *5*, 804.
- [16] Krüger, J. Interface engineering in solid-state dye-sensitized solar cells, Ecole Polytechnique Fédérale de Lausanne, 2003.

- [17] Moser, J. E.; Noukakis, D.; Bach, U.; Yasuhiro, Y.; Klug, D. R.; Durrant, J. R.; Humphry-Baker, R.; Grätzel, M. *J. Phys. Chem. B* **1998**, *102*, 3649.
- [18] Duffy, N. W.; Peter, L. M.; Rajapakse, R. M. G.; Wijayantha, K. G. U. *J. Phys. Chem. B* **2000**, *104*, 8916.
- [19] Huang, S. Y.; Schlichthörl, G.; Nozik, A. J.; Grätzel, M.; Franck, A. J. *J. Phys. Chem. B* **1997**, *101*, 2576.
- [20] Nakade, S.; Kambe, S.; Kitamura, T.; Wada, Y.; Yanagida, S. *J. Phys. Chem. B* **2001**, *105*, 9150.
- [21] Kambe, S.; Nakade, S.; Kitamura, T.; Wada, Y.; Yanagida, S. *J. Phys. Chem. B* **2002**, *106*, 2967.
- [22] Enright, B.; Redmond, G.; Fitzmaurice, D. *J. Phys. Chem.* **1994**, *98*, 6195.
- [23] Sapp, S. A.; Elliott, C. M.; Contado, C.; Caramori, S.; Bignozzi, C. A. *J. Am. Chem. Soc.* **2002**, *124*, 11215.
- [24] Papageorgiou, N.; Grätzel, M.; Infelta, P. *Sol. Energy Mater.* **1996**, *44*, 405.



The aim of the present work was to find and study efficient alternative redox couples for the dye-sensitized solar cell that could rival the classical triiodide/iodide couple. The compounds studied here were triarylaminines, platinum complexes and cobalt complexes.

Triarylaminines and platinum complexes did not match our expectation with respect to photoelectrochemical efficiencies. Triarylaminines showed low solubility properties and important diffusion problems, giving low photocurrents and *IPCE* values. Using a liquid triarylamine, TMEPA, however solved the solubility problems and gave the highest performances amongst all the investigated triarylaminines but high dark currents reduced its efficiency. Though electrolyte optimizations with platinum complexes were realized, photoelectrochemical efficiencies remain very low and never rivaled those of triiodide/iodide couple. This results mainly from interactions between the platinum complex and the dye, a ruthenium complex, anchored on the TiO<sub>2</sub> surface. Absorption spectroscopy showed that the sensitizer desorbed from the surface after interacting with the platinum complex. This effect reduced the *IPCE* nearly to zero.

Cobalt complexes displayed far more interesting behavior when used as redox couples in dye-sensitized solar cells. The experiments carried out have shown that derivatives of the [Co(bip)<sub>2</sub>]<sup>3+/2+</sup> complexes are the most promising candidates to be used as redox mediators. Their photoelectrochemical and kinetic behavior can rival the performance of the triiodide/iodide redox couple. Many optimizations of the system were performed during this study. In particular, the following ones:

### *Interfaces optimization*

- The interaction between the sensitizer and the redox mediator in solution is of greatest importance for the rate of dye regeneration. Heteroleptic dyes were found to belong to the most appropriate category of dye. Using long alkyl chains bound to these dyes the DSSC efficiency was further improved through the reduction of the dark current within the cells.
- Co-grafting sensitizer and co-adsorbent HHDA has yielded improved photovoltaic efficiencies through an increased photocurrent. The increase in current was explained by a reduction of the trap density in the TiO<sub>2</sub> and a reduction of the electron recombination rate with the dye through the barrier effect brought about by the long chains of the co-adsorbent.
- Silver addition in the dye solution lead to a global improvement of the photovoltaic parameters. The chemical reaction of Ag<sup>+</sup> with the thiocyanate ligands of the dye molecules allowed a higher dye molecules density on the TiO<sub>2</sub> surface.
- Due to diffusion problems when using such big molecules as cobalt complexes within a DSSC, very thin nanocrystalline TiO<sub>2</sub> layers were employed, e.g. the optimal system comprised of a 2–3 μm nanocrystalline layer used with a large 3–4 μm scattering layer.
- As cobalt complexes may undergo electrochemical processes on the SnO<sub>2</sub> layer deposited on the glass support, a blocking layer of compact TiO<sub>2</sub> had a beneficial effect on the dark current of the cell.
- Even if electrochemical reactions can be observed with SnO<sub>2</sub> and cobalt complexes, these are not fast enough to support cell function and the counter electrode must be covered with either a platinum or gold layer to ensure a sufficient rate of electron transfer to the oxidized complex.

### *Optimization of electrolytes*

The optimization of the electrolyte mainly concerned the choice of solvent, the redox mediator concentration, the degree of oxidation, the additives that can be used to improve the photovoltaic parameters and finally how to increase the redox couple solubility.

The best efficiencies were reached using the AN/EC (2:3) solvent mixture. Nevertheless,  $\gamma$ -butyrolactone used with higher redox concentration (e.g. 0.18 M) gave promising results. Methoxyacetonitrile used with the [Co<sup>III/II</sup>(dobip)<sub>2</sub>] couple also performed well.



With the AN/EC solvent mixture, the optimal redox mediator concentration was found to be between 0.10 M to 0.15 M. At higher concentrations, although the rate of dye regeneration still increases, the viscosity of the electrolyte also increases, which reduces the fill factor and therefore the efficiency. With a 10% concentration of the oxidized Co(III) species present, the current density reaches its maximum and the photovoltage remains at high values.

4-*tert*-butylpyridine (TBP) and lithium perchlorate were tried as additives in the electrolyte. TBP tends to increase the photovoltage whereas  $\text{Li}^+$  improves the photocurrent. The optimized concentrations of these two additives was TBP 0.05 M and  $\text{LiClO}_4$  0.1 M when the total cobalt complex concentration was 0.1 M.

### ***Mass-transport optimizations***

Mass-transport within the cell is one of the most crucial limitations when using cobalt complexes as redox mediators. Attempts to reduce the solvent viscosity through the use of alternative solvents to the AN/EC mixture were not successful as the cobalt complex was not soluble enough in that kind of solvents. One efficient way to solve the diffusion problem was to irradiate the cell from the counter electrode side. This method works well at high irradiation intensities but is useless under 50% Sun. Shortening the distance between the electrodes also reduced the diffusion limitation. However even with open cells where the distance between the two electrodes was at the minimum, this diffusion limitation was still seen.

### ***Photoelectrochemical results***

Efficient dye-sensitized solar cells using optimized cobalt based electrolytes and electrode interfaces were measured with the solar simulator. The best results were obtained using  $[\text{Co}(\text{dbbip})_2](\text{ClO}_4)_2$  0.13 M,  $[\text{Co}(\text{dbbip})_2](\text{ClO}_4)_3$  0.015 M,  $\text{LiClO}_4$  0.2 M and TBP 0.1 M in AN/EC (2:3). The photoelectrode was dipped into a dye solution containing the heteroleptic dye Z907 and  $\text{AgNO}_3$  (2:1) in *tert*-butanol/acetonitrile. This photoelectrode consisted of a thin  $\text{TiO}_2$  layer of 3  $\mu\text{m}$  deposited on a TCO glass with a blocking  $\text{TiO}_2$  underlayer used to prevent the reduction of Co(III) on the  $\text{SnO}_2$  layer and covered by a 3  $\mu\text{m}$  scattering layer. The counter electrode was platinized TCO glass. The cell was an open cell. Photoelectrochemical data are shown in Table 1 and some I/V curves in Figure 1.

**Table 1.** Example of high efficiency DSSC obtained with an electrolyte made of  $[\text{Co}(\text{dbbip})_2](\text{ClO}_4)_2$  0.13 M,  $[\text{Co}(\text{dbbip})_2](\text{ClO}_4)_3$  0.015 M,  $\text{LiClO}_4$  0.2 M and TBP 0.1 M in AN/EC (2:3). Sensitizer: Z907 and  $\text{AgNO}_3$  (2:1) in tert-butanol/acetonitrile. Photoelectrode: compact  $\text{TiO}_2$  blocking underlayer on TCO glass, 3  $\mu\text{m}$  thick nanocrystalline  $\text{TiO}_2$  layer, 3  $\mu\text{m}$  thick diffusive layer. Counter electrode: platinum layer deposited onto TCO glass.

Irradiance [ $\text{W} \cdot \text{m}^{-2}$ ]	12	90	950
$V_{\text{oc}}$ [mV]	700	790	865
$J_{\text{sc}}$ [ $\text{mA} \cdot \text{cm}^{-2}$ ]	0.23	1.35	9.50
$FF$ [-]	0.77	0.75	0.54
Efficiency [%]	7.77	8.16	4.42

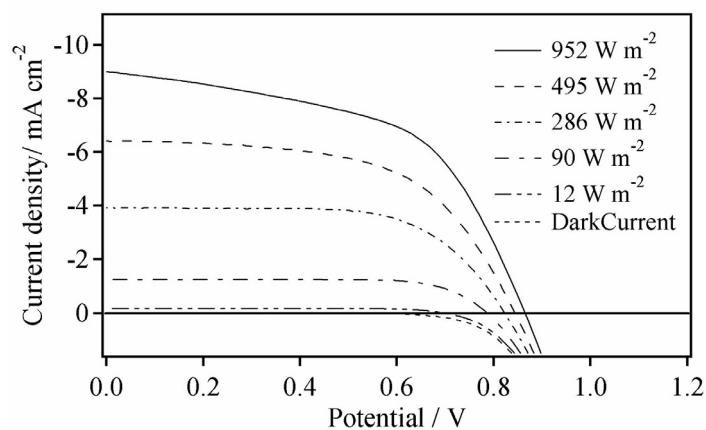


**Figure 1.** Example of I/V curves at different irradiance using the same electrolyte and electrodes as described in Table 1.

---

CHAPTER  
**SIX**

Appendix

6

---

## 1. List of symbols

Symbol	Description	Units
$\alpha$	absorption coefficient	$\text{cm}^{-1}$
$a$	diameter	m or Å
$a$	radius of an UME	$\mu\text{m}$
$A$	area	$\text{m}^2$
$A$	optical absorbance	–
$b$	bulk layer thickness	$\mu\text{m}$
$\beta$	dumping factor	$\text{Å}^{-1}$
$c$	concentration	$\text{M} = \text{mol} \cdot \text{L}^{-1}$
$\delta$	diffusion layer thickness	$\mu\text{m}$ or Å
$D$	diffusion coefficient	$\text{cm}^2 \cdot \text{s}^{-1}$
$\Delta_{\text{O}}$	ligand-field splitting parameter	eV
$\varepsilon$	molar extinction coefficient	$\text{mol}^{-1} \cdot \text{L} \cdot \text{cm}^{-1}$
$E$	energy	J or eV
$E^\circ$	standard reduction redox potential	V
$E^{\circ'}$	formal reduction redox potential	V
$E_{1/2}$	half-wave potential	V
$E_{\text{f}}$	Fermi level	eV
$E_{\text{g}}$	band gap energy	eV
$\varepsilon_{\text{p}}$	porosity	–
$\phi$	electrochemical potential	V
$\phi$	incident radiative flux or irradiance	$\text{W} \cdot \text{m}^{-2}$
$\Phi$	quantum yield	–
$FF$	fill factor	%
$\Gamma$	coverage	$\text{cm}^{-2}$
$\eta$	photovoltaic efficiency	%
$\eta$	viscosity	cP or $\text{Pa} \cdot \text{s}$
$I$	current	A
$I_{\text{d}}$	limiting diffusion current	A
$IPCE$	incident photon-to-current conversion efficiency	%
$I_{\text{ph}}$	photocurrent	A

Symbol	Description	Units
$I_s$	saturation current	A
$I_{sc}$	short circuit current	mA
$J$	current density	$\text{mA} \cdot \text{m}^{-2}$ or $\mu\text{A} \cdot \text{cm}^{-2}$
$J_{sc}$	short circuit density current	$\text{mA} \cdot \text{m}^{-2}$ or $\mu\text{A} \cdot \text{cm}^{-2}$
$k$	rate constant	$\text{s}^{-1}$
$k^\circ$	standard heterogeneous rate constant	$\text{cm} \cdot \text{s}^{-1}$
$l$	nanocrystalline film thickness	$\mu\text{m}$
$\lambda$	wavelength	nm
$LFSE$	ligand field stabilization energy	eV
$LHE$	light harvesting efficiency	%
$M$	molar mass	$\text{kg} \cdot \text{mol}^{-1}$
$n$	ideality factor	–
$n$	number of electrons	–
$\nu$	wavelength	nm
$P_{in}$	incident radiation power	W
$P_m$	maximal power output	W
$\theta$	angle	°
$\rho$	density of electronic acceptor states	$\text{nm}^{-2}$
$r$	radius	$\mu\text{m}$ or $\text{Å}$
$R_L$	load resistance	$\Omega$
$R_s$	series resistance	$\Omega$
$R_{sh}$	shunt resistance	$\Omega$
$\sigma$	cross-section	$\text{nm}^2$ or $\text{cm}^2$
$\tau$	electron lifetime	s
$T$	temperature	K or °C
$T$	transmission	%
$\tau_{1/2}$	half reaction time	s
$V$	volume	$\text{m}^3$ or $\text{Å}^3$
$V_a$	applied voltage	V
$V_{oc}$	open circuit voltage	V
$V_t$	thermal voltage	V

## 2. Glossary of abbreviations

Abbreviation	Definition
1-TNATA	4,4',4''-tris-(N-(1-naphthyl)-N-phenylamino)-triphenylamine
AM	air mass
a-Si	amorphous silicon
ATR	attenuated total reflection spectroscopy
bipy	2,2'-bipyridine
cb	conduction band
CE	counter electrode
CIS	copper indium diselenide
dbbip	2,6-bis(1'-butylbenzimidazol-2'-yl)pyridine
DDS	dodecylsulfate
DH-TPD	N,N'-diphenyl-N,N'-bis(3-hydroxyphenyl)-(1,1'-biphenyl)-4,4'-diamine
DMBI	1,2-diethyl-3-butylimidazolium
dmbip	2,6-bis(1'-methylbenzimidazol-2'-yl)pyridine
dmebip	2,6-bis(1'-methoxyethylbenzimidazol-2'-yl)pyridine
DMPBPA	N,N'-bis-(3,4-dimethylphenyl)biphenyl-4-amine
DM-TPD	N,N'-diphenyl-N,N'-bis(3-methylphenyl)-(1,1'-biphenyl)-4,4'-diamine
dobip	2,6-bis(1'-octylbenzimidazol-2'-yl)pyridine
DSSC	dye-sensitized solar cell
EC	ethylenecarbonate
EMI	1-ethyl-3-methylimidazolium
FTIR	Fourier transform infrared spectroscopy
FZ	float zone
GB	4-guanidinobutyrate
$\gamma$ BL	$\gamma$ -butyrolactone
HDMA	hexadecylmalonic acid
HHDA	16-hydroxyheadecanoic acid
HOMO	highest occupied molecular orbital
LUMO	lowest unoccupied molecular orbital
M	redox mediator
M+	oxidized redox mediator
MLCT	metal-to-ligand charge transfer
MPN	methoxypropionitrile
N3	<i>cis</i> -di(thiocyanato)-bis(2,2'-bipyridyl-4,4'-dicarboxylic acid)-ruthenium(II)

Abbreviation	Definition
N621	<i>cis</i> -di(thiocyanato)-(2,2'-bipyridyl-4,4'-dicarboxylic acid)(4,4'-ditridecyl-2,2'-bipyridyl)-ruthenium(II)
N719	<i>cis</i> -di(thiocyanato)-bis(2,2'-bipyridyl-4-carboxylate-4'-carboxylic acid)-ruthenium(II)
N820	<i>cis</i> -di(thiocyanato)-(2,2'-bipyridyl-4,4'-dicarboxylic acid)(4,4'-dimethyl-2,2'-bipyridyl)-ruthenium(II)
N823	<i>cis</i> -di(thiocyanato)-(2,2'-bipyridyl-4,4'-dicarboxylic acid)(4,4'-dihexyl-2,2'-bipyridyl)-ruthenium(II)
NMR	nuclear magnetic resonance
OPO	optical parametric oscillator
OTf	trifluoromethanesulfonate
Ox	oxidized species
PE	photoelectrode
phen	1,10-phenanthroline
<i>p</i> -MTDATA	4,4',4''-tris-( <i>N</i> -3-methylphenyl)- <i>N</i> -phenylamino)-triphenylamine
PTS	<i>p</i> -toluenesulfonic acid
QMS	quasi-monocrystalline silicon
Red	reduced species
S	sensitizer in its fundamental state
S*	sensitizer in an excited state
S <sup>+</sup>	oxidized sensitizer
SC	semiconductor
SCE	standard calomel electrode
TBP	4- <i>tert</i> -butylpyridine
TCO	transparent conducting oxide
terpy	2,2':6',2''-terpyridine
Tf <sub>2</sub> N	bis((trifluoromethyl)sulfonyl)amide
TFMC	trifluoromethanecarboxylate
TFSI	bis(trifluoromethanesulfonyl)imide
TMS	tetramethylsilane
ttpy	4'-(4-tolyl)-2,2':6',2''-terpyridine
UME	ultramicroelectrode
UV	ultraviolet light
Vis	visible light
XPS	x-ray photoelectron spectroscopy
XRD	x-ray diffraction

Abbreviation	Definition
Z316	<i>cis</i> -di(thiocyanato)-(2,2'-bipyridyl-4,4'-dicarboxylic acid)(4-methyl-4'-hexadecyl-2,2'-bipyridyl)-ruthenium(II)
Z907	<i>cis</i> -di(thiocyanato)-(2,2'-bipyridyl-4,4'-dicarboxylic acid)(4,4'-dinonyl-2,2'-bipyridyl)-ruthenium(II)



### 3. Physical constants

Symbol	Description	Value
$c$	speed of light	$2.9979 \cdot 10^8 \text{ m} \cdot \text{s}^{-1}$
$e$	elementary charge	$1.6022 \cdot 10^{-19} \text{ C}$
$F$	Faraday constant	$9.6485 \cdot 10^4 \text{ C} \cdot \text{mol}^{-1}$
$h$	Planck constant	$6.6262 \cdot 10^{-34} \text{ J} \cdot \text{s}$
$k$	Boltzmann constant	$1.3807 \cdot 10^{-23} \text{ J} \cdot \text{K}^{-1}$
$N_A$	Avogadro number	$6.0220 \cdot 10^{23} \text{ mol}^{-1}$

## 4. Curriculum vitæ

Hervé Nusbaumer, born on May 2, 1975 in Moutier (BE), Switzerland.

2000 - 2003                    **Ecole Polytechnique Fédérale de Lausanne, Laboratoire de photo-  
nique et interfaces**

PhD Thesis: Alternative redox systems for the dye.sensitized solar cell

2000                             Diploma Degree in Chemical Engineering

1999 - 2000                   **Ecole Polytechnique Fédérale de Lausanne, Laboratoire de photo-  
nique et interfaces**

Diploma work: Développement de cellules solaires à colorant de grandes dimensions.

1994 - 2000                   **Ecole Polytechnique Fédérale de Lausanne**

Studies in chemical engineering

1991 - 1994                   **Lycée cantonal de Porrentruy**

### 4.1. Publications

Nusbaumer, H.; Moser, J.-E.; Zakeeruddin, S. M.; Nazeeruddin, M. K.; and Grätzel, M. **Co<sup>II</sup>(dbbip)<sub>2</sub><sup>2+</sup> Complex Rivals Tri-iodide/Iodide Redox Mediator in Dye-Sensitized Photovoltaic Cells** *J. Phys. Chem. B* **2001**, *105*, 10461-10464.

Nusbaumer, H.; Zakeeruddin, S. M.; Moser J. E.; and Grätzel, M. **An Alternative Efficient Redox Couple for the Dye-Sensitized Solar Cell System** *Chem. Eur. J.* **2003**, *9*, 3756-3763.

### 4.2. Conferences

Joint Meeting of the Italian, French, and Swiss Photochemistry Groups, February 25-27, 2001, Lausanne, Switzerland.

10th International Conference on Unconventional Photoactive Systems (UPS'01) September 4-8, 2001, Les Diablerets, Switzerland.

14th International Conference on Photochemical Conversion and Storage of Solar Energy (IPS), August 4-9 2002, Sapporo, Japan.

### 4.3. Posters

Nusbaumer, H.; Moser, J.-E.; Zakeeruddin S. M.; and Grätzel M. **Effect of a New Redox Mediator on the Interception of Back Electron Transfer in the Dye Sensitization of Nanocrystalline TiO<sub>2</sub>**. Presented at the Joint Meeting of the Italian, French, and Swiss Photochemistry Groups, February 25-27, 2001, Lausanne, Switzerland.

Nusbaumer, H.; Zakeeruddin, S. M.; and Grätzel, M. **Alternative Efficient Redox Couple for the Dye-Sensitized Solar Cell**. Presented at the IPS conference, August 4-9 2002, Sapporo, Japan.

